Development of DEPFET sensors with advanced functionality for applications in X-ray astronomy

Dissertation
der Mathematisch-Naturwissenschaftlichen Fakultät
der Eberhard Karls Universität Tübingen
zur Erlangung des Grades eines
Doktors der Naturwissenschaften
(Dr. rer. nat.)

vorgelegt von
Dipl.-Ing (FH) Alexander Bähr
aus Landshut

Tübingen
2017

Gedruckt mit Genehmigung der Mathematisch-Naturwissenschaftlichen Fakultät der Eberhard Karls Universität Tübingen.

Tag der mündlichen Qualifikation:	31.07.2017
Dekan:	Prof. Dr. Wolfgang Rosenstiel
1. Berichterstatter:	Prof. Dr. Andrea Santangelo
2. Berichterstatter:	Prof. Dr. Josef Jochum

Eberhard-Karls-
Universität Tübingen

Max-Planck-Institut für
extraterrestrische Physik

Abstract

Athena is ESA's next generation observatory for X-ray astronomy. One of its two focal-plane instruments is the WFI, a large area, pixelated silicon-detector for imaging spectroscopy that will provide an unmatched field of view and the capability to observe even brightest radiation sources with high throughput.
The WFI's sensor will be based on the combined sensor-amplifier structure DEPFET. This concept provides a high flexibility in terms of device readout and permits to add various functional features into each pixel of the detector.
It is for instance, possible to implement a pixel wise electronic shutter and furthermore, provide every pixel with an additional storage area. In this thesis, these DEPFET concepts with enhanced functionality are evaluated with respect to a potential use as building block for Athena's WFI. The focus was thereby on the application of a DEPFET based sensors as high count rate spectrometer and the influence and mitigation of readout artifacts on the spectral response of the sensor.
To improve the understanding of the different concepts, a series of device simulations was carried out. Parts of these simulations were used as input for the layout of novel devices.
To study the properties of the different DEPFET devices, a flexible measurement setup was designed, assembled and operated. With that setup, the properties of different DEPFETs were investigated. Especially time dependent readout artifacts were studied and models to describe these were developed. In the course of this thesis it was furthermore possible to confirm the basic functionality of the first devices providing an additional storage area.
Based on the device simulations as well as measurements, spectral simulations were conducted. These show that a DEPFET is capable to do spectroscopy even at fastest timings. However, the spectral performance will deteriorate drastically due to readout artifacts. While the pixel-wise built-in shutter provides good spectral response it severely limits the throughput at fast timings due to the required deadtime. An additional storage area provides both, good spectral performance and high throughput even at fastest timings.

Zusammenfassung

Athena ist das nächste große Observatorium für Röntgenastronomie der ESA. Eines der zwei Instrumente in Athenas Fokalebene ist der WFI, ein großflächiger, pixelierter Silizium Sensor für ortsaufgelöste Röntgenspektroskopie, der gleichzeitig ein bisher nicht erreichtes Gesichtsfeld und höchste Zählratenfähigkeit bietet.
Der Sensor des WFI basiert auf der kombinierten Sensor-Verstärker Struktur DEPFET. Neben der hohen Flexibilität bezüglich der Auslese, ist es möglich verschiedenste zusätzliche Eigenschaften in jeden Pixel eines größeren Sensors zu Implementieren.
So ist es zum Beispiel möglich jeden Pixel mit einer elektronischen Blende zu versehen. Diese kann außerdem um einen Speicherbereich für Elektronen erweitert werden.
In dieser Arbeit wurden diese verbesserten DEPFET Konzepte in Hinblick auf einen Einsatz für den WFI untersucht. Der Fokus wurde dabei auf die Anwendung eines DEPFET-basierten Sensors als Hochzählratenspektrometer gelegt. Insbesondere wurden Ausleseartefakte und möglichkeiten zur Unterdrückung dieser untersucht.
Zum besseren Verständnis der verschiedenen Konzepte wurden Device Simulationen durchgeführt. Teile dieser Simulationen wurden für das Design von neuartigen Sensor Strukturen verwendet.
Im Rahmen dieser Arbeit wurde ein flexibler Messaufbau designet, aufgebaut und genutzt um die verschiedenen Sensorstrukturen zu vermessen. Insbesondere wurden Zeitabhängige Ausleseartefakte untersucht und Modelle um diese zu beschreiben erarbeitet. Im Rahmen dieser Messungen wurde außerdem die grundsätzliche Funktionalität der ersten DEPFET Prototypen mit eingebautem Speicherbereich nachgewiesen.
Basierend auf Device-Simulationen und Messergebnissen wurden spektrale Simulationen angefertigt. Diese zeigen, dass ein DEPFET Sensor auch bei hohen Frame-Raten als Spektrometer genutzt werden kann. Aufgrund der hohen Wahrscheinlichkeit für Auslesartefakte verschlechtern sich jedoch die spektroskopischen Eigenschaften. Durch einen eingebauten Shutter, wird eine Beeinflussung der spektroskopischen Eigenschaften verhindert, jedoch ist der Durchsatz einer solchen Struktur bei schnellem Betrieb durch die auftretende Totzeit limitiert. Durch einen zusätzlichen Speicherbereich, wird diese Totzeit vermieden und eine gute spektrale Auflösung mit hohen Durchsatz ermöglicht.

Table of Contents

1. Introduction

"No matter how fast light travels, it finds the darkness has always got there first and is waiting for it."

— Terry Pratchett, Reaper Man

For every answered question at least one new is raised. Nevertheless, the knowledge of mankind is extended one step at a time using available tools and new ideas to access previously unknown territories.

One example for this process is the vast field of X-ray astronomy. X-rays were first detected in the end of the 19th century. With their discovery and the following research a rapid progress in several fields as medicine, material analysis, engineering and science in general took place. Within this progress, attempts to observe the sky in the X-ray band were undertaken. Since X-rays are not capable to penetrate the earth's atmosphere, the observation of extraterrestrial X-ray sources requires the operation of instrumentation at high altitudes. First studies to examine the X-ray emission of the nearest celestial objects like the Sun and Moon were done in the late 1940s using sounding rockets. As a result of these experiments, the first celestial X-ray source (Scorpio X-1) was discovered in 1962 (see Giacconi et al. 1962). Later these experiments were extended with observations by balloons and satellites to grant longer exposure times. Actually, from the beginning until the present day, X-ray astronomy has utilized innovative technologies and has thus been capable of providing new discoveries with astounding continuity. In several cases new or improved detector properties, such as angular resolution, time resolution or high spectral accuracy, made it possible to observe phenomena which were previously unknown (for a comprehensible history of X-ray astronomy with a focus on instrumentation see e.g. Fraser 1989).

Today the Instrumentation portfolio of astrophysicists includes several satellites. Two of the most famous X-ray observatories are Chandra and XMM-Newton. Chandra was launched 1999 by NASA. Its mirror system provides an effective area of 800 cm^2 for low energetic photons and an angular resolution of 0.5" Full Width at Half Maximum (FWHM). It is equipped with two Charge Coupled Device (CCD) based instruments, ACIS-I and ACIS-S. ACIS-I provides imaging over a Field of View (FOV) of 16.9' x 16.9' with moderate spectral resolution. The primary objective of ACIS-S is the readout of Chandras two high resolution grating spectrometers. In addition it can also be used for imaging spectroscopy similar to ACIS-I (Chandra X-ray Center 2016). XMM-Newton was launched at the end of 1999 and is operated by the ESA. It is equipped with a mirror system that provides 1600 cm^2 of effective area and an spatial resolution

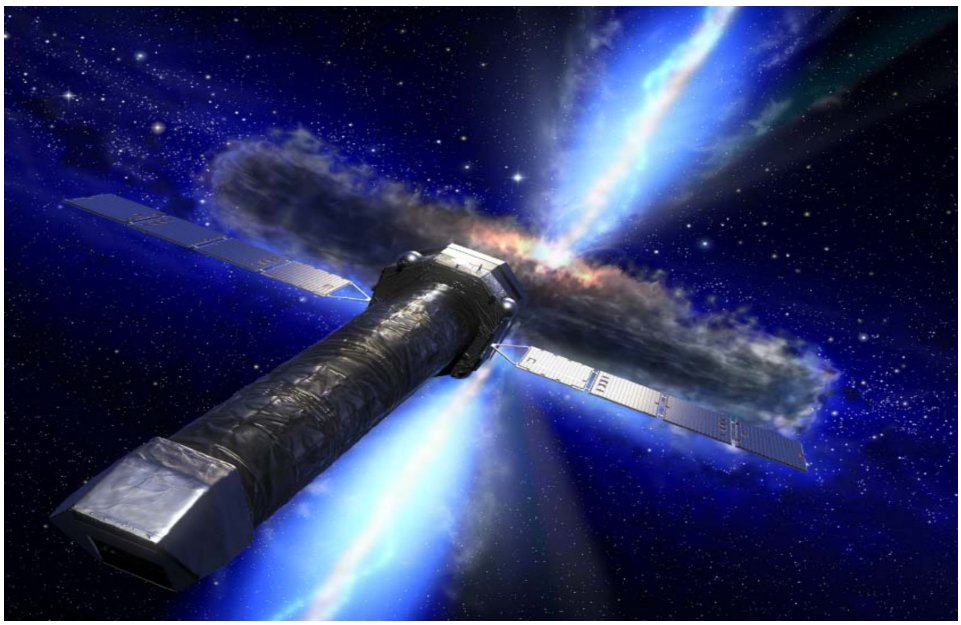

Figure 1.1.: ATHENA is the next generation X-ray observatory and currently under development. Shown is an artist's view of the ATHENA satellite.

of about 6" FWHM. It is equipped with multiple CCD based spectrometers for imaging spectroscopy over a FOV of 30' x 30' and a grating instrument for high resolution spectroscopy. In addition XMM-Newton is equipped with a co-aligned UV/optical telescope, the Optical Monitor (OM), that provides simultaneous observations of X-ray and optical emission (XMM-Newton SOC 2016).
The next large mission for X-ray astrophysics is the Advanced Telescope for High ENergy Astrophysics (ATHENA). An artist's view of the ATHENA satellite is shown in figure 1.1. ATHENA is part of the Cosmic Vision program of the European Space Agency (ESA) and will be designed to answer key questions of "The Hot and Energetic Universe" (Nandra et al. 2013). ATHENA is going to provide order-of-magnitude leaps in observational capabilities. As experience has shown these will unquestionably result in breakthroughs of our astrophysical understanding (Lumb et al. 2012).

Prospect of the Following Chapters

This thesis is divided into five chapters. In the first chapter, the science cases Athena is intended to address are discussed. Furthermore, the Athena satellite and its payload, consisting of a large scale X-ray mirror assembly and two spectroscopic instruments will be described. In chapter 3, the physical limitations of silicon sensors in general and the properties of DEPleted Field Effect Transistors (DEPFETs) in particular will be introduced. The focus is thereby on the typical operation of DEPFET matrices for spaceborn applications and X-ray spectroscopy. Furthermore, the effect of timing related readout artifacts is discussed.

In chapter 4 new DEPFET concepts are presented and investigated using device simulations as well as experimental tests results. Furthermore, a study of the spectral response of different DEPFET devices operated in "fast timing" conditions is presented. In addition, the benefit provided by a built-in shutter and an additional storage is discussed in that chapter. Although the functionality of the tested prototypes was proven, a number of possible improvements for future devices is discussed. A summary of all simulations and measurements is provided in section 4.5.
The conclusions can be found in chapter 5. In addition further steps as well as applications of the studied DEPFET concepts in other fields of science are illustrated.

"Why bother with a cunning plan if a simple one will do?"

—TerryPratchett, Thud!

2. Science Case and the Athena Mission

Over the course of the last century, X-ray observations lead to a rapid progress of our understanding of both astrophysics and cosmology. This is largely owed to the improvements in instrumentation that allowed new and higher quality observations . So it is to date largely assured, that the universe consists of baryronic- and dark matter as well as dark energy. Furthermore, all observational evidence hints, that the universe expanded from a small, dense state into the large scale structures we observe today. Although current cosmological and astrophysical models are capable to describe many of the observations made (e.g. evolution of stars, expansion of the universe, apparent acceleration of the universes expansion), the exact values of model parameters, and in some cases even the models to use, are not well constrained.
Astrophysical observations cover the complete range of the electromagnetic spectrum from microwaves over the infrared and visual band, UV, soft and hard X-rays from a few eV up to several hundred keV and Gamma-rays in the TeV range. The X-ray band, from about 0.1 keVup to 20 keV, provides unique insight into the composition of hot gases and plasma, which is the primary state of matter within stars, in the intergalactic medium and matter accreting towards dense objects.
While current and planned X-ray observatories are capable to provide many information about the universe, their capabilities in terms of angular resolution, time resolution, spatial and spectral resolution as well as collection area, are limited and show an incomplete picture of our universe. The ATHENA observatory will be unique in its combination of large effective area, good angular resolution, high spectral resolution, large field of view and high count-rate capability. This combination will allow observations with unprecedented accuracy.
Before providing details about the ATHENA satellite, its optics as well as X-ray spectrometers, the scientific objectives will be presented. In addition, one particular science case, which is the measurement of the spin of black holes, that of bright galactic black hole binary systems in particular, is discussed in more detail.

2.1. Science Case

The ATHENA mission is designed to address the science cases presented in the white paper "The Hot and Energetic Universe" (Nandra et al. 2013). The two astrophysical questions stated therein are "How does ordinary matter assemble into the large scale structures we observe today?" and "How do black holes grow and shape the universe?".

In the following sections, the observational goals and the proposed scientific outcome, will be discussed. By answering these questions, ATHENA will provide a major leap forward in our understanding of Cluster, Group and Galaxy formation, the interplay of SMBH at the center of galaxies with their surrounding and shed light on the growth of SMBH and the evolution of baryonic matter over cosmic time scales. The discussion follows the white paper (Nandra et al. 2013) as well as the ATHENA supporting papers (Pointecouteau et al. 2013; Ettori et al. 2013; Croston et al. 2013; Kaastra et al. 2013; Arid et al. 2013; Georgakakis et al. 2013; Cappi et al. 2013; Dovciak et al. 2013; Motch et al. 2013) and references therein.

2.1.1. The Hot Universe: How does ordinary Matter assemble into the large Scale Structures we observe Today

Galaxies, composed of planets, stars, black holes, hot gas and dust clouds are observed in larger gravitationally bound structures like groups and clusters. Within groups and clusters, a hot gas, the Intra Cluster Medium (ICM), fills the space between galaxies and independent clusters are connected through filaments of gas. While clusters are still in the process of formation until today, local groups and clusters mark the endpoint of their evolution. The observed large scale structure can be explained through dark matter, that only interacts through gravity and not or only weakly through other means. In addition, the observed accelerated expansion of the universe further requires so called dark energy that causes the increasing expansion rate.
Utilizing astrophysical simulations, including dark and baryonic matter as well as dark energy, the formation history of galaxies and clusters can be inferred (Springel et al. 2005). The current understanding is, that groups and clusters form within gravitational wells formed by overdensities of dark matter. Baryonic matter is attracted by the potentials formed by dark matter and drawn to the center of these mass concentration. This is illustrated in figure 2.1.

On a smaller scale, the first stars, black holes and galaxies are formed. The latter are structured in groups and clusters within the dark matter halo. This hierarchical formation process leads to the final structures observable today within nearby groups and clusters.
Over time, the gas within galaxies is enriched with heavier element through stellar processes. In addition, both, supernovae and accretion onto black holes feed kinetic energy into the galactic gas heating it up, inducing winds and even expelling it from the galaxy into the ICM. At the same time, the supply of gas within a galaxy is continuously refuelled from the ICM. While stars and black holes have a large influence on the growth of galaxies, groups and presumably even clusters, the largest fraction of the baryonic matter content is of the form of hot gas (either the ICM or the Warm Hot Intergalactic Medium (WHIM)).
All these different objects, stars, accreting black holes, Active Galactic Nucleus (AGN), the ICM and the WHIM, emit radiation over a large range of the electromagnetic spectrum. However, the X-ray band in the range from 0.1 keV up to 20 keV is unique in

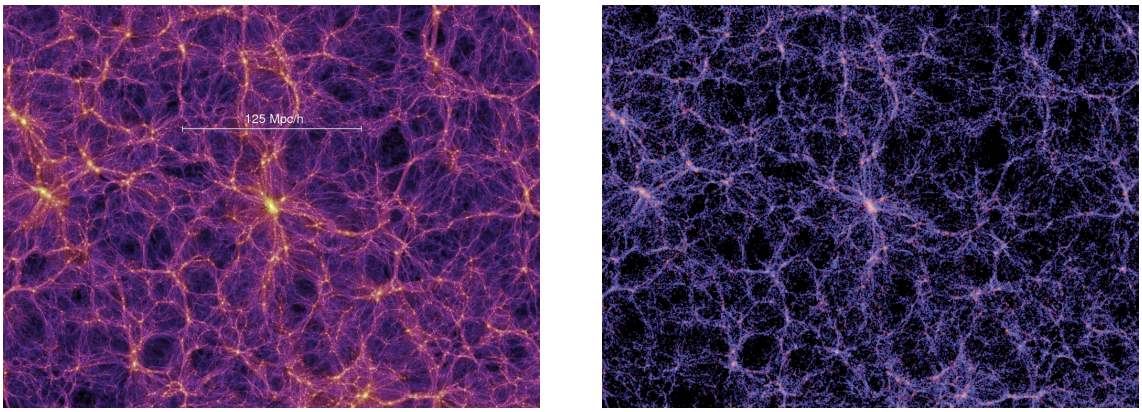

(a) **(b)**

Figure 2.1.: The two pictures show the result of the millenium simulation for dark matter (a) and baryonic matter (b) (Springel et al. 2005). As can be seen the baryonic matter follows the distribution of dark matter. Pictures taken from https://wwwmpa.mpa-garching.mpg.de/galform/virgo/millennium/

tracing the emission from these objects and determine their chemical composition.
The planned sensitivity of Athena, its large effective area and the excellent spectroscopic capability will allow for detailed studies of close by and far away objects in a fraction of the time required by other instruments. This large improvement will revolutionize our understanding of astrophysics and cosmology. A number of examples where this leap in observational capability will further our understanding are pointed out in the following.

2.1.1.1. The formation and evolution of Galaxy Groups and Clusters

The peak of galaxy group and cluster formation as well as the maximum of star formation and accretion rate appears at redshifts of about z=2.5 (Hopkins and Beacom 2006; Merloni, Rudnick, and Matteo 2004). These processes heavily influence the properties of the ICM as they feed gas and heavy elements from galaxies as well as kinetic energy into the ICM. Simultaneously, its mass increases through infalling matter from the filamentary structures (Voit 2005) and merger events. Although a coherent picture of the local Universe with z<0.5 is established, the evolution history of clusters from their formation until today is not well understood. The observations described in the following paragraphs are aimed to answer three questions as discussed in (Pointecouteau et al. 2013).

- What is the interplay of galaxy, supermassive black hole, and intergalactic gas evolution in the most massive objects in the Universe – galaxy groups and clusters?

- What are the processes driving the evolution of chemical enrichment of the hot diffuse gas in large-scale structures?

- How and when did the first galaxy groups in the Universe, massive enough to bind more than 10^7 K gas, form?

Energy deposition History of the ICM Both, measurements and astrophysical simulations indicate, that the growth and evolution of SMBH and their host galaxies is tightly correlated. To deeper understand the co-evolution of SMBH and the ICM it is required to determine the feedback process controlling energy injection into the ICM and the flow of mass towards the black hole. The energy deposition into the ICM can be derived from surface brightness and temperature measurements. Through these, the entropy and thus the history of energy deposition into the ICM can be quantified (Pointecouteau et al. 2013).
The entropy distribution of multiple cluster will be measured with high accuracy by ATHENA utilizing its large effective area and the high spectral resolution of its X-Ray Integrated Field Unit (XIFU). While current observatories, as XMM-Newton and Chandra provided precise calibration data for clusters up to redshifts of z$\sim$0.6, ATHENA will push this to z$\sim$2 and down to the group regime (Pointecouteau et al. 2013).

Chemical evolution of Halos through cosmic Time The first population of stars certainly produced and distributed the first elements heavier than helium within the Universe. Nevertheless, the majority of these elements and their spreading over the Universe likely originated from the period of most intense star formation activity at redshift z about z$\sim$2.5 (Bouwens et al. 2009). Elements heavier than Si are produced by type Ia supernovae whereas elements between O to Si stem from core-collapse supernovae (Pointecouteau et al. 2013). Lighter elements like N, C and F are bred in Asymptotic Giant Branch (AGB) stars (Werner et al. 2008). As metals provide a sustained cooling of their environment through the emission of spectral lines, they have a crucial role in the thermodynamic balance of most astrophysical systems.
Multiple processes as merger events, galaxy-galaxy interaction and others as supernova winds and AGN feedback lead to a distribution of metals over the ICM. Within the ICM, the gas is in an thermal and ionisation equilibrium and its high temperature prevent a condensation into dust grains. Massive halos of gas can thus be seen as fossil records of the metal production by stellar processes that happened in the early Universe. To have a complete picture of the evolution processes that enriched the ICM with heavy elements, observation over a large range of redshifts and over the range of the center of galaxy clusters to its outskirts are required.
A large effective area will allow measurements at higher redshifts, while a good angular resolution is required to map the clusters. To disentangle the chemical abundance ratios, a high spectral resolution is required. To date ATHENA is the only instrument providing all the properties to measure elemental abundance ratios out to redshifts of z$\sim$0.5-2 (Pointecouteau et al. 2013).

The Cosmic Web in formation and evolution Although it is known that the peak of group and cluster formation as well as the highest star formation rate and accretion

activities appear at redshifts between z∼0.5 to z∼4 (Hopkins and Beacom 2006; Merloni, Rudnick, and Matteo 2004), it is yet unknown when the first galaxy groups large enough to bind gas with temperatures of the order of 10^7 K formed.
ATHENA will be able to detect groups and clusters at high redshifts as extended sources through its large effective area and good spatial resolution over its complete FOV. In addition, to enable the detection of these structures, a low instrument background is mandatory.

The chemical History of hot Baryons Encoded within the X-ray emission of the ICM is also the chemical abundance of its baryonic matter content. Different types of supernovae and accretion processes lead to different ratios of metals within the ICM. X-ray spectra from clusters over large ranges of redshifts will allow to determine the chemical evolution of clusters and the primary mechanism leading to the enrichment with elements heavier than helium. As a matter of fact, X-rays are the only means to determine the chemical abundance within hot plasmas that are composed of highly ionized atoms (Pointecouteau et al. 2013).
Not just will it be possible to evaluate the chemical abundance of the ICM, the proposed properties of ATHENAs mirror system and the XIFU instrument will allow the measurement of gas motions and turbulences within the hot gas. These will further allow to understand how the baryonic gas evolves in the dark matter potentials and reveal its physical state. Furthermore, apart from ATHENA, no mission available in the foreseen future provides the capabilities to measure the chemical abundance of the ICM over cosmic time-scales, or out to high redshifts respectively.

2.1.1.2. The Astrophysics of Galaxy Groups and Clusters

In addition to providing new insights into the history of galaxy group and cluster formation, ATHENA will also enable the study of the astrophysics governing the evolution of baryonic matter, in dark matter potentials.
Clusters form the nodes of the cosmic web with 80% of their mass being made up of dark matter that can only be detected indirectly. The remaining mass is formed by baryonic matter a large fraction of which is contained within the ICM. Radiation from the ICM provides information about the interplay of hot and cold gas with dark matter. The complete story of the structural growth and how gravitational and non-thermal components of their energy are dissipated however is still beyond the grasp of current X-ray facilities.
An X-ray observatory with the capabilities proposed for ATHENA will be able to answer the following questions as stated in Ettori et al. 2013.

- How do hot diffuse baryons accrete and dynamically evolve in dark matter potentials?

- How and when was the energy that we observe in the ICM generated and distributed?

- Where and when are heavy elements produced and how are they circulated?

The thermodynamic Properties of large scale Structures In the established structure formation scenario, the large scale structures observed today form hierarchically. The largest fraction of the mass energy budget is thereby made up by dark energy with about 72 %, followed by dark matter with about 23 % and baryonic matter with about 5%. The baryonic matter is collected in dark matter potentials and forms galaxies and clusters as we observe them today. However, the formation processes are not understood well enough to formulate theoretical models to make precise prediction from first principles (Ettori et al. 2013). The most active regions of the high redshift universe are the birthplace for galaxy clusters. These proto-cluster regions are mapped as concentrations of strong star formation at redshifts z about z$\sim$2-4 (Steidel 2011) and associated with AGN activity and metal enrichment in the high redshift ICM. In turn this high activity in the high redshift Universe leaves its marks in the thermodynamic and chemical properties of the low redshift ICM (Ettori et al. 2013).
Measurements of the X-ray emission from the ICM and galaxies within clusters will show the interplay of hot and cold components of the baryonic matter. These on the other hand require high angular and spectral resolution.

How do hot Baryons dynamically evolve in Dark Matter Potentials Baryons are attracted by the dark matter potential wells. During cluster formation, the matter falls into the potential well, releasing its potential energy. The energy is expected to be dissipated within the cluster gas through the generation of turbulences and bulk motions. However, these have never been observed conclusively. To date only upper limits on the bulk motion velocities of the coolest, brightest central gas with values between 300 km/s and 500 km/s are accessible (Sanders and Fabian 2013).
The spectral and spatial resolution of ATHENA will enable the measurement of detailed velocity maps of the ICM with a measurement precision of the order of 10 km/s. A simulated velocity field as observed by ATHENA is shown in figure 2.2 on the left. On the right, the concept of measuring the turbulent velocities from spectral line-broadening is illustrated. The large effective area of ATHENA will furthermore enable these measurements also for sources that are too faint for other X-ray observatories.

How and when was the Energy in the ICM generated and distributed? Feedback processes from supernovae and SMBH are suggested to have a major role in the history of all massive galaxies and the evolution of groups and clusters. These non-gravitational processes are likely to feed energy into the ICM and prevent the cooling of gas within cluster cores and a condensition of the gas into molecular clouds. They are also assumed to be responsible for the excess entropy observed in the centers of group and cluster ICM (Ettori et al. 2013). Winds from supernovae, jets from AGN or yet unknown effects are capable to inject energy into the ICM. The interplay of the different feedback processes and cooling influences the overall thermodynamic properties of the ICM. The key to understand the role of different processes are the gas entropy measurements and the

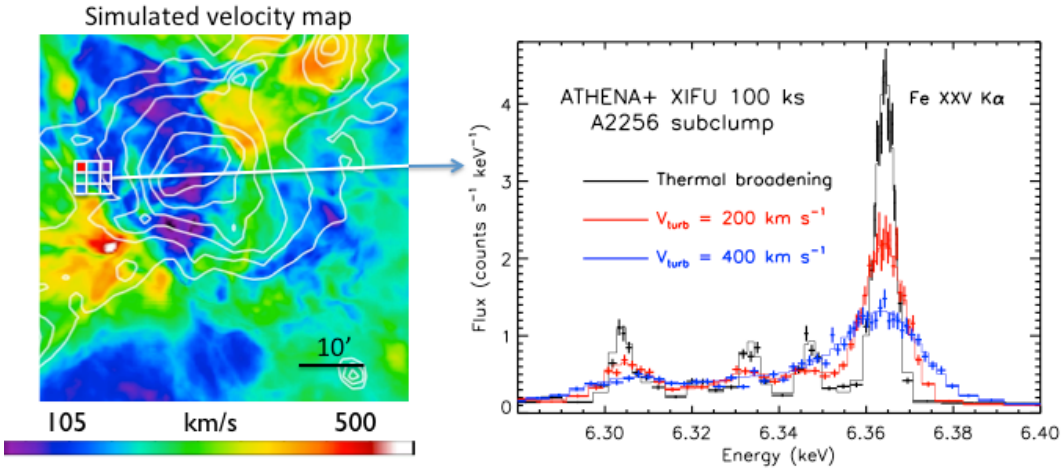

Figure 2.2.: The left shows a velocity map from a cosmological hydrodynamic simulation of a pertubed galaxy cluster. On the right a 100 ks observation with the XIFU for a 1.5' x 1.5' region is shown corresponding to one of the 9 small regions shown in the left. The simulation shows that the XIFU will be able to identify the broadening of the Fe XXV K_α line and measure the thermal and turbulent broadening of that line. Picture taken from Nandra et al. 2013.

metallic enrichment. Entropy increases every time energy is introduced into the ICM and decreases when it is carried away e.g. through cooling. The entropy expected from gravitational collapse is known (Voit 2005). Deviations from this simple baseline can be linked to non-gravitational processes as feedback and cooling. Unfortunately, to date only the outskirts of few bright objects are accessible (Ecker et al. 2013).
With ATHENA it will be possible to routinely measure entropy and metallicity profiles even of faint sources. The proposed good spatial resolution will provide the means to localise the energy input from non-gravitational events over the complete cluster volume from its center to its outskirts (Ettori et al. 2013).

Production and Circulation of Heavy Elements Since the first supernovae explosions, the baryonic content of clusters is continuously enriched with heavy elements. Through that, the metal abundance of the ICM is a tracer for supernovae activity and provides information what sort of enrichment process is dominant in which epoch. In addition to the production, these elements are transported from within galaxies into the hot ICM. Both AGN jets and supernovae winds are capable to expel metal enriched gas out of a galaxy into the ICM. In the case of AGN jets, the range of metal enriched outflows is found to scale with jet power (Kirkpatrick, McNamara, and Cavagnolo 2011). Complementary to direct velocity measurements, metalicity profiles can be used to trace turbulences and gas motions induced by AGN outflows.
ATHENA will be able to provide a coherent picture of the metal enrichment processes, the distribution of metals within clusters and constrain feedback and mixing models.

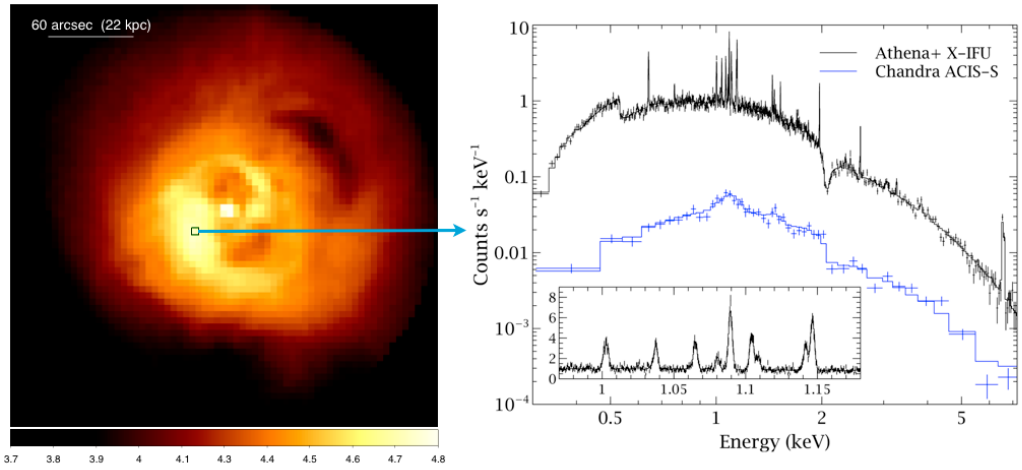

Figure 2.3.: The left part shows a simulation of a 50 ks observation of the perseus cluster with ATHENA's XIFU. On the right, the spectrum of a 5x5 squared minute of arc region is shown and compared with a observation made by Chandras ACIS-S instrument. The higher throughput of ATHENA will provide detailed information (velocity distribution, temperature, metallicity etc.) of many clusters and groups. Picture taken from Croston et al. 2013.

2.1.1.3. Feedback in Clusters of Galaxies

AGN feedback, regulating the cooling of intragroup and -cluster gas is suggested to play a crucial role in galaxy and cluster formation. Mechanical feedback from AGN jets has become one of the most promising candidates to suppress star formation by heating the hot gas of galaxies. However, the balance between gas cooling and AGN feedback is not well understood. In addition, the significance of radiative heating from quasars as a function of epoch and environment is not clear.
Key questions as stated in Croston et al. 2013 are:

- How is the energy from jets dissipated and distributed throughout the hot gas atmosphere of the cluster or group?
- How does feedback operate to regulate gas cooling and AGN fuelling?
- What is the cumulative impact of powerful radio galaxies on the evolution of baryons from the epoch of group and cluster formation to the present time?

The observational goals to answer these questions are discussed in the following paragraphs.

How is Jet Energy dissipated and distributed? Today, the energetics of AGN feedback is reasonably well explained. Accretion onto SMBH, that is suggested to be the source for the feedback process, regulates the conditions of sources nine and more orders of magnitude larger. Until now only in the nearest and brightest clusters, first clues on the distribution of the mechanical energy of jets has been found. The originally strongly

directed jet power seems to be isotropically distributed to the surrounding gas through sound waves and weak shocks (Fabian 2012). While the energy of these disturbances is sufficient to prevent heating, neither the energy transfer nor the spatial scales on which they happen are known.
Velocity field mappings of the ICM will provide new insight into the AGN feedback process. These are acquired through detailed measurements of line profiles. Variations of line centroids provide characteristic spatial scales and velocity amplitudes while the total widths of the line provides the total kinetic energy stored in stochastical gas motions. A simulation of a gas velocity map as expected from ATHENA is shown in figure 2.3. From these, the gas viscosity and energy dissipation mechanism can be determined and the full calorimetric energy input of AGN into the ICM can be derived for the first time. These measurement require an instrument as the XIFU and a large, square meter class mirror system. The FOV of the Wide Field Imager (WFI) will provide large area maps of the ICM surface brightness giving the first population study of AGN induced perturbations over a large range of systems and spatial scales.

How does Feedback operate to regulate Gas Cooling and AGN Fuelling? While it is sure that jets are powered by accretion of matter onto black holes and the release of its gravitational energy, the fueling process itself is not well understood. While short cooling times are observed in a large fraction of hot gas structures, the lack of cold material and star formation can not be explained without a feedback between jet induced heating and AGN fuelling (McNamara and Nulsen 2007). Different models for AGN fuelling predict largely different accretion rates (Bondi 1952; Gaspari, Ruszkowski, and Sharma 2012). Testing these models requires a thorough understanding of the cooling processes. In addition, galaxy clusters are an ideal laboratory to observe matter over a wide temperature range and X-rays are where the bulk of the energy output happens. Previous observations already showed, that there is much less cool material emitting X-rays in the center of galaxy clusters than would be expected from radiative cooling (Peterson et al. 2003; Sanders et al. 2008). Since the cooling timescale of gas is of the order of 10^7 years, an energy feedback cycle must operate on shorter timescales to suppress cooling.
ATHENA will provide largely improved observational capabilities compared to other facilities. Through these improvements, it will be possible to measure in detail the temperature distributions in the cores of clusters and groups.

What is the Cumulative Impact of Powerful Radio Galaxies? Within the cores of nearby galaxy clusters, mechanical feedback is tightly coupled to cooling with a constant feedback being required to prevent cooling. Due to the observed persistence of steep abundance gradients, feedback can not only rely on strong shock heating as this would disagree with observations. However, in the nearest powerful radio galaxies, jets appear to transfer more energy into their environment than is required to counter cooling. It is likely that this type of AGN heating was common in earlier epochs where groups and clusters formed. This could explain the origin of excess entropy in groups

and clusters (Ettori et al. 2013). Through the observation of shock heated gas, surrounding expanding radio lobes, X-ray observations are the only way to test numerical simulations of radio galaxy evolution. While current observatories were able to provide measurements of shocked gas (Chandra and XMM) for few nearby clusters, a large area high throughput high spectral resolution mission as ATHENA will provide detailed studies of radio galaxies and reveal their dynamics.

2.1.1.4. The missing Baryons and the Warm-Hot Intergalactic Medium

In the early universe baryons were relatively cold and homogeneously distributed. The overall baryon distribution in the early universe can easily be detected through the observation of redshifted HI lines in the optical band (the so-called "Lyman Gamma Alpha Forest") (Rauch 1998; Weinberg et al. 1997). Through the formation and evolution of stars, galaxies and clusters, the state of baryons and the underlaying physics became more complex. In contrast to cosmological predictions and the baryons density in the high-z universe, observations of todays baryons can only account for less than 60% of the expected baryon density (Shull, Smith, and Danforth 2012). In other words, baryons are missing at low redshifts, and today's observations can only account for a fraction of the baryons predicted by precision cosmology, and observed in the high-z Universe. In addition, by comparing the baryonic mass to the total mass of a galaxy, it can be deduced that even most galaxies fall short of baryons (McGaugh et al. 2010). An explanation may be given by feedback processes that expel gas from galaxies and push it into the gaseous outskirts of the virilized structures (galaxies and clusters) (Cen and Ostriker 1999). This WHIM is structured in the form of a cosmic web. Its temperature in the range of 10^5 K to 10^7 K causes emission primarily in the X-ray band. However, its low density makes it near invisible for current X-ray instruments. Questions that need to be answered according to Kaastra et al. 2013 are.

- Where are the baryons still missing from the cosmic budget at $z<1$? Do they really trace the filaments of the cosmic web, as the theory predicts? What is their physical state and composition?
- Where have the missing baryons in galactic halos, including our own Galaxy, gone? Do we see them in the circumgalactic space?
- What is the role of feedback by galactic winds and active galactic nuclei in the process of galaxy formation?
- What is the fate of the gas? How much material is accreted, how much is blown out, and what fraction is locked-up temporarily in stars?
- What are the relative contributions from accretion versus outflows in structure formation?

The observational aims are discussed in the following paragraphs.

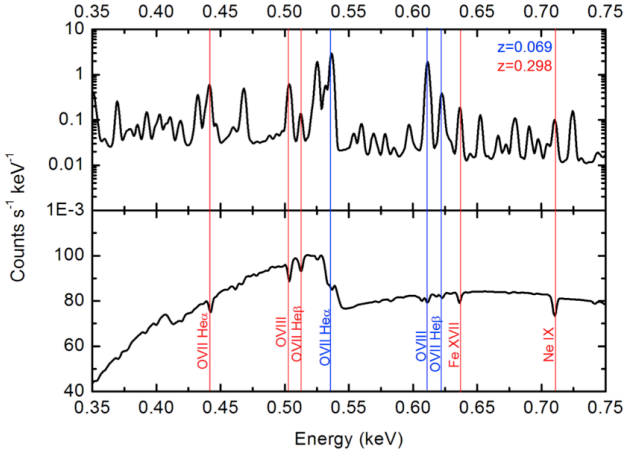

Figure 2.4.: Shown are the emission (upper panel) and absorbtion (lower panel) line spectra of two overlapping filament structures at different redshifts as simulated for a 2'x2' region and a 1 Ms ATHENA observation. Through the high spectral resolution it is possible to disentangle the different contributions. Picture taken from Kaastra et al. 2013.

Filaments and large scale Structure The evolution model of our universe predicts, that a large fraction of baryons populate the filaments that built the cosmic web. The majority of this gas is assumed to have temperatures of the order of $10^{5.5}$ K forming a plasma that is best detectable through the interaction of its highly ionized atoms. Through the large distance of filaments from external influences, they are ideal to study the structure formation process and metal enrichment history in the universe (Kaastra et al. 2013).
ATHENA will be capable to detect and resolve filaments through absorbtion line and emission line spectroscopy from their hot gas. In addition, it is possible to observe a pronounced gamma-ray burst behind large scale superstructures. Furthermore, ATHENA will also probe the outskirts of clusters. Details are provided in the following four subparagraphs. Until now there is no convincing observational proof for absorbtion lines of baryons in the WHIM (Nicastro et al. 2013). An obvious task for ATHENA is the unambiguous detection of absorbtion lines caused by filaments of the WHIM. Absorbtion line measurements are expected to tightly constrain the physical properties of the WHIM.A negative result, i.e. no detection of the WHIM on the other hand will put the current understanding of baryonic structure formation in question.
The detection of absorbtion lines requires a known "candle" that provides the primary X-ray spectrum. Both AGN outbursts or Gamma Ray Burst (GRB) afterglows can be used for that purpose. In addition to large area, good spatial and high spectral resolution this requires a sufficiently fast reaction time to AGN or GRB triggers. Although present, emission lines from the WHIM especially in filaments are significantly weaker and thus harder to detect. Nevertheless, ATHENA should be able to provide emission line spectra for a significant fraction (about 30%) of systems identified through absorbtion lines (Kaastra et al. 2013). The combination of absorbtion and emission line

spectroscopy will provide model independent measurements of the gas density, length scale, ionization and excitation mechanism respectively gas temperature as well as elemental abundance (Kaastra et al. 2013). As emission lines are more likely to be found in high density environments within the cluster outskirts, they bridge the gap between filaments and the ICM and potentially allow to trace the gas infall into the virilized objects.
An example for an absorbtion/emission line spectrum is shown in figure 2.4. With its good angular resolution, ATHENA will be capable to remove the contribution of point-like X-ray sources and give high quality spectra of the WHIM alone (Kaastra et al. 2013).

Gamma Ray Bursts behind Walls Absorbtion line measurements rely on bright background sources as AGN and GRB. Their bright emission is usually short lived and not predictable. The statistical nature of AGN activity and GRB will provide an unbiased study of absorbtion lines caused by the WHIM as no line of sight is preferred (Kaastra et al. 2013). Under fortunate instances, a background source can be found behind one of the most pronounced structures of the cosmic web as was the case for the blazar H2356-309 behind the Sculptor Wall. This event was observed both by Chandra and XMM and showed a strong absorbtion line for O VII (Fang et al. 2010).
With respect to the oxygen density illuminated by such an outburst, ATHENA will be capable to provide sufficient statistics to determine the O VII absorbtion lines in the fraction of the time required by other available instruments, provided the reaction time to such an event is sufficiently small (of the order of 2 h - 8 h).

Cluster Outskirts Cluster outskirts are a melting pot, where cosmic baryons convert the kinetic energy of their infall into the thermal energy of the hot gas. The state of baryons in this region is expected to show a wide spectrum of thermal and kinematic properties.
These studies have just become feasible with current instruments. ATHENA with its high energy resolution, high collecting area and large field of view will reveal the full picture of baryons on large scales (Kaastra et al. 2013).

Galactic Halos As already mentioned, gas accretion and galactic winds as well as shock heating are poorly understood (Voort et al. 2011). Through accretion and winds gas is moved from the inner area of galaxies to their outskirts. This shock heated gas with temperatures of 10^6 K and above may contain as many heavy atoms as the galaxies (Tumlinson et al. 2011). Without feedback the gas would cool and fall back onto the galaxy and cause star formation rates well above those observed. Feedback and winds may be the explanation for this contradiction. Observations hint to the presence of a gas in the outskirts of galaxies that moves with several $100 \cdot 10^3$ km/s relative to the galaxies, as expected if feedback and winds expel the gas from the galaxies (Veilleux, Cecil, and Bland-Hawthorn 2005). To date, the picture however incomplete. The formation and evolution of galaxies and the evolution of the gas around them are thus closely

intertwined (Kaastra et al. 2013).
Detection of multiple metal lines will give details about the physical conditions of hot gas while a good angular resolution allows to map the position of gas clouds from the outskirts to the center of clusters. The ATHENA observatory will provide the means to understand both gas accretion and galactic winds.

2.1.2. The Energetic Universe: How do Black Holes grow and shape the Universe?

The evolution of galaxies and that of the SMBH appears to be closely coupled. During their build-up SMBH release energies that exceed the binding energy of their host galaxy by a factor of 10-100 (Nandra et al. 2013) requiring a self-regulating feedback process that connects the SMBH growth and the star formation of its galaxy. The close environment of black holes belong to the most exotic places within our universe. The strong gravity of black holes provide a direct test environment for our understanding of general relativity. As exotic as black holes appear, it is largely agreed that these objects can be fully characterized by only two properties, their mass and spin. The following section discusses the observational goals that will improve our understanding of SMBH growth, feedback and the close environments of black holes.

2.1.2.1. The formation and growth of the earliest SMBH

Both the processes that cause the initial formation of SMBH and their following growth are unknown. To shed light onto these processes, ATHENA strives to answer the following questions (Arid et al. 2013).

- How do the "seeds" of the first SMBHs form?
- What processes drive the initial growth of SMBHs and trigger AGN activity in the early Universe?
- What influence do early AGNs have on structure formation, reionisation of the Universe and the evolution of the first galaxies?

The observational goals that are related to the questions stated above are discussed in the following paragraphs.

The initial Growth of SMBH The nature of the seeds that grow to todays SMBH are unknown. Two different seeding and evolution processes are in discussion. Either early stars collapse into a black hole and undergo a phase of heavy accretion or SMBH seeds form directly from primordial gas leading to seeds with a higher start mass that go through a phase of more moderate accretion (Arid et al. 2013). In both cases, high accretion rates are required to built up the 10^9 solar masses of currently known SMBH at redshifts $z>6$ (Li et al. 2007), that power luminous quasars out to $z=7$ (Mortlock et al. 2011). While these luminous optical quasars constrain the models of early growth,

their high masses and luminosity indicate a sustained high accretion rate, so that their final properties are nearly independent from the initial seed conditions. Through a population study of lower mass SMBH and obscured AGN at z>6, it will be possible to tightly constrain the seeding and initial growth mechanism of the majority of SMBH. While AGN feedback is likely to have a crucial impact on the evolution of galaxies, the impact of early AGN growth on the Universe is unknown.
ATHENA's large effective area will push the limits of observational capabilities to make population studies of AGN possible. Combined with the large field of view of the WFI, these studies will be done two orders of magnitude faster than with current observatories. In addition, the high sensitivity of its two spectrometers will push the observational limitation out to high redshifts allowing the detection of a statistical sample of luminous AGN at redshift z>6 and track their growth and constrain models for the fuelling mechanism.

Identifying high Redshift AGN A census of AGN requires the measurement of its bolometric luminosity while minimising obscuration and contaminations from other sources. While multiple technics in different bands of the electromagnetic spectrum are capable to identify AGN, X-rays are uniquely capable to provide a census of AGN up to high redshifts (Arid et al. 2013). X-rays can penetrate obscuring matter and provide a near contamination free way to identify AGN and measure their luminosity. However, current facilities lack the sensitivity or effective area so that to date no confirmed AGN at redshift z>6 has been identified (Civano et al. 2011; Trichas et al. 2012).
Here the improved observational capabilities of ATHENA are required to reveal early AGN and further our understanding of SMBHs formation and growth in the early Universe.

Understanding the build-up of SMBH and Galaxies at the Heyday of the Universe The peak of accretion activity and thus the largest rate of SMBHs growth is observed to happen in the redshift range between z=1-4 (Merloni, Rudnick, and Matteo 2004). In addition, observations indicate that SMBHs growth is among the most relevant processes in galaxy evolution (Georgakakis et al. 2013). Open questions, as stated in Georgakakis et al. 2013 are:

- What are the physical conditions (e.g. fuelling mode, trigger mechanism), that initiate major black hole accretion events?
- What is the nature of AGN feedback and does it plays a significant role in the evolution of galaxies?

The observational goals are discussed in the next paragraphs.

Obscured Accretion and Galaxy Formation Population studies with XMM-Newton and Chandra demonstrate the complexity of AGN growth (Alexander and Hickox 2012). There is evidence for different fuelling modes and trigger mechanisms for accretion

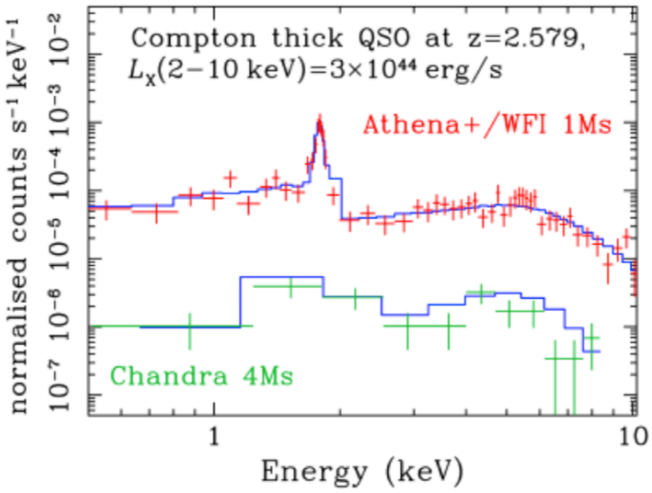

Figure 2.5.: Shown is a direct comparison of a Compton thick AGN as observed over a period of 4 Ms with Chandra and a simulated spectrum as expected for 1 Ms ATHENA observation. Through its large effective area and sensitivity ATHENA provides a major leap in survey power. The picture was taken from (Georgakakis et al. 2013).

(Georgakakis et al. 2009; Kocevski et al. 2012). In addition, the correlation between star-formation in the host galaxy and accretion rate is not well understood (Rosario et al. 2012). It is yet unsure how AGN reach the masses observed today. In either known birth scenario, an AGN will undergo a high rate of accretion building up its mass. Much of the initial growth is suggested to appear behind clouds of obscuring gas that limit our ability for a direct observation. While the most heavily obscured and Compton thick AGN represent a major fraction of black hole growth, their properties are poorly known (Akylas et al. 2012). These objects are thought to represent the early phases of accretion events in galaxies and provide important tests for models of AGN and galaxy co-evolution. Unfortunately, due to the observational difficulty only few highly obscured or Compton thick AGN have been detected (Brightman 2012).

An example for a spectrum recorded with Chandra over a time period of 4 Ms is shown in figure 2.5. In contrast, the shown simulated 1 Ms observation will provide certain detection and characterization of Compton thick AGN within a fraction of the time required by current instruments. A thorough understanding of the growth of black holes over cosmic time, with respect to their large scale environment and surroundings is one of the goals of ATHENA. The required observations are enabled through ATHENAs large effective area and the foreseen sensitivity of its instruments.

Cosmic Feedback Matter outflows from local Seyfert galaxies have been revealed by XMM-Newton and Chandra as blue-shifted absorbtion lines from ionised elements (Tombesi et al. 2010; Tombesi et al. 2013). These show, that the bulk of energy and mass flux of AGN driven winds are of the form of highly ionized material, invisible in wavelength other than X-rays (Cappi et al. 2013). Provided AGN winds are responsible

for the correlation between SMBH and galaxy growth, they should be widely visible in the redshift range of z 1-4, where star formation and SMBH accreation activity peaked (Hopkins and Beacom 2006; Merloni, Rudnick, and Matteo 2004). Current facilities are limited to the nearby Universe or bright sources (Georgakakis et al. 2013).
ATHENA will be the key to understand feedback processes due to its large effective area, high sensitivity and good spatial as well as spectral resolution. Surveys with ATHENAs WFI will be able to identify AGN outflows and set constraints on the outflow velocities, ionisation states and column density. Follow up observations with the XIFU will determine the wind properties further. A population study for a significant sample size with the combined knowledge about outflows in nearby systems will provide sufficient information for a test of AGN and galaxy co-evolution scenarios.

2.1.2.2. Galaxy Scale Feedback

AGN feedback is invoked in cluster evolution and suggested to heat the ICM. Equally crucial is the removal of gas from the AGNs host galaxy through AGN jets, that suppress star formation. While jets are regarded as the most effective way to transport energy from the AGN into its host galaxy (Cappi et al. 2013) the following questions are still unclear.

- How do accretion discs around black holes launch winds/outflows, and how much energy do these carry?
- How are the energy and metals accelerated in winds/outflows transferred and deposited into the circum-galactic medium?

Using X-ray observatories, it is possible to determine the physical state of AGN outflows and understand the feedback processes as discussed in the following.

How do AGN launch Winds/Outflows and how much kinetic Energy do these Winds carry? AGN winds are observed as blue shifted and broadened absorbtion lines in the UV and X-ray band of a substantial fraction of AGN. These winds have a wide range of velocities and physical conditions, carrying different amounts of kinetic energy and momentum from the AGN and into the larger scale environment. While simulations of accretion discs and outflows show, that several physical mechanisms are capable of launching winds (Blandford and Payne 1982; Kazanas et al. 2012), the energetically dominant mechanism is not yet understood. These outflows can take the form of a warm absorber medium, found in about 50 percent of AGN (McKernan, Yaqoob, and Reynolds 2007), that likely originates in the dusty torus around the central SMBH having only low mass and kinetic energies of the order of 1 percent of the bolometric energy of the SMBH (Blustin et al. 2005). In contrast, Ultra Fast Outflow (UFO)s, that are observable in 30-40 percent of AGN and reach velocities of several tenth the speed of light (Tombesi et al. 2010) carry significant kinetic energy. While it is possible to observe these winds and models for their launch and acceleration exist, it is to date unclear which model applies. To understand the processes leading to the generation of

winds/outflows, detailed characterizations of their physical properties on a dynamical time-scale (Cappi et al. 2013) are needed.
With ATHENA it should be possible to provide sufficiently elaborate observational data to constrain the fundamental processes launching winds/outflows from AGN.

How do AGN Winds/Outflowas interact with their Environment? Numerical simulations indicate, that outflows with kinetic energies in the range of a few percent the power of the bolometric luminosity, have a significant impact on the evolution of the host galaxy (e.g. Wagner, Umemura, and Bicknell 2013). The transfer of energy from these outflows into the interstellar medium and furthermore the interplay on AGN feedback and its apparent regulating effect on star formation are not well understood (Cappi et al. 2013). In nearby AGN outflows and feedback can be probed directly through imaging spectroscopy.

For 3-D mapping, a high spectral resolution is required to disentangle overlapping components while a spatial resolution of a few seconds of arc is necessary to resolve outflow patterns (Cappi et al. 2013). Feedback from AGN and starbursts are expected to have an important role in the building of galaxies. Mergers destabilize cold gas and trigger star formation as well as accretion onto SMBH including AGN activity. By spatially separating these activities it will be possible to understand how they are linked. Through ATHENAs XIFU and the good angular resolution of its mirror system, it will be possible to map the velocity distribution of hot gas within galaxies and thereby probe the interaction of AGN and starburst induced winds with the surroundings in local galaxies. From these observations, it will be possible to understand the process of AGN feedback in further away, higher redshift galaxies, where the wind shocks can not be resolved.

The nearest Laboratory for "AGN-type" Feedback: The Galactic Center and SGR A* current and past Activity The black hole at the center of our own galaxy, SGR A*, can be used as case study for the interaction of a SMBH with its environment (Cappi et al. 2013). Despite its mass of $4 \cdot 10^6$ solar mass it has a luminosity only 300 times brighter as our sun. That indicates a low or radiative inefficient accretion activity. Though it is usually found in a quiescent state, SGR A* emits flares in the X-ray and NIR band on daily timescales (Porquet et al. 2008). These intense activities are believed to originate within a few gravitational radii of the event horizon (Genzel et al. 2003) and are suggested to come from sudden increases of accretion activity or the release of magnetic energy. However, to date neither the general rate of accretion nor the ejection mechanism causing flares are understood.
A large effective area combined with good angular and time resolution will allow to follow the spectral evolution of SGR A* from quiescent to flaring. In combination with observations at other wavelengths this will provide unreached precision for models of flare emission. Furthermore, detailed high spectral resolution maps of SGR A* will provide information about its activity over the past millenium (Cappi et al. 2013).

2.1.2.3. The Physics of Accretion

The most active part of an AGN is the region within a fraction of gravitational radii from the SMBH. Here, matter will lose up to half its energy, leading to the emission of large amounts of X-rays. Winds and jets are assumed to be generated within this area where the effects of General and Special relativity are most prominent. It is also within this close environment, were the effects of black hole spin on the metric of space time become apparent. Understanding the processes encountered close to a black hole will give insight into four questions of astrophysics (Dovciak et al. 2013).

- How does the most efficient energy release mechanism in the Universe work?
- How does strong gravity affect the behaviour of matter and radiation?
- How are the physics of accretion and ejection related?
- What is the spin distribution of black holes?

Several observations, that will be discussed in the following paragraphs are capable to provide new details about the processes leading to X-ray emission from matter accreting towards black holes. In addition, these direct observations also provide information about the black hole itself.

The close Environment of Black Holes While falling towards the black hole, matter within an accretion disk is heated through turbulent friction. This leads to the emission of thermal photons, that can already be observed also in X-rays and furthermore the formation of a hot corona in the vicinity of the black hole. Here thermal photons can gain more energy through inverse Compton scattering. Part of these photons will illuminate the disc, be reprocessed and lead to the emission of both hard and soft X-rays. The effects of strong gravity become more and more relevant the closer to the black hole photons are emitted. Within a few gravitational radii from the black hole these effects have to be fully taken into account . That in turn offers the opportunity to test General relativity itself.

Time Lags and Reverberation Mapping The X-ray spectra of black holes are composed of several characteristic emissions that happen in different distances to the center. An already employed and common technique is the observation of time lags between changes of different components of the X-ray spectrum. Hard X-rays are suggested to originate in a hot corona close to the black hole. The photons are emitted uniformly in all directions so part is reaching an observer directly while part of the photons are emitted towards the accretion disc. Here the photons are reprocessed and lead to the emission of lines and a reflection both in hard and soft X-rays. Measurements of these time lags also called reverberation mapping (Matt and Perola 1992) are already employed and provide a model independent method to map the inner accretion flow (Fabian et al. 2009).
Where other facilities are limited to few bright AGN and low frequencies, ATHENA will provide the timing capability, throughput and effective area to significantly improve time lag observations.

Measuring the Spin of Black Holes Black holes are characterized by their mass and spin, and a proper census of black holes requires the measurement of both parameters. The spin of a black hole can be measured using several methods, that will be discussed in more detail in section 2.1.3. The yet most widespread method is the measurement and fitting of relativistically broadened iron K_α lines (Fabian et al. 2000). However, to date only a small number of spin estimates for black hole spectra are available (Walton et al. 2013).
ATHENA will be able to perform measurements that allow the application of multiple independent methods that can be used to estimate the spin of black holes. In addition, it will be possible to observe both galactic black hole systems, that are too bright for other instruments, and sources that are so faint, that a reliable spin measurement is not possible with current instruments.

The Nature of soft X-ray Emission In most radio-quiet AGN an excess emission of X-rays in the energy range from 0.5 keV to 1 keV is observed. At least part of this excess emission is attributed to reflection on the ionized accretion disc (Ross and Fabian 2005). In addition, there is evidence that this excess is caused by comptonised UV photons rather than reflected hard X-rays (Done et al. 2012). As current facilities are not able to spectrally distinguish this additional component from multiple reflected components the origin of the excess emission is still unknown.
With its large effective are for soft X-rays and the spectral capabilities of its XIFU ATHENA will provide the data required to explain the excess emission (Dovciak et al. 2013).

Mapping the Circum-Nuclear Matter Within the region where the gravitational potential of a black hole exceeds that of its host galaxy, matter is found in a manyfold of dynamical and ionization states. Through emission and absorbtion lines emitted from this sphere of influence, it is in principle possible to determine size and velocity of the emitting regions (Dovciak et al. 2013). An example would be the iron K_α visible in near all AGN spectra (Nandra 2006). However, the position within the circumnuclear gas can not be resolved through the lack of spectral resolution of current instruments.
Through its large effective area and the good spatial resolution, ATHENA will be able to map the innermost regions around a black hole.

2.1.3. Measuring Black Hole Spin

Black holes belong to the most exotic objects in our universe. According to general relativity a black hole can be characterized using only its mass, spin and electric charge. Extensive theoretical work on this "no hair conjecture" was done in late 60's and early 70's. The implicit assumptions of these theorems were thereby justified by Hawking (see Hawking 1973)[1].

[1]For more details about uniqueness or no hair theorems the reader may refer to Mazur 2000. Furthermore, recent work indicates that black holes may be more hairy than initially suggested as

In the past 20 years extensive observations and data analysis have yielded a list of black hole candidates and constrained their mass (these candidates can be found e.g. in Remillard and McClintock 2006). Furthermore, it was possible to begin the determination of the spin of a small number of these black holes. The proper description of large masses and their surroundings requires Einsteins theory of general relativity. In case of both, non rotating and rotating spherical mass distribution, the solution to Einsteins field equations are given by the Schwarzschild- and Kerr-metric (see Schwarzschild 1916 and Kerr 1963) respectively. These solutions imply the existence of a horizon around a high mass object where the required escape velocity exceeds the speed of light. Anything within the enclosed volume is unable to leave the gravity well and is thus invisible for an outside observer. If the density is sufficiently large, the object itself is inside this Schwarzschild-radius and "invisible"(thus the name black hole). The Schwarzschild-radius also defines the Innermost Stable Circular Orbit (ISCO) around a black hole. In addition to its mass, the spin of a rotating mass also distorts the surrounding space-time. Matter falling towards such an object appears to be dragged along by the mass's angular momentum. This frame-dragging is described by the Kerr-metric and changes the ISCO with respect to that of a non rotating black hole.
Black holes can be found in the form of SMBH at the center of galaxies in which case accretion onto black holes can lead to the formation of an AGN that emits large amounts of electromagnetic radiation over the complete spectrum. Similarly, galactic black holes can be observed through the accretion of matter (although in that case the matter is mostly donated by a companion star) and in different states of activity. Though the difference in mass of SMBH and their smaller counterparts is several orders of magnitude, galactic black holes can bee seen as scaled down models of SMBH at the center of galaxies. As also the dynamic behaviour of galactic black holes is scaled down, these objects provide the mean to study accretion flows and dynamic processes inaccessible in SMBH (Motch et al. 2013). A star is a rather complex system, which maintains a stable state through the balance of gravitational force, and the fusion driven radiation pressure. In the end of its life cycle, when it is no more possible to maintain energy yielding fusion processes, a star will collapse and form a dense object. If its initial mass is sufficiently large, the gravitational force causes the star to collapse into a point like physical singularity. The star will become a black hole, one of the possible endpoints of stellar evolution. While a large number of its initial properties are lost during the collapse, mass and spin of a black hole are highly determined by its previous form.
As already mentioned, the extreme gravity in the vicinity of a black hole prevents a direct observation. Fortunately, stellar objects often form binary systems. As discussed in the next section, such systems emit X-rays that are characteristic for the objects in the system. A more detailed discussion of the X-ray emission of black holes can be found e.g. in Psaltis 2004 or Remillard and McClintock 2006.

Black Hole Binary X-ray emission Binary systems consist of two stellar objects. These may be either two stars, a star and a compact object (white dwarf, neutron star

summarized in Chruściel, Costa, and Heusler 2015

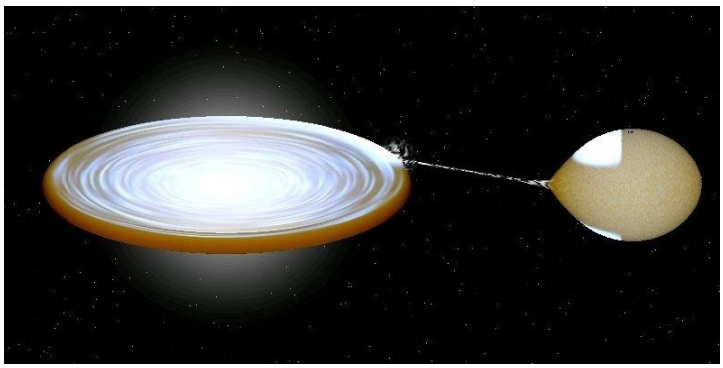

Figure 2.6.: Artistic interpretation of the black hole binary Cygnus X-1. The proximity of the black hole to its companion enforces a direct flow of mass from the companion towards the black hole. The momentum of the emitted mass and the gravitational force of the black hole results in the formation of a accretion disc surrounding the black hole.

or black hole), or even two compact objects. In the following, only the properties of a binary system consisting of a black hole and a companion star are taken into account. In such a system, the gravitational field of the black hole will result in a mass transfer from the companion towards the black hole. This happens either directly by Roch-Lobe overflow, if the two companions are close and the mass of the dense object is high enough (see figure 2.6 for an artistic depiction), or by stellar winds, which are emitted from the companion and caught by the black holes gravity (see e.g. Psaltis 2004 for more details).

The angular momentum of matter released from the companion and the gravitational force of the compact object will lead to the formation of an accretion disc. While matter falls towards the discs center, it mixes with matter from smaller radii. The viscous mixing gives rise to turbulences and induces magnetic fields, effectively causing a transfer of angular momentum from the inside of the disc to its outside while matter moves into the opposite direction. Altogether, the kinetic energy of the falling matter is converted into heat by the turbulent friction inside the accretion disc, leading to an increase of temperature with decreasing radius. The high temperatures near the center of the disc causes the formation of a hot plasma.

Several processes will lead to the emission of photons with different energies that all contribute to the observed spectrum. An example of an X-ray spectrum for an accreting black hole and a illustration of the different components contributing to it is shown in figure 2.7. First, the disc itself will emit thermally generated photons with an emission spectrum that can be modelled by a multi temperature black-body. As the emission itself is in all directions, photons from the disc will move through the surrounding plasma and gain energy by inverse Compton-scattering. The energy distribution of these photons is typically modelled by a power-law spectrum with a high energy cut-off. The spectral emission is proportional to $E^{-\Gamma}$ with typical values of Γ in the range of 1.4 to 2. Since the scattering process is undirected, Comptonized photons can move towards the disc. Here they are again scattered and a part of the incident radiation is "reflected" into the direction of the observer. The corresponding spectral component is then composed of

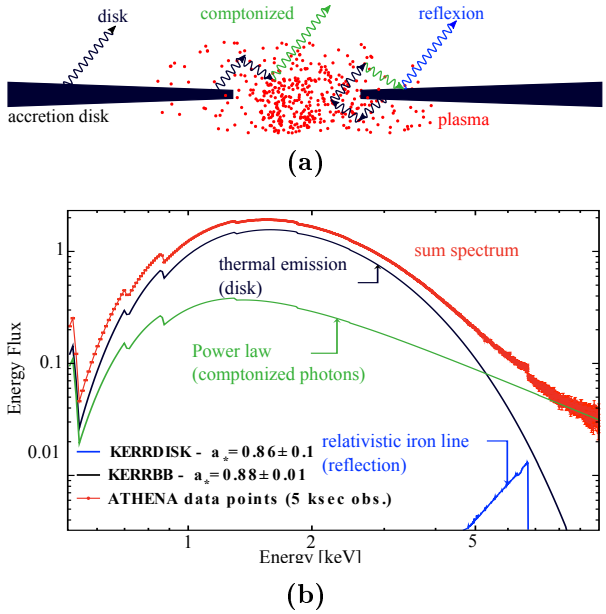

Figure 2.7.: a) The temperature of an accretion disc gradually increases towards its center, generating a surrounding, hot plasma. The disc emits thermally generated photons. Some of these traverse the hot plasma and gain energy by inverse Compton scattering. These high energetic photons can in turn be reflected on the accretion disc. b) The shown simulated spectrum of a black hole consists of a thermal component, a power-law continuum and a reflection component, here primarily visible as a relativistically broadened iron line. (Figure from Lumb et al. 2012)

the reflected photons and characteristic fluorescence lines as illustrated in figure 2.7. For an external observer, the emitted fluorescence lines are blue or red-shifted by gravity and rotation. The exact composition of the relativistically broadened lines is thereby largely depending on the origin inside the disc.
As pointed out beforehand, the smallest possible orbit around a black hole, the ISCO, is defined by the black holes mass and spin. Since the ISCO defines the shape of the accretion disc, the X-ray emission of a black hole binary system is in turn characterized by the mass and spin of the black hole.

Measuring the Black Hole Spin All in all, there are two methods based solely on X-ray spectroscopy that can be used to determine the spin of a black hole.
The first uses the thermal emission from the accretion disc. The disc temperature increases towards its center. According to the Kerr-metric, the ISCO around the black hole is tied to its spin. Since higher temperatures are emitted from smaller radii of the disc, the characteristic multi-temperature black body emission depends on the black holes spin. An exact model of this thermal component can be (and already is) utilized for spin measurements.
The second way is the determination of the relativistically broadened iron-K line profile

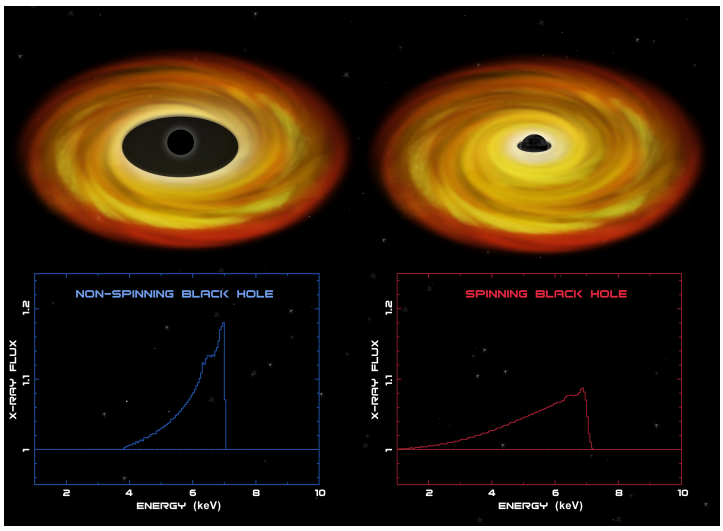

Figure 2.8.: The reflection component of a black hole binary largely depends on the spin of the black hole. The reason for this is that the spin of the black hole distorts space time and thus influences the innermost stable circular orbit around the black hole (Illustration: NASA/CXC/ M. Weiss; Spectra: NASA/CXC/SAO/ J. Miller 2003).

around 6.4keV energy range. The red shift of a photon is determined by its origin inside the accretion disc. Thus photons emitted from different positions inside the disc will show different red shifts. The exact shape of this relativistically broadened iron-K-line is given by the mass and spin of the black hole, the position of the emitting material within the accretion disc and other factors. Spectra as expected from black holes with largely different spins are indicated in figure 2.8. An exact measurement and modelling of the iron K line can be used as a direct measure for the spin of the central black hole.
A third method requires sufficient timing capabilities of the used sensor and is based on the timing properties of the emitted spectrum. The power spectra of black hole binaries show distinct timing features as quasi-periodic oscillations. Furthermore intensity changes of different energy bands show a time lag that is tied to the movement of photons over the macroscopic distances of the accretion disc. A thorough understanding of these effects could be used to determine the properties of black holes. In addition these spectral features can be used to probe the current understanding of general relativity.
For further details on X-ray binaries, their spectral and timing properties as well as methods to determine black hole spin refer to Remillard and McClintock 2006 and references therein.
The different spin measurement methods are still in a process of gradual improvement. Ideally, the different methods should yield the same result for a given black hole. Provided an instrument is capable to deliver spectral data that allow to apply more than one method on the same set of data, the different methods could be used to cross check the underlying models. This should finally yield highly accurate spin estimations.
This, however, requires an instrument that has sufficient spectral resolution as well as count rate capability to observe bright galactic sources. In addition, a time resolution

sufficient to resolve flux changes in the different energy bands related to the black holes mass and spin would be beneficial.

2.2. The Athena Mission

ATHENA is intended to provide a leap in observational capability with respect to current and planned facilities to address the topics discussed in the previous section. For this, ATHENA's payload will consist of a focussing X-ray optics and two X-ray spectrometers. These are the XIFU and the WFI. The XIFU will provide excellent spectral resolution, but only over a limited field of view, while the WFI, will grant moderate spectral resolution and high sensitivity over a large field of view. Furthermore, the WFI will be able, to observe even brightest radiation sources.
ATHENA is suggested to be stared in 2028 by an Ariane V class launch vehicle into an L2 orbit. Its foreseen life-time is 5 years with 5 years of extension. From the scientific objectives discussed beforehand, a number of requirements for the different parts of ATHENA can be derived. A detailed confrontation of observational goals and requirements can be found i.e. in Nandra et al. 2014. In the following a justification for the respective science requirements with respect to the herein presented science will be provided. Following this introduction, ATHENA's mirror system and its two spectrometers will be discussed.

2.2.1. Science Requirements

Parameter	Requirement
Effective Area	2 m^2 at 1 keV 0.25 m^2 at 6 keV
PSF HEW	5" on axis 10" on axis
XIFU Energy Resolution	2.5 eV
XIFU Calibration Accuracy	0.4 eV
XIFU FOV	5' diameter
XIFU threshold	0.2 keV
WFI FOV	40' x 40'
WFI Energy Resolution	80 eV at 1 keV 170 eV at 7 keV
WFI count rate capability	1 Crab with 80 throughput and less than 1 % pile-up
WFI time resolution	$<$80 µs
Instrumental Background	$<$5x1e-3 cts/cm^2/s/keV

Table 2.1.: Requirement for the ATHENA mission.

To measure and identify faint objects as either early groups or the WHIM a large effective area for both low energetic X-rays (E $<$ 1 keV) and higher energetic emission (E = 6 keV) is required. Furthermore, to disentangle different sources from each other or to provide detailed velocity maps e.g. to measure the effects of AGN jets and their energy deposition into the ICM, a spatial resolution better than 5" on axis and better than 10" off axis are necessary. To determine the process of matter assembly in clusters, the energy dissipation of jets and to record a census of baryons in

the warm hot phase, the XIFU must provide an energy resolution of 2.5 eV FWHM. Simultaneously, its absolute accuracy should reach 0.4 eV.

A sufficient FOV for the XIFU to provide enough details about matter assembly, metal production and dissipation as well as the dissipation of jet energy is deemed to be 5 minutes of arc. The lower energy limit of the XIFU is suggested to be 0.2 keV to get all information of warm hot baryons, the physical properties of the WHIM and the interaction of winds and outflows with their environment. Through its FOV of 40 x 40 square minutes of arc, the WFI will help to identify early groups, provide information about non-gravitational heating, help to understand the metal production and dispersion in galaxies and clusters and provide a population study of high z AGN as well as a complete census of AGN at the peak of star formation and accretion activity. To fulfill the different science requirements, a sufficient energy resolution is mandatory. At low energies of about 1 keV, the FWHM energy resolution is meant to be about 80 eV to provide sufficient resolution for the detection of highly red shifted X-ray lines. For spin measurements and reverberation measurements of black holes on the other hand an energy resolution of 170 eV FWHM at 7 keV is necessary. For the observation of bright, galactic black holes, a count rate capability sufficient to observe a Crab-like source with less than 20 percent dead time is required. One Crab flux unit about $2.4 \cdot 10^9$ erg/s/cm^2 over the energy range of 2 keV to 10 keV. With the expected effective area of ATHENA's mirror system, that equals a count-rate of about 10^5 cts/s.
To achieve the sufficient sensitivity for faint sources, an instrument background below $5 \cdot 10^3$ cts/s/cm^2/keV is demanded. By providing the above discussed instrument requirement, ATHENA will be able to address questions of matter assembly, non-gravitational heating, metal production and dispersion and a complete census of AGN at the peak of activity in the Universe. There are furthermore constraints on ATHENAs astrometric accuracy and the efficiency and response time to GRBs. These are largely related to the spacecraft, respectively the telemetry and data analysis, and a discussion is beyond the scope of this work. However, details can be found in (Nandra et al. 2014) and references therein. In the next subsections the properties of ATHENAs mirror system and its two spectrometers will be discussed.

2.2.2. Mirror Assembly

The observation of faint sources is usually accomplished using optics that focus the light from a large collection area onto a sensor. In the optical band this can be accomplished using lens or mirror systems that work on near normal incident. The focussing of X-rays is more complicated as for optical light. Usually, a system of two surfaces in a so called Wolter configuration are used. Multiple surfaces with different diameters are used to build a Wolter-telescope (Wolter 1952), that focusses radiation over a large bandwidth range onto an X-ray sensitive detector.
For ATHENA and its predecessors, a new mirror design for a Wolter 1 telescope has been developed (Willingale et al. 2013). It utilizes Silicon Pore Optics (SPO) technology (Beijersbergen et al. 2004). The complete mirror is built of modules, that in turn consist of two stacks of silicon wafers. Each wafer is groove cut such, that only a thin layer of

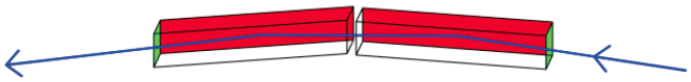

(a)

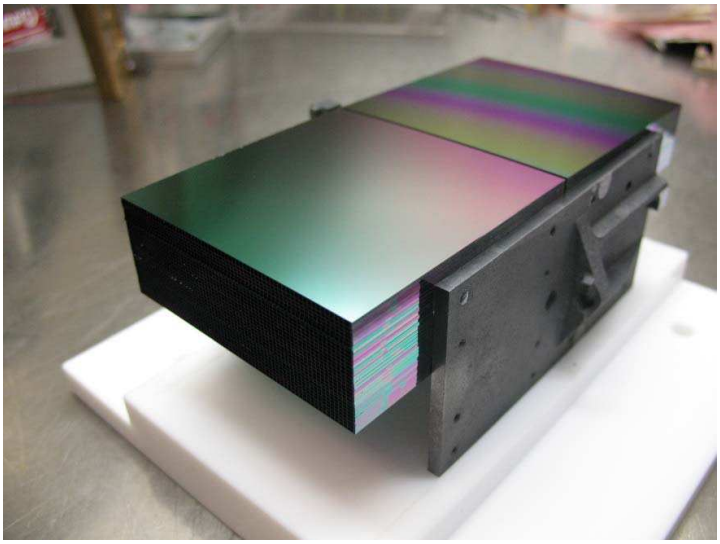

(b)

Figure 2.9.: a) shows the functional principle of a single pore of an SPO. These pores are formed through stacking multiple groove cut wafers. By aligning two of these wafer stacks, a single mirror module is formed. Each pore is a small sector of a Wolter-I telescope. Multiple mirror modules are assembled into a mechanical frame to form the complete ATHENA mirror system as shown in figure 2.10.

about 150 µm is left. Through stacking of several wafers, the grooves form pores and the thin layer is the surface of reflection for incident X-rays. Two pores, aligned correctly to each other, form a small sector of a Wolter 1 telescope as shown in figure 2.9a. A complete module, formed of two wafer stacks is shown in figure 2.9b. The wafers are stacked on a precision mandrel to achieve the required curvature, and cold bonded onto each other. The stacking process results in a conical approximation of a Wolter optics. Multiple modules are assembled in a proper mechanical frame shown in figure 2.10, to form the complete mirror system. Compared to other mirror technologies, the SPO technology provides a drastic reduction of mass for the same effective area (Willingale et al. 2013). For an effective area of about 2 m^2, a diameter of 3 m and a focal length of 12 m are required (Nandra et al. 2014). To populate this area, about 1000 mirror modules are necessary. Through a tightly controlled manufacturing process, it should be possible to achieve an on-axis HEW of 5" for the complete mirror system. In fact, it was already demonstrated, that single modules are able to achieve the required spatial resolution (Willingale et al. 2013). To improve the low energy response of the mirror

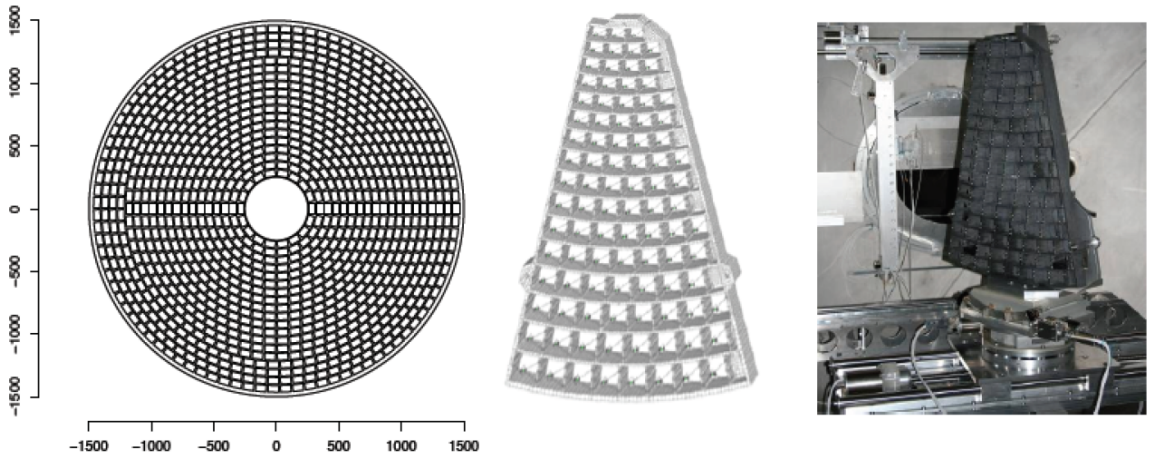

Figure 2.10.: The complete mirror assembly, as shown on the left is composed of multiple mechanical frames, shown in the middle picture, that in turn are populated by mirror modules shown in figure 2.9b. The modular approach will lead to an effective area of 2 m^2 and an angular resolution of 5 seconds of arc on axis.

system, it is possible to coat the wafers with a high-Z material. In addition, different module assemblies to improve the angular resolution of the final mirror system are under development (Willingale et al. 2013).
The current state of the SPO mirror system for ATHENA is reasonably progressed to assume that the requirements to achieve the observational goals for ATHENA can be fulfilled.

2.2.3. X-ray Integrating Field Unit

A single cell of the XIFU consists of an absorber and a Transition Edge Sensor (TES) that have a strong thermal connection. The TES is weakly coupled to a cryogenic bath and operated close to its transition between super- and normal conduction (Irwin and Hilton 2005). An incident photon will deposit its energy in the absorber and heat it up. The heating will cause the TES to switch from super- to normal conducting. The heat is dissipated through the weak link to the cryogenic bath, with a time constant characterized by the thermal capacity of the absorber and TES and the thermal coupling to the cryogenic bath. The TES generates a current signal that is amplified by a Superconducting Quantum Interference Device (SQUID) that is operated at 50 mK. The SQUID signal is further processed by a low noise amplifier.
Multiple pixel of the TES are connected to the same SQUID. The signal multiplexing is done through Frequency Domain Multiplexing (FDM). Each pixel is equipped with an LC circuit in series with the resistance of the TES. Each pixel is excited through its respective resonance frequency. Through the switching from super- to normal-conduction, the quality of the resonance circuit is drastically reduced, leading to a modulation of the resonance signal. The TES resistance change is later demodulated, the signal pulse

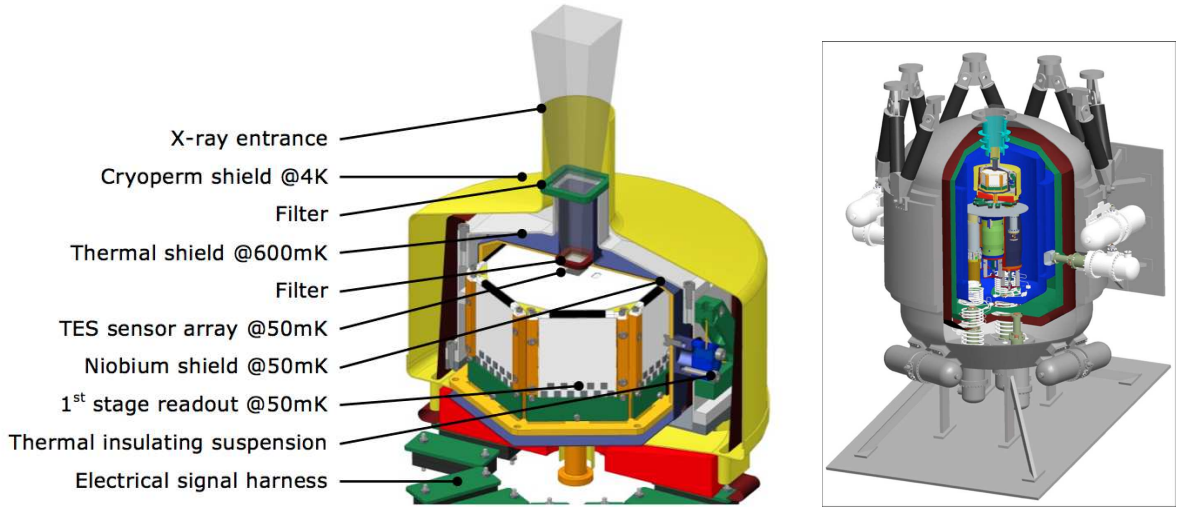

(a) **(b)**

Figure 2.11.: a) Shows the FPA of the XIFU consisting of the sensor, thermal and magnetic shielding, and the first readout stage. b) The FPA is embedded in the complete instrument and surrounded by several thermal shields and the different cooling stages.

reconstructed and the energy information retrieved. This multiplexing scheme allows to read 3840 TES sensors using only 96 readout channels.
The XIFU is equipped with an anticoincidence filter that is used to suppress background events. Foreseen is a cryogenic TES based anticoincidence filter with Silicon as absorber and Iridium as TES (Macculi et al. 2014). The anticoincidence will be comprised of four TES arrays. Required is a rejection of primary particles larger than 98%, a low energy threshold of 20 keV and a size of 18 x 18 mm^2 with a rise time faster than 30 µs. Prototypes fulfilling these requirements have been produced (Macculi et al. 2014).
The FPA of the XIFU, shown in figure 2.11a, will provide the thermal and mechanical support for the sensor, the anti-coincidence detector, and the cold electronics. It will also provide the required magnetic shielding. Two magnetic shields are foreseen and attenuation of fields by a factor of $1.6 \cdot 10^5$ have already been measured (Barret et al. 2013). Furthermore, a filter wheel with an optical blocking filter, a beam diffuser for the observation of bright point sources, a closed position and an calibration source will be implemented.
The cooling chain consists of several stages with two major components. The upper cooling chain provides cooling down to 2 K while the last stage grants the cryogenic bath at 50 mK (Rando et al. 2010). A model of the complete instrument including cooling stages and thermal shields is shown in figure 2.11b, with the FPA embedded in the center.
The exceptional energy resolution over a sufficiently large sensor array, of the XIFU will grant a new deep look into the Universe.

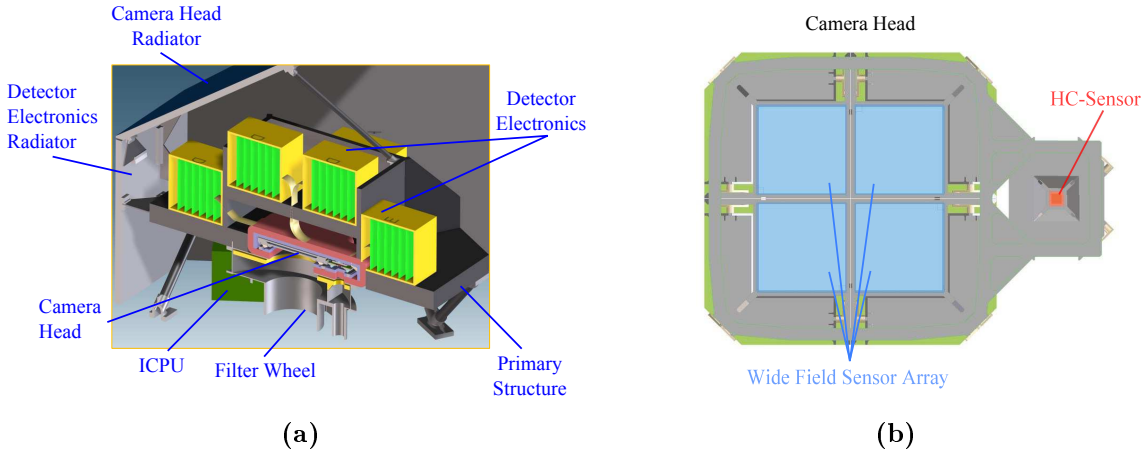

Figure 2.12.: a) The WFI consists of its camera head, corresponding detector electronics, the ICPU, a filter wheel, radiators and the mechanical structure. b) The focal plane of the camera head is formed by 5 silicon based sensors. 4 of these are combined to provide an field of view of 40'. Adjacent to this large area sensor array, is an additional fifth sensor. This device will be optimized to cope with even highest count rates.

2.2.4. Wide Field Imager

The WFI will consist of the camera head, the surrounding detector electronics, the instrument control and power conditioning unit as well as the required radiators and mechanical structure as shown in figure 2.12a. The camera head will be composed of 5 individual solid-state-sensors and the required front-end Application Specified Integrated Circuits (ASICs).
The sensors will be based on silicon, which has a long heritage as sensor material in science and X-ray astrophysics. Well known are the properties of Hybrid Pixel Detectors, CCDs and Silicon Drift Detector (SDD). The developments for future X-ray missions are currently focussed on Active Pixel Sensors (see Holl et al. 2003 and Bautz et al. 2009). One Active Pixel Sensor (APS) concept is the so-called DEPFET that was developed at the MPI-HLL in Munich.
ATHENA's WFI will utilize the DEPFET technology for all its detectors. 4 monolithic sensors, based on the DEPFET technology, with an area of about 7×7 cm^2 each will form a large scale sensor array providing highest sensitivity over an unprecedented field of view of 40 minutes of arc. In addition, to be able to observe even brightest radiation sources the WFI will be equipped with a fifth sensor designed to accommodate high count-rates.

High-Count-Rate Sensor

Black hole binary systems, especially galactic binary sources, tend to be among the most luminous, respectively brightest, sources in the sky. In addition, many usually

quiet sources as e.g. AGN regularly undergo phases of intense emission. During these they exceed their quiescence flux by several orders of magnitude. While it is possible to observe bright (and therefore potentially interesting) sources also with current instruments, their limitations significantly hamper our ability to make progress in the understanding of these objects as either most of the flux is discarded as pileup (Motch et al. 2013), or their spectral performance is too poor to provide sufficient spectroscopic information for the determination of e.g. black hole spin.
Pile-up appears when the arrival time of two consecutive incident photons is smaller than the readout time constant of the respective pixel of the detector. In that case, the two signals "pile up" on each other and it is not possible to discriminate these events and, in the worst case, they have to be discarded. For ATHENA's WFI, a requirement of less than 1 % pile-up at a source brightness equal to that of the crab nebula is defined. Simultaneously, the instruments throughput should be larger than 90 %. Furthermore, an energy resolution better than 150 eV and a time resolution better 80 µs are demanded according to Nandra et al. 2014.
The high count-rate sensor of the WFI will be designed to accommodate count-rates of bright sources with minimal pile-up. It will thus be capable to provide high quality spectra of bright sources in a fraction of the time required by current instruments. Apart from the obvious benefit of reduced observation time, this will furthermore enable the observation of fast variations within these sources, which is not possible with current instruments of otherwise comparable spectral resolution.
Using a DEPFET based sensor, there are two possibilities to reduce pile-up. The first is to spread the incident photons over several pixels and thus reduce the count rate for each individual pixel. The second way would be to increase the readout speed of the whole sensor. It is furthermore possible to settle for a moderate combination of these two extremes.
In this thesis, different advanced DEPFET concepts are studied with respect to a high count-rate achieved through a fast readout.

3. The Spectral Response of a DEPFET Sensor

Radiation passing a solid state sensor interacts with electrons and nuclei of the sensitive material. While elastic processes only change the momentum of incident particles, inelastic processes will cause the transfer of energy and momentum resulting in the generation of electrons and ionized atoms. Overall these processes result in the generation of a charge cloud inside the sensor. Thus, it is possible to detect a broad spectrum of radiation, as light and heavy charged particles as well as electromagnetic radiation from a few eV up to several hundred keV.
From a technical point of view, the detection of radiation is then just the process of counting the number of electrons generated inside a sensor by incident radiation. As simple as this may sound, there is a number of processes that deteriorate the counting process.
A perfect sensor system would be capable to detect every incident particle, reconstruct its energy and position with arbitrary accuracy and do this infinitely fast. A real detectors has limitations that arise from the physical processes that allow the detection of incident radiation and from imperfections of the detector system. Both will be discussed in the following sections.
The discussion starts with the interaction processes leading to the generation of the primary charge cloud, followed by its transport to a read node. The amplification of the collected charge is then considered on the example of the DEPFET amplifier structure. Covered are the charge amplification, noise and different readout schemes.
The energy signal of incident photons is distorted by the physical processes that allow their detection and the corresponding statistical fluctuations. Incident photons of a single energy will thus not generate a single output signal but a spectrum that is characteristic for the sensor and energy. That response function can be seen as a probability distribution that describes the output signal with respect to a given incident radiation. In the third part of this chapter an analytical formulation of that response function for silicon as detector material will be derived.
The applied readout method may introduce further deteriorations of the response function e.g. due to the readout method. In the fourth part of this chapter, the spectral response is extended for time dependent readout artifacts to describe the response of DEPFET based sensors, read out on demand.

3.1. Detection of Radiation

This section discusses the interaction of incident radiation and the processes leading to the generation of a charge cloud inside a silicon based sensors. The focus is thereby set to electromagnetic radiation in the energy range from 0.1keV up to 10keV(which is the typical range of astrophysical observatories for soft X-rays).
The generated charge carriers are subject to the electric field inside the sensor. This field has to be shaped such that the electrons are moved to a read node and any charge loss is avoided. The shape of the field is determined by surface contacts as pn-junctions and MOS-structures. These structures as well as the electron transport will be considered in the second part of this section.

3.1.1. Detection of Radiation

As this work is focused on spectroscopic devices for applications in X-ray astrophysics, particle interaction will be neglected. Furthermore, we will focus on the electromagnetic regime of interest from 0.1keVup to 10keV. Although elastic scattering effects as Thompson and Rayleigh scattering as well as inelastic Compton scattering are present in this energy regime, the dominant interaction process is the photoelectric effect of electromagnetic radiation with the silicon 1s or K-shell electrons.
Therefore, the discussion will be limited to the photoelectric effect and related secondary interaction. For a discussion of all interaction mechanisms the reader is referred to standard literature (see Knoll 1999; Sze and Ng 2007).

3.1.1.1. Photoelectric Effect

The photoelectric effect is the absorbtion of a photon by an atom and the following emission of a photoelectron. In this process, the energy E_{ph} of the photon, propagating into the direction $\overrightarrow{k}$ is transferred to a bound electron. If the photon energy exceeds the electron binding energy E_{bind}, this causes the emission of the electron to an unbound state of Energy $E_{pe} = E_{ph} - E_{bind}$ with momentum $\overrightarrow{p}$ as depicted in figure 3.1a. The probability for this interaction process is given by the interaction cross section σ_{shell}. Extensive tabulations of cross sections for different materials and photon energies are provided e.g. by the National Institute of Standards and Technology (NIST)[1] and The Center for X-ray Optics (CRXO)[2](the there listed values are based on Seltzer 1993 and Henke, Gullikson, and Davis 1993). Graphs of the cross sections for silicon, silicon-nitride and silicon-oxide are provided in appendix C.
Since the electrons are excited by the electric field of the photon, the angular distribution of photoelectron-emission peaks into the direction of the electric field. In addition, in the absorbtion process, the photons momentum is also transferred to the electron causing the emission distribution to have a slight preference pointing into the photons propagation

[1] `http://www.nist.gov/pml/data/xraycoef/`
[2] `http://henke.lbl.gov/optical_constants/`

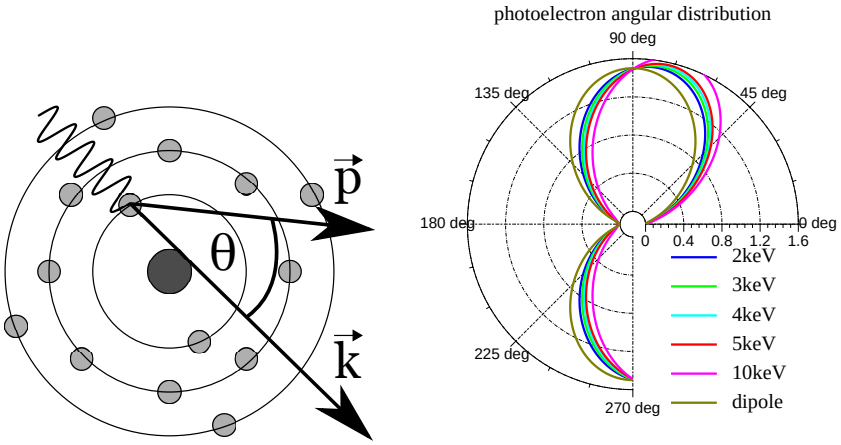

(a) **(b)**

Figure 3.1.: a) shows a schematic depiction of the photoelectric effect. An incident photon with wavenumber k excites a bound electron, in the shown case from the K-shell into an unbound state. The electron will move into the direction of p. The angle θ between incident photon and excited electron can be described by equation (3.1). The distribution for incident photon energies from 2 keV up to 10 keV is depicted in b).

direction. While analytic calculations allow qualitative insight to the physical process (see Sauter 1931a; Sauter 1931b) and describe the dependency of the cross section on atomic number and photon energy, they are not sufficient for quantitative analysis (Pratt, Ron, and Tseng 1973).

In the following, the formula proposed by Cooper (Cooper 1992) for the differential cross section $\frac{\mathrm{d}\sigma_{shell}}{\mathrm{d}\Omega}$ of unpolarized incident radiation is utilized. Including asymmetries for the emission probability this formula is given through

$$\frac{\mathrm{d}\sigma_{shell}}{\mathrm{d}\Omega} = \sigma_{shell} \cdot \frac{1}{4\pi}(1 - \frac{\beta}{4}(3cos^2(\theta) - 1) + (\frac{\gamma}{2}\sin^2(\theta) + \delta)cos(\theta)). \tag{3.1}$$

Here θ denominates the angle between direction of propagation $\overrightarrow{k}$ of the incident photon and direction of emission $\overrightarrow{p}$ of the electron. The factor σ_{shell} is the interaction cross section for the respective atomic shell and incident photon energy, while the parameters β, γ and δ correspond to electric dipole, quadrupole, and magnetic dipole transitions. All parameters dependent on the energy of the incident photon, electron orbital and atomic number (see Trzhaskovskaya, Nefedov, and Yarzhemsky 2001; Trzhaskovskaya et al. 2006). The tabulated values for silicon are listed in appendix C. Figure 3.1b shows the angular distribution of photoelectrons with energies from 3 keV - 10 keV emitted by a silicon atom, together with emission in dipole approximation (corresponding to a β value of 2).

The absorbtion probability for an incident photon is, as mentioned above, given by the

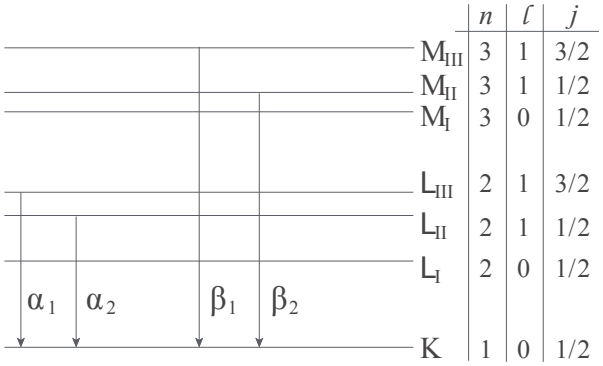

Figure 3.2.: The notation for X-ray fluorescence lines starts with a Greek letters that denote the initial shell of the electron transition. Any fine structure of these lines is denoted by numbers in ascending order of the transition energy. Shown are only those transitions that are allowed by the selection rules.

interaction cross section of the single shells of an atom. A more common description for the absorbtion of photons is given by Lambert-Beers Law

$$I(z) = I_0 \exp(-\mu z)\,. \tag{3.2}$$

Here $I(z)$ is the intensity observed in the depth z, I_0 is the incident intensity and μ the absorbtion coefficient. A quantity also used is the absorbtion length, which is the reciprocal of the absorbtion coefficient. The absorbtion coefficient μ and the sum of the individual shell cross-section σ_{tot} are related by

$$\sigma_{tot} = (\mu/\rho) m_a / N_A\cdot, \tag{3.3}$$

Here, ρ is the density of the material, m_a the molar mass and N_A the Avogadro number. Graphs and selected tabulated values for the absorbtion length are provided in figure C.1 and table C.1 summarized in appendix C.

3.1.1.2. Atomic Relaxation

As discussed above, the incident photon causes the emission of a photoelectron from a bound state and thus generates furthermore an atom in an excited state. The relaxation of that atom happens by radiative or non-radiative transition processes. Subsequently the vacant atomic shell will be filled by electrons from higher shells. This relaxation process is accompanied by the emission of photons or electrons. The probability for a fluorescence process (the emission of a photon) is given by the fluorescence yield ω. The energy of the emitted photon is defined by the difference in binding energy of the participating shells, which allows the identification of the process causing the fluorescence. Correspondingly the photon is named by the participating shells, starting with the vacant shell (K,L,M) typically followed by an index α or β depending on if the shell is filled by an electron from the next higher or the next but one higher shell. Furthermore the different energy levels for one shell can be distinguished by indexing

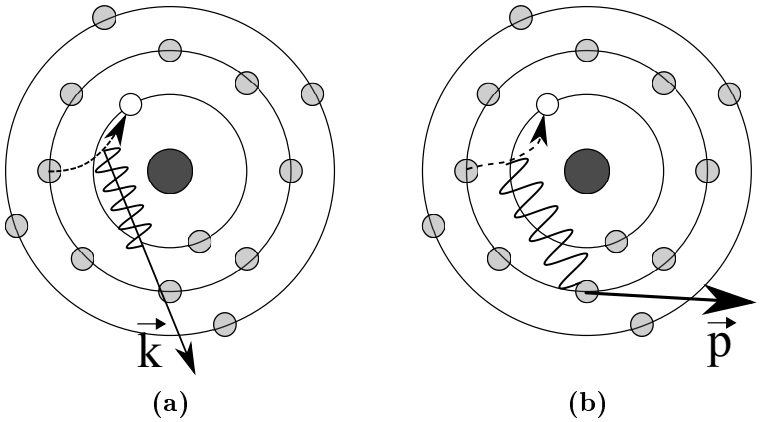

Figure 3.3.: A vacancy caused by photoelectric absorbtion will subsequently be filled by electrons from higher energy states. During this relaxation process either a fluorescence-photon a) or an auger-electron b) is emitted.

the transitions. The naming scheme for allowed transitions is depicted in figure 3.2.
The second relaxation process is the Auger-effect. Here the energy of the relaxation process is transferred to another electron, that subsequently enters an unbound state. The energy of the emitted Auger-electron is characteristic for the bound states of the participating electrons. Auger electrons are thus labelled by 3 characters naming all participating shells. The first character defines the vacancy. The second character corresponds to the shell the first electron is originated from, the third character is the shell of the emitted electron. A K-shell vacancy may e.g. be filled by an electron from the L-shell. Instead of the emission of a K_α fluorescence photon, the resulting energy is transferred to another electron from the L-shell leading to the emission of a KLL-Auger-electron.
For elements with $Z < 17$, less than 10% of all transitions are followed by the emission of a photon (see Perkins, Chen, and Hubbel 1991). Thus the dominating relaxation process is the Auger-process. In the case of silicon (Z=14) 95% of the excited atoms relax by the emission of an K-shell auger-electron while only 5% relax by emission of a K-shell photon. The Auger-electron emission probabilities and the fluorescence yield for silicon are summarized in table C.3.

3.1.1.3. The Range of Energetic Electrons

As pointed out in the previous section the photoelectric absorbtion inside a solid will most likely cause the generation of a photoelectron and an Auger-electron. These electrons will be subject to further interactions. In the energy range of interest the dominating processes are elastic scattering, changing the electrons direction and inelastic scattering, mostly changing its energy. The characteristic values corresponding to these processes are the inelastic and elastic mean free path. Both define the mean range elec-

trons travel before undergoing an interaction. The electron will interact in this manner until all its energy is dissipated or it leaves the solid. The average number of charge carriers N_e generated by an electron is defined by its initial energy E_{kin} and the mean energy necessary to generate a single electron hole pair. For silicon this pair-creation energy is $w = 3.66\text{eV}$ (see Scholze, Rabus, and Ulm 1998). Provided that the complete energy E_{ph} of an incident photon is deposited inside the sensitive volume of the sensor, the number of generated electron hole pairs is

$$N_e = \frac{E_{ph}}{w}. \tag{3.4}$$

With decreasing energy, the probability that an electron is subject to a scattering process increases. Thus electrons will dissipate the majority of their energy on the final part of their way.
In total exists a variety of range parameters, which are commonly used to describe the mean, average, extrapolated or maximum distance an electron with the kinetic energy E_{kin} travels through a material (see Iskeff, Cunningham, and Watt 1983 for a discussion of the different range parameters).
For analytical considerations, approximations based on measurement data can and are widely used. Two common approximations are the formulas stated by Iskeff for the approximated range of energetic electrons inside a material (Iskeff, Cunningham, and Watt 1983) and Fittings relation for the maximum range (Fitting 1974). In the scope or this thesis the formula of Fitting for the maximum range

$$R_{max} = 90 \cdot \frac{E_{kin}^{1.3}}{\rho^{0.8}} \tag{3.5}$$

will be used. The formulas only variables are the material density ρ and the kinetic energy E_{kin} of the electron.
The influence of energetic electrons on the spectral response function is twofold. For once it is possible, that the primary electrons deposit only a fraction of their energy inside the sensitive volume. This leads to the formation of several "flat shelfs" in the spectrum (see section 3.3.2.5). Furthermore, the charge cloud has a starting diameter largely defined by the incident photons energy. Imperfections and Impurities close to the sensor surface may cause the recombination of generated charge carriers (for more details see section 3.1.2.2) and give raise to a characteristic tail in the spectral response function (see section 3.3.2.2).

3.1.2. Electron Transport in Silicon Sensors

What remains, once an energetic electron has deposited all its energy to the silicon, is a charge cloud composed of electrons and holes. The number of generated pairs is thereby proportional to the energy of the incident photon. Thus, to measure the energy of the incident photon it is sufficient to "count" the number of either electrons or holes. For this it is necessary to transport the charge carriers from their point of origin to a read

node. Furthermore, a recombination or loss of charge carriers has to be avoided.
Inside a semiconductor, charge is transported either by diffusion due to a density gradient or, if an electric field is present, by a drift of the charge carriers. The most basic structures to build a silicon sensor is a pn-junction. While a simple diode can be used to detect radiation, high quality X-ray spectroscopy requires more sophisticated techniques as e.g. the principle of sidewards depletion. Furthermore, the generation of a defined electrostatic profile inside the sensor often requires MOS-structures e.g. to avoid a current flow between p-contacts on different potentials.
For in depth discussion of semiconductor physics refer to Sze and Ng 2007 and similar literature. The following will only discuss the above mentioned structures and the charge transport as required in the scope of this thesis.

3.1.2.1. The Electric Field inside a Sensor Device

The dominating charge transport mechanisms inside semiconductors are diffusion due to an imbalanced carrier density and drift caused by the application of an external electric field.
The movement of charge carriers due to diffusion always points from regions of high carrier density to regions of low carrier density. Assuming a spot-like carrier distribution, which is a sufficient first approximation for the carrier distribution directly after the conversion process of a photon, diffusion will cause the charge carriers to move uniformly into all directions.
In contrast, a drift of charge carriers caused by an electric field is defined by the direction of the electric field. On their path the electrons will be accelerated by the electric field until they are subject to an interaction with other electrons or the semiconductor crystal. Due to these interaction processes charge carriers are not accelerated infinitely when moving inside a solid. The mean velocity of charge carriers inside a solid is defined by the carrier mobility and the external field. The mobility μ depends on the mean free path length and the sensor material. In silicon, the mean free path length increases with decreasing temperature due to the reduced probability of phonon scattering. The velocity v of electrons subject to an external electric field E is

$$v = E \cdot \mu. \tag{3.6}$$

At high electric fields the electrons will gain more energy between two interaction processes but also transfer more energy by scattering. This results in a saturation of the electron velocity at a maximum value. In the temperature range from 4.2 K and 300 K the saturation velocity in silicon is decreases from $v_{sat} = 1.4 \cdot 10^7 \frac{\mathrm{cm}}{\mathrm{s}}$ to $v_{sat} = 0.96 \cdot 10^7 \frac{\mathrm{cm}}{\mathrm{s}}$(Canali and Ottaviani 1970).

3.1.2.2. PN-Junction

A pn-junction is formed when p- and n- doped semiconductor materials are in contact. If no external bias is applied to these contacts, the concentration difference of majority

charge carriers will result in their drift from one region into the other.
This in turn causes the formation of a region with fixed charge carriers inside the semiconductor, the so called space charge region. In thermal equilibrium, implying an equal Fermi-level for both semiconductor regions, the difference of electrostatic potential, also referred to as built-in potential V_{bi} can be expressed by (Sze and Ng 2007)

$$V_{bi} = \frac{kT}{q} \ln\left(\frac{N_A N_D}{n_i^2}\right). \tag{3.7}$$

With k as the Boltzmann-constant, T the temperature, q the elemental charge, N_A the acceptor, N_D the donor and n_i the intrinsic charge carrier density. The application of an external bias will affect the depletion width. If donor and acceptor concentration show a high asymmetry, $N_A >> N_D$ the space charge region will primarily be formed in the n-doped region. In dependency of the applied bias voltage V_{ext} , the width W_D of the depletion region can be expressed by

$$W_D = \sqrt{\frac{2\varepsilon_0\varepsilon}{qN_D}\left(V_{bi} - \frac{2kT}{q} - V_{ext}\right)}. \tag{3.8}$$

In this equation, ε_0 is the vacuum dielectric constant, ε the relative material permittivity and V_{ext} the applied external bias.
A positive voltage drop between p- and n-doped region will compensate the built-in potential and reduce the depletion width. If that forward bias is sufficient, the small width of the depletion region will result in the recombination of electrons and holes and thus an increase of the current flow. The rate of recombination, and thus the current flow, is exponentially depending on the applied voltage.
Applying a reverse bias voltage increases the depletion width. In this mode only a small current is present. That leakage current is primarily caused by the generation of electron hole pairs due to thermal excitation. Especially crystal defects inside the silicon lattice and unsaturated bonds on the sensor surface act as generation and recombination centers as they introduce intermediate energy states in the silicon band-structure. These intermediate states open a path for a two staged excitation process, with each process requiring a smaller excitation energy. Defects are the main cause for leakage current of silicon devices. Thereby the recombination/generation rate U is defined by the Shockley-Read-Hall relation (Sze and Ng 2007)

$$U = \frac{pn - n_i^2}{\tau_p\left(n + n_i \exp\left[\frac{E_t - E_i}{kT}\right]\right) + \tau_n\left(p + n_i \exp\left[\frac{E_i - E_t}{kT}\right]\right)}. \tag{3.9}$$

The variables n and p are the electron and hole densities, E_t is the energy level of the intermediate state, E_i the mid-gap energy and τ_n and τ_p are the lifetimes for electrons and holes respectively.
In the scope of this thesis, the effect of generation and recombination is discussed in the form of leakage current (see section 3.2.4.2) and a tail in the response function characteristic for the sensor entrance window (see section 3.3.2.2).

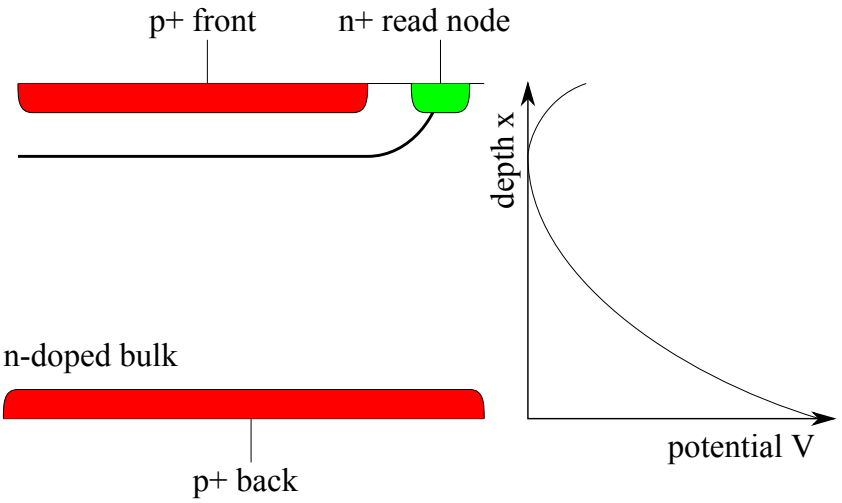

Figure 3.4.: On the left side the basic concept of sidewards depletion is shown. By implanting a p+ contact on top and bottom of the sensor, the device is depleted from both sides. The n+ contact, which also serves as readout node, is placed on the side of the device. In that way, the size of the read node and thus its capacity can be minimized. The resulting parabolic potential profile is depicted on the right. It depends on the sensor thickness, the applied front- and backside voltages as well as the bulk doping.

The most basic structure for the detection of electrons is a diode. To increase the sensitive volume, these devices can be build using low doped or near intrinsic substrate material with p and n contacts on top and bottom. A typical value for a low n^--doped substrate is a donor concentration of $N_D = 10^{12}$ cm^{-3}. Using this value and equation (3.8) it is possible to show that already a bias voltage of 10 V is sufficient to deplete PIN-diodes with a thickness of 100 µm while voltages in the range of 100 V to 200 V are sufficient to deplete devices of up to half a millimeter. Such devices provide high quantum efficiencies up to photon energies of 10 keV. The electric field inside the thus created space charge region will separate electrons and holes and move the former into the direction of the n+ contact and the latter to the p+ contact.

3.1.2.3. Sidewards Depletion

A large improvement of sensor properties is provided using the principle of sidewards depletion. By contacting the sensor over p+ implantations on front- and backside and a small n+ contact on the frontside of the sensor it is possible to reduce the necessary depletion voltage and minimize the readout node capacitance. The principle was first stated by Gatti and Rehak 1984. It is depicted in figure 3.4. The potential distribution inside the sensor can be found assuming a fully depleted volume. Starting from Poissons equation the potential $\Phi(x)$ at the position x inside a depleted silicon sensor is

$$\frac{\delta^2\Phi(x)}{\delta x^2} = -\frac{qN_D}{\varepsilon\varepsilon_0}. \tag{3.10}$$

The potentials on the front $\Phi(x = 0)$ and backside $\Phi(x = d)$ have to match the voltages applied to front and backside contact V_F and V_B. Including these boundary conditions the potential can be expressed by

$$\Phi(x) = -\frac{qN_D}{2\varepsilon\varepsilon_0} \cdot x^2 + \frac{qN_D}{2\varepsilon\varepsilon_0} \cdot x \cdot d + \frac{V_B - V_F}{d} \cdot x + V_F. \tag{3.11}$$

Therefore, the potential $\Phi(x)$ inside the sensor will follow a parabolic profile, which is defined by the voltages applied to frontside V_F and backside contacts V_B, the material permittivity ε, the sensor thickness d_{sd} and the bulk doping concentration N_D. If frontside and backside are biased with the same voltage, the potential minimum for electrons will be located at $x = d_{sd}/2$. Position and value of the potential minimum can be changed by applying a differing bias to front and backside. The position of the minimum is then

$$x_{min} = \frac{1}{2} \frac{qN_D d_{sd}^2 + 2\varepsilon\varepsilon_0 V_B - 2\varepsilon\varepsilon_0 V_F}{d_{sd} qN_D}. \tag{3.12}$$

Combining minimum position and equation (3.11) the potential at the minimum can be calculated to be

$$\Phi_{min} = \frac{1}{8} \frac{qN_D d_{sd}^2}{\varepsilon\varepsilon_0} + \frac{1}{2} (V_B + V_F) + \frac{\varepsilon\varepsilon_0}{2qN_D d_{sd}^2} (V_B - V_F)^2 . \tag{3.13}$$

In the approximation of a fully depleted sensor the influence of any additional structure can be found using the principle of superposition.
The major advantages of a sidewards depleted device are firstly the reduction of the required bias voltages and secondly the minimized read node capacitance. The benefit of the reduced read node capacity will become more obvious in section 3.2.4.

3.1.2.4. MOS-Structure

The MOS structure is built by a SiO_2 insulator sandwiched between the silicon bulk and a metal layer (most commonly built of aluminum or poly-silicon). For this thesis a MOS-structure on top of a n-doped bulk is considered. Depending on the applied voltage the three different states shown in figure 3.5 can be distinguished.

3.1.2.4.1. Accumulation If the potential of the bulk is kept at zero, applying a positive voltage will result in a similar configuration as for a plate capacitor. The positive potential applied to the gate induces a sheet layer of negative charge carriers inside the bulk, below the oxide. Similar to a plate capacitor, the induced charge is (Sze and Ng 2007)

$$V_G - V_{FB} = -\frac{Q_{acc}}{C_{ox}}. \tag{3.14}$$

With V_G being the voltage applied to the gate, Q_{acc} the induced charge, C_{ox} the sheet capacitance of the gate contact. In this formulation the flat-band voltage V_{FB} only

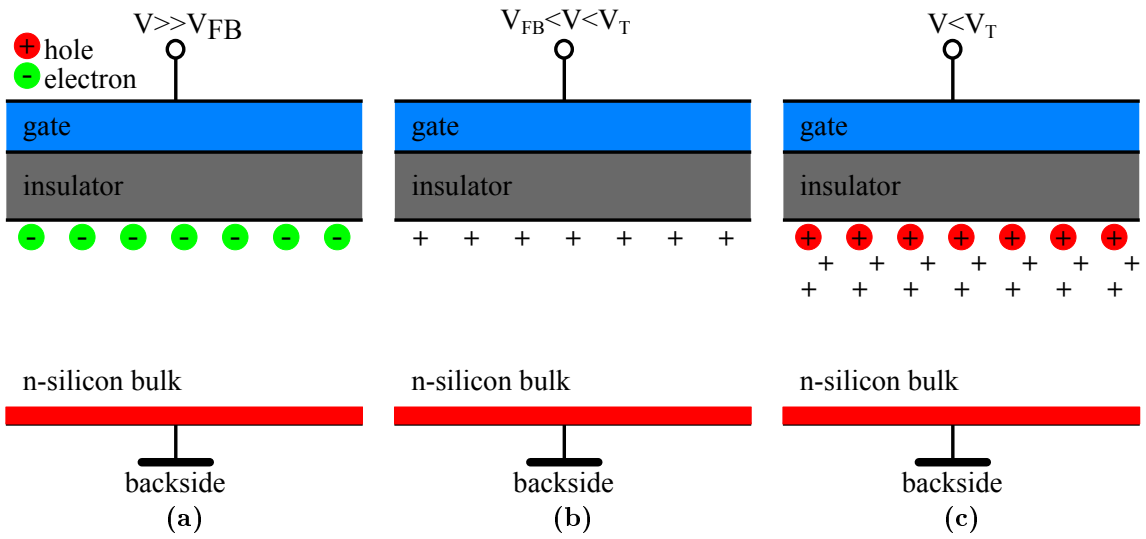

Figure 3.5.: a) Applying a bias more positive than the flat-band voltage will accumulate majority charge carriers below the MOS-structure. b) If the applied voltage is slightly more negative than the flat-band voltage, a depletion region will be formed. c) If the negative bias is further increased, minority charge carriers (e.g. generated by thermal excitation) will be drawn underneath the MOS-structure.

incorporates the difference of the fermi level of the gate material and the silicon bulk. For more sophisticated considerations it would be necessary to take e.g. fixed charges in the oxide into account.

3.1.2.4.2. Depletion The application of a voltage slightly more negative than the flat-band voltage will repel electrons from the region below the silicon-oxide. This result in the formation of a depletion layer below the MOS-structure. The relation of depletion width d_s and applied bias voltage V_G is

$$V_G - V_{FB} = -\frac{qN_D d_s}{\varepsilon_0}\left(\frac{d_s}{2\varepsilon_s} + \frac{d_{ox}}{\varepsilon_{ox}}\right). \tag{3.15}$$

In that relation, the flatbandvoltage V_{FB} is the difference of workfunction of the gate metal and the bulk material. The electric constant is denoted by ε_0 while the relative permittivity of the depleted volume is denoted by ε_s and the oxide permitivity by ε_{ox}. Respectively the thickness of the depleted volume and the oxide are given by d_s and d_{ox}.

Inversion If the negative bias is reduced further the depletion region will increase. As it was assumed that the bulk potential is zero, the forming negative space charge will cause thermally generated electron hole pairs to separate and direct the holes towards the surface. For a gate voltage $V_G << V_{FB}$, the width x_d of the resulting hole or inversion

layers is

$$x_d = \sqrt{\frac{4\varepsilon_{Si}\Phi_F}{qN_D}}. \tag{3.16}$$

3.2. Charge Amplification using the DEPFET

In the previous section the basic interaction leading to the generation of a charge cloud and its transport parallel to the electric field vector inside the sensor was discussed. To detect the generated charge, it is necessary to move it to a read node and amplify the signal. A device that combines the read node and the first amplification stage on top of the sensitive volume is the DEPFET. The DEPFET principle was proposed first in 1987 (J.Kemmer and G. Lutz 1987). Since then, a variety of DEPFET designs optimized for the application in several fields of science have been developed.
One example for the implementation of DEPFET detectors in planetary science is the Mercury Imaging X-ray Spectrometer (Fraser et al. 2010), one of the instruments on board of the 5th ESA cornerstone mission BepiColombo (Benkhoff et al. 2010).
Another example for the use of a DEPFET based sensors will be present at the low-energy beam-line of the european X-FEL. Here a fast detector with tailored dynamic range, the DEPFET-Sensor with built in Signal Compression (DSSC), will be used to count single photon events as well as several 10k photons at once. This DEPFET based instrument is thus suited for diffraction experiments (Porro et al. 2012).
Another example is the innermost part of the Vertex Detector of the BELLE II experiment (Abe et al. 2010). In this case the DEPFET is built on a thinned silicon wafer to minimize the material in the trajectory of the observed particles. In that way, scattering is minimized and the accuracy of particle track reconstruction is optimized.
As pointed out before, a DEPFET based sensor is also proposed as basic building block for ATHENA's WFI. This sensor will be optimized to provide high count-rate capabilities, near Fano-limited energy resolution and a large field of view (Nandra et al. 2013).

3.2.1. Introduction to DEPFET technology

A DEPFET consists of a p-MOS-transistor and an adjacent clear structure implemented on the surface of a high resistive n-type silicon bulk. A cutaway of a circular DEPFET alongside the corresponding equivalent circuit is depicted in figure 3.6.
A DEPFET is built on a substrate that is fully depleted by means of sidewards depletion (see section 3.1.2.3). A deep n-implantation below the MOS-gate forms a potential minimum for electrons, the so-called internal gate. Charge carriers generated within the bulk by incident photons or thermal generation will be collected in the internal gate, modulate the transistor conductivity and can thus be detected. The modulation is proportional to the number of collected charge carriers. Deviations from a linear characteristics are possible due to the capacitive coupling of the internal gate on source and drain. The so-called clear structure formed by clear gate and clear, is used to remove

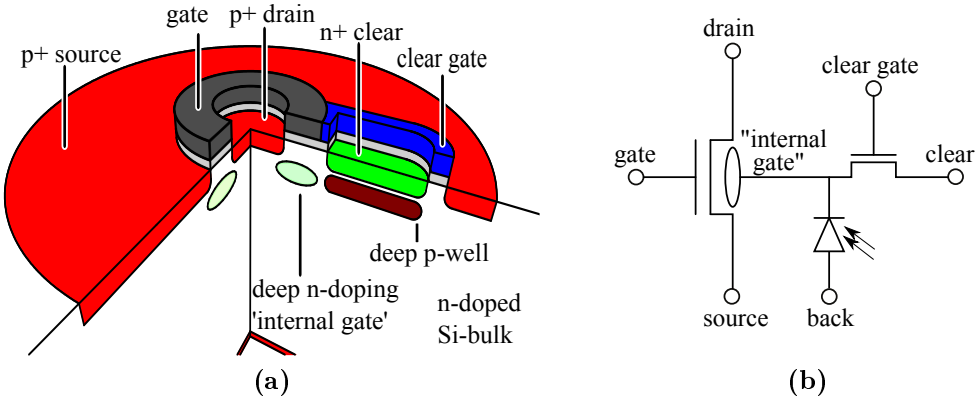

Figure 3.6.: (a) cutaway of a circular DEPFET. (b) equivalent circuit of a DEPFET.

collected charge carriers from the internal gate.
As the p-MOS transistor serves as amplifier, these devices implement the first amplification stage directly on the sensitive volume. The minimized capacity maximizes the devices amplification and, as will be discussed in section 3.2.4.2 provides an optimized signal to noise ratio. The intrinsic amplification of DEPFET based sensors provides exceptional properties for application in several scientific fields. By means of sidewards depletion DEPFET devices are sensitive over the whole bulk thickness. Because of this property, DEPFETs can be backside illuminated, which results in 100% fill factor. Devices built on a 450 µm silicon substrate grant high quantum efficiency for X-rays over the energy range of 100eV-10keV. Furthermore the backside illumination provides radiation tolerance due to self-shielding. In addition, a DEPFET pixel can be modified to provide additional properties. Examples are sensor-integrated signal compression (Porro et al. 2012), the repetitive readout of charge carriers (S. Wölfel 2007), a built-in shutter (Bähr et al. 2014) and a redirection of charge into storage areas. The functionality of these features has successfully been proven on test devices. Further properties are possible and even a combination of several characteristics may be feasible (Lutz et al. 2007). The DEPFET amplifier structure can be surrounded by drift electrodes. If several concentric electrodes are biased with sufficient voltage, a potential gradient toward the DEPFET is formed. Charge generated inside this structure will be directed into the internal gate of the DEPFET. By means of these drift electrodes, the sensitive area of DEPFETs can be scaled from 24µm^2 up to 10mm^2 and further.

3.2.2. DEPFET matrices

As demonstrated for the Mercury Imaging X-ray Spectrometer (MIXS), BELLE II and X-ray Free Electron Laser (X-FEL) DEPFETs can be used as unit cell of pixelated sensors. These sensors permit individual addressing and readout of pixels or rows of a matrix. With an adequate interconnection scheme and front-end electronics, as e.g.

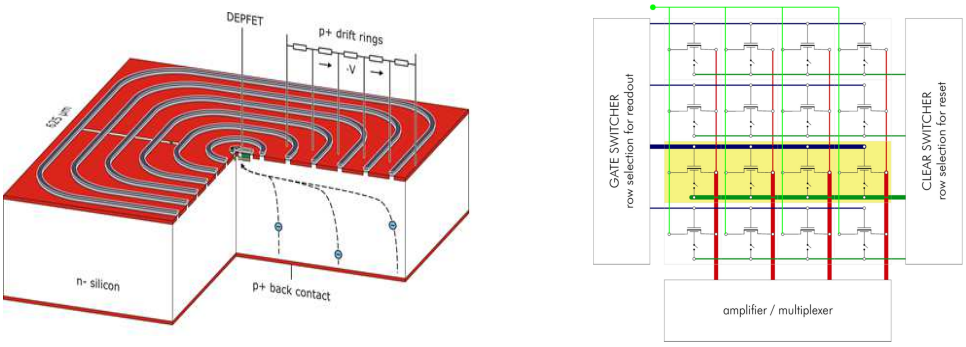

(a) (b)

Figure 3.7.: By embedding a DEPFET into a SDD structure the active area of single pixels can be scaled to match experimental demands (a). The connection scheme of DEPFET matrices defines the readout scheme. A common example is the scheme shown in (b). Here the gates, clear gates and clear contacts are connected row wise while the sources of one column are connected and the drain is common for all pixel. In this connection scheme all pixel of one row are read out in parallel. By successively addressing the single rows the signal of the complete matrix is processed.

realized for the DSSC, it is even possible to process the signal of the entire matrix simultaneously.
An example of a common connection scheme for space borne applications is shown in figure 3.7b. Here the gates, clear gates and clear contacts are connected row-wise. With a global drain contact and a column wise connection of the source nodes, always one row of DEPFETs is addressed and all pixels of that row are read out in parallel. By successively addressing all rows of the matrix, the complete sensor is read out in the so called rolling shutter mode.
Since the DEPFET is an integrating device, collecting incident charge in the off as well as the on state the rolling shutter is beneficial for applications that have limited electrical and thermal power resources as e.g. satellite missions. Here the rolling shutter readout provides a favourable compromise in terms of readout speed and power consumption.

3.2.3. Charge Gain

The primary structure of the DEPFET is a Metal Oxide Semiconductor Field Effect Transistor (MOSFET). The main difference to a conventional MOSFET is the intentional collection of charge generated in the bulk below the conductive channel. These charge carriers modulate the transistor current similar to a change of the voltage V_G applied to the gate. The proportionality factor between collected charge and the corresponding voltage change is given by the capacitance C_G of the external gate. A parasitic coupling of the internal-gate to e.g. source and drain is taken into account by a proportionality factor f_m. Based on the equations for an ideal transistor, the current voltage

characteristic for a DEPFET is (Lutz 1999)

$$I_{drain} = -\frac{W}{L}\mu_p C_{ox}\left(f_m\frac{Q_{sig}}{C_G} + (V_G - V_T) - \frac{V_D}{2}\right)V_D \tag{3.17}$$

for a drain-source voltage V_D smaller than $V_G - V_T$. The transistor current is thereby defined by the geometry of the transistor characterized by its width W, length L and the sheet capacity C_{ox} of its gate. For a source-drain voltage V_D larger than $V_G - V_T$ the current through the transistor saturates. The saturation current is

$$I_{drain,sat} = -\frac{W}{L}\mu_p C_{ox}\left(f\frac{Q_{sig}}{C_G} + (V_G - V_T)\right). \tag{3.18}$$

From these relations the small signal parameters $g_m = \frac{\delta I_{drain}}{\delta V_G}$ and $g_q = \frac{\delta I_{drain}}{\delta Q_{sig}}$ can be derived. In the saturation region the small signal parameters are

$$g_m = -\frac{W}{L}C_{ox}\left(f_m\frac{Q_{sig}}{C_G} + (V_G - V_T)\right), \tag{3.19}$$

and

$$g_q = -\frac{W}{L}f_m\frac{C_{ox}}{C_G}\left(f_m\frac{Q_{sig}}{C_G} + (V_G - V_T)\right). \tag{3.20}$$

The above equations are based on the assumption of an ideal transistor. For this reason they are only valid for large devices. For real devices several parasitic effects as e.g. short channel effects have to be taken into account. Although further effects need to be taken into account, the above equations can be used for first order approximations regarding changes of the charge gain and transconduction with reduced device size.

3.2.4. Noise of a DEPFET Sensor

The signal generated by the conversion processes described in section 3.1.1 will be subject to statistical fluctuations. The dominating contributions are the so called Fano-noise, electronic noise and charge loss processes. The following gives a brief introduction to the different noise sources with a focus on the DEPFET amplifier structure.

3.2.4.1. Fano-Noise

As described in section 3.1.1.3 energetic electrons moving inside a solid will undergo elastic and inelastic interactions and dissipate their energy by generating lattice vibrations and additional electron hole pairs. The underlying statistic was first described by Ugo Fano (Fano 1947) assuming a correlation between the individual scattering events. The number variation of the generated charge carriers is

$$\sigma_{Fano} = \sqrt{\frac{E_{ph}}{w}f}. \tag{3.21}$$

As shown in section 3.1.1.3, the factor E_{ph}/w is just the mean number of generated electron hole pairs. The Fano factor f results from the correlation of the single processes. Empirical values for the Fano factor of silicon are in the range $f = 0.11..0.12$. For the calculations shown in this work we refer to the value of $f = 0.118$ and $w = 3.66$ given in Lowe and Sareen 2007 for silicon close to room temperature.

3.2.4.2. Electronic Noise

Several processes inside electronic circuits cause random fluctuations of the observed signal. These fluctuations are often characterized by their spectral distribution instead of the underlying physical process. In this manner electronic noise is usually attributed by one of the following terms (Tietze and Schenk 2002).

a) White Noise: The most common example for white noise is the noise of a resistor due to the brownian movement of charge carriers. This random movement induces voltage fluctuations, which are observable as noise. Due to the constant spectral density up to several GHz this effect is called white noise.
b) 1/f Noise or Flicker Noise: Every effect causing a noise density propotional to $1/f^n$, with $n \approx 0.5..1.5$ is referred to as flicker or $1/f$ noise. There are several effects causing a $1/f$ like spectral distribution. Impurities in a semiconductor for example can cause the trapping and de-trapping of charge carriers. Several superposed traps, each with a different time constant can cause a spectral density proportional to $1/f$.
c) Parallel or Shot Noise: Shot noise is caused by the discrete nature of electrons and the resulting number fluctuation of electrons moving through a conductor cross section in a defined amount of time. The standard example for shot noise is the leakage current of a reverse biased diode. While the mean number of electrons crossing the potential barrier caused by the pn-junction is constant, the absolute number fluctuates according to poisson statistics (Knoll 1999).

The electronic noise of a detector system is usually expressed in terms of the Equivalent Noise Charge (ENC). The ENC is the root mean square value of the detector noise, expressed by the number of electrons at the input node, that would cause a signal of the same height(Gatti et al. 1990). Using a given shaping circuit, the noise $\sigma_{ENC_{sh}}$ can be described by

$$\sigma_{ENC^2_{sh}} = \frac{a_1}{\tau} C^2_{det} A_1 + a_2 C^2_{det} A_2 + a_3 \tau A_3. \tag{3.22}$$

The factors $a1$, $a2$ and $a3$ characterize the noise density of white, $1/f$ and shot noise. In the same way, A_1, A_2, and A_3 characterize the filtering function for the single noise contributions. The value C_{det} is the detector capacitance and τ corresponds to the processing time of the signal-filter. It is obvious, that the detector noise reduces with detector capacity. Since white noise scales with $\frac{1}{\tau}$ and the shot noise contribution is proportional to τ, there has to be an optimum processing time τ as shown in figure 3.8. This minimal ENC value for a given detector system is only limited by the $1/f$ noise contribution of the detector system.
For a MOS-transistor the following considerations for the different noise sources can be made.

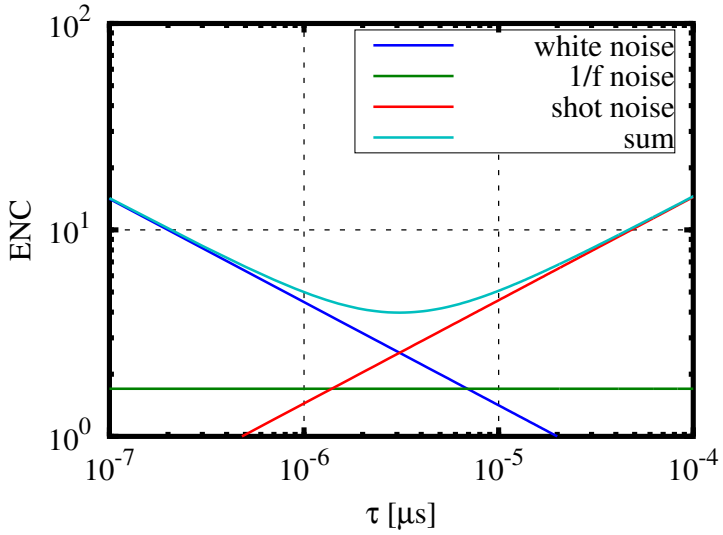

Figure 3.8.: The ENC is composed of three contributions. These are the white noise, 1/f noise and shot noise. 1/f noise is independent from the applied shaping time, while white noise decreases and shot noise increases with larger shaping times. Thus the ENC shows a minimum value, which is determined by its three components.

3.2.4.2.1. a) White Noise Similar to resistive elements, transistor devices generate noise due to the thermal motion of charge carriers in the conductive channel. Assuming the channel to be constructed by several resistors in series and integrating over the hole channel length, it is possible to derive the voltage noise density a_1 for a MOS-transistor to be

$$a_1 = \sqrt{\frac{4kT}{g_m}} \tag{3.23}$$

Here k is the Boltzmann-constant, T the absolute temperature and g_m the transconductance of the transistor (Tietze and Schenk 2002). The equation shows that g_m directly influences the white noise of a MOS-transistor. This has to be taken into account if the geometry of the a DEPFET is changed since a change of geometry also affects the transconductance.

3.2.4.2.2. b) 1/f or Flicker Noise Two different models are most frequently used to describe the $1/f$ noise of MOS-transistors. In the conduction fluctuation model it is supposed, that the conductivity of the channel is modulated due to carrier scattering on lattice vibrations.
The number fluctuation model, in contrast, assumes that charge carriers in the channel are trapped in interface states and released after a certain time. A single trap would cause a $1/f^2$ behavior. The interference of several traps with different time constant results in the $1/f$ like behaviour.
It is likely that both effects are present in any given device. However, typically one of

these effects is dominant. The exact composition is highly depending on the transistor geometry, technology and furthermore, its operational parameters. For a more thorough examination of Flicker Noise refer to Tsividis 1999 and references therein.

3.2.4.2.3. c) Leakage Current Noise For a sidewards depleted device, the major contribution to leakage current is caused by impurities and lattice defects either inside the sensitive volume or at the surface of the sensor. As discussed in section 3.1.2.2 these defects serve as generation and recombination centers for charge carriers. The generation rate is thereby determined by the Shockley-Read-Hall relation given by equation (3.9). A good approximation is that the corresponding leakage current I_{lc} halves for every seven degree reduction of the device temperature. To minimize the corresponding noise contribution solid state sensors are often cooled and usually built of a high purity mono-crystalline base material. The spectral noise density $a3$ (see section 3.22) of a current flow I is given by (Schottky 1918)

$$a3 = 2I_{lc}/e, \tag{3.24}$$

with e as the elementary charge.
However, depending on the readout scheme of the sensor, the effect of leakage current noise may be twofold. If the arrival of charge carriers at the read node triggers the readout, a mode which is commonly referred to as time-continuous readout, the noise contribution to the read noise $\sigma_{ENC_{sh}}$ can be estimated using the filter coefficients, shaping time and the leakage current (see section 3.2.4.2).
If the sensor is operated in an integrating mode, with readout on demand (also referred to as time-variant readout), where charge carriers are collected and preserved until the readout takes place, the collection of leakage current electrons during this illumination time t_i will cause an additional contribution to the noise. While the mean number $N_{lc} = (I_{lc} \cdot t_i)/e$ is supposed to be constant in time, the absolute number of collected carriers will fluctuate according to Poisson statistics. Taking this effect into account, the noise σ_{ENC_R} of a DEPFET sensor read out on demand can be calculated to be

$$\sigma^2_{ENC_R} = \sigma^2_{ENC_{sh}} + (I_{lc} \cdot t_i)/e \tag{3.25}$$

In an experimental environment, DEPFETs are usually subject to particle irradiation. While these interact with the semiconductor lattice they can cause additional generation centers, which increases the leakage current and degrade especially the energy resolution of those devices. Practically the only way to counter these negative effects is cooling the sensor to suppress the increase in leakage current.
In addition to volume and surface leakage current, an incorrect biasing of the device may induce effects which have a similar appearance in the energy spectrum as leakage current. An example is the biasing of the clear contact, that is embedded in a deep-p well that forms a potential barrier towards the bulk and the adjacent internal gate. Depending on its bias conditions, that barrier can be overcome.
A too negative bias voltage of the clear n+-contact pushes electrons from the clear into the bulk or internal gate. The effects can be seen directly as an increase of the leakage

current and the ENC.
For too positive bias conditions charge can be lost into the clear contact. If the probability for charge losses is small, the loss of electrons will follow Poisson statistics. This loss of electrons is only present, if signal electrons were generated. The loss appears as tail on the low energy side of the signal peak within the energy spectrum. Thus, although the effect increases the FWHM of the sensor it can not be observed in the ENC.
In most cases, a proper biasing should avoid these and similar effects. Nevertheless, especially for new layouts both cases have to be evaluated to optimize the operating conditions for the detector.

3.2.4.3. Reset Noise

Reset noise is introduced by an incomplete removal of charge carriers from the internal gate. While the average number of not removed charge carriers may be constant, the process is subject to statistical fluctuations that introduce an additional noise contributions. For an integrating readout this causes an additional noise contribution proportional to the square root of the mean number of electrons not removed from the device. In practice, this contribution is zero for correct biasing of DEPFET devices. Nevertheless an insufficient biasing of the clear voltage or a too short clear time can cause an incomplete removal of charge carriers.

3.2.4.4. Energy Resolution

The energy resolution of a detector for a monochromatic line at a certain energy is defined as Full Width at Half Maximum of the corresponding signal peak. Provided that the shape of the signal peak is not distorted by charge losses (e.g. at the entrance window), the energy resolution is determined by the Fano-noise and the ENC of the sensor. The Fano-noise is also the absolute limit for the energy resolution of a silicon sensor.
Assuming that Fano-noise and ENC are uncorrelated the width of the signal peak is the root-mean-square of the single contributions. Taking into account the conversion factor $\sqrt{8\ln 2} \approx 2.355$ from the standard deviation of a gaussian distribution to its FWHM, the energy resolution in eV is

$$FWHM = 2.355 \cdot w\sqrt{\sigma_{ENC}^2 + \sigma_{Fano}^2}. \tag{3.26}$$

With respect to the later shown measurements the Energy resolution of an ideal, silicon based sensor and an incident photon energy of 5.9 keVcan be calculated to be 119 eV. The energy resolution of a sensor is a crucial measure for its performance. However, especially the conversion process of photons into a charge cloud gives rise to a complete sensor response function that will be discussed in more detail in section 3.3 and section 3.4.

3.2.5. Readout Methods

The readout methods discussed in the following have a strong focus on the DEPFET. However, the basics regarding read node and signal shaping can also be applied to other sensor-amplifier systems.
The readout of DEPFET devices can be distinguished by read node, signal and shaping method. For the first one can chose between the drain and the source of the DEPFET transistor. Secondly it is possible to measure the change in conductivity either through a current or a voltage change. Finally a DEPFET can be read out time continuous, such that the incident photon triggers the readout or the charge is collected and preserved in the DEPFET's internal gate until a time variant readout is triggered externally. While read node, signal and method can be combined in any arbitrary fashion, the following discussion is restricted to the readout schemes relevant for this thesis. In terms of read node and read signal, this are a drain current based readout and a readout in source follower configuration. Furthermore two shaping schemes, a time-continuous semi gaussian shaping and a time-variant trapezoidal shaping will be discussed.

3.2.5.1. Drain Current Readout

For the drain current readout, the voltages applied to gate, source and drain are fixed and define the point of operation of the transistor. Thus the change in channel conductivity causes a proportional current modulation ΔI_{drain}, which is determined by the charge gain g_q.

$$\Delta I_{drain} = g_q \cdot Q_{sig} \tag{3.27}$$

Provided that the rise time of the readout electronics is sufficiently fast, the signal rise time is given by the charge collection time of the DEPFET. The operation of DEPFET matrices demands a practicable number of bias contacts. So the voltages applied to all pixels of a matrix is identical. Variations between the individual pixels of a matrix result in deviations of the bias currents for the pixels. A typical bias current value is 100µA. The variations between devices is in the range of a few percent (Bergbauer 2015), resulting in deviations of some µA. However, since these deviations are coupled to variations of implantation-concentration and/or variations of the MOS-structure sizes they are constant in time. Thus a sufficient calibration is capable to avoid any degradation of the spectroscopic performance.
The number of signal $e^-$for e.g. a 6keVphoton is in the order of 1640e^-. Assuming a charge gain of 300pA per electron this results in a current signal of 492nA. As can be seen, the signal is in the same range as the fluctuations related to the production process of few µA. This deviation has to be compensated by the connected readout electronics.

3.2.5.2. Source Follower Readout

In source follower operation, a current source connected to the DEPFET source drives a constant current flow through the transistor. Any change in DEPFET channel conductivity caused by collected charge carriers is compensated by the current source by

adjusting the source potential. The corresponding signal gain G is determined by the ratio of charge gain g_q and transconductance g_m.

$$G = \frac{g_q}{g_m} \tag{3.28}$$

Again considering a charge gain of $300\frac{\mathrm{pA}}{e^-}$ and assuming a g_m value of 50 µS, the gain is $G = 6\frac{\mu\mathrm{V}}{e^-}$. Within limitations, fluctuations in operational parameters, as e.g. threshold variations between different pixels, are compensated by the current source. Due to this feature, a source follower readout is comparably robust regarding fabrication related shifts in operational parameters, that cause variations between single DEPFET Pixels. However, in this readout scheme the DEPFET has to supply the signal voltage step to the summed capacitances of the readout line and the input node (current source and preamplifier input). In other words the signal rise time is defined by the capacitance at the preamplifier input node C_{in} and the DEPFET transconductance g_m.

$$t_{rise} = \frac{C_{in}}{g_m} \tag{3.29}$$

In addition, the settling after applying a clear or switching the DEPFET on is also determined by this time constant.

3.2.5.3. Time Continous Readout

When applying time continuous readout the signal processing is triggered by the arrival of charge carriers. A standard example for this is a semi-Gaussian shaper connected to a peak sensing Analog to Digital Converter (ADC). A semi-Gaussian shaper is composed of one integration and at least one but up to n differentiation stages. Its response to a signal step on its input is a pulse which is ideally proportional to

$$v_{sg} = A(\frac{t}{\tau_{sg}})^n \exp\frac{-t}{\tau_{sg}} \tag{3.30}$$

here A is a gain factor, t the time and τ_{sg} the peaking time of the shaper. The pulse response approaches a gaussian form for large n. This kind of signal shaping provides low and high frequency cutoffs. A system with time continuous readout is relatively insensitive to incomplete charge removal or low frequency fluctuations. In addition the signal response can be tailored for high count rates or low noise readout. However, this readout is only sensitive to arriving charge when the corresponding channel/pixel is active. A matrix, consisting of several pixels, would require a readout and digitization circuit for every single pixel. While this is in principle possible, especially for space borne applications the resulting high power dissipation entails a complicated electrical and thermal design.

3.2.5.4. Readout on Demand

A connection scheme of a DEPFET based sensor matrix is shown in figure 3.7b. In this scheme it is possible to address individual DEPFET pixels by applying the $gate_{on}$

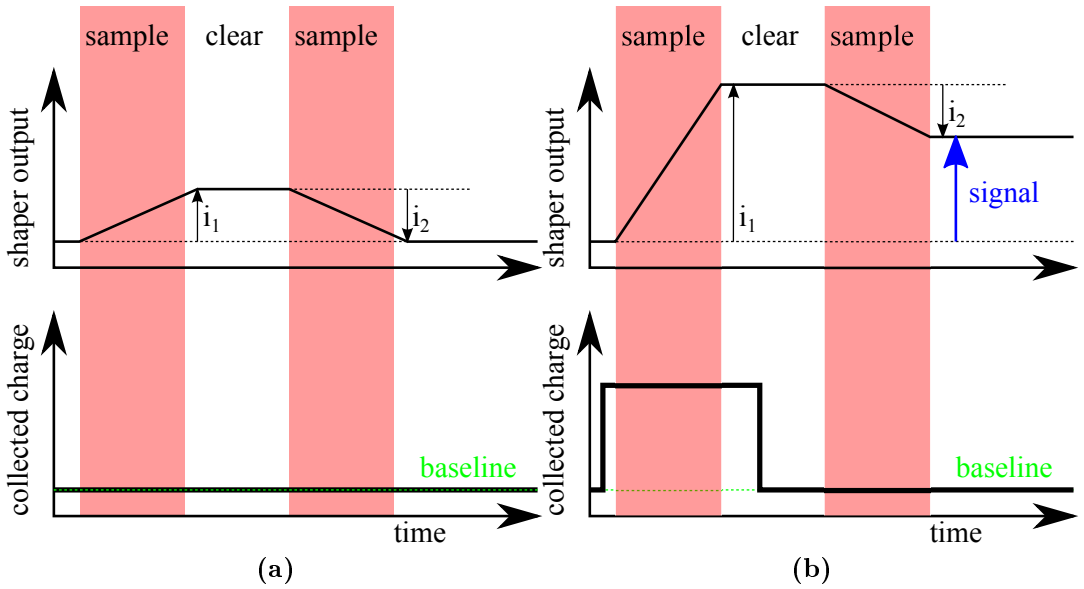

Figure 3.9.: (a) Basic trapezoidal weighing without charge deposition in the internal gate. The readout consists of two consecutive sampling/de-sampling times with an intermediate flat top.[3](b) Charge, which is collected before the processing starts, will cause a higher output level after the first sampling. Since the charge carriers are removed by the clear, signal and baseline sampling will provide different levels. The difference of the two samplings is proportional to the amount of charge collected.

voltage and reading the voltage of the source node. This feature can be used to address for example a single row of DEPFET pixels which is then read out in parallel, while the rest of the matrix collects arriving charge carriers. Reading all rows successively until the whole matrix is processed significantly reduces the power consumption.
In this so called rolling shutter readout the signal is usually processed using an optimized readout ASIC as for example the ASTEROID (Active current Switching Technique ReadOut In x-ray spectroscopy with Depfets (ASTEROIDs)). This ASIC processes the signal of 64 channels in parallel. Each channel provides a current source for source follower readout and applies a trapezoidal weighting of the charge collected in the addressed pixel (Porro et al. 2010). For the trapezoidal filtering scheme the signal level (in case of the ASTEROID, the voltage of the source node) is first integrated over a defined time interval $t_{sample1}$. After that, sufficient positive voltages are applied to clear and clear gate, which remove any collected charge carriers from the internal gate. This clear process is followed by a settling of the source node. Following that, the baseline level is integrated over the same time interval $t_{sample2}$. Since the DEPFET response is linear and integration time for signal level and baseline are equal, $t_{sample1} = t_{sample2} = t_{sample}$, the resulting output signal is proportional to the number of charge carriers collected in the internal gate.

[3]Actually, the sampling processes are really integrations of the signal over the respective time interval. However, to avoid confusion of this and other integration times the term was avoided.

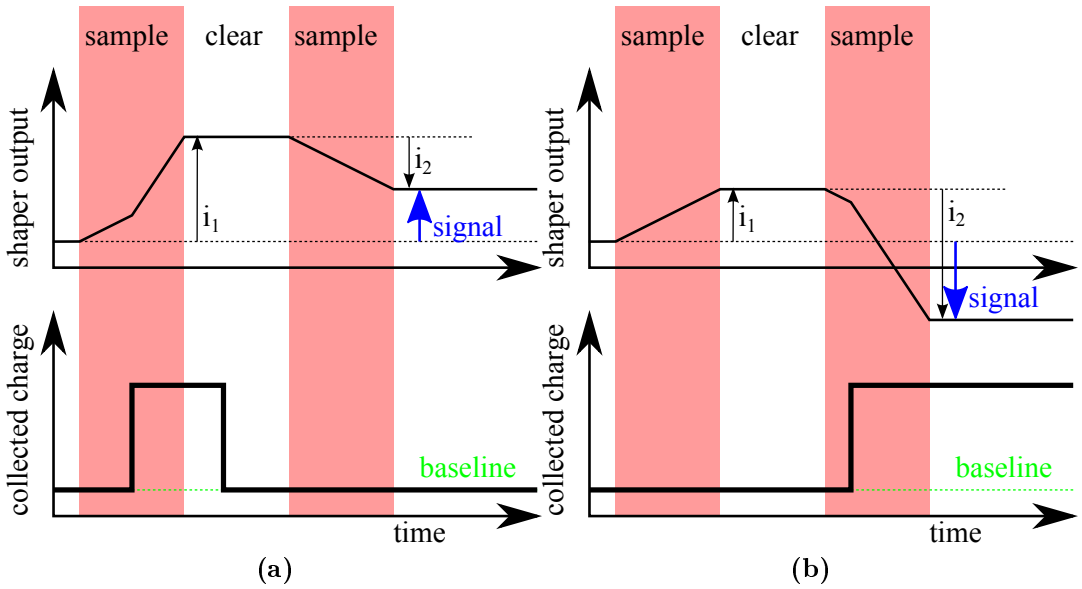

Figure 3.10.: If charge is collected during the first sampling of the trapezoidal weighting, the corresponding output signal will be reduced in amplitude (a). Charge collected during the second sampling will result in a negative signal (b). These effects, so called misfits, have a negative impact on the spectral response.

The trapezoidal weighting is illustrated in figure 3.9. If no charge is present in the internal gate the integration of signal and baseline cancel each other (see figure 3.9a). If charge is collected before the weighting starts, the sampling of signal and baseline will yield unequal results. The difference of these two values is the output signal, which is proportional to the amount of charge originally collected in the internal gate and removed during the clear(see figure 3.9b). While this operation mode is suitable for several applications, it also implies drawbacks that have to be considered.

First, the time resolution of a sensor operated in this way will be limited by the frame-rate. Although, a DEPFET based sensor may overcome this issue by addressing a region of interest, which is read out with a faster timing, while the rest of the matrix can be processed at a lower frame rate.

The second limitation arises from the fact that DEPFETs are always sensitive to arriving charge carriers. Since radiation sources, if not specifically designed otherwise, emit photons randomly with a uniform probability distribution in time it is also possible to collect signal charge during the signal processing. If signal charge is collected in the first readout phase, the corresponding output signal is proportional to the signal charge and the difference between arrival time and start of the first sampling time. These so-called positive misfits are illustrated in figure 3.10a. Similarly, a photon incident in second sampling period will generate a negative signal that is depending on the signal charge and arrival time as shown in figure 3.10b. Equal to events that arrive during the flat top, they generate a negative signal amplitude. Altogether these events are referred to as negative misfits. The effects of misfits on the spectral redistribution will be discussed

in section 3.4.

3.3. Material Response Function

The spectral response describes the probability $\frac{dp}{dE}(E, E_{ph})$ to observe a certain energy E with respect to the energy of incident photons E_{ph}. One contribution to the spectral response that was discussed in section 3.2.4 is the Fano-noise. In addition, x-ray spectra reveal several other features, which are caused by the sensor itself. As will be discussed in the following, these features are determined by the composition of the sensor entrance window. A schematic depiction of the entrance window composition of a typical DEPFET sensor and the resulting spectral response are shown in figure 3.11.

On top of the sensitive volume a shallow p+-implantation (ICC-layer) provides the electrical contact for the backside potential. Furthermore, the silicon bulk is covered by a layer stack of silicon-oxide (layer a) and silicon-nitride (layer b). In addition, the measurements were carried out in a dry air atmosphere (layer c).[4]

Characteristic features of the spectrum like the main-peak, low energetic tail, escape-peak and flat shelf will be discussed and analytical expressions will be derived. The argumentation is oriented on the work of Scholze and Procop (Scholze and Procop 2009) as well as Reed and Ware (Reed and Ware 1972). Features as e.g. fluorescence-peaks (although present) are not discussed.

All spectra presented later on were taken using an ^{55}Fe source, that emits two lines at 5.9keV and 6.4 keV. The discussion is on focussed these photon energies detected by a silicon based sensor. However, the herein made considerations can also be used for other photon energies.

The output signal of the sensor is quantized in energy bins. The mathematical formulation is briefly discussed in the last part of this section.

3.3.1. Radiation Source

The radioactive isotope ^{55}Fe is used as a standard calibration source. It has a half life of 2.7 years and decays by electron capture to ^{55}Mn. The excited atom relaxes as described in section 3.1.1 by the emission of auger-electrons or characteristic photons. Since the radioactive source used is sealed in a stainless steel capsule with an beryllium window, the emitted radiation consists near solely of characteristic K_α and K_β photons. For the purpose of the following discussion, the source is considered to emit photons with an energy of 5.895 keV and 6.492 keV and an emission ratio of $K_\beta/K_\alpha = 0.138$ (Schötzig 2000).

[4] Other combinations of oxide and nitride thickness as well as a optical blocking filter based on aluminum can also be realized. However, herein only the entrance window of the actually tested sensors is discussed in detail.

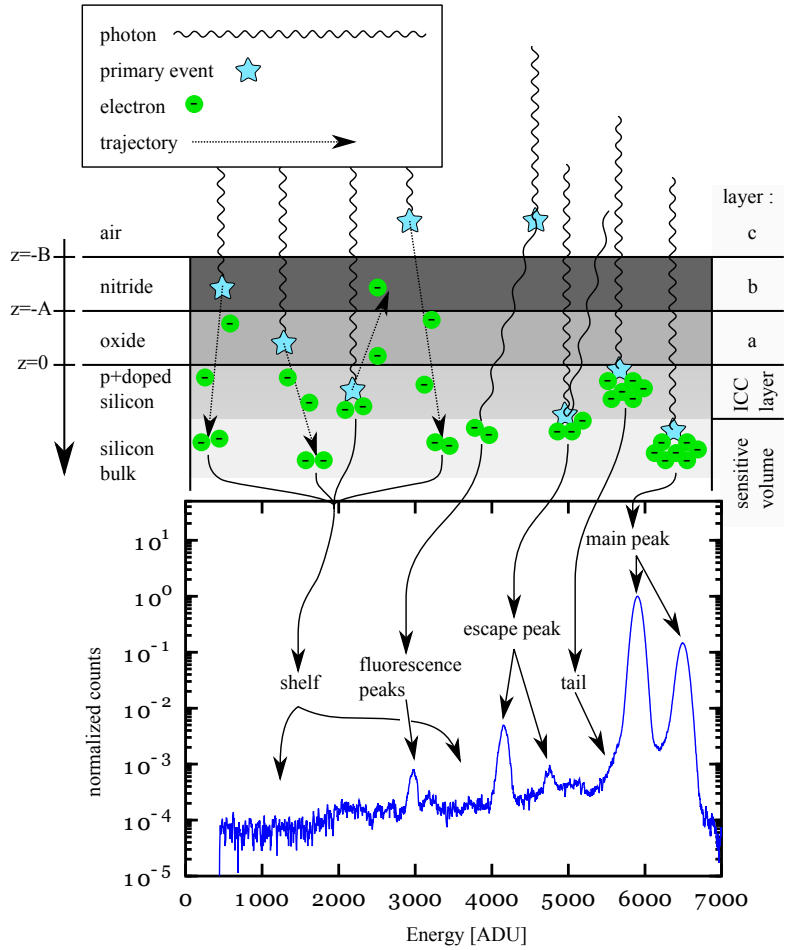

Figure 3.11.: The entrance window of silicon sensors based on the principle of sidewards depletion is usually composed of a shallow p+-implantation, covered by optional passiviation layers of silicon-oxide and silicon-nitride. Depending on the absorbtion position of the incident photon only part of its energy will be deposited inside the sensitive volume. This gives raise to several features in the spectra of X-ray sensors. The most dominant of these are the main peak, a low energetic tail, escape peaks and a flat shelf. (Figure after Granato 2012)

3.3.2. Spectral Contributions

The individual contributions to the spectral response, discussed in the following are the main peak, its low energetic tail, a simple charge loss model, the escape peak and the flat shelf. As the discussion will show, especially the flat shelf is determined by the composition of the sensor entrance window shown in figure 3.11. For the sensors discussed in this thesis, the entrance window is composed by a stack of 30nm silicon-oxide (layer a) and 40nm silicon-nitride (layer b). Furthermore all measurements were done in a dry air atmosphere (layer c).

3.3.2.1. Main Peak

The probability p_{Event} that a photon interacts inside the silicon bulk can be calculated from Lambert-Beers equation (see equation (3.2)). If absorbtion within the top layer (air, nitride and oxide) is neglected, the probability for absorbtion can be calculated from the absorbtion coefficient μ and the thickness of the sensitive volume d. The probability p_{Event} is then

$$p_{Event} = 1 - \exp(-\mu_{Si} \cdot d_{sens}). \tag{3.31}$$

All events that do not contribute to the tail, charge loss function, escape peak or flat shelf are attributed to the main peak at $E_x = E_{ph}$. Here, the variable E_x represents the amount of deposited energy without including statistical fluctuations caused by Fano-or electronic noise. If the probability for the other contributions is known, the probability that an event contributes to the main peak is

$$p_{Main} = p_{Event} - p_{Tail} - p_{Loss} - p_{Escape} - p_{Shelf}. \tag{3.32}$$

3.3.2.2. Low Energetic Tail

The interface between silicon and silicon-dioxide $z = 0$ inherently shows a high concentration of imperfections as crystal defects and unsaturated bonds. These defects of the crystal serve as generation and recombination centers for charge carriers. A charge cloud generated in the sensor close to its entrance window is likely to lose a certain amount of carriers by recombination. Usually this is accounted for by a charge collection efficiency function (CCE). Here a CCE of the form

$$CCE(z) = \begin{cases} C_0 + (1 - C_0) \cdot f(z) & 0 \leq z < z_0 \\ 1 & z \geq z_0 \end{cases} \tag{3.33}$$

is used. The parameter C_0 defines the fraction of charge detected if the absorbtion occurs at the interface, $z = 0$. The variable z_0 is the range at which the detected charge reaches unity and the function $f(z)$ describes the behaviour over the distance $0 \leq z < z_0$.
A simple relation well suited to describe the observed spectra is (see Scholze and Procop 2009 for details)

$$f(z) = \left(\frac{z}{z_0}\right)^{\alpha}. \tag{3.34}$$

Here, the exponent α can be adjusted to match the shape of charge losses observed in X-ray spectra. The dependency of energy and absorbtion position can then be expressed by.

$$E_x(z) = E_{ph} \begin{cases} C_0 + (1 - C_0) \left(\frac{z}{z_0}\right)^{\alpha} & 0 < z < z_0 \\ 1 & z > z_0 \end{cases} \tag{3.35}$$

To find an expression for $\frac{\mathrm{d}p_{tail}}{\mathrm{d}E_x}$ it can be divided into the differential probability $\frac{\mathrm{d}p_{tail}}{\mathrm{d}z}$ that an event will be generated at the position z and the differential quantity $\frac{\mathrm{d}z}{\mathrm{d}E_x}$

$$\frac{\mathrm{d}p_{tail}}{\mathrm{d}E_x} = \frac{\mathrm{d}p_{tail}}{\mathrm{d}z} \frac{\mathrm{d}z}{\mathrm{d}E_x} \tag{3.36}$$

The probability for an event at the position z is

$$\frac{\mathrm{d}p}{\mathrm{d}z} = \mu_{Si} \exp\left(-\mu_{Si} \cdot z\right). \tag{3.37}$$

Provided z is small compared to the reciprocal of the absorbtion coefficient, $z << 1/\mu_{Si}$ the exponential term can be replaced by 1. The absorbtion length for a 6 keV photon is in the order of 30 µm. The extension for events contributing to the low energetic tail is given by the doping profile forming the backside contact that has a depth of 200 nm-300 nm and the size of the primary charge cloud that is also in the order of 200 nm. As these are about three orders of magnitude smaller than the absorbtion length, the assumption $z << 1/\mu_{Si}$ is well justified. Solving the equation $E_x(z) = E_{ph} \cdot CCE(z)$ for z and deriving the result for E_x yields the equation for $\frac{\mathrm{d}z}{\mathrm{d}E}$. Multiplying this by μ_{Si} one can find that in the energy range from $C_0 \cdot E_{ph} < E_x < E_{ph}$

$$\frac{\mathrm{d}p_{tail}}{\mathrm{d}E_x} = \mu_{Si} z_0 \frac{\left(\frac{E_x - E_{ph} \cdot C_0}{(E_{ph}(1-C_0))}\right)^{\frac{1}{\alpha}}}{\alpha(E_x - E_{ph}C_0)}. \tag{3.38}$$

The overall probability p_{Tail} that an event contributes to the tail is $p_{Tail} = \mu_{Si} z_0$. Conveniently, a large simplification of equation (3.38) can be found a value of $\alpha = 1/2$. In this case the relation is

$$\frac{\mathrm{d}p_{tail}}{\mathrm{d}E_x} = 2\mu_{Si} z_0 \frac{E_x - E_{ph} \cdot C_0}{E_{ph}^2 (1 - C_0)^2} \tag{3.39}$$

and linear over the respective energy range.

3.3.2.3. Charge Losses

Apart from charge losses close to the sensor surface it is possible that the actual sensor structure causes the loss of a certain amount of charge carriers. E.g. a charge cloud originating close to the sensor border is likely to lose charge carriers to the insensitive region surrounding the sensor.
In the scope of this thesis, a slightly modified version of the charge loss function derived beforehand will be used. In equation (3.38) the product $\mu \cdot z_0$ is equal to the probability that an event contributes to the tail. This value is replaced by the variable p_{Loss} denoting the probability that an event shows charge losses not caused by the entrance window. In equation (3.38) the spectral appearance of these charge losses is described by the exponent α and the value C_0. Herein the value of α is chosen to be 1/2. Furthermore, the minimal fraction of charge collected in the presence of charge losses is represented by C_C. The differential distribution of charge losses over the spectrum $\frac{\mathrm{d}p_{Loss}}{\mathrm{d}E_x}$ is then expressed by

$$\frac{\mathrm{d}p_{Loss}}{\mathrm{d}E_x} = 2p_{Loss} \frac{E_x - E_{ph} \cdot C_C}{E_{ph}^2 (1 - C_C)^2}. \tag{3.40}$$

3.3.2.4. Escape Peak

For silicon, the excitation of a K-shell electron can successively cause the emission of a fluorescence photon. The probability for this transition is 4.87% (Perkins, Chen, and Hubbel 1991). This photon may either be reabsorbed inside the sensitive volume or leave the sensor. The corresponding signal either contains the full energy or is reduced by the fluorescence-energy of 1.74 keV. This results in the formation of a peak at lower energies than the actual signal peak.
Following the argumentation of (Reed and Ware 1972) the probability that an event contributes to the escape peak can be calculated as the product of the probability for absorbtion by the K-shell at the position z and the probability for a fluorescence photon to leave the sensitive volume.
Again, the differential probability $\frac{\mathrm{d}p}{\mathrm{d}z}$ to absorb a photon at the position z can be taken from the derivative of Lambert-Beers equation. Taking only K-shell absorbtion events into account by multiplying with the respective probability p_k the differential probability that an absorbtion event by the K-shell happens is

$$\frac{\mathrm{d}p}{\mathrm{d}z} = p_k \cdot \mu_{Si} \exp\left(-\mu_{Si} \cdot z\right), \tag{3.41}$$

with μ_{Si} being the absorbtion coefficient of incident photons.
The differential probability to emit a photon into a certain direction $\frac{\mathrm{d}p}{\mathrm{d}\Omega}$ is considered to be uniformly

$$\frac{\mathrm{d}p}{\mathrm{d}\Omega} = \frac{1}{4\pi}. \tag{3.42}$$

Here the fraction of solid angle $d\Omega$ is

$$\mathrm{d}\Omega = \sin\phi \mathrm{d}\phi \mathrm{d}\varphi. \tag{3.43}$$

Since the emission is independent from the azimuthal angle φ it can be stated that

$$\frac{\mathrm{d}p}{\mathrm{d}\phi} = \frac{1}{2}\sin\phi. \tag{3.44}$$

The excited atom recombines either by emission of an Auger-electron or by fluorescence. The fraction of events causing the emission of a fluorescence photons is denoted by the fluorescence yield w_k. Depending on the path length d and the absorbtion coefficient μ_K a fluorescence photon may leave the sensitive volume or be is reabsorbed inside the sensitive volume. The fraction F of photons that leave the sensitive volume of the sensor is expressed by

$$F = \exp\left(-\mu_K \cdot d\right). \tag{3.45}$$

Thereby, the distance d is related to the interaction depth z and emission angle ϕ by $d = z/\cos\phi$.
The quantity of interest to determine the escape peaks height, is the fraction of all events, that contribute to its formation. Up to know equations for the probability $\frac{\mathrm{d}p}{df z}$ that an incident photon will be absorbed in the depth z inside the sensitive volume, the

probability w_K that the excited atom emits a fluorescence photon, the probability $\frac{\mathrm{d}p}{df\theta}$ that the photon will move into the direction θ and the probability F that this photon leaves the sensitive volume were derived. Multiplying all these quantities yields the overall probability that an event contributes to the silicon-escape peak. With respect to absorbtion depth z and emission angle θ that probability becomes

$$\frac{\mathrm{d}p}{\mathrm{d}z} \cdot \frac{\mathrm{d}p}{\mathrm{d}\phi} \cdot w_k \cdot F = \frac{\mathrm{d}p_{EscapePeak}}{\mathrm{d}z\mathrm{d}\phi} = p_k \cdot w_k \cdot \mu_{Si} \cdot \exp\left(-\mu_{Si} \cdot z\right) \frac{1}{2} \sin\phi \exp\left(-\mu_k \cdot \frac{z}{\cos\phi}\right). \tag{3.46}$$

Assuming an infinite extension of the sensitive volume the probability $p_{EscapePeak}$ for K-shell photons to escape the sensitive volume is found by integrating over all emission angles and absorbtion depth

$$p_{EscapePeak} = \int_0^{\infty} \int_0^{\pi/2} \mathrm{d}z\mathrm{d}\phi \frac{1}{2} p_k w_k \mu_{Si} \exp\left(-\left(\mu_{Si} + \frac{\mu_K}{\cos\left(\phi\right)}\right) \cdot z\right) \sin\left(\phi\right). \tag{3.47}$$

The integration will finally deliver the result

$$p_{EscapePeak} = p_k \cdot \omega_k (1 - \frac{\mu_k}{\mu_{Si}} ln(1 + \frac{\mu_{Si}}{\mu_k}) \tag{3.48}$$

for the probability that an absorbtion event actually contributes to the escape peak. The formation of the K-escape peak requires the excitation of the K-shell. Thus the minimum energy for this process is equal to the binding energy of the K-shell electrons. As shown in several works (Reed and Ware 1972; Lauf 2011; Granato 2012), this equation is well suited to describe the number of events contributing to the escape peak.

3.3.2.5. Composition of the "Flat Shelf"

The conversion process of a x-ray photon generates with highest probability a photo- and an Auger-electron. Depending on the position of interaction and the emission direction these electrons will deposit either all or only a fraction of their energy inside the sensitive volume of the sensor.
Contrary to photons, electrons transfer their energy in multiple scattering processes. The range of these electrons is e.g. described by equation (3.5) for the maximum range R_{max} of electrons inside a material of density ρ. In the following it is further assumed that the electrons move in a straight line and loose their energy gradually along their path. After covering the distance d an electron has the remaining energy E_r. The relation between maximum range, travelled distance and remaining energy is

$$R_{max} - d = 90 \cdot \rho^{-0.8} \cdot E_r^{1.3}. \tag{3.49}$$

The rest of the argumentation uses again the derivative of Lambert-Beers equation as to describe the differential probability for absorbtion of an event at the position z

$$\frac{dp}{dz} = \mu_{Si} \cdot \exp\left(-\mu_{Si} \cdot z\right). \tag{3.50}$$

After an absorbtion event, the electrons will be emitted into the fraction of solid angle $d\Omega$. The differential cross section is given by equation (3.1). The equation is composed of a constant σ_{shell}, defining the cross section of the atom and an angle dependent part that describes the probability $\frac{dp}{d\Omega}$ to emit a photoelectron into a fraction of solid angle $d\Omega$

$$\frac{dp}{d\Omega} = \frac{1}{4\pi} \cdot \left[1 - \frac{\beta}{4}\left(3\cos^2\theta - 1\right) + \cos\theta\left(\frac{\gamma}{2}\sin^2\theta + \delta\right)\right]. \tag{3.51}$$

Since equation (3.51) is capable to describe uniform as well as dipole and other emission

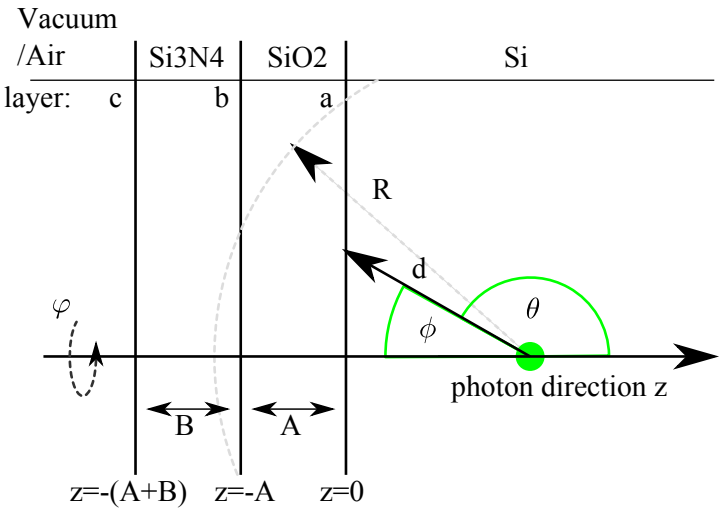

Figure 3.12.: The absorbtion of a photon generates two energetic electrons. Depending on the absorbtion positions these electrons may move into the direction of θ and φ carrying the kinetic energy E_{kin} and thus having a maximum range R. After covering the distance d, the electron has the remaining energy E_r. For the depicted example of an absorbtion event inside the silicon bulk and an electron moving towards the sensor surface the energy deposited inside the silicon equals $E_x = E_{kin} - E_r$. Based on the geometry shown here and equation (3.1) it is possible to derive analytical expressions for the differential probability that an electron deposits a certain amount of energy inside the sensitive volume.

distributions, it is suitable for Auger-electrons (uniform emission) as well as photoelectrons. The solid angle $\mathrm{d}\Omega$ depends on the angles φ, ϕ and θ as indicated in figure 3.12 by

$$\mathrm{d}\Omega = \sin\theta \mathrm{d}\theta \mathrm{d}\varphi = -\sin\phi \mathrm{d}\phi \mathrm{d}\varphi, \tag{3.52}$$

where ϕ and θ are related through

$$\phi = \pi - \theta. \tag{3.53}$$

The incident photon can be absorbed inside the sensitive volume ($z > 0$) as well as in the top layers ($z < 0$). In the following it is necessary to distinguish interaction inside the sensitive volume (z>0) and in the top layers (z<0). In the next two paragraphs both these cases will be discussed.

3.3.2.5.1. Sensitive Volume ($z > 0$) For an interaction inside the sensitive volume, z, d and ϕ are related by

$$\cos\phi = \frac{z}{d}. \tag{3.54}$$

By deriving z for d and ϕ one can find that

$$-\sin\phi \mathrm{d}\phi = \frac{z}{d^2} \cdot \mathrm{d}d. \tag{3.55}$$

Since equation (3.51) is independent of φ, the integration over the range from $0 < \varphi < 2\pi$ just yields a factor of 2π. The probability $\frac{dp}{dd}$ that an electron emitted from the position z travels the distance d is found by exchanging $\sin^2\theta$ with $1 - \cos^2\theta$, then substituting θ for $\pi - \phi$ and replacing all occurrences of $\cos\phi$ by $\frac{z}{d}$. The differential probability to observe a certain distance d is then

$$\frac{\mathrm{d}p}{\mathrm{d}d}(d,z) = \frac{1}{2}\frac{z}{d^2} \cdot \left[1 - \frac{\beta}{4}\left(3\frac{z^2}{d^2} - 1\right) - \left(\frac{z}{d}\frac{\gamma}{2} \cdot (1 - \frac{z^2}{d^2}) + \delta\right)\right]. \tag{3.56}$$

As seen this equation depends only on z, d and the emission parameters β, γ and δ. Now it is possible to derive the probability distribution $\frac{\mathrm{d}p_d}{\mathrm{d}d}$ for an electron to travel the distance d by simply integrating over all interaction depth z. Including that only a fraction y of all absorbtion events actually results in the generation of an energetic electron (i.e. only % of all events yield an Auger-electron) $\frac{\mathrm{d}p_d}{\mathrm{d}d}$ becomes

$$\frac{\mathrm{d}p_d}{\mathrm{d}d}(d) = y \cdot \int_0^d \mathrm{d}z \frac{\mathrm{d}p}{\mathrm{d}z}(z) \cdot \frac{\mathrm{d}p}{\mathrm{d}d}(d,z). \tag{3.57}$$

As the electron-range is typically several orders of magnitude smaller than the absorbtion length the exponential term in $\frac{\mathrm{d}p}{\mathrm{d}z}$ can be taken as 1. With this simplification the exponential term vanishes

$$\frac{\mathrm{d}p_d}{\mathrm{d}d}(d) = \mu_{Si} y \int_0^d \mathrm{d}z \frac{1}{2}\frac{z}{d^2} \cdot \left[1 - \frac{\beta}{4}\left(3\frac{z^2}{d^2} - 1\right) - \frac{z}{d}\left(\frac{\gamma}{2}\left(1 - \frac{z^2}{d^2}\right) + \delta\right)\right]. \tag{3.58}$$

and the result of the integration is

$$\frac{\mathrm{d}p_d}{\mathrm{d}d} = \frac{\mu_{Si} y}{4}\left(1 - \frac{1}{8}\beta - \frac{2}{15}\gamma - \frac{2}{3}\delta\right). \tag{3.59}$$

As the above equation shows, the of the integration is even independent of d and the probability $\frac{\mathrm{d}p_d}{\mathrm{d}d}$.
The energy corresponding to the incident photon is the sum of a photoelectron and either the corresponding auger-electron or fluorescence photon. Although it is possible that both leave the sensitive volume it is assumed that one of the participants deposits all its energy inside the sensitive volume. With this assumption, the observed energy E_x is connected to the remaining energy E_r by $E_x = E_{ph} - E_r$. Using equation (3.49),

substituting E_r and solving the result for d and afterwards deriving $d(E)$ for E_x it is found that

$$\frac{\mathrm{d}d}{\mathrm{d}E_x} = 1.3 \cdot 90 \cdot \rho^{-0.8} \cdot \left(E_{ph} - E_x\right)^{0.3}. \tag{3.60}$$

Now it is possible to substitute $\mathrm{d}d$ and derive an analytical expression for the shelf distribution $\frac{\mathrm{d}p_{shelf_{Si}}}{\mathrm{d}E_x}$. Taking into account that the electron only carries its kinetic energy, the probability to observe a certain energy can be expressed by

$$\frac{\mathrm{d}p_{shelf_{Si}}}{\mathrm{d}E_x} = \begin{cases} \frac{\mu_{Si} y}{4}\left(1 - \frac{1}{8}\beta - \frac{2}{15}\gamma - \frac{2}{3}\delta\right) \cdot 1.3 \cdot 90\dot{\rho}^{-0.8} \cdot \left(E_{ph} - E_x\right)^{0.3} & E_{ph} - E_{kin} \leq E_x \leq E_{ph} \\ 0 & E_{ph} < E_x < E_{ph} - E_{kin} \end{cases} \tag{3.61}$$

This function, with the respective constants for a photoelectron caused by a 5.895keV incident photon is depicted in figure 3.13a. Although this model provides an analytic description of the energy distribution, it also includes several simplifications. First of all it is assumed that the electron moves in a straight line from its origin towards the surface while gradually losing energy. The actual process includes multiple scattering processes, each changing the electrons energy and direction. In addition, the shelf region of x-ray spectra usually shows no or only very few structure (apart from fluorescence and escape peaks) (Scholze and Procop 2009). Thus, the contribution of energetic electrons will be considered in the flat shelf approximation herein denominated by $\frac{\Delta p_{Shelf_{Si}}}{\Delta E}$. This requires the probability $p_{Shelf_{Si}}$ that an electron contributes to the shelf. This quantity is just

$$p_{Shelf_{Si}} = \int_0^{E_{ph}} \frac{\mathrm{d}p_d}{\mathrm{d}E_x}\mathrm{d}E = \int_{d(0)}^{d(E_{ph})} \frac{\mathrm{d}p_d}{\mathrm{d}d}\mathrm{d}d = \int_0^R \frac{\mathrm{d}p_d}{\mathrm{d}d}\mathrm{d}d. \tag{3.62}$$

Next this probability is equally distributed over the energy range from $E_{ph} - E_{kin}$ to E_{ph}. In the approximation of a flat shelf the energy distribution for energetic electrons generated in the silicon crystal can thus be expressed by

$$\frac{\Delta p_{Shelf_{Si}}}{\Delta E_x} = \begin{cases} \frac{\mu_{Si} y}{4}\left(1 - \frac{1}{8}\beta - \frac{2}{15}\gamma - \frac{2}{3}\delta\right)\frac{R}{E_{kin}} & E_{ph} - E_{kin} < E_x < E_{ph} \\ 0 & E_{ph} < E_x < E_{ph} - E_{kin} \end{cases}. \tag{3.63}$$

3.3.2.5.2. Top Layer ($z \leq 0$) For the top layers the set of starting equations is slightly different. The relation of z and d is given over the angle θ by

$$\cos\theta = -\frac{z}{d}. \tag{3.64}$$

Deriving z for d and θ it is possible to find that

$$\sin\theta \mathrm{d}\theta = \frac{z}{d^2} \cdot \mathrm{d}d. \tag{3.65}$$

Nevertheless, the finally obtained result for the probability $\frac{\mathrm{d}p_d}{\mathrm{d}d}$ is equal to equation (3.57).
The next step is the integration over the absorbtion position z. Since the top layers

are in the range of several 10 nm, the travelled distance d may easily exceed the layer thickness.
The discussion starts with the layer a. For $d < A$ the integration over z has to be done from $-d$ to 0. The equation is then

$$\frac{\mathrm{d}p_{d_a}}{\mathrm{d}d} = y \cdot \int_{-d}^{0} \mathrm{d}z \frac{dp}{dz} \cdot \frac{dp}{dd}. \tag{3.66}$$

If d is larger than the layer thickness, the lower boarder is given by the layer thickness and the integration is over the range from $-A$ to 0 leading to

$$\frac{\mathrm{d}p_{d_a}}{\mathrm{d}d} = y \cdot \int_{-A}^{0} \mathrm{d}z \frac{dp}{dz} \cdot \frac{dp}{dd}. \tag{3.67}$$

This results in the following distance distribution for events absorbed in the top layer a

$$\frac{\mathrm{d}p_{d_a}}{\mathrm{d}d} = \begin{cases} -\frac{\mu_{Si} y}{4} \left[1 - \frac{1}{8}\beta + \frac{2}{15}\gamma + \frac{2}{3}\delta\right] & 0 \le d \le A \\ -\frac{\mu_{Si} y}{4} \left[\left(1 + \frac{1}{4}\beta - \frac{3}{8}\beta\frac{A^2}{d^2}\right)\frac{A^2}{d^2} + \left(\frac{1}{3}\gamma + \frac{2}{3}\delta\right)\frac{A^3}{d^3} - \frac{1}{5}\gamma\frac{A^5}{d^5}\right] & A \le d \le R \end{cases}. \tag{3.68}$$

In the flat shelf approximation the next step is to calculate the average probability to observe an electron with the energy E_x. For the top layers, observed and remaining energy are equal $E_x = E_r$. Using this relation $\frac{\Delta p_{shelf_a}}{\Delta E}$ becomes

$$\frac{\Delta p_{shelf_a}}{\Delta E_x} = \frac{1}{E_{kin}} \int_0^{E_{kin}} \frac{\mathrm{d}p_d}{\mathrm{d}E_x} \mathrm{d}E_x = \int_R^0 \frac{\mathrm{d}p_{d_a}}{\mathrm{d}d} \mathrm{d}d. \tag{3.69}$$

An equal distribution over the kinetic energy of the electron results in

$$\frac{\Delta p_{shelf_a}}{\Delta E_x} = \begin{cases} \frac{\mu_{Si} y}{4} \frac{R}{E_{kin}} \left[\left(2 + \frac{1}{4}\gamma + \delta\right)\frac{A}{R} - \left(1 + \frac{\beta}{4}\right)\frac{A^2}{R^2} \right. \\ \qquad \left. - \left(\frac{\gamma}{6} + \frac{\delta}{3}\right)\frac{A^3}{R^3} + \frac{\beta}{8}\frac{A^4}{R^4} + \frac{\gamma}{20}\frac{A^5}{R^5}\right] & 0 < E_x < E_{kin} \\ 0 & 0 > E_x > E_{kin} \end{cases}. \tag{3.70}$$

In the same manner, the contribution of the layers b and c can be derived. For b the integration over z is to perform over $-d$ to $-A$ for $d < B$ and from $-B$ to $-A$ for $d > B$. The resulting partially defined equation is to be integrated by d accordingly. And the overall probability is then distributed equally over the respective energy range.
The same applies for events absorbed in the layer c with the difference that the integration by z must be done from $-d$ to $-(B + A)$. As the electrons require a minimum energy E_B to move through the layers a and b the events can only contribute over the energy range from 0 up to $E_{kin} - E_B$.
In the approximation of a flat shelf the events will only be distributed over the respective energy range. Since the calculation follow otherwise the same scheme as before the equations are omitted. The final results for the layer b is

$$\frac{\Delta p_{shelf_b}}{\Delta E_x} = \begin{cases} \frac{\mu_{Si} y}{4} \frac{R}{E_{kin} - E_A} \left[\left(2 + \frac{\gamma}{4} + \delta\right)\frac{B - A}{R} - \left(1 + \frac{\beta}{4}\right)\frac{B^2 - A^2}{R^2} \right. \\ \qquad \left. - \left(\gamma + 2\delta\right)\frac{B^3 - A^3}{6R^3} + \beta\frac{B^4 - A^4}{8R^4} + \gamma\frac{B^5 - A^5}{20R^5}\right] & 0 \le E_x \le E_{kin} \\ 0 & 0 > E_x > E_{kin} \end{cases}, \tag{3.71}$$

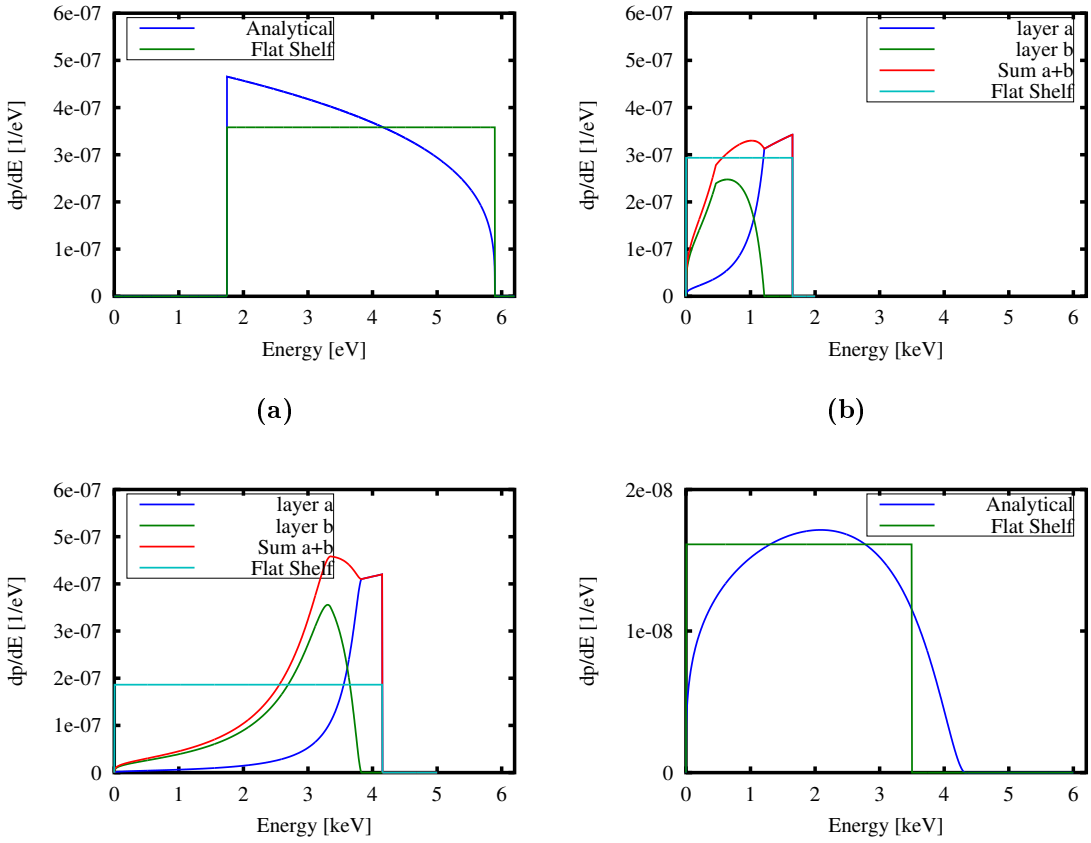

Figure 3.13.: The four graphs show the analytical expressions alongside the respective flat shelf approximations. In a) the spectral distribution for photoelectrons originating in the sensitive volume is shown. b) illustrates the distribution of auger electrons generated in the top layers while c) shows the distribution for the higher energetic photoelectrons. In d) the spectral contribution of photoelectrons originating from layer c is shown.

and the result for the layer c is

$$\frac{\Delta p_{shelf_c}}{\Delta E_x} = \begin{cases} \frac{\mu_{Si} y}{4} \frac{R}{E_{kin}-E_B} \left[1 - \frac{\beta}{8} + \frac{2\gamma}{15} + \frac{2\delta}{3} + \left(-2 - \frac{\gamma}{60} - \frac{\delta}{3}\right) \frac{B}{R} \right. \\ \quad \left. + \left(1 + \frac{\beta}{4}\right) \frac{B^2}{R^2} + \left(-\frac{\gamma}{6} - \frac{\delta}{3}\right) \frac{B^3}{R^3} - \frac{\beta}{8} \frac{B^4}{R^4} + \frac{\gamma}{20} \frac{B^5}{R^5} \right] & 0 \leq E_x \leq E_{kin} - E_B \\ 0 & 0 > E_x > E_{kin} - E_B \end{cases} . \tag{3.72}$$

The analytical equations alongside their flat shelf approximations are plotted in figure 3.13. Using the same argumentation as for the flat shelf approximation of silicon itself it seems acceptable to simplify the distributions shown in figure 3.13b and figure 3.13d by the also shown flat shelf functions.

In case of photoelectrons, which are generated in the silicon-nitride (layer b) or silicon-oxide (layer a), as shown in figure 3.13c, the analytical expression and flat shelf approx-

imation show large deviations. Within the above calculations the electrons trajectory was approximated by a straight line, neglecting any and all statistical processes that take place. The statistical nature of the energy transfer and also the electrons trajectory will smooth the spectral distribution leading to a convergence of the analytical expression towards the flat shelf approximation. Although, the shown discrepancy is large, it will be assumed that these statistical processes smooth the distribution sufficiently such that the flat shelf approximation is sufficient for all layers. Further analysis of the entrance window are left for future work.

3.3.3. Sensor Noise

The sensor response can be expressed as the sum of Dirac functions (Main-Peak and Escape-Peak), charge loss functions (Tail and Charge-Losses), and the "flat shelf", whereas the flat shelf is actually the sum over several flat shelf functions. As described in section 3.2.4 Fano-noise and electronic noise can be described by a single Gaussian distribution

$$p(E, E_x) = \frac{1}{\sqrt{2\pi}\sigma(E_x)} \exp\left(-\frac{1}{2}\frac{(E-E_x)^2}{\sigma^2(E_x)}\right) \tag{3.73}$$

with an energy dependent width $\sigma(E_x)$. Here E_x is the energy actually deposited inside the silicon, E the energy measured and

$$\sigma(E_x) = \sqrt{ENC^2 + \sigma_{Fano}^2} \tag{3.74}$$

the squared mean of Fano-noise and electronic noise. Multiplying the spectral redistribution with the Gaussian and summing over all values of E_x will yield the finally observed energy distribution

$$\frac{\mathrm{d}p}{\mathrm{d}E} = \int_{-\infty}^{\infty} \frac{dp}{dE_x} \cdot \frac{1}{\sqrt{2\pi}\sigma(E_x)} \exp\left(-\frac{1}{2}\frac{(E-E_x)^2}{\sigma^2(E_x)}\right). \tag{3.75}$$

This is in fact identical to a convolution of the two distributions. The mathematical implication of this operation is that the Dirac distributions will be changed to Gaussian function with width and height defined by the energy position E_x of the Dirac distribution and the ENC. If the energy dependence of σ is neglected, the convolution of a shelf function of height 1 ranging from E_{min} to E_{max} with a normalized Gaussian results in

$$\varsigma = \frac{1}{2}\left[\mathrm{erf}\left(\frac{1}{\sqrt{2}}\frac{E-E_{min}}{\sigma(E_{min})}\right) - \mathrm{erf}\left(\frac{1}{\sqrt{2}}\frac{E-E_{max}}{\sigma(E_{max})}\right)\right]. \tag{3.76}$$

In that case, ς denotes the flat shelf approximation when noise is taken into account. The error function $erf(x)$ is defined as the integral over a Gauss-function. As the equation indicates, the plateau will be unchanged in height, but the steps in the spectra will be smoothed by the convolution. Similarly charge loss and tail function will be smoothed by the convolution with the Gaussian.

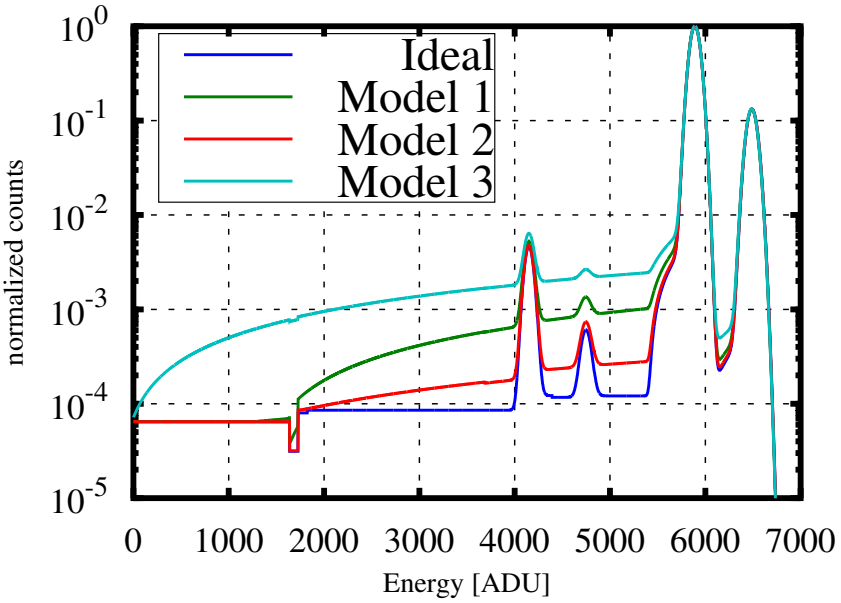

Figure 3.14.: Spectral response models for ^{55}Fe based on the previous considerations. Depicted are the ideal case as well as large, moderate and small charge losses

3.3.4. Response Function

In the previous sections, the single contributions to the spectral response function were discussed. As mentioned before, the single contributions can be seen as probability distributions. In principle combinations of the single contributions are possible. For example it is possible, that an event that is generated close to the entrance window results in a photoelectron, leaving the sensitive volume and the emission of a fluorescence photon. However, as the probability of these events is extremely low, they will be neglected. In that case, the response function is the sum of all the single contributions. The single equations are summarized in appendix A.
The values for absorbtion length, material density and the emission distributions are given in the tables listed in appendix C. For the pair-creation energy the value 3.66 eV was used. Furthermore a Fano-factor of 0.118 was applied (Lowe and Sareen 2007). For the tail values of $C_0 = 0.92$ and $z_0 = 3 \cdot 95$ nm in accordance with Granato 2012 were chosen. In agreement with Scholze and Procop 2009, the value of α was chosen to be 0.5. In addition the ideal case is compared with models including large (5%, Model 3), moderate (1.5%, Model 1) and small (0.25%, Model 2) charge losses. The models are depicted in figure 3.14.

In table 3.1 the charge loss parameters for the single models are summarized. The typical figures of merit to qualify a X-ray sensor are the energy resolution in terms of FWHM of the $Mn{-}K_\alpha$ peak and the ratio of peak height (here the height of the $Mn{-}K_\alpha$ peak) to the averaged background over the range from 900-1100 eV. Furthermore the values for the energy ranges from 2400-2600 eV and 4400-4600 eV help to further qualify

Model	p_L	C_C
ideal	0	0
1	$1.5 \cdot 10^{-2}$	0.28
2	$2.5 \cdot 10^{-3}$	0.3
3	$5 \cdot 10^{-2}$	0

Table 3.1.: The table summarizes the assumed charge loss parameters used for the analytical spectra plotted in figure 3.14.

	Energy Resolution	Peak-to-Background ratio			
Model	FWHM (eV)	at 1 keV	at 2.5 keV	at 3.5 keV	at 4.5 keV
ideal	126.9	15851	11825	11825	8204
1	127.1	15527	3421	1890	1288
2	126.9	15522	8591	6241	4270
3	127.8	1977	856	627	496

Table 3.2.: The table summarizes the spectral performance in terms of FWHM and peak height to background ratio at different energies for the 4 analytical models.

the spectral performance. These values are presented in table 3.2.

The shown loss models assume, that a small fraction of all events is subject to large charge losses. As the summary in table 3.2 shows, the main effect of the charge losses is a drastic decrease of the peak-to-background ratio, while the energy resolution is nearly not affected. If in contrast, lost charge fraction becomes smaller, a more and more dominant shoulder would form on the left side of the signal peak. That would deteriorate the energy resolutions, while having only low impact on the peak-to-background ratio.
The derived spectral response is compared with measurement data in section 4.3.2.2. As that comparison show, the model can be used to quantify e.g. charge losses. Overall the here shown analytical considerations provide a sophisticated prediction of the spectral response of a silicon based sensor. Nevertheless, it is possible to improve this analytical model. With respect to the calibration source ^{55}Fe it would be necessary to include its low probability transitions. Furthermore a more sophisticated charge loss model as well as a revision of the flat-shelf approximations and the model used for the electron transport should provide an even more realistic response function.

3.3.5. Quantization and Redistribution Matrix Function

Typically the spectral response of a sensor will be quantized in energy bins. For a monochromatic source, it is then common practice to express the probability to observe an event at in the energy range from E_j to $E_j + \Delta E$ by $S(E_j, \Delta E, E_{ph}) = \int_{E_j}^{E_j+\Delta E} \frac{\mathrm{d}p}{\mathrm{d}E}(E_{ph})\mathrm{d}E$. Taking this one step further the response of the sensor can be expressed in terms a matrix $R(E_j, E_{ph})$ and a source spectrum by a vector $S_{in}(E_{ph})$. The single elements of $R(E_j, E_{ph})$ can be calculated from the redistribution function by

integrating over the respective energy bins leading to

$$R(E_j, E_{ph}) = \int_{E_j}^{E_{j+1}} \frac{\mathrm{d}p}{\mathrm{d}E}(E, E_{ph})\mathrm{d}E. \tag{3.77}$$

The same can be done for the incident spectrum to provide a bin integrated vector $S_{in}(E_{ph})$. The output spectrum

$$S_{out}(E_j) = S_{in}(E_{ph}) \cdot R(E_j, E_{ph}) \tag{3.78}$$

is then just the product of $S_{in}(E_{ph})$ and $R(E_j, E_{ph})$.

3.4. Spectral Response for Readout on Demand

As discussed in section 3.2.5.4, the readout on demand of DEPFET devices can cause a distortion of the output signal, which depends on the exact arrival time of the incident photon. The main effect of this is, that the spectral redistribution function shows an additional component, that depends on the exact timing of the sensor. The spectral response of a DEPFET based sensor, which is read out on demand, can thus be seen as a combination of the material response MF, Fano-noise FN, a time dependent response function TF and the electronic noise EN of the detector system. The complete redistribution function RF is the convolution of the single contributions

$$RF = MF * FN * TF * EN \tag{3.79}$$

The first two components can not be improved beyond the limits determined by the physical properties of silicon (see section 3.3. The time dependence is defined by the respective readout scheme while the noise is in addition defined by the sensor geometry. The electronic noise is well described by a Gaussian function of width σ_{ENC_R} defined by equation (3.25). To determine the time dependent redistribution TF it is first necessary to find an expression for the measured energy in dependency of the arrival time. That will be done in the following. Next the spectral response TF corresponding to that time dependence is derived and an expression for the peak-to-background ratio with respect to the device timing is developed. In the last part of this section the limitations of that model, which is strictly only valid for makroscopic single pixel devices, will be discussed using measurement data from a DEPFET matrix.

3.4.1. Time Dependent Output Signal

The timing is composed of six time intervals as illustrated in figure 3.15. Together, these time intervals comprise one readout. Each cycle starts with an illumination time t_i, followed by the signal weighting composed of the first sampling time, flat top and second sampling time as discussed in section 3.2.5.4. As shown, the flat top is formed by the clear time t_{clear} and a settling time t_{set}. After the signal weighting an additional time may be required e.g. for the digitization of the output-signals. Thus the time t_{mux}

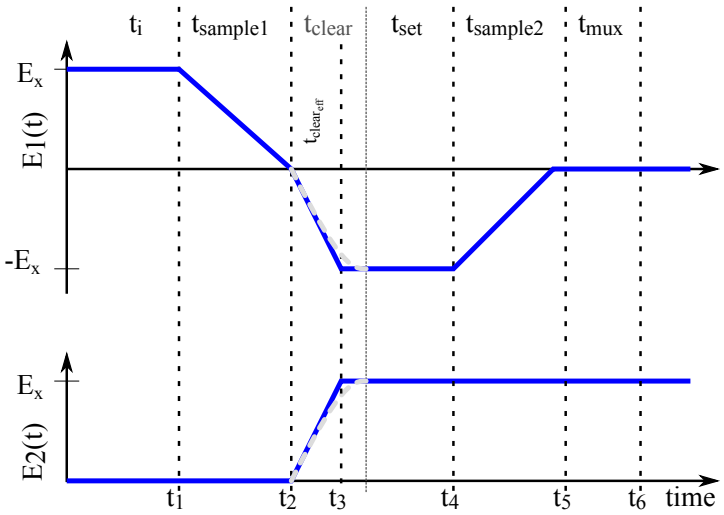

Figure 3.15.: It is possible to take the considerations made in section 3.2.5.4 one step further. Depending on the photon arrival time the signal $E_1(t)$ takes a value between $-E_x$ and E_x. Furthermore, if charge arrives after the clear process, it may even generate a signal $E_2(t)$ in the next readout cycle.

follows the signal weighting.

Depending on the arrival time, incident charge will generate an energy signal of amplitude $E_1(t)$ in this readout cycle and an energy signal of amplitude $E_2(t)$ in the following one. In figure 3.15 three time intervals with a linear dependency of signal and arrival time can be seen. While this is (assuming a short signal rise time) a good approximation for the sampling times, the model is only partially applicable for the clear, as the amount of charge not removed from the device and present in the internal gate during the negative sampling and the next readout cycle is a more complex function of time and also position as indicated in figure 3.15.

However, since a more elaborate model is not available a linear dependency of removed charge fraction and arrival time is used. Furthermore the removal is assumed to take the effective clear time $t_{clear_{eff}}$ which is the mean time required to completely remove a charge cloud from the device. Provided all charge is removed during the clear process, the clear time t_{clear} will always be longer than than its linear approximation $t_{clear_{eff}}$. The difference between $t_{clear_{eff}}$ and t_{clear} can be regarded as a dead time of the device. However, this will not be taken into account. In terms of a mathematical relation, the energy detected in the first cycle is

$$E_1(t) = E_x \begin{cases} 1 & 0 < t < t_1 \\ 1 - \frac{t-t_1}{t_{sample}} & t_1 < t < t_2 \\ -\frac{t-t2}{t_{clear_{eff}}} & t_2 < t < t_3 \\ -1 & t3 < t < t4 \\ -1 + \frac{t-t3}{t_{sample}} & t4 < t < t5 \\ 0 & t5 < t < t6 \end{cases} . \tag{3.80}$$

Here E_x is the energy deposited by the incident photon and t the arrival time during the first readout cycle. Charge generated during or after the clear process will cause a positive signal in the next readout cycle. The energy E_2 detected in the second readout cycle is

$$E_2(t) = E_x \begin{cases} 0 & 0 < t < t_2 \\ \frac{t-t2}{t_{clear_{eff}}} & t_2 < t < t_3 \\ 1 & t3 < t < t6 \end{cases} . \tag{3.81}$$

3.4.2. Timing Dependent Spectral Redistribution

Based on equation (3.80) and equation (3.81) it is possible to construct the timing dependent spectral redistribution TF, that describes the relation between the deposited energy E_x and the shaped energy signal E_y. If the photon rate η_{cr} and thus the probability to observe a photon at a given time is constant the probability for an event during a given time interval is just η_{cr} times the respective time interval Δt. Even with a readout time of a few ms this assumption should be sufficiently accurate for typical astrophysical sources. If however the observed radiation source shows a time dependency in the order of the readout time this would require further considerations.
For time intervals where the signal is independent from t, the corresponding spectral contribution can be represented by a dirac-function at the respective energy multiplied by the probability $p = \eta_{cr} \cdot \Delta t$. If the signal has a linear dependency on time the spectral contribution is equally distributed over all energies. The corresponding spectral density is then given by $\frac{\mathrm{d}p}{\mathrm{d}E} \frac{\eta_{cr} \cdot \Delta t}{E_{ph}}$. If all contributions from the first and second readout cycle are taken into account the timing dependent spectral redistribution can be represented by

$$TF = \eta_{cr} \begin{cases} t_i + t_{set} + t_{sample} + t_{mux} & E_y = E_x \\ (t_{sample} + t_{clear}) / E_x & 0 < E_y < E_x \\ (t_{sample} + t_{clear}) / E_x & -E_x < E_y < 0 \\ t_{set} + t_{sample} & E_y = -E_x \end{cases} . \tag{3.82}$$

Since the single time intervals are additive it is furthermore possible to substitute the sums. For events correctly evaluated the time $t_c = (t_i + t_{set} + t_{sample} + t_{mux})$ can be identified. Since the shelf between E_x and $-E_x$ is constant in density the time $t_s = (t_{sample} + t_{clear})$ is introduced. Lastly the time a negative signal is evaluated can be expressed by $(t_{-c} = t_{set} + t_{sample})$. With this simplifications the time dependent spectral response becomes

$$TF = \eta_{cr} \begin{cases} tc & E_y = E_x \\ \frac{t_s}{E_x} & -E_x < E_y < E_x \\ t_{-c} & E_y = -E_x \end{cases} . \tag{3.83}$$

As stated beforehand the spectral response of a DEPFET sensor is just the convolution of the single contributions. Using the associative law, which applies for convolutions it

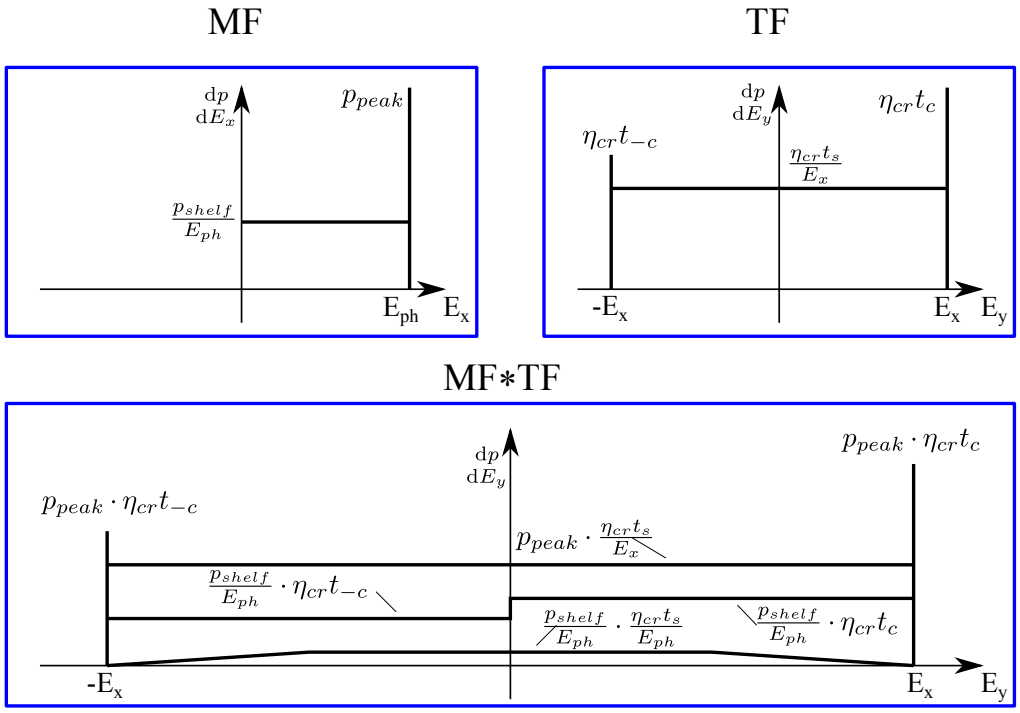

Figure 3.16.: The primary contributions from a convolution of material response (MF) and timing response (TF) will be the single contributions of one function with the dirac-like distribution of the other. In the here shown simplified example this can be seen by considering the spectral density of the single contributions. In most cases the height of the dirac-distributions will be in the order of one half to one. Respectively the shelfs are typically three to five orders of magnitude smaller than the dirac-distributions. The convolution of two shelf function of spectral density $\frac{p_{shelf}}{E_{ph}}$ and $\frac{\eta_{cr}t_s}{E_{ph}}$ results in a distribution that is several orders of magnitude lower than the convolution of one of these functions with the corresponding dirac-distribution.

is possible to reframe equation (3.79) to

$$RF = MF * TF * FN * ENC. \tag{3.84}$$

Usually Fano and electronic noise are represented by a Gaussian distribution. The convolution of two Gaussian functions and thus the overall noise of the detector is again a Gaussian with width $\sigma = \sqrt{\sigma_{fano}^2 + \sigma_{ENC}^2}$. The material response can be expressed as the sum of a dirac-distribution describing the main peak, a tail function, a second dirac-distribution to account for the escape-peak, eventual charge losses and the characteristic shelf as discussed in section 3.3.
Respectively the timing response can be expressed by a dirac-distribution at the Energy $E_y = E_x$ a negative dirac function at the energy $E_y = -E_x$ and a shelf in between as shown in equation (**??**). A simplified depiction of these two function and what the result of their convolution looks like is shown in figure 3.16. As depicted the main contribution of the convolution results from the Dirac-distributions and the shelfs. In fact the convolution of two shelf functions will typically be several orders of magnitude

smaller than any other contribution to the spectrum.
For this reason only the convolutions of the Dirac-functions with the single step-functions are taken into account. With these simplification, the spectral response results in a Dirac pulse plus several step functions and the material characteristics as tail, eventual charge loss and the escape peak. Based on the here made spectral response, next a model for the relation between peak-to-background ratio and the sensor timing will be derived. That model is compared with measurement data in section 4.3.3.2.2 on page 129.

3.4.3. Peak to Background of a DEPFET Sensor Read Out on Demand

It was already pointed out that the typical quantities to characterize the spectral performance of a silicon based X-ray sensor are the energy resolution in terms of FWHM and the peak-to-background ratio. While the timing dependent contribution of the DEPFET readout has no effect on the width of the signal peak, it introduces a component to the spectral response that is related to the sensor timing. As shown in the previous section the main effect is an increase of the flat shelf of the spectral redistribution discussed in section 3.3 and thus a reduction of the peak-to-background ratio. The dependence of the peak-to-background ratio on the exact sensor timing is discusses in the following.

3.4.3.0.1. Peak Height The signal peak of a DEPFET read out on demand is the convolution of the dirac-distribution from the material response, time response and a Gaussian representing Fano and electronic noise. The peak height p_{peak}, is then the product of count rate and collection time $\eta_{cr} \cdot t_c$ divided by the area of the normalized Gaussian. The width of the signal peak is defined by Fano-noise σ_{Fano} and electronic noise for a readout on demand ENC_R. Since a readout on demand is considered, the leakage current noise $\sqrt{I_{lc} \cdot t_c}$ can not be neglected. Furthermore an energy spectrum is considered and the noise in electrons must be multiplied with the pair creation energy w. The standard deviation of the signal peak in terms of energy is then $w \cdot \sigma = w \cdot \sqrt{\sigma_{Fano}^2 + ENC_{shaper}^2 + I_{lc} \cdot t_c}$, and the peak height

$$P = \frac{\eta_{cr} t_c}{w \cdot \sqrt{2\pi(\sigma_{Fano}^2 + ENC^2 + I_{lc} \cdot t_c)}}. \tag{3.85}$$

3.4.3.0.2. Entrance Window As shown in section 3.3 the spectral density of background events B_{EW} has a rather small energy dependence and can be assumed to be constant over a defined energy range $\Delta E = E_1..E_2$.
Since the peak height is highly dependent on electronic noise and leakage current, the peak-to-background ratio of a sensor too is depending on these characteristics. That dependency is for example problematic to compare different sensors e.g. with different entrance window technologies. For every detector it is possible to define an ideal peak-to-background ratio $\frac{P}{B} max$ that would be measured if the energy resolution is

only Fano-limited. With this ideal value, the spectral density of the background can be expressed by

$$B_{EW} = \frac{\eta_{cr} \cdot t_c}{w \cdot \sqrt{2 \cdot \pi} \cdot \sigma_{Fano}} \left(\frac{P}{B} max \right)^{-1} \tag{3.86}$$

3.4.3.0.3. Positive Misfits The probability for an misfit event is the count rate multiplied with the respective time interval $\eta_{cr} \cdot t_{sample}$. Taking into account the uniform distribution of events over the energy rang from zero eV up to the photon energy E_{ph} the spectral density B_{MF} of positive misfit events can be expressed by

$$B_{MF} = \frac{\eta_{cr} \cdot t_{sample}}{E_{ph}}. \tag{3.87}$$

3.4.3.0.4. Negative Misfits A negative misfit may contribute to the positive spectrum provided that signal charge is already present in the internal gate. The probability for charge being present in the internal gate is the count rate η_{cr} times the collection time t_c. Furthermore, the probability for a negative misfit is η_{cr} times t_{sample}. These events will be distribute over the energy range from 0 up to E_{ph}. The corresponding spectral density for negative misfits B_nMF is

$$B_{nMF} = \eta_{cr} \cdot t_c \cdot \frac{\eta_{cr} \cdot t_{sample}}{E_{ph}}. \tag{3.88}$$

3.4.3.0.5. Clear The last contribution, which is taken into account is caused by the charge removal. The signal generated by incident radiation is a charge cloud with a defined size, formed by several charge carriers. If this cloud arrives during the clear process, a part of the charge carriers is removed. The amount of removed charge depends on several factors such as arrival time and original generation position. The amount of removed charge carriers is assumed to be linearly depending on time. The mean time necessary to remove all charge carriers of a charge cloud is denoted $t_{clear_{eff}}$.
The effect causes a false evaluation of the signal similar to misfits. However a clear event is surely causing two events, one with negative and one with positive amplitude. Similarly as for positive and negative misfits a spectral density for those events can be derived. For positive events the spectral density is

$$B_{CL} = \frac{\eta_{cr} \cdot t_{clear_{eff}}}{E_{ph}}, \tag{3.89}$$

while events with a negative amplitude only contribute to the positive side of the spectrum if charge was already present in the internal gate. The corresponding spectral density is

$$B_{nCL} = \eta_{cr} \cdot t_c \cdot \frac{\eta_{cr} \cdot t_{clear_{eff}}}{E_{ph}}. \tag{3.90}$$

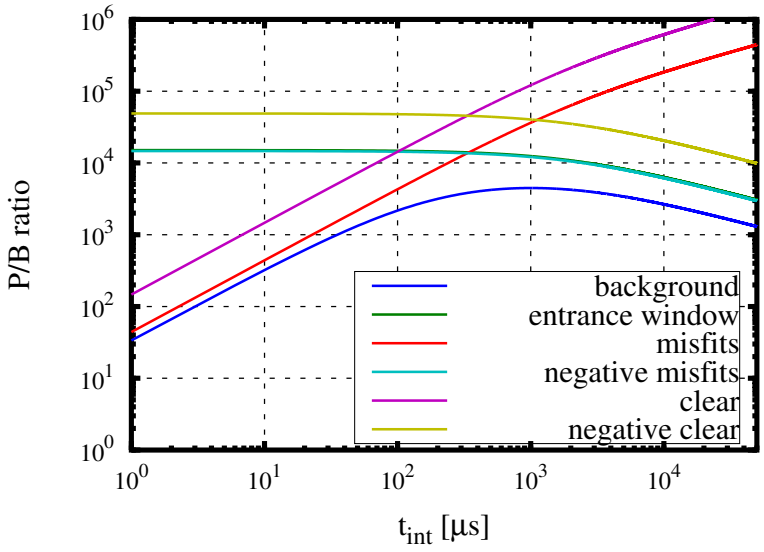

Figure 3.17.: The graph shows the various contributions to the overall background of a DEPFET sensor. The background is evaluated over the energy range from 900 eV to 1100 eV. The curves were calculated assuming an electronic noise of 4.8e$^-$, a leakage current rate of 0.1 e$^-$µs^{-1}, a sampling time of 1µs, an effective clear time of 300ns and an entrance window limited P/B value of 16000:1. Furthermore, a radiation source producing 5.9keV photons with a count rate of 3kcps is assumed. As shown especially at short integration timings misfits dominate the background. Additionally, events during clear and baseline sampling contribute to the formation of the background.

3.4.3.0.6. Misfit related Peak to Background The P/B is calculated from the ratio of peak height divided by the background at a certain energy. The single P/B contributions are

$$\frac{P}{B_{EW}} = \frac{\sigma_{Fano}}{\sqrt{\sigma_{Fano}^2 + ENC^2 + I_{lc} \cdot t_c}} \frac{P}{B} max \tag{3.91}$$

from the entrance window,

$$\frac{P}{B_{MF}} = \frac{t_c}{t_{sample}} \frac{E_{ph}}{\sqrt{2 \cdot \pi} \cdot w \cdot \sqrt{\sigma_{Fano}^2 + ENC^2 + I_{lc} \cdot t_c}} \tag{3.92}$$

for positive misfits,

$$\frac{P}{B_{nMF}} = \frac{1}{\eta_{cr} \cdot t_c} \frac{t_c}{t_{sample}} \frac{E_{ph}}{\sqrt{2 \cdot \pi} \cdot w \cdot \sqrt{\sigma_{Fano}^2 + ENC^2 + I_{lc} \cdot t_c}} \tag{3.93}$$

for negative misfits and

$$\frac{P}{B_{CL}} = \frac{t_c}{t_{clear_{eff}}} \frac{E_{ph}}{\sqrt{2 \cdot \pi} \cdot w \cdot \sqrt{\sigma_{ano}^2 + ENC^2 + I_{lc} \cdot t_c}} \tag{3.94}$$

as well as,

$$\frac{P}{B_{nCL}} = \frac{1}{\eta_{cr} \cdot t_c} \frac{t_c}{t_{clear_{eff}}} \frac{E_{ph}}{\sqrt{2 \cdot \pi} \cdot w \cdot \sqrt{\sigma_{Fano}^2 + ENC^2 + I_{lc} \cdot t_c}} \tag{3.95}$$

for background contributions related to the clear. These single contributions are depicted in figure 3.17 for a monochromatic radiation source of 5.9keV and a count rate of 3000cps. The noise was assumed to be 4.8e$^-$, the leakage current was set to 0.1e$^-\mu$s^{-1}. Furthermore, a typical sampling time of 1µs and an effective clear time of 0.3µs were assumed. The entrance window limited $\frac{P}{B} max$ ratio in the shown case is 16000:1. [5] If the leakage current is sufficiently small, the signal integration time is long enough and the count rate is low it should be possible to reach only entrance window limited P/B values. However in normal operation the constraints of experiments have to be fulfilled and in most cases the ratio of signal processing to signal integration time is set by the time necessary to read the hole matrix and the processing time of one pixel. If the sensor is operated in a window mode the processing and integration time will be in the same order of magnitude. Especially at this fast timings the dominating contribution to the background will be caused by misfits.

3.4.4. Misfits in Matrices

In section 3.2.5.4 the formation of Misfits occurring during the device readout was discussed. The derived model implies, that any kind of split events during the processing of a pixel can be neglected, i.e. the presented model is only valid for a well collimated or large DEPFET pixel.[6] In this section a model to describe the time dependent background of DEPFET matrices is introduced. However, further work to improve this model is necessary. Especially an exact study of the time dependence of the charge collection in a matrix is required to provide a more sophisticated model.

DEPFET matrices are usually read out row wise, hence all pixels of one row are read out in parallel. The processing time for a row t_{row} is equal to the processing time of a single pixel. The timing of each row is composed of a first settling time, the first sampling, the clear, a second settling time, the second sampling and an additional overhead time to e.g. multiplex the signal of all pixels of one line. The schematic readout for a matrix is depicted in figure 3.18a.

Typically, the frame time t_{frame} required to process the complete matrix is the product of the number of lines n_R and the line time $t_{frame} = n_R \cdot t_{row}$.

In addition to misfits, matrices show further readout artifacts. These affect the spectral response and are caused by the position and time dependence of the signal. For the basic concept only events split over two pixels are taken into account. Also similar effects for

[5] These values are taken from a least square fit on measurement date discussed in section 4.3.3.2.2 on page 129.

[6] Even for a pixel as large as 10 mm^2 the background is dominated by unrecognized split events on the device boarder.

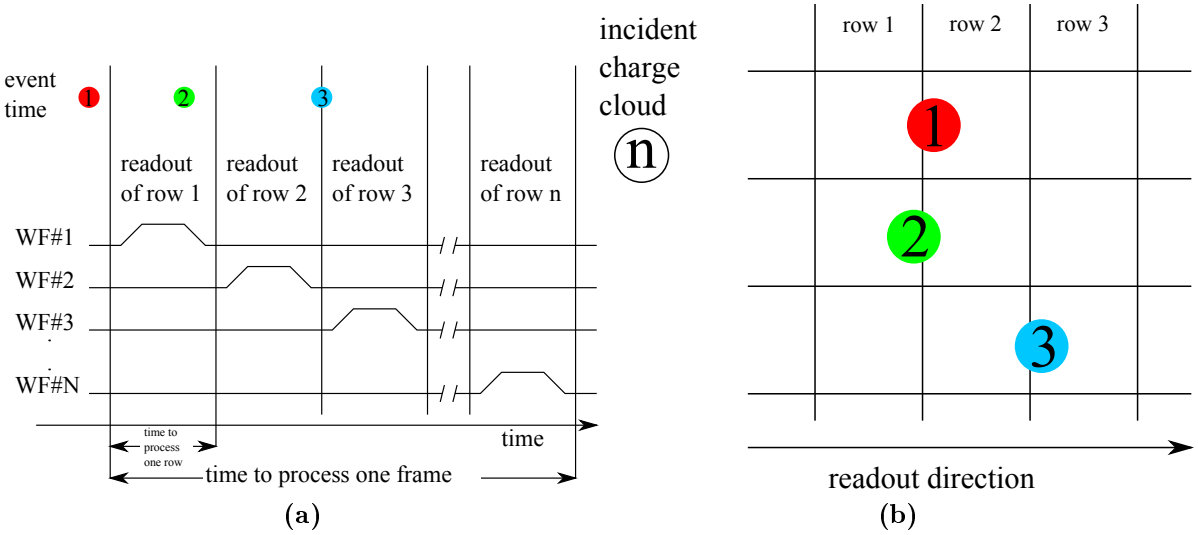

Figure 3.18.: When read out on demand, every row ($\#1 - \#N$) of a DEPFET matrix is processed using a trapezoidal weighting function (WF) as discussed in section 3.2.5.4 and section 3.4.1. By addressing all rows successively, the complete matrix is read out in a rolling shutter mode as indicated in a). In addition three points in time for incident photons are marked. With respect to its incident position, a photon deposits its energy in one, two or even more pixels. To illustrate the effect of those split events three cases for double split events are depicted in figure b). Depending on incident position and time a photon can be reconstructed correctly (case 1), causes a misfit (case 2) or causes further readout artifacts (case 3).

higher multiplicities are possible those are not discussed. Furthermore, these effects are not present for events that deposit all their charge in a single pixel (single-pixel events). The basic concept of split events is illustrated in figures 3.18a and 3.18b. There the following three cases are depicted.

1) Normal Event: Charge collected before the readout of one frame starts can be split over two pixels of two consecutive rows, here row one and row two. Since these are processed one after the other, the energy of the incident photon is reconstructed correctly.
2) Misfit: The signal charge is again spread over pixels belonging to row one and row two. If the charge arrives while the signal of row one is processed then part of the signal will be weighted false. Since the final signal is the sum of the false weighted signal of row one and the remaining correctly evaluated signal charge or row two, the overall signal will be corrupted. This causes a spectral contribution identical to misfits within a single pixel and adds to the shelf of the spectral response. As events collected after the first sampling time generate a negative signal, these can easily be identified and discarded. An advanced data analysis software may even be able to reconstruct such events (Lauf 2011).
3) Frame Split: The last case regards a split event over pixels from row two and row three. The charge arrives after the signal of row 2 is processed, but before the

processing of row 3 has started. In this case the charge is not just spatially split over two pixels, but also distributed over two consecutive frames. This results in two contributions to the shelf of the spectral redistribution.

The above considerations indicate that the effect of split events is complex and depending on the exact timing of the matrix and the split statistics (and thus the pixel size and biasing conditions).

For the following, the overall background of a matrix is supposed to be composed of the following three contributions

3.4.4.0.1. Entrance Window The spectral response of silicon to incident radiation has been discussed in section 3.3. To calculate the peak to background ratio, the simplifications introduced in section 3.4 that the spectral response is section-wise constant is kept. In this case the background caused by the entrance window is given by equation (3.86).

3.4.4.0.2. Misfits and Clear Events In their appearance misfits, either positive or negative as well as clear events show a rather similar behaviour. The spectral contribution for single-pixel events is described by equation (3.87) to equation (3.90). Split events, which include a misfit or clear-event will be considered to contribute identically to single pixel events. Furthermore, provided the count-rate is low, the effect of negative misfits and negative clear events can be neglected.[7] As already introduced in section 3.4.2 the time constants for sampling time t_{sample} and effective clear time $t_{clear_{eff}}$ can be merged to $t_s = t_{sample} + t_{clear_{eff}}$. Thus the misfit background is approximated by

$$B_{MMF} = \frac{\eta_{cr} \cdot t_s}{E_{ph}}. \tag{3.96}$$

3.4.4.0.3. Inter Frame Split Events While the basic principle of inter frame split events appears simple, their exact distribution and the corresponding influence on the spectral redistribution is hard to apprehend since several effects have to be taken into account. An extended simulation of a DEPFET matrix including the exact readout scheme, time dependent variations of the split statistic and similar effects would be highly beneficial. For the scope of this thesis and the following considerations, events generated during the time t_{row} a row is active (meaning its external gate is in the on state) will be assumed to contribute with a probability p_1 to the background. To account for the fact that events may be discarded by the data analysis software the additional parameter t_u is introduced. Moreover, these split events are assumed to be distributed equally over the energy spectrum. In this case, the spectral density is expressed by

$$B_{split} = p_1 \frac{\eta_{cr} \cdot (t_{row} - t_u)}{E_{ph}}. \tag{3.97}$$

[7] As long as the count rate per pixel per frame is in the percent order per frame, the contribution of these events is two orders of magnitude smaller than that of positive misfit and clear events.

3.4.4.0.4. Peak to Background Taking into account the peak height (see equation (3.85)) and substituting the time t_c for the frame time t_{frame}, the P/B ratio for a DEPFET matrix becomes

$$\frac{P}{B} = \frac{1}{FWHM}\sqrt{\frac{4\ln 2}{\pi}} \cdot \frac{1}{\cdot \frac{t_x}{t_{frame} \cdot E_{ph}} + p1 \cdot \frac{t_{row} - t_u}{t_{frame} \cdot E_{ph}} + B_{EW}} \tag{3.98}$$

3.4.4.0.5. Comparison with Measurements In the scope of this thesis no measurements on matrices were done. Thus for a test of the above model, measurement data acquired in the scope of the MIXS project are used. The DEPFET matrix of MIXS is built by 64×64 pixel with each $300 \times 300\mu m^2$. The matrix is split in two hemispheres, each read out by an ASTEROID ASIC. The matrix was illuminated by a ^{55}Fe source as described in section 3.3.1. The timing was varied by changing the time between two successive line readouts. Thus the time a row is active and the frame time are changed simultaneously and the ratio of the two is equal to the number of rows n_R, $t_{frame} = n \cdot t_{row}$. With that consideration equation (3.98) becomes

$$\frac{P}{B} = \frac{1}{FWHM}\sqrt{\frac{4\ln 2}{\pi}} \cdot \frac{1}{\cdot \frac{t_x}{t_{frame} \cdot E_{ph}} + p1 \cdot \frac{t_{frame}/n_R - t_u}{t_{frame} \cdot E_{ph}} + B_{EW}} \tag{3.99}$$

The most meaningful way to determine the different variables would be to fit the model to the measurement data. Unfortunately it was not possible to find a set of measurements were all unknown parameters could be determined simultaneously. For the measurements done up to now, that is largely because the single parameters are depending on each other. As will be discussed later, that is a result of the measurement method, that results in a similar spectral appearance of charge losses, misfit and frame split event.
The set of measurement data used as well as three model functions based on equation (3.99) are shown in figure 3.19. The model values are summarized in table 3.3 The values for $FWHM$ and n_R were taken from the available data. t_x is estimated using the known positive sampling time of 0.9 µs and assuming a value of 350 ns for the effective clear time. The detector entrance window is composed of the previously introduced passivation layers and an additional aluminum layer to block optical light. With respect to this layer stack a value of $7.5 \cdot 10^{-7}$ for the entrance window background is a reasonable

Model Name	FWHM [eV]	n_R	p_1	t_x [µs]	t_u [µs]	B_{EW}
Misfits	135	32	0	1.25	0	$7.5 \cdot 10^{-7}$
Intrinsic	135	32	0	1.25	0	$2.44 \cdot 10^{-6}$
Splits	135	32	0.382	1.25	1.365	$7.5 \cdot 10^{-7}$

Table 3.3.: The table summarizes the model parameters used with equation (3.99) producing the model functions shown in figure 3.19. Here n_R is the number of rows, read out per frame, p_1 is the probability for an event resulting in a frame split event (including its multiplicity), t_x is the time available for misfit and clear events t_u a correction factor accounting for discarded frame split events and B_{EW} the entrance window limited background.

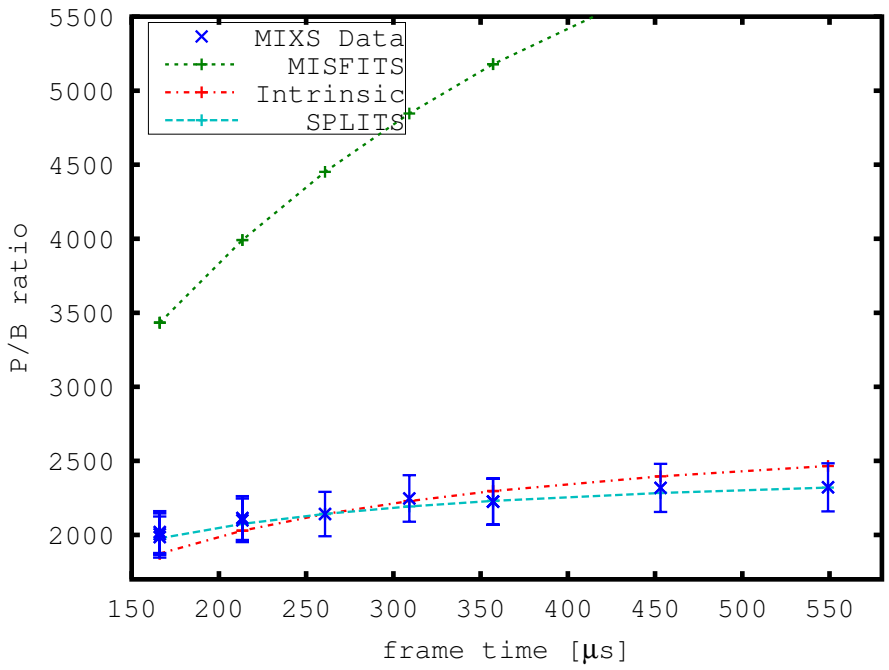

Figure 3.19.: The figure shows three models based on equation (3.99) alongside measurement data acquired in the scope of the MIXS calibration campaign. The frame time of the measurements was varied by introducing a waiting time at the end of each line. The model parameters are summerized in table 3.3.

guess which would result in a P/B ratio of approximately 10000:1. The value is close to the values presented in Granato 2012 that were measured using pn-Charge Coupled Device (pnCCD) with a similar entrance window. However, since especially the aluminum layer is thinner a lower value for the background was chosen.
The Misfit model, depicted as green dotted function in figure 3.19 totally neglects any kind of split events and systematically predicts larger values for the P/B.
There are two possible explanations for the lower P/B ratio. The first is charge losses, which increase the background. Fitting the model with B_{EW} as free parameter, but still neglecting any split events, the value providing the best approximation to the measurement data was found to be $B_{EW} = 2.44 \cdot 10^{-6}$. This intrinsic model is plotted as red dash-dotted curve in figure 3.19. Although the curve apparently describes the measurement data better, there is still a non-negligible deviation.

The second explanation for the reduced P/B ratio are the previous described split events. Thus, for this model, depicted as dashed, cyan line, B_{EW} was set to the initial value of $1 \cdot 10^{-6}$ and p_1 as well as t_u were estimated using a least square fit. As depicted this last curve is capable to approximate the measurement data closer than both the other models. However, the way the frame time variation was done causes an ambigu-

ity between background caused by split events and background caused by the entrance window. Therefore it is, at the moment not possible to determine the reason for the comparable low peak to background ratio of DEPFET matrices.

The above considerations show that, equal as for single pixel devices, misfits cause a reduction of the spectroscopic performance of matrices which is largely dependent on the timing. However they are not the sole effect related to the readout method, which introduces an additional contribution to the flat shelf of the spectral response. Especially split events can, due to the rolling shutter readout significantly reduce the spectral performance.
To further determine the effect of these frame split events it is necessary to separate frame time and row time by introducing an distinct illumination time at the begin of each frame. In this manner it would be possible to vary the frame time without changing the row time. If the illumination time, and thus the frame time becomes large, the contributions of misfits and split frame events to equation (3.98) approach zero. The only remaining contribution to the peak to background ratio, provided the illumination time is long enough, is then related to the entrance window and the underlaying physical processes. It is emphasized that future measurements should include a detailed study of these effects.

4. DEPFET with Built in Shutter and Storage

In the previous chapter the basic properties of a silicon sensor and especially the spectral response of a DEPFET read out on demand were discussed. As shown, the rolling shutter readout and the fact that incident charge is always collected in the DEPFET's internal gate deteriorates the intrinsic spectral response caused by the base material. To maintain the spectral response it is necessary to avoid these misfit events. That should be possible by the pixel-wise implementation of an electronic shutter. That shutter could then be used to suppresses the charge collection during the device readout and thus prevent a degradation. To overcome the dead time introduced by the shutter, it is furthermore possible, to provide a storage region that collects charge while the DEPFET is read out. In the following sections the basic principle of DEPFET devices that provide these additional properties is introduced and 4 existing layout concepts are presented. In the course of this work, 2 of these concepts were studied extensively using device simulations and measurements. These are presented in section two and three. Based on these results, a time-dependent spectral response was derived and spectral simulations were conducted. The results are presented in the fourth part of this chapter while a summary of the results is given in the last part of this chapter.

4.1. Pixel Designs

In this section the development of DEPFET devices with built-in shutter and additional storage feature will be discussed. Starting from the basic idea four concepts, marking milestones in the process of this development will be presented. The discussions in this part are limited to qualitative explanations of the functional principles. For simulations and measurements, done on prototype devices based on two of the here presented concepts refer to the next two section.

4.1.1. A DEPFET with Built-In Shutter

To model the behaviour of semiconductor devices, it is necessary to solve a set of differential equations. These are Poissons equation and the transport equations for electrons and holes Roosbroeck 1950. Since the majority of the sensor volume is fully depleted a qualitative discussion can neglect the transport equations. Then, the potential inside the

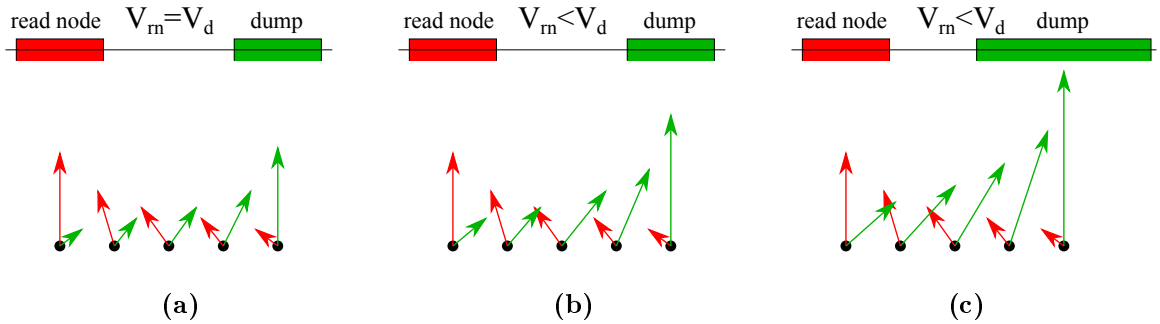

Figure 4.1.: To shield a read node from electrons, an additional contact to dump these is required. The effect of that dump on electrons depends on the position of the generated electrons, and the dumps extension as well as the applied potential. If both contacts have the same extension and are biased with the same potential, the electric field caused by either contact solely depends on the position inside the sensor (a). If a more positive bias is applied to the dump, the electric field caused by the dump will increase and electrons are moved into the direction of the dump (b). That effect can be increased by increasing the size of the dump contact (c).

sensitive volume is shaped by surface structures as MOS-capacitors, pn-junction, transistors and deep implantations. Qualitatively, a contact on top of a silicon sensor can be seen as a charge distribution $\rho(r')$ at the position r'. The distribution is thereby depending on the kind of structure and the applied bias voltage. The electrostatic potential $\phi(r)$ at the position r caused by such a charge distribution is

$$\phi(r) = \frac{1}{4\pi\varepsilon} \int \mathrm{d}^3 r \frac{\rho(r')}{|r - r'|}. \tag{4.1}$$

Its influence on the potential inside the bulk and thus charge carriers is depending on its size and the charge distribution $\rho(r')$ that in turn is given by the applied bias conditions. Simplified it can be stated that the larger a contact and the more positive the applied bias voltage, the larger its attraction towards electrons.

To extend the DEPFET with a built-in shutter at least one additional contact is required. This contact must be designed such that the following criteria are met.

- The charge collection in the sensitive state is not affected
- A change of bias conditions is sufficient to reject the collection of incident charge in the internal gate
- Already collected charge is not affected by the change of the bias voltages

For the moment only the rejection of charge is considered. If the DEPFET is treated as read node and the additional contact as electron dump as shown in figure 4.1a, the following considerations can be made. If both contacts have the same extension and are biased with the same potential, charge generated in the bulk will move to the contact

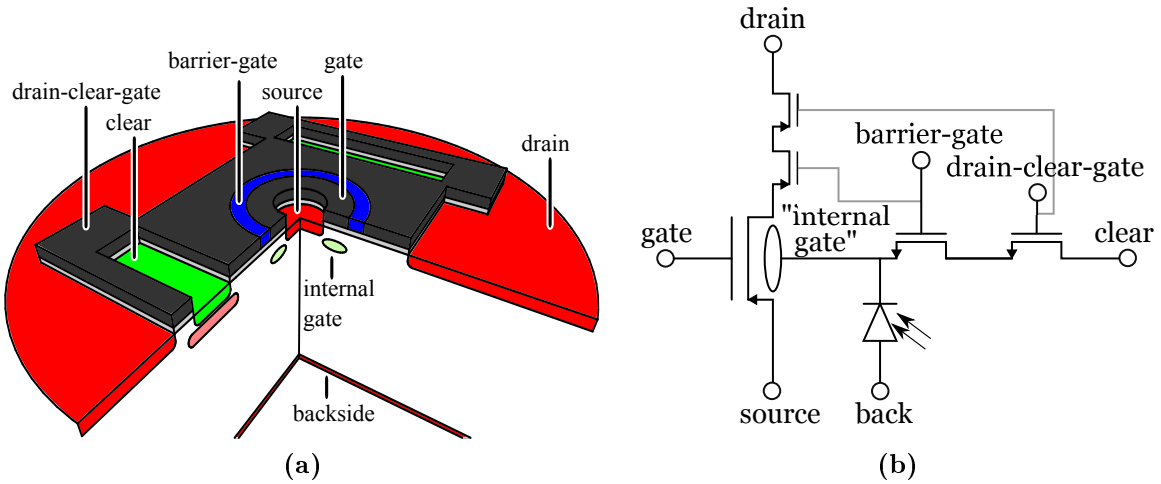

Figure 4.2.: The Barriergate Pixel layout is shown in a). The device consists of 3 overlapping gate contacts that provide the built-in shutter capability. The equivalent circuit, shown in b), consists of three transistors in series. The voltages applied to their gate-contacts control the current-flow between source and drain and the device sensitivity simultaneously.

that is closer. The rejection respectively the fraction of charge collected in the dump can be increased by increasing the potential applied to the dump as indicated in figure 4.1b. In addition, it is possible to improve the rejection by increasing the area of the shutter as shown in figure 4.1c. These tasks will improve the rejection.
However, in the sensitive state, the dump contact must be biased such that all charge is moved towards the read node. As large contacts biased with a constant potential introduce large areas with small potential gradients these are prone to increase the charge collection times. Furthermore, especially MOS-structures and n-contacts can introduce local potential minima for electrons, which cause their loss. This would both collide with the first constraint for a Gateable DEPFET.
Finally it is necessary to keep in mind that the barrier between collection node and dump has to be sufficient to avoid any and all losses of already collected charge. While a small distance between collection node and dump benefits the rejection it is also obvious that this reduces the barrier between the two.
The next section will introduce two different concepts for Gateable DEPFET devices, which both provide the built-in shutter functionality.

4.1.1.1. Barriergate Pixel

The so-called Barriergate Pixel concept was designed by Gerhard Lutz (Lutz et al. 2007). A cross section alongside the equivalent circuit are shown in figure 4.2. As the layout shows, the gate is surrounded by the barrier gate and the drain-clear-gate, in which the clear contact is embedded. The drain-clear-gate and the clear-contact are used to remove charge from the internal gate and furthermore provide the shutter feature. In the sensitive state, the drain-clear-gate is in inversion to extend the drain contact. In

the insensitive state, clear and drain-clear-gate are biased with a positive potential and electrons generated in the bulk are attracted by the clear. A loss of charge collected in the internal gate is prevented by the barrier-gate.
The functionality of the electron dump is provided by the combined properties of clear-contact and drain-clear-gate. While the former is used to remove the electrons from the device, the latter provides the area to achieve sufficient rejection ratios.
figure 4.2b. Depending on the voltage levels of the terminals clear, drain-clear gate, barrier-gate and gate, the device can be set into 4 distinct states, which are the readout state, the clear state, the sensitive and the insensitive state.

- In the sensitive state, charge is collected in the pixels internal gate. For that, drain-clear-gate and barrier-gate are biased with a negative potential forming an inversion layer underneath the MOS-structures. A positive voltage at the external gate causes the internal gate to be the most positive region of the device.

- In the readout state the gate is set into inversion. The device can now be read out due to the current-flow from source towards drain. In this mode the internal gate still forms the most attractive potential for electrons.

- For the clear state, a positive voltage is applied to clear, drain-clear-gate and barrier-gate. Adjusted in the right manner the resulting potential distribution will have a stairway like profile leading from the internal gate to the clear thus causing electrons to be removed from the device.

- The insensitive state is reached by applying a positive voltage to clear and drain-clear-gate while leaving the barrier-gate in inversion. This causes a barrier between the internal gate and the drain-clear-gate, which electrons can not pass. Thus already collected charge will be preserved in the internal gate. Charge carriers generated in the bulk will be attracted by the positive drain-clear-gate and the clear-contact, preventing the collection of charge.

While a standard Barriergate Pixel can not be read while it is insensitive, it should be possible to modify the layout to enable that feature. I.e. it is possible to cut open the drain-clear-gate and extend the drain contact inside this trench so that the barrier-gate is directly connected to the drain. However, in that case several three dimensional effects have to be taken into account.

4.1.1.2. Blindgate Pixel

The basic idea behind the Blindgate Pixel is to use two separate n+ contacts, one for clearing and one for blinding. In this way, the standard topology of the DEPFET can

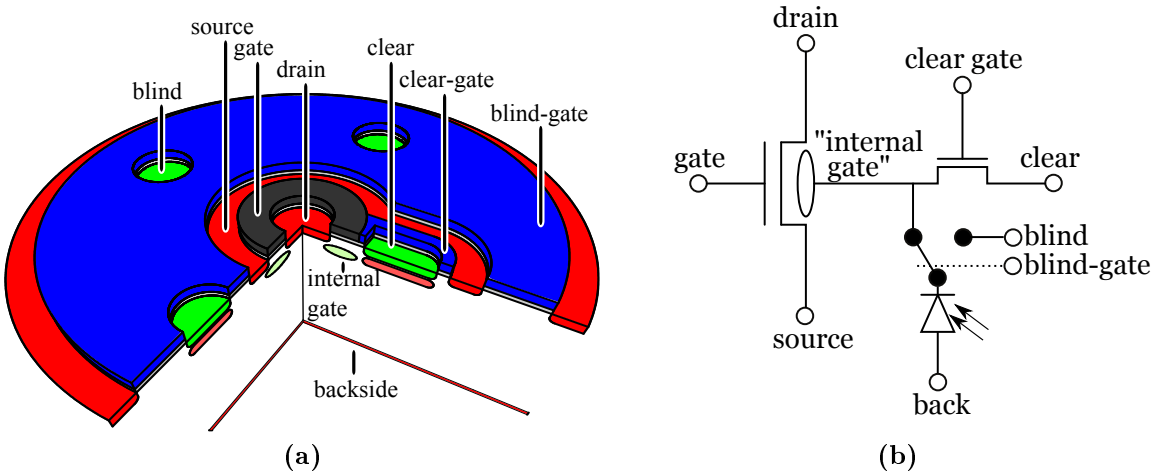

Figure 4.3.: A Blindgate Pixel is formed by surrounding a standard cut-gate DEPFET with a MOS-gate. Electrons collected underneath are removed by three embedded n+-contacts. The layout is illustrated in a). The layout provides a built-in shutter functionality and allows the readout of the device in the insensitive state as the equivalent circuit in b) indicates.

be used for the pixel itself, avoiding drawbacks of the barrier-gate design like e.g. worse W/L and large poly-overlap. In addition, the barrier between internal gate and shutter structure can be formed by an implanted barrier rather than an influenced one.
For the Blindgate Pixel the shutter is implemented by a MOS-contact named blind-gate, which surrounds the cut-gate DEPFET. The charge is removed from the device over three n+-blind-contacts,. A cutaway as well as the corresponding equivalent circuit are shown in figure 4.3.
In the sensitive state the blind-gate is biased with a negative voltage, thus inducing an inversion layer, which is biased by the source contact. The blind-contacts have to be biased with a sufficient voltage such that neither charge loss nor back-injection is possible. In the insensitive state, both contacts are set to a positive potential. Therefore, electrons generated inside the bulk will be attracted towards blind-gate and blind. Charge losses from the internal gate towards blind-gate and blind are avoided by the source implantation, which forms a barrier around the internal gate.
Since the DEPFET itself and the current-flow through the conductive channel are not affected by the biasing conditions of blind-gate and blind, a readout of this device during the insensitive state is possible.

4.1.2. DEPFET with Additional Analog Storage

The obvious disadvantage of the Gateable DEPFET is, that during the Blind phase, no charge from the bulk will be collected. Therefore, the effective observation time is reduced. Thus the logical improvement is the implementation of an additional area to store charges carriers, which arrive while the shutter is active. In this way, it will be

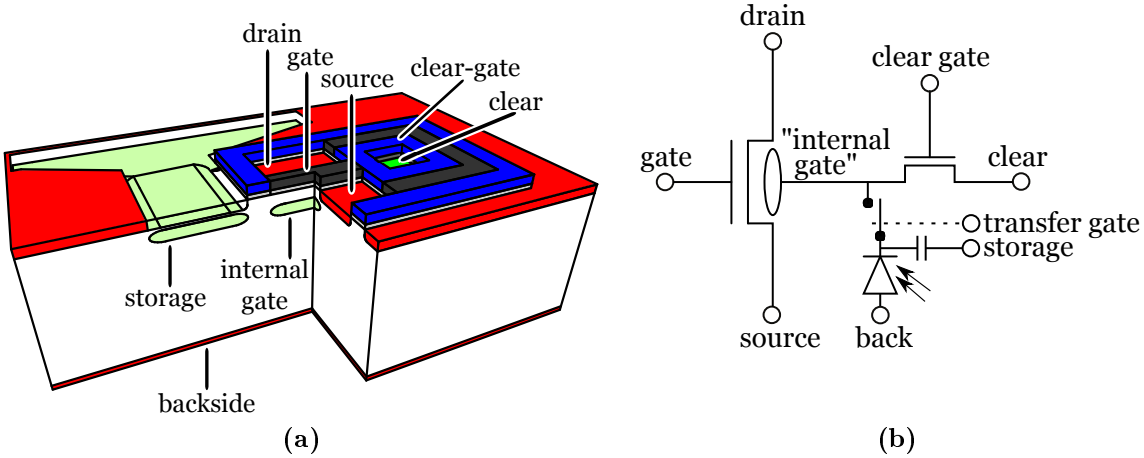

Figure 4.4.: To redirect incident charge, a linear DEPFET is surrounded by a large area p+-implantation. The drift into the storage is realized using several overlapping deep-n-implantations. The layout is shown in a). As the equivalent circuit, shown in b), indicates, the operation of the DEPFET and the collection of charge in the storage are separated.

possible to built devices that have (nearly) no dead time. In the following two conceptual different approaches to this concept will be presented.
One consideration common to both these approaches concerns the depth of the storage area. The surface of a silicon wafer typically has a large number of unsaturated bonds. These can act as recombination centers. To avoid a loss of charge carriers generated in the bulk, it is necessary to implement the storage region in a certain depth below the surface. The effects of charge losses on surface states have e.g. been observed in S. Wölfel 2007. Here the transfer of charge between two internal gates to reduce the DEPFET read noise was investigated. In the course of that work, the loss of charge due to interface traps was observed. Furthermore, it was shown that these charge losses can be avoided using a deep-n implantation in a depth of 1.2µm. In later work (Bähr 2010) it was demonstrated that charge losses can also be prevented using a medium energy-implantation forming the potential minimum in a depth of approximately 600nm, which is similar to the depth of the internal gate.

4.1.2.1. Internal Storage Pixel

The first presented concept is based on a linear DEPFET. Drain, gate, source and the adjacent clear-structure are surrounded by the transfer-gate, which provides a barrier towards the surrounding p+-implantation, as illustrated in figure 4.4a. Below this large area contact, a number of staggered deep-n-implantations forms a drift field, which directs incident charge into the storage directly in front of the DEPFET.
Applying a sufficiently positive voltage to the p+-contact in combination with its large area should provide a sufficient rejection of charge collection in the internal gate. At the same time, the barrier formed by the transfer gate will prevent any loss of charge

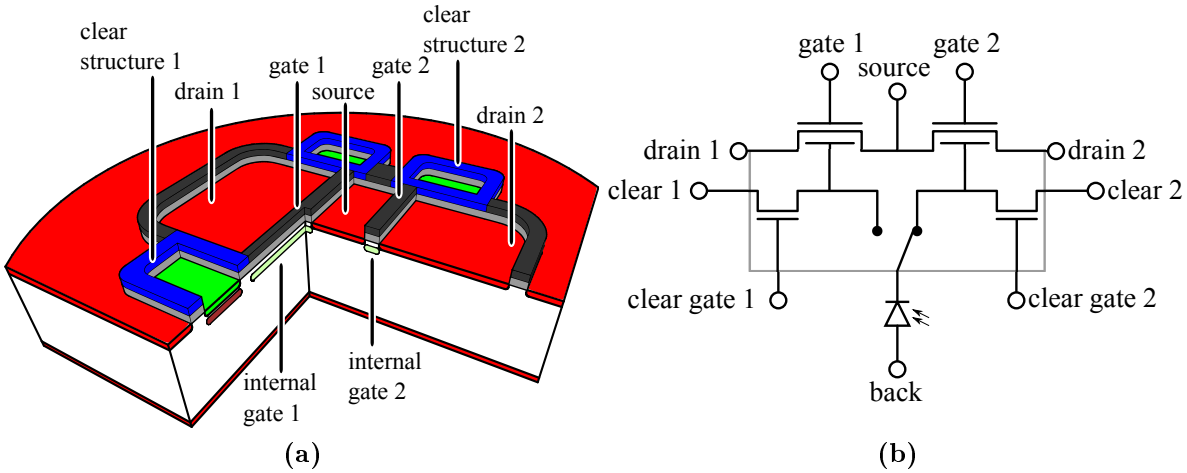

Figure 4.5.: The Infinipix concept utilizes two DEPFET devices as shown in a). Depending on the voltages applied to the drain-contact, charge is collected in one of the two DEPFETs while the other is insensitive and can be read out. This is also illustrated in the equivalent circuit shown in b).

already collected in the internal gate towards the storage.
To transfer the charge from the storage into the internal gate it is necessary to apply a sufficiently negative bias to the p+-contact. This should cause electrons to move from the storage over the MOS-spacer into the internal gate.

4.1.2.2. Infinipix

The second concept is also based on a linear DEPFET. It uses two DEPFET, which are are built close to each other as depicted in figure 4.5a. The functional principle is illustrated by the equivalent circuit shown in figure 4.5b.
Depending on the applied bias conditions always one of the two DEPFET is sensitive while the other is insensitive. The selectivity of charge collection is controlled by the voltages applied to the drains. Setting e.g. the drain of DEPFET 1 to source potential (0V) while DEPFET 2 is biased with a negative drain voltage (-5V), charge will be repelled by the negative and attracted by the positive drain. Thus charge collection is done normally in DEPFET 1 and rejected by DEPFET 2. In addition, the applied voltages enable the readout of the insensitive DEPFET.
As the equivalent circuit indicates, the sensitivity is determined by the voltages applied to drain 1 and drain 2. By inverting the bias conditions of the drain-contacts it is possible to switch the sensitive state of the two DEPFETs.

4.2. Device Simulations

In the previous chapter different device concepts of DEPFETs with built-in shutter and consecutively an additional storage region have been presented and discussed qualitatively. In this chapter two structures will be discussed more in detail by using 2 dimensional device simulations. The concepts discussed are the Blindgate Pixel and INFINIPIX DEPFETs. For closer investigations of the other structures see for example Lutz et al. 2007 or Aschauer et al. 2014

4.2.1. Simulation Tools

The simulations were done using the tools DIOS and TOSCA. The former calculates implantation profiles based on analytical models for different energies, doses and annealing procedures. The latter calculates 2-dimensional, numerical solution to the Poisson and transport equations using the finite element method. The calculations assuming either an infinite extension in one direction or a circular geometry of the device layout.These tools can be used for first quantitative analysis of new detector concepts.
To provide a simple to use basis, a library of 2D profiles for the relevant implantation profiles has been set up. These especially provide information on the implantation profile on edges caused by MOS-structures or lithographic masks. Based on these profiles and the knowledge of design and processing technology the properties of the real device can be approximated.
However, depending on the exact device geometry deviations between 2-dimensional simulations and measurements are unavoidable.

4.2.2. Blindgate Pixel

Dios as well as Tosca are primarily intended to yield a solution to the set of coupled equations describing the physics inside a semiconductor, (Poissons and transport equations for electrons and holes) for a fixed device geometry. Furthermore, while changes of voltage parameters in one simulation are possible, it is rather complex to set up wide ranged parameter sweeps.
For the simulations presented in the following section a script implementing a two step simulation procedure was established.

4.2.2.0.1. Preparing the Simulation Area In the first step the device geometry is defined. A schematic depiction is shown in figure 4.6a. These simulations were done on a fixed grid of 70µm width and 450µm depth. Utilizing an implantation library prepared using Dios, the doping arrangement caused by MOS-gates and masks is defined. In contrast to the structure presented in section 4.1.1.2 the blind-contact is implemented as a trench in the blind-gate. The area of this trench was adjusted such that the overall area of the blind-contact is equal to the area of the blind contacts in the produced devices. Its position in x-direction is equal to the distance of the blind contacts from the center. After setting up the simulation area, the device is depleted and the voltages suggested

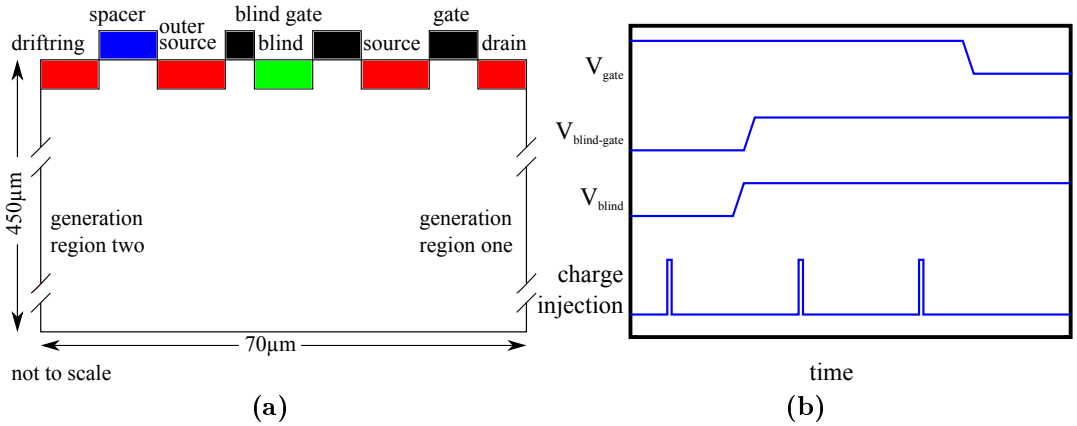

Figure 4.6.: The Blindgate Pixel simulations were intended to evaluate the influence of different device parameters, as geometry and voltage, on its characteristics. a) show the simulation area. Using the timing shown in b) it is possible to evaluate the charge collection Ξ and rejection ν.

for charge collection are applied.

4.2.2.0.2. Simulation of Charge Collection, Charge Rejection and Charge losses In the second step, the charge collection as well as the rejection and potential charge losses are evaluated. This is done following the simulation scheme depicted in figure 4.6b. First, charge is injected while the device is in the sensitive state (blind and blind-gate are in the low state). An example for the potential profile inside the substrate for this state is depicted in figure 4.7a. Since it is expected, that the charge collection and rejection are depending on the injection position, two injection regions are possible. Region one is placed directly below the internal gate while region two is set to the outskirts of the simulation area.
1µs after the charge injection in region two, the device is set into the insensitive state by applying the high voltages to the shutter structure ($V_{blind-gate_{high}}$ and $V_{blind_{high}}$). Successively, charge is injected once in generation region one (x=1µm y=200µm) and once in generation region two (x=67µmy=200µm). The potential profile for this state is shown in figure 4.7b. Due to the electrostatic potential all charge should be moved to the blind-gate and be removed from the device over the blind contact. After each charge injection a delay of 2µs is implemented to avoid any influence on successive injections.
As a final step, the external gate of the device is switched into the on (low) state for 3µs. In this state, the potential of the internal gate is substantially lowered, thus charge losses over the source contact into the adjacent blind-structure are possible. Since the amount of injected charge is known, charge losses can easily be identified.
To describe critical device parameters, the following terms are introduced:

- rejection ratio ν: Ratio of charge collected in the internal gate and injected charge for the insensitive state

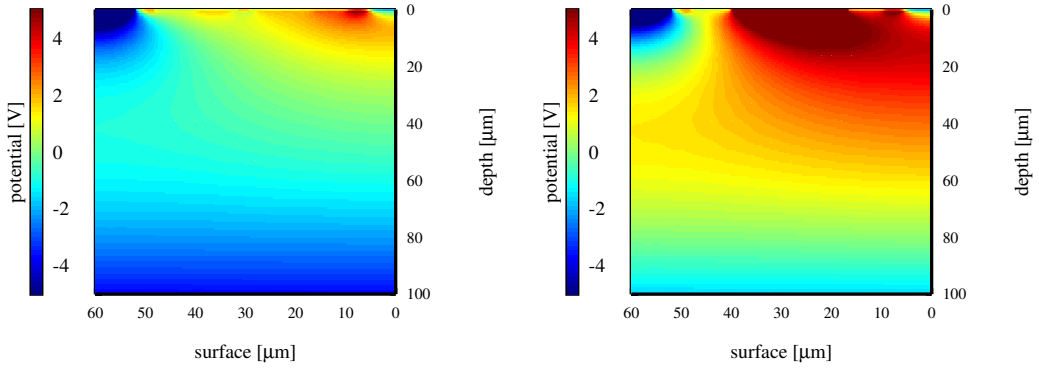

Figure 4.7.: Shown are the potential distributions for the sensitive (a)) and the insensitive (b)) state. Charge carriers will move perpendicular to the iso-potential lines. In the sensitive state, the potential distribution inside the Blindgate Pixel directs charge generated in the bulk into the internal gate, while in the insensitive state charge is directed into the blind.

- collected charge fraction Ξ: Ratio of charge collected in the internal gate and injected charge for the sensitive state

4.2.2.1. Voltage Variations

Equipped with the described simulation tools it is possible to perform sweeps of critical voltage parameters at different bias conditions. While typical parameters such as $V_{G_{off}}$, $V_{G_{on}}$, V_{source} etc. are expected to be known for the fabrication technology used, it is obvious that several voltages will have a significant influence on the performance of the device. First of all, the influence of the backside voltage will be evaluated, as this determines the overall potential profile in the substrate. The second crucial parameter is the high voltage applied to the blind-gate as this directly determines the attraction of the blind-structure for electrons and thus the rejection ratio ν.
The influence of different bias conditions will be evaluated for four drain voltages.

4.2.2.1.1. Backside Variation The backside voltage determines the depth of the charge drift path as well as the potential of that path. For that reason, it has to be expected that especially the charge rejection depends on the applied backside bias. For the simulations presented herein, the backside voltage was varied from -80 V to -140 V in 5 V steps. As shown in, figure 4.8 the charge collection is nearly independent from the drain voltage and complete (=1) for backside voltages more negative than -90V. For more positive voltages, the charge is not completely collected and a real device would be not fully depleted. In the simulation however, the device is depleted in a prior simulation step and thermal generation of charge is shut off by setting the quasi-fermi-levels sufficiently high. With insufficient backside voltage, an intermediate potential minimum is formed inside the bulk. In this way, charge generated in the bulk, during the pre-defined

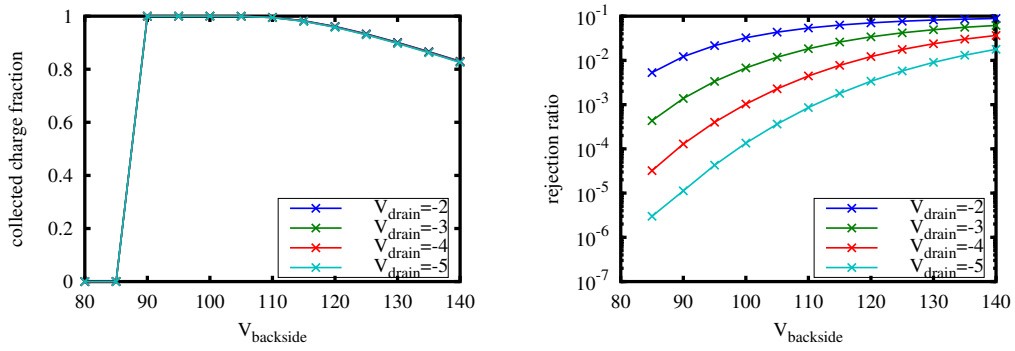

(a) **(b)**

Figure 4.8.: a) To fully deplete the device and completely collect charge in the internal gate a minimum bias for the backside of -90V is required. A too negative backside voltage will however cause the loss of charge carriers. b) The rejection ratio increases, meaning more charge is collected although the device should be insensitive, with decreasing backside voltage. The upper limit for the backside voltage is given by charge losses and the required rejection ratio. While the drain voltage has no effect on the charge collection, the rejection ratio improves with more negative drain voltage.

simulation step, is not able to reach the internal gate.
It can also be seen that all simulations show an incomplete charge collection for backside voltages exceeding approximately -110 V. As indicated by the geometry (see figure 4.6a) the charge has to cross over the structure formed by drift-ring-spacer, outer source, blind-gate and blind before reaching the internal gate. Depending on the applied potentials, each of these structures is capable to cause the formation of local or even global (blind-gate and blind) potential minima.
Since charge is subject to drift caused by the electrostatic field as well as to diffusion caused by the concentration gradient, it is possible that charge carriers cross potential barriers. The probability for this is defined by the height of the potential barrier as well as its size.
For comparably positive backside voltages, the trajectory of electron movement defined by the electrical field is located in a depth of several 10µm. Furthermore, a potential barrier between this path and the local potential minima exists. However, for more negative backside voltages, the electric field will push the charge carriers closer to the surface before they reach the internal gate. In addition, the potential barrier between the electron trajectory and the surface structures will be lowered by the more negative backside voltage. Both these effects cause charge losses for backside voltages lower than approximately -110 V (see figure 4.8a).
In figure 4.8b the dependency of the rejection ratio on the backside voltage is shown. The graph depicts the charge rejection for a injection close to the center of the device. As the data show a more negative backside voltage causes a reduction of the rejection ratio. This effect can be explained in the same way as the dependence of the charge

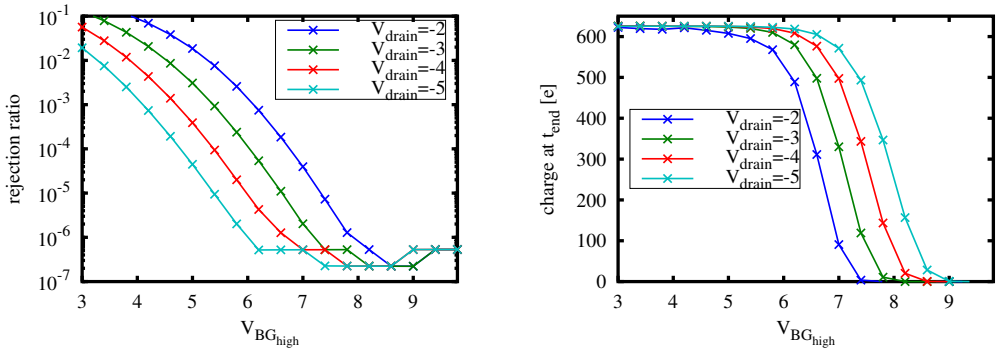

(a) **(b)**

Figure 4.9.: a) The blind-gate high voltage has major impact on the rejection ratio. However, a more positive blind-gate voltage will also lower the barrier of the source and induce charge losses as shown in b). Both, rejection ratio and charge losses can be influenced by the drain voltage.

collection on the backside voltage. For a more negative backside voltage, the trajectory of the charge carriers will be moved closer to the surface and furthermore the potential on the electron path is reduced. Thus it is more likely to involuntarily collect a certain amount of undesired charge in the internal gate for more negative backside voltages.

4.2.2.1.2. Blind Gate Variation It is rather obvious, that the voltage applied to the blind gate has to have a large impact on the charge rejection. Furthermore the close vicinity of the internal gate implies that it is at least possible to lose charge carriers if a certain threshold for this voltage is reached.
Following the simulation scheme described in the beginning of this section, the charge collection, charge rejection and charge loss for four different drain voltages has been evaluated. While the drain voltage has no effect on the charge collection, it strongly influences charge rejection and charge losses as shown in figure 4.9. The behaviour of the charge rejection is simply caused by the fact that a more negative drain contact has a larger repelling effect on electrons and thus enhances the charge rejection.
To understand the dependency of charge losses on the drain voltage it is necessary to evaluate the loss mechanism in more detail. Figure 4.10 shows the potential below the surface for drain voltages ranging from -2 V to -5 V. These plots were recorded for the same, moderate blind-gate high voltage of $V_{BG_{high}} = 4.7$V. Although, for these biasing conditions none of the simulations shows charge losses, it is possible to identify a saddle point at approximately 10µm in surface direction and about 2µm in the depth. If the voltage applied to the blind-gate becomes more positive, this point will also become more positive until the potential barrier is lowered so far that charge losses become possible. A more negative drain voltage, in contrast, will shift the potential of this saddle point to more negative values and thus increase the potential barrier. These considerations

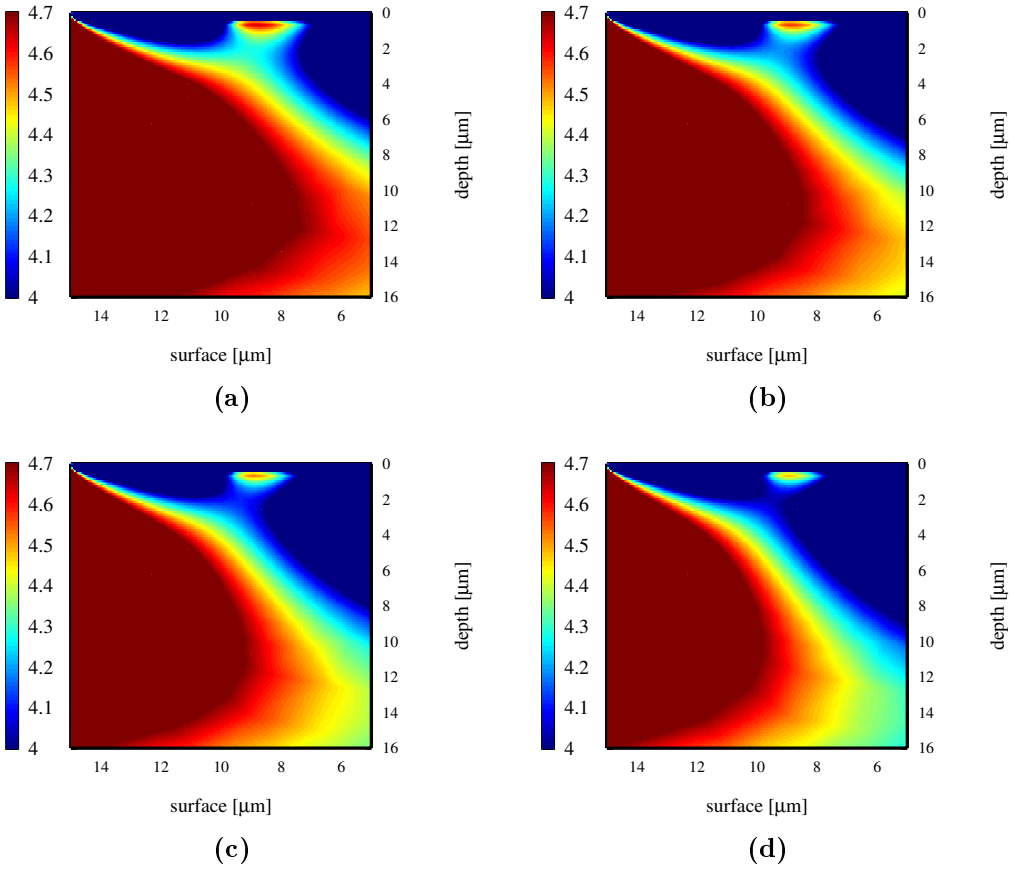

Figure 4.10.: Shown are the potential distributions on the device surface for drain voltages of a) -2 V,b) -3 V, c) -4 V, d) -5 V. As shown, the more negative drain voltage deepens the barrier between internal gate and blind-gate.

clarify the dependence of charge losses on blind gate high and drain voltage.

4.2.2.2. Geometry Variation

The voltage variations shown in the previous section have been performed with the default geometry of 5µm drain width, 5 µm gate width, 5µm source width 25 µm blind-gate width, with the blind embedded, an outer source width of 7 µm, and a driftring spacer of 5 µm. There are two dominating geometry parameters for the functionality of the built in shutter. The first is the width of the source contact, since it determines the distance of the shutter-structure to the internal gate. In this way, it determines the potential barrier towards the internal gate and thereby possible charge losses into blind-gate and blind. The second parameter is the area of the blind-structure, which mainly defines the charge rejection.
For the simulations shown in the following, the source width was varied from 5µm up to 8µm. To keep the extension of the device constant, the size of the blind-gate was reduced accordingly from 25µm down to 22µm. This simulations help to determine the effects of

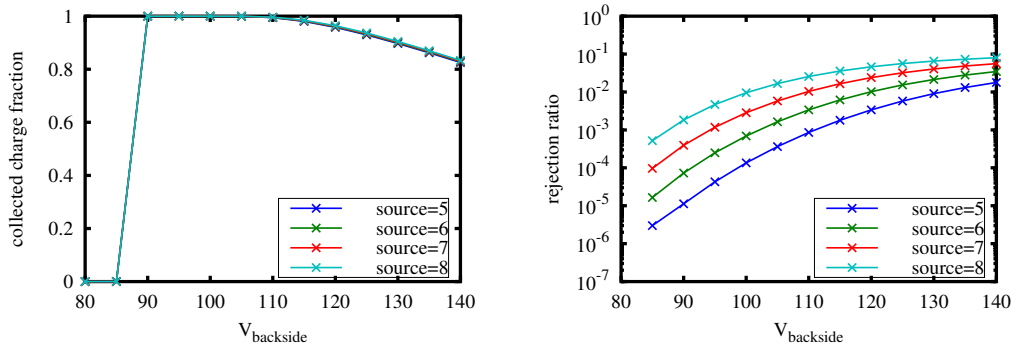

(a) **(b)**

Figure 4.11.: The variation of the source extension does not change the collection behaviour of the device as shown in a). However, as illustrated in b) a larger source leads to a worse rejection ratio at the same blind-gate high voltage.

deviations from the ideal cylinder geometry which are present in the produced devices. Otherwise the simulations are identical to those presented in the previous subsection. A variation of the backside voltage as well as the blind-gate-high voltage was performed.

4.2.2.2.1. Backside Variation The dependency of charge collection and rejection ratio on the backside voltage has already been discussed in detail in the previous section. Although the change of the source width causes slight changes in the collection behaviour, the basic dependency on the backside voltage as well as the corresponding explanation are the same as discussed in section 4.2.2.1.1.
For the charge collection, it is possible to observe a slight improvement for very negative backside voltages (see figure 4.11a). The reason is that the larger source node is more attractive and thus electrons are more likely to be collected if the source size is larger. This is, however, a minor effect.
Way more significant is the reduction of the rejection ratio for a larger source size. Due to the nature of the simulations (the extension of the device was kept constant on the cost of blind-gate area), a larger source implies a smaller area of the blind-structure. Since the bias conditions for all simulations were chosen to be the same, the smaller blind-gate is less attractive for electrons. This is the reason that for a larger source the rejection is reduced.

4.2.2.2.2. Blind Gate Variation The variation of the blind-gate high voltage show that the charge-rejection as well as charge-loss are highly depending on the source width (see figures 4.12a and 4.12b).
The reason for the first is again linked to the size of the blind-gate area, which reduces with increasing source width. The reduced blind-gate is in turn less attractive for electrons. Thus an increase of the source width reduces the charge rejection for a given blind-gate high bias voltage.

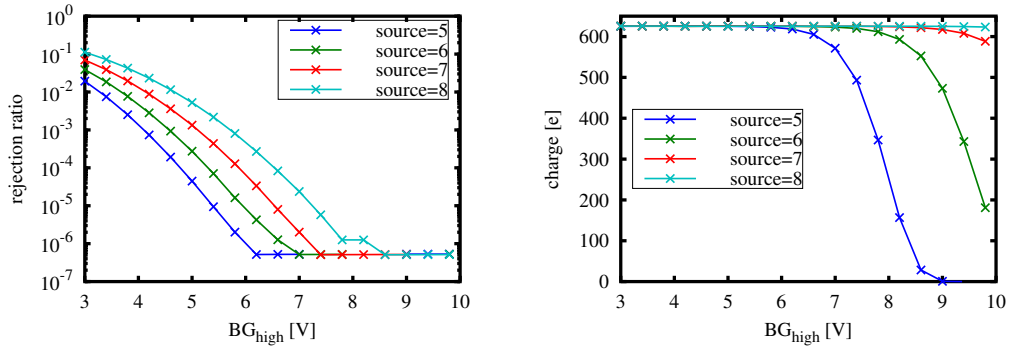

(a) **(b)**

Figure 4.12.: As already discussed, the rejection ratio (a)) and charge losses (b)) are primarily influenced by the blind-gate-high voltage. As shown, both characteristics can be influenced by the source width. Overall, for the simulated source width, a larger source increases the voltage required to reach a certain rejection ratio but also increases the operation window for the blind-gate-high voltage.

source width	blind gate high operation window
5	1.1
6	1.7
7	2.5
8	3.3

Table 4.1.: Operation voltages for the blind-gate high in dependence of the source width.

As was discussed in section 4.2.2.1.1 charge losses from the internal gate towards the blind-structure must happen over the source contact. A larger source increases the distance between the internal gate and the blind-structure, which in turn improves the barrier between the two. Thus charge losses appear for more positive blind-gate high voltages if the source is larger.
One important conclusion that can be drawn from this simulations. If the area of operation for the blind-gate high voltage in dependence of the source width is estimated, it can be seen that this window increases for larger source widths. Although it is extremely likely that the observed increase of the operation window will not be infinite, it is still obvious that even for a fixed maximum extension of a Barriergate Pixel device it is favourable to use a larger width for the source node.

4.2.2.2.3. Blind Gate Variation Two In this final simulation on the Blindgate Pixel the source width was varied, but this time the blind-gate width was kept constant at a value of 25µm. Although this is only a moderate change to the simulation presented in the previous section, the results presented in figure 4.13 are impressive. While the behaviour

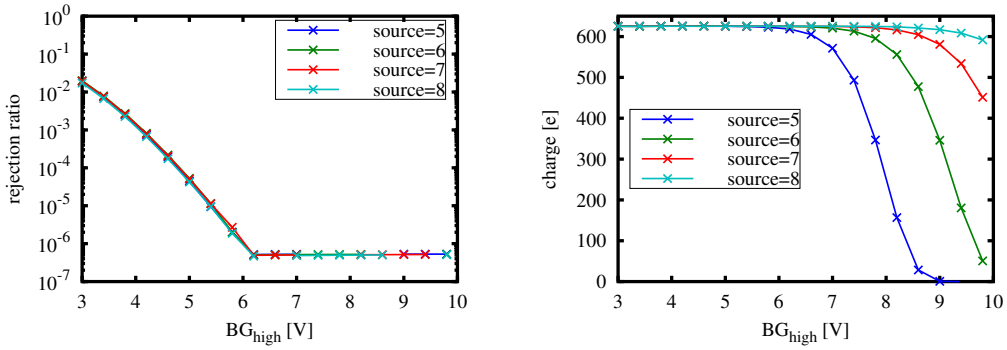

(a) (b)

Figure 4.13.: For the shown simulation results, the extension of the blind-gate was kept constant, effectively increasing its area. Shown are again the rejection ratio (a)) and charge losses (b)). Again both characteristics are influenced by the source width. However, since here the blind-gate area increases with larger source width, the charge rejection improves.

source width	blind gate high operation window
5	1.4
6	2.3
7	3.2
8	4.0

Table 4.2.: Operation voltages for the blind-gate high in dependence of the source width, with a fixed blind-gate length.

of charge losses stays nearly the same as in figure 4.9b, the rejection behaviour is quite different.

Figure 4.13a shows, that in contrast to the previous simulations the rejection ratio is now almost independent from the source width. This is mainly because the the size of the blind-gate is constant. Since the simulation is cylinder symmetric and the blind-gate is shifted to increasingly larger radii the area of the blind-gate increases. Therefore, since distance of the blind-gate from the internal gate and its area increase, the rejection ration is independent from the source size. As the larger source reduces charge losses, the operation window of the blind-gate high voltage increases in comparison to the values depicted in table 4.1. The new values are shown in table 4.2.

4.2.3. Infinipix

During the course of this thesis the so-called INFINIPIX DEPFET devices were developed at the HLL. As described in section 4.1.2.2, these devices consist of two DEPFETs in close proximity to each other. At any given time, one of the two subpixel is sensitive and collects arriving charge carriers, while charge collection in the other is prevented.

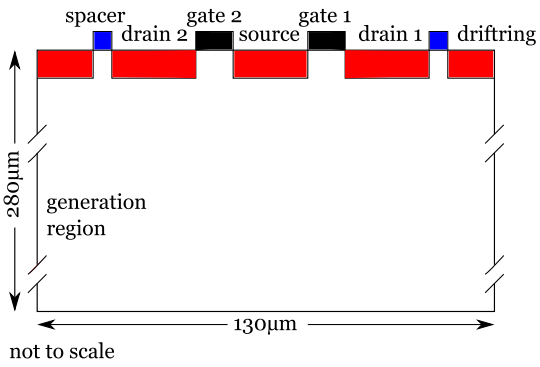

Figure 4.14.: To simulate the Infinipix concept, the above shown two dimensional cut through the device was used.

Furthermore, signal charge that was collected in the previous sensitive state, can be read out while the respective subpixel is insensitive.
Similarly to the Blindgate Pixel, the backside voltage is one of the critical parameters for the functionality of the INFINIPIX. Furthermore, the exact geometry, especially the size of the source contact, and the drain contacts define the rejection.

To evaluate the influence of these parameters, a simulation procedure similar to that of the previous section was set up. Since the backside voltage appeared to be the most influential parameter these simulations are intended to evaluate the operation window of the backside voltage for different geometries and bias parameters.
The simulations were performed on a fixed grid with 130µm width and 280µm depth. A schematic of the simulated geometry is depicted in figure 4.14

4.2.3.1. Backside Variation

A single backside variation is a stepwise sweep of the backside voltage from a starting voltage V_{B1} to a final voltage V_{B2}. After each voltage change, charge is injected into the device. The simulation scheme is depicted in figure 4.15. To evaluate charge collection and charge rejection, the amount of charge collected in the two internal gates as well as the charge in the bulk is recorded. The point of injection is chosen such that the charge has to first drift over the insensitive pixel before being collected by the sensitive pixel.
The only parameter changing between two consecutive charge injections is the applied backside voltage as shown in figure 4.15a The simulation starts at a backside voltage which is too positive to fully deplete the device, such that electrons generated in the bulk will not be able to reach the internal gate. Since at every simulation step the backside voltage is decreased, it is expected that at some point all electrons will move out of the bulk towards the surface and ideally into the internal gate of the sensitive pixel. In figure 4.15b the charge in the two internal gates as well as the charge inside the bulk is plotted against the simulation time. As soon as the backside voltage is sufficiently negative, all charge accumulated in the bulk is collected in the internal gate of the sensitive pixel. As the simulations show, more and more charge will be collected in the insensitive pixel with further decreasing backside voltage . From these simulation it is possible to derive

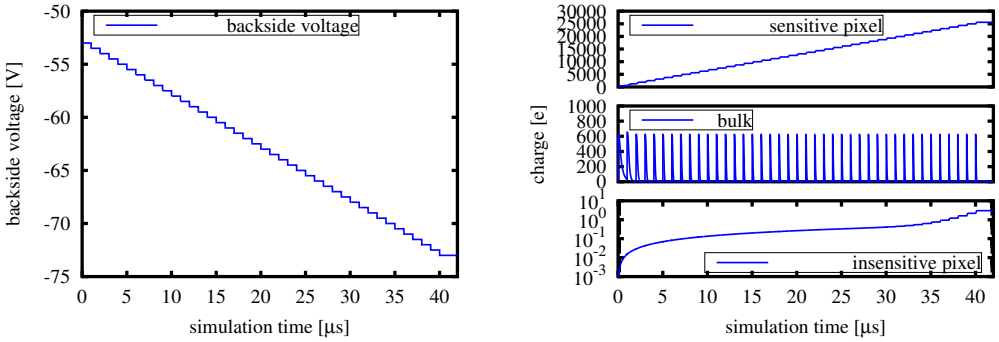

(a) (b)

Figure 4.15.: In the previous section it was shown that one of the major influences on the rejection of a Gateable DEPFET is the backside voltage. It is expected that the Infinipix shows a similar behaviour. The simulations were primarily aimed at the influence of the backside voltage. Each simulation consisted of a stepwise decrease of the backside voltage as shown in a). For each of these simulation steps, about 600 e^-- of charge was injected into the bulk. The fraction of charge collected in either of the two subpixel is observed (b)).

a operation window for the backside voltage, in which the following criteria are fulfilled:

- generated charge is collected completely in the two DEPFETs
- the fraction of charge collected in the insensitive pixel is below a certain threshold $(1 \cdot 10^{-3})$

For the chosen example of geometry and biasing conditions, this operation window is 15V.
In addition to the fraction of charge collected in each pixel, it is possible to extract the charge drift time from the point of origin into the internal gate. The time required to collect 90 % 99 % and 99.9 % of the generated charge in the DEPFETs internal gate is depicted in figure 4.16. As can be seen, the values depend on the backside voltage. The step-like behaviour of the collection time most likely is an artifact of the simulation, owed to the fact that the simulations were optimized to yield a result of the later presented geometry variations within a time less than a week. This optimization seems to affect the accuracy of the collection time estimation. However, it was ensured that neither the completeness of the charge collection nor the rejection ratio are affected by stepwise changing the simulation grid from fine to rough and comparing the respective results.

4.2.3.2. Ideal Geometry Parameters

In the previous section, the simulation procedure for a single geometry variant has been established. It is now possible to calculate the operation window of the backside for a larger variety of geometries. The result for such a variation is shown in figure 4.17a. The simulations indicate, that there is an optimum for the size of source and drain. At this

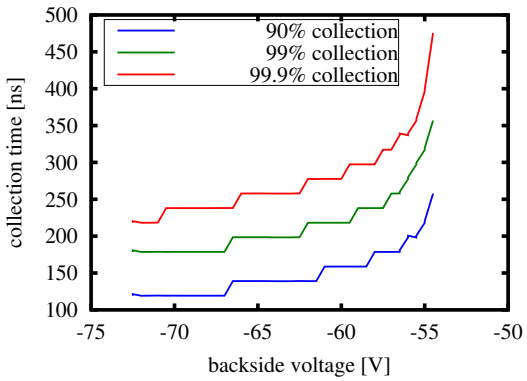

Figure 4.16.: A charge cloud generated in the bulk requires a certain amount of time to be collect in either of the two subpixel. The collection time is thereby largely dependent on the applied backside voltage.

optimum voltage the operational window is 15 V. With respect to the mean backside voltage of approximately 60 V, the operation window for the backside voltage is in the range of 25 percent. Both backside voltage and bulk doping concentration affect the potential profile inside the bulk similarly. Thus, the 25 percent of backside voltage can be seen as the maximally tolerable bulk doping variation.
The typical fluctuations of the bulk doping are in the range of 15 percent peak to peak (see Beole et al. 2001) on one wafer. This indicates that for a wafer scale device further optimizations are necessary. As can be seen in figure 4.17b, it is possible to adapt the operating conditions of the device to increase the operational window. In the corresponding simulations, the drain off voltage was set to +1 V. This change increases the operation window for all geometries. In the region of the optimum geometry, the operation window reaches and even exceeds 20 V. Assuming that this voltage is used to compensate fluctuations of the bulk doping concentration it would be possible to accommodate a deviation of up to 30 percent.

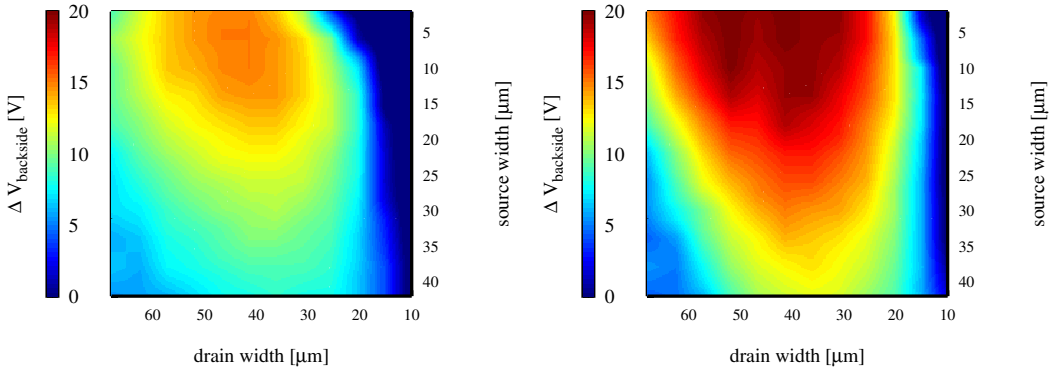

Figure 4.17.: The device geometry has a crucial influence on the charge rejection of the insensitive pixel. Using the here presented simulation scheme, it is possible to implement a geometry variation for e.g. the source and drain extensions. For each geometry combination a simulation as shown in figure 4.15 was performed. For each of these combinations, the point of complete charge collection and the point of insufficient charge rejection can be taken. The resulting operation window for the backside voltage with respect to drain and source extension is shown in a). as can be seen, there exists an optimum for that operation window at about 45 µm drain width and 5 µmsource width. By increasing the voltage applied to the drain of the insensitive pixel by 1 V it is possible to increase the operation window of the backside contact from about 15 V to about 20 V

4.3. Measurement Results

In this chapter, measurements and the corresponding results will be presented. For the qualification of the different DEPFET devices with respect to operational voltages and device timing, a flexible measurement setup was designed, that will be discussed first. Next, measurements done with that setup are presented. These start with spectroscopic measurements on DEPFET macropixel devices, followed by measurements on different devices providing either a built-in shutter, a built-in shutter with the option for a repetetive-non-destructive-readout and measurements on a device providing a built-in shutter and an additional storage region.

4.3.1. Measurement Setup

The SPIX-II measurement setup was designed in the scope of this thesis to provide a flexible measurement platform. The setup uses a modular approach to offer a highly adaptable measurement system for single-pixel-DEPFET-detectors or small matrices of 4×4 DEPFETs. Figure 4.18 shows a block schematic and a photograph of the setup. All measurements presented within this thesis have been carried out using the SPIX-II. The heart of the setup is formed by the Base-Board. It can be equipped with a Switcher-Board, Interlink-Board and Readout-Board tailored for the respective application. The Base-Board is connected to the so-called X-Board that serves as digital control unit and

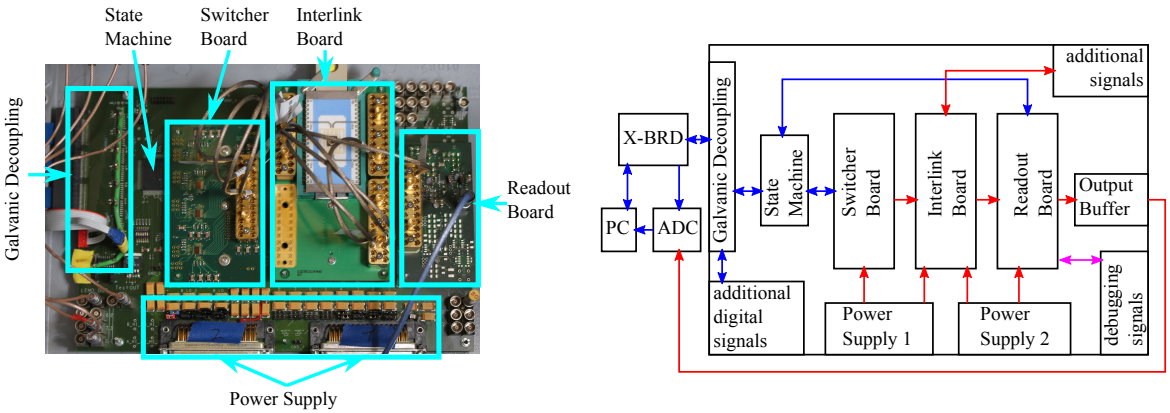

(a) **(b)**

Figure 4.18.: The SPIX-II consists of the Base-Board, carrying the switching electronics (Switcher-Board), readout electronics (Readout-Board) as well as the device under test (on the Interlink-Board) as shown in a) and a digital control unit (X-Board), the required ADC and a computer. As the block diagram in b) shows, digital (blue) and analog (red) signals of the SPIX-II are separated as much as possible. Synchronization of the complete setup is provided by the ISEQ-sequencer running on a Virtex-5 FPGA on the X-Board. The single-ended digital signals from the X-Board are decoupled by digital opto-couplers and translated to the required signal levels by a Spartan-3 FPGA (State Machine) on the Base-Board. These signals control the switching as well as readout electronic used to operate the device under test mounted on the Interlink-Board. The analog signal is buffered by an output buffer on and fed to an ADC. Data-processing as well as sequencer programming are done using a computer.

provides control and synchronization of all hardware parts. The digital control signals are routed through a spartan-FPGA XC3S50AN that serves as intermediate stage between the digital control and the analog switching and readout-electronics. The data acquisition is done using a 14-Bit ADC.
The state machine, in combination with the modularity of the switching and readout boards, offers a large flexibility to operate different switching as well as readout electronics. Besides the testing of new DEPFET concepts, the SPIX-II setup can also be used to test new ASICs either in a stand-alone test or in combination with a sensor. Furthermore, the setup could be used to provide the basis of a high performance measurement system. For this, a taylored PCB needs to be designed, combining Switcher-Board, Readout-Board and Interlink-Board in a single design. The "standard" configuration of the setup is based on well tested electronic components and will be discussed in the following.

4.3.1.1. Switching Electronics

In the standard configuration, the switching of analog signals is done using the Switcher-S control ASIC(Treis et al. 2010). The Switcher-S is designed in 0.35 µm HV CMOS AMS process and is usually used to control matrices of DEPFET devices. Each Switcher-S has 2 ports with 64channels each. The measured delay to a trigger signal is 8 ns with a deviation of 2 ns. The switching rise time of the signals is in the range of 5 ns with an overshot of less than 0.5 V as shown in figure 4.19. The overshot can be reduced

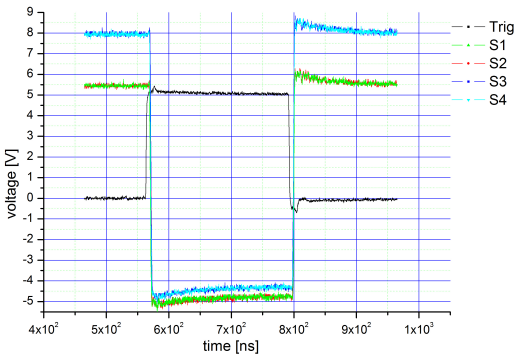

Figure 4.19.: Switching behaviour of the Switcher-S

by increasing the capacitive load. A too large capacitance, however, will also affect the signal rise time. The digital sequencing of the setup is done with a speed of 80 MHz, which equals a time resolution of 12.5 ns. Hence by using the Switcher-S devices, a change of signal is achieved within a single clock cycle.

4.3.1.2. Readout Electronics

As described in chapter 3.2.5, DEPFET devices can be read out using different filtering techniques and either drain current or source follower readout. In this work, both readout schemes were used to study the device performance.

4.3.1.2.1. Discrete Drain-Current Readout For the SPIX-II setup, a discrete drain-current readout board, as schematically shown in figure 4.20 was designed. The DC-current of the input signal is subtracted by the resistor R_{sub} and the voltage source V_{sub}. Any changes of the input current are amplified by the current-to-voltage converter formed by an operational amplifier and its feedback network R_F. Further amplification as well as filtering and a offset correction are provided by the second amplifier. To avoid distortion in the analog transmission line, the single ended signal is converted to a differential signal by the differential buffer. The amplitude of the output signal V_{out} can be matched to the dynamic range of the connected ADC by adjusting the gain of the three stages. The DC level can be changed using the substraction and offset voltages V_{sub} and V_{off}. The signal V_{I-V} at the output of the current voltage converter can be

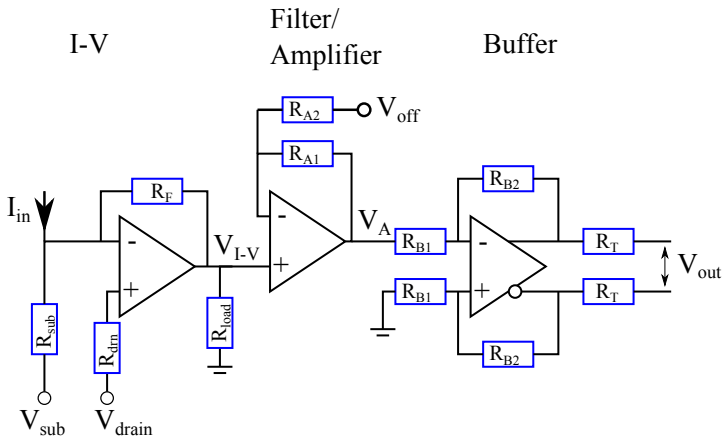

Figure 4.20.: The drain current readout is realized by a current-voltage converter followed by a positive amplifier and a buffer circuit converting the single ended signal into a differential one.

expressed in terms of the feedback resistor R_F, substraction resistor R_{sub}, the voltage applied to its positive input V_{drain} and the substraction voltage V_{sub} by

$$V_{I-V} = I_{in} \cdot R_F - (V_{sub} - V_{drain}) \frac{R_F}{R_{sub}}. \tag{4.2}$$

To adapt the frequency response of the I-V-converter a suitable load impedance can be applied [1]. This signal is further amplified and shifted by the second stage. The voltage V_A at the output of the second amplifier is

$$V_A = V_{I-V} \left(1 + \frac{R_{A1}}{R_{A2}}\right) - V_{off} \frac{R_{A1}}{R_{A2}}. \tag{4.3}$$

The following differential buffer converts the single ended input voltage to a differential signal. Its differential output-voltage V_{out} is given by

$$V_{out} = V_A \frac{R_{B2}}{R_{B1}}. \tag{4.4}$$

The buffer output line is equipped with a line termination resistor R_T. The various parts of the circuit have to be selected with respect to the required bandwidth, dynamic range, system noise and stability. Further considerations on circuit noise and stability are discussed in appendix B.

4.3.1.2.2. Source Follower Readout using the ASTEROID ASIC The ASTEROID ASIC provides a source follower readout for DEPFET matrices performing a trapezoidal weighting of the signal. It is optimized for the readout on demand of DEPFET based sensors. Despite the 64 channels, the SPIX-II setup requires only a single channel of the ASTEROID to read out the DEPFET single pixel. The equivalent circuit of a single

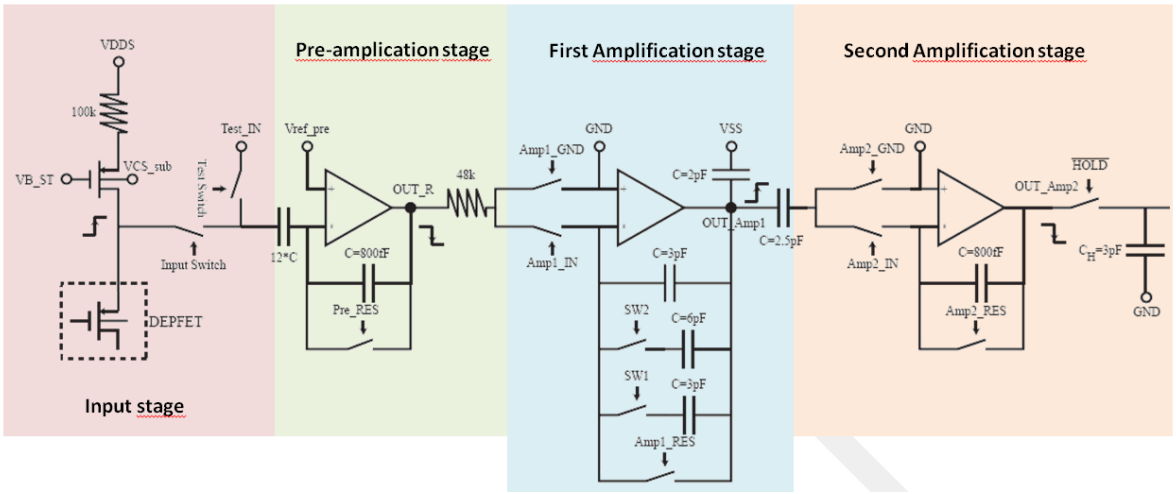

Figure 4.21.: Schematic of one readout channel of the ASTEROID ASIC. Each of its 64 channels provides a current source for source follower readout, a pre-amplifier as well as two additional amplification stages, used to implement the trapezoidal weighting function. The output signal of each channel can be buffered on a hold-capacitor and is serialized by a 64-1 multiplexer.

channel is shown in figure 4.21. Each individual channel of the ASIC consists of a current source, a pre-amplifier, a shaping circuit built of an integrator and a subtraction stage, and a sample-and-hold stage. To provide the trapezoidal weighting function the signal is integrated by the first amplification stage for a defined time, that is typically in the order of 1 µs. The resulting voltage is stored in the second amplification stage. After resetting the first amplification stage and removing the collected charge carriers from the internal gate of the DEPFET, an integration of the baseline level is done. The difference of the two voltage levels is stored on the sample and hold stage.
The ASTEROID is equipped with an internal RAM register. It consists of a set of static programming bits that define e.g. the gain of the pre-amplifier or the number of channels that are multiplexed to the output-buffer and a dynamic part. Here, the registers control the dynamic switches in the ASIC and thus define the weighting function. The dynamic register and the state of the different switches is controlled by an external sequencing clock. Overall, the weighting function can be adapted using either the ASTEROID's internal RAM or the timing sequence provided by the X-Board.

4.3.2. DEPFET Macropixel

As described in section 3.2.1, it is possible to surround a DEPFET by one or more drift rings, to form a so-called DEPFET macropixel. While interesting in itself as drift-detector with on-chip amplification, the increased active area allows the study of the DEPFET's properties in a spectroscopically clean environment, with minimal influence of split events on the device boarder. The measurements presented in the following were

[1]Usually it is sufficient to apply no distinct load, respectively leave the resistance infinite.

done using DEPFET macropixel devices with an active area of 10 mm^2. Furthermore, the devices were equipped with a zirconium on-chip collimator to suppress partial events on the device border. In addition to the study of these devices, the measurements were used to qualify the spectroscopic capabilities of the SPIX-II measurement setup (see section 4.3.1).

4.3.2.1. Method

The measurements were done using the SPIX-II setup as described in section 4.3.1 in combination with the discrete drain current readout circuit. The output of this circuit was connected to a semi-Gaussian shaper. The digitalization was done using a Pulse Sensitive Multi Channel Analyzer (PMCA).
To keep charge from accumulating in the internal gate, the DEPFET is cleared after fixed time intervals. The time between two clear pulses was 1000 µs. During the clear time and the following recovery time of the readout circuit, the signal acquisition was suppressed. The corresponding dead time was set to 10 µs.
For these measurements, a ^{55}Fe source as discussed in section 3.3.1 was used. This source emits two dominant lines at 5.9 keV and 6.4 keV. Furthermore, a spectrum with a sufficient number of counts exhibits the presence of the corresponding Si-escape lines. For the data analysis K_α, K_β and the silicon K_α-escape peaks were fitted each with a Gaussian function. The energy calibration is then done by a linear fit of the ADU values to the respective energies. The energy resolution is extracted from the width of the fitted K_α peak. The P/B is calculated using the fitted peak height and the mean background over the energy ranges from 800 eV to 1200 eV, 2300 eV to 2700 eV, 3300 eV to 3700 eVand 4300 eV to 4700 eV.

4.3.2.2. Spectral Performance

Spectral measurements on DEPFET macropixels were done for two devices. Representative spectra of these, taken with the same sequencing, temperature and shaping time, are shown in figure 4.22. Shown alongside the measurement data are the spectral response model derived in section 3.3, for moderate (Model 1) and small (Model 2) additional charge loss. Overall, the models show a good agreement with the measurement data. However, there are several deviations. The three dominant ones are the valley between the K_α and K_β peaks, the tail on the low energy side of the K_α peak and the additional peaks in the measurements at energies of 2.7 keV, 2.9 keVand around 5 keV.
The valley is caused by the semi-Gaussian shaper. After a signal, the shaper settles back to its baseline level. The baseline restoration can be adjusted. A mis-adjustment of that restoration circuit causes either an overshot of the output or respectively a slow settling [2]. In both cases, a second event will pile up on the small, unsettled signal of the previous peak. That results in a slight increase of the signal level for that event. These events introduce a tail on the high energy side of a signal peak that is not included in the spectral response model.

[2] the keyword here is pole-zero cancellation

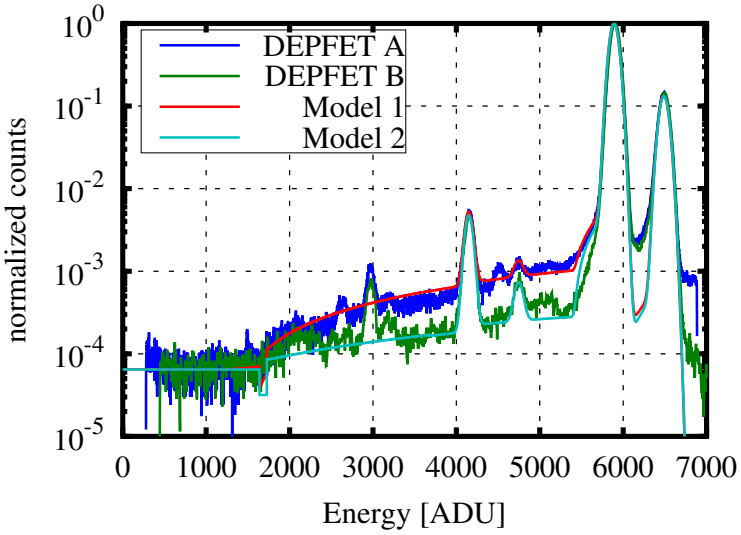

Figure 4.22.: Spectra of two DEPFET macropixel devices and the model functions 1 (moderate additional charge loss) and 2 (small additional charge loss) from section 3.3.4. As shown, the deviation of the measurement data can be attributed to an additional charge loss that is different for the two devices (1.5 percent for DEPFET A and 0.25 percent for DEPFET B).

As the low energetic tail was not fitted but the respective parameters were taken from the work of Scholze and Procop 2009, and Granato 2012 it is no surprise that the description is not perfect. Nevertheless, the model matches the measured data well.
The spectrum shows a number of fluorescence peaks, the most dominant at about at 2.95 keV and 3.2 keV. As the measurements were done in a dry air atmosphere, these peaks can be attributed to argon[3]. The feature around 5 keV is caused within the radioactive ^{55}Fe source. In that case the de-excitation of the Mn-K shell happens by a combination of fluorescence and Auger-process that leads to the generation of both a photon and an electron. While the electron can not pass the source's Be-window, the photons can reach the sensor. As these additional features were not included in the model function that deviation between model and measurement is expected.
The characteristics of the two measured devices are summarized in table 4.3. A deviation of the spectral response for energies higher than 2000 eV can be seen. As the respective model functions indicate, the explanation for that are charge losses that were more dominant for DEPFET A. The analytical models were derived in section 3.3. The peak-to-background values are summarized in table 3.2. With the model values from table 3.1 it can be suggested, that for DEPFET A about 1.5 percent of all events show charge losses while only 0.25 percent of all events measured with DEPFET B are affected. The explanation could be differences in the fabrication of these devices since they were manufactured on two different wafers, or a misplacement of the on-chip collimator that increases the amount of partial events.

[3]The argon fluorescence lines are at $K_\alpha = 2.96$ keV $K_\beta = 3.19$ keV.

	Energy Resolution	Peak-to-Background ratio			
Chip	FWHM (eV)	at 1 keV	at 2.5 keV	at 3.5 keV	at 4.5 keV
DEPFET A	125.1	14610±466	3614±60	2426±34	1359±20
DEPFET B	125.8	14818±758	7022±250	6309±213	4218±164

Table 4.3.: Summary of the measured characteristics. Energy resolution and peak height were extracted from a Gaussian, fit to the measurement data and are assumed to be "exact". The Background and its statistical fluctuation were evaluated over the stated energy ranges. The measurement error of the peak-to-background ratio is dominated by the fluctuations of the background and calculated from these.

Parameter	I_{drn}	V_{drn}	T	τ
Value	100 µA	-6 V	-20°C	1 µs

Table 4.4.: Standard operation parameters for the tested macropixel devices

4.3.2.3. Variation of DEPFET Parameters

To evaluate the device performance, four operational parameters were varied systematically. These are the drain-current I_{drn}, the drain voltage V_{drn}, the temperature T and the shaping-time τ. The respective standard values are summarized in table 4.4. The gain of a DEPFET is mainly defined by the current density in its conductive channel. A higher DC-current also causes a larger current change due to charge collected in the internal gate. Thus, with increasing DC-current, the gain increases. Since the gain directly affects the signal to noise ratio, the spectral performance is related to the current flow through the DEPFET channel. For the measurements shown in figure 4.23a, the current was varied from 80 µA up to 140 µA. To adjust the current, V_{sub} of the discrete drain-current readout and the external gate voltage were adjusted. As seen in figure 4.23a the higher gain enhances the energy resolution. The second parameter varied is the drain voltage. To keep the drain-current constant at a value of 120µA, the On-voltage of the external gate was adjusted for each drain voltage. The results are shown in figure 4.23b. The voltage applied to the drain directly influences the form of the internal gate. This is illustrated by the improvement of the energy resolution for drain voltages from -3 V to -5 V. The more negative drain-voltage repels electrons from the drain towards the source node. This distortion effectively reduces the internal gate area and thus increasing the amplification. For values below -5V down to approximately -7V only small changes of the energy resolution appear.
For even more negative drain voltages, a significant deterioration of the energy resolution can be observed. This can be attributed to a high field region formed in the transition region between drain and gate. Here charge carriers may be able to accumulate sufficient energy to generate additional charge carriers by impact ionization. (see e.g. S. Wölfel 2007). These charge carriers are equal to an additional leakage current which contributes to the noise and thus reduces the spectral performance of the device.

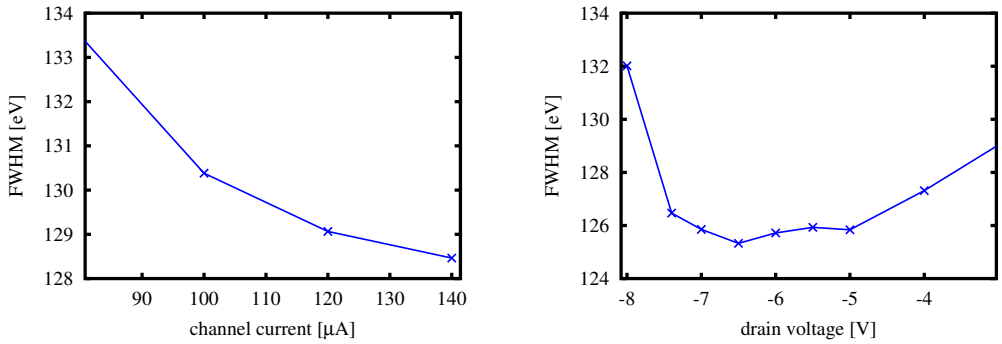

(a) (b)

Figure 4.23.: The gain of the DEPFET depends on the current through its conductive channel. As shown in a), an increase of the drain-current at constant V_{DS} improves the measured energy resolution. In b) the influence of the drain voltage on the energy resolution for constant drain-source-current is shown. The drain voltage affects the point of operation of the P-MOS-transistor and the shape of the internal gate. These two effects together cause the improved energy resolution in the range from -3 V to -6.5 V. The rapid decrease of the energy resolution beyond -6.5 V is attributed to impact ionization within a high field region at the transition region from the drain to the external gate.

4.3.2.4. Temperature Performance

To evaluate the spectral performance of the macropixel, the spectral resolution at different temperatures but otherwise constant operational parameters has been measured. The spectral performance for values from room temperature (20 °C) down to -20 °C is shown in figure 4.24a.

The overall behaviour is as expected. As discussed in section 3.2.4 the energy resolution is composed of fano noise, white noise, 1/f noise and leakage current noise. The noise of a silicon sensor was discussed in section 3.2.4. Using equation (3.22) and equation (3.26), the energy resolution of a silicon detector can be expressed by

$$FWHM = 2.355 \cdot w \sqrt{\sigma_{Fano} + \frac{a_1}{\tau} C_{det}^2 A_1 + a_2 C_{det}^2 A_2 + a_3 \tau A_3} \tag{4.5}$$

Here, a_1, a_2, a_3 represent the spectral density of white noise, 1/f- noise and leakage current noise while A_1, A_2, A_3 represent the respective filter-coefficients. The detector capacity is given as C_{det} and the shaping time as τ while the intrinsic Fano-noise is again σ_{Fano}. The noise values are chosen such that the respective unit is electrons. The conversion factor from a RMS noise value in electrons to the energy resolution in FWHM is the pair-creation energy w of silicon and the conversion factor 2.355 from the sigma of a Gaussian to its Full Width at Half Maximum. Especially the last term in this equation shows a large temperature dependence. If the weak temperature dependence of thermal-, 1/f- and Fano-noise is neglected. The energy resolution can be expressed

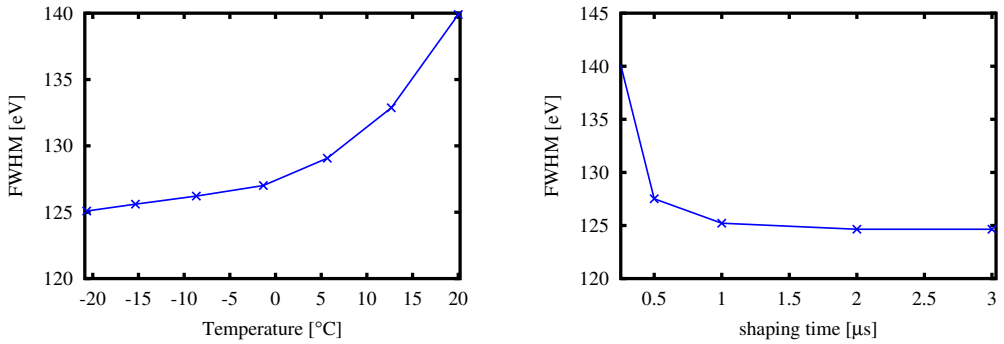

(a) **(b)**

Figure 4.24.: The operated devices provided a decent energy resolution of 140 eV already at room temperature. a) By cooling the device the leakage current decreases and the energy resolution improves. In addition, the energy resolution can be improved by changing the shaping time as shown in figure b). The steep deterioration for short shaping times is caused by the limited bandwidth in the order of 50 ns to 100 nsof the I-to-V converter used.

by

$$FWHM = \sqrt{k1^2 + k2 \cdot 2^{(-\frac{T-T_0}{7})}}. \tag{4.6}$$

In this case the value of $k1$ is the energy resolution with respect to Fano-noise, white noise and 1/f noise. At $T_0 = 20°\mathrm{C}$, the factor k2 is the product of the respective leakage current noise, shaping time and filter coefficient

$$k2 = 2.355 \cdot w \cdot a_3 \tau A_3. \tag{4.7}$$

The coefficient a_3 is given by equation (3.24). A least square fit of the measured data yields $k1 = [(125.15 \pm 0.1)\,\mathrm{eV}]^2$ and $k2 = [3959.7 \pm 73]\,\mathrm{eV}^2$ and shows a good agreement between model and measurement data. The contribution $k2$ of of leakage current noise to the energy resolution in terms of FWHM is

$$k2 = \frac{2I}{e} \cdot \tau \cdot A_3 \left(2.355 \cdot w\right)^2. \tag{4.8}$$

Using a filtering coefficient of $A_3 = 3.58$ for the semi gaussian shaper (Gatti et al. 1990) and the shaping time of $\tau = 1\mu\mathrm{s}$ the leakage current at room temperature is

$$I = 1.19\mathrm{pA}. \tag{4.9}$$

With the device area of 10 mm^2 this results in a leakage current of about 12 $\frac{\mathrm{pA}}{\mathrm{cm}^2}$. While this value is good it is within the expected range of 10 pA to 100 pA usually found for test-diodes.

Figure 4.25.: Layout of a Blindgate Pixel. The color code is equal to figure 4.3a. The red areas mark p+-implantations as drain, source and the surrounding drift-ring. The n+-implantations of blind and clear are marked in green, while the blue areas are the clear-gate and blind-gate contacts, implemented in the first poly-silicon-layer. The black donut-shape is the external gate, implemented in the second poly-silicon layer.

4.3.2.5. Shaping Time

The last measurement presented in this section is a variation of the shaping time of the semi-Gaussian shaper from 0.25 µs up to 3 µs. The measurement was performed at -20 °C. The drain-current as well as the applied voltages are equal for all measurements. The result is illustrated in figure 4.24b.
The best measured energy resolution of 125.1 eV is reached with a shaping time of 2 µs. In addition, the energy resolution at 1 µs and 3 µs only slightly deviates from this optimum value (125.2 eV and 124.6 eV). However, a rather fast degradation of the energy resolution for a shaping time of 0.5 µs and 0.25 µs can be seen. With the considerations of section 4.3.1.2.1 the explanation of this behaviour is as follows. The signal rise time is limited by the feedback resistor and the parasitic capacity on the printed-circuit-board. This reduces the signal bandwidth and, furthermore, reduces the output signal at short shaping times disproportional. For that reason, also the noise and furthermore, the energy resolution degrade faster than ideally expected.

4.3.3. Blindgate Pixel

The concept of the Blindgate Pixel is discussed in section 4.1.1.2. The actual layout of the investigated device is shown in figure 4.25. As the layout shows, the source node, surrounding the DEPFET is implemented asymmetrically to provide sufficient space for the required contact holes. In addition, the perfect cylinder symmetry assumed for the simulations discussed in section 4.2.2 is also broken by the clear-structure. Both these asymmetries limit the charge rejection in the insensitive state.
To evaluate the performance of the Blindgate Pixel, a series of measurements was carried out. The rejection and timing properties of the device were studied using an optical laser, while the spectroscopic performance was determined using a ^{55}Fe source as described in

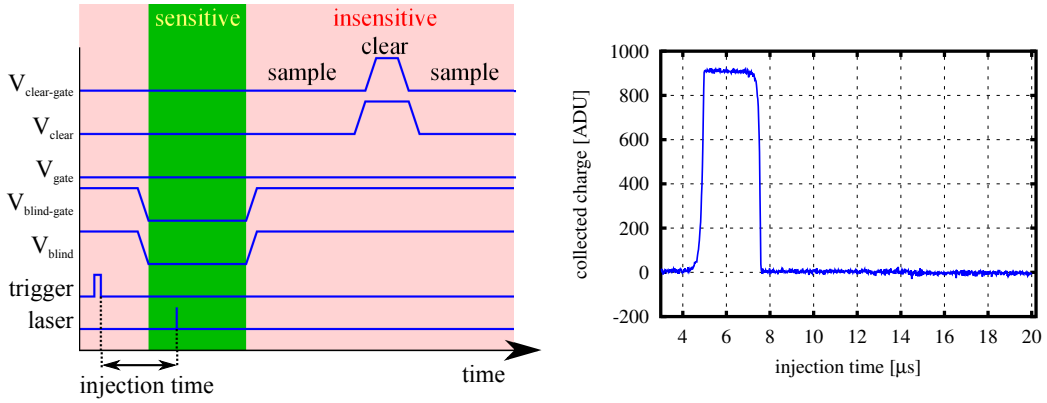

Figure 4.26.: The timing sequence for a proof of concept is shown in figure a). The device is active for a short, distinct illumination time, and insensitive otherwise. By sweeping the charge injection time over the complete sequence, the collection and rejection of the Blindgate Pixel can be evaluated. The result of this measurement is shown in figure b). The sensitive and insensitive time interval are clearly visible. Furthermore, the measurements demonstrate that a readout of a Blindgate Pixel in the insensitive state is possible.

section 3.3.1.

4.3.3.1. Laser Measurements

While spectroscopic measurements are mandatory to qualify a spectroscopic sensor, they only provide indirect access to the properties of a Blindgate Pixel, such as rejection ratio, charge losses and shutter transition time. To evaluate these characteristics, a pulsed laser was used.

4.3.3.1.1. Proof of Principle For this first measurement, a Blindgate Pixel was operated using the timing scheme shown in figure 4.26a. The device was set into the sensitive state for a distinct time interval by applying the blind and blind-gate low voltages. The time of charge injection was swept over the complete sequence length. For each injection time, two measurements were made, one with the laser injecting charge and one without laser injection to provide the baseline level, without charge injection. The differences of the two values for all injection times are shown in figure 4.26. Referred to the trigger, the device was sensitive from 4.5 µs to 7.8 µs and insensitive otherwise. The mean signal collected in the sensitive phase is 909 Arbitrary Digital Units (ADU), while the average signal in the insensitive phase is 0.2 ADU. This results in a rejection ratio of $2.2 \cdot 10^{-4}$. In addition, it is demonstrated that the pixel can be read out in the insensitive state.

4.3.3.1.2. Blindgate High Voltage As discussed in section 4.2.2, the blind-gate high voltage as well as the drain voltage are two of the crucial parameters for the charge

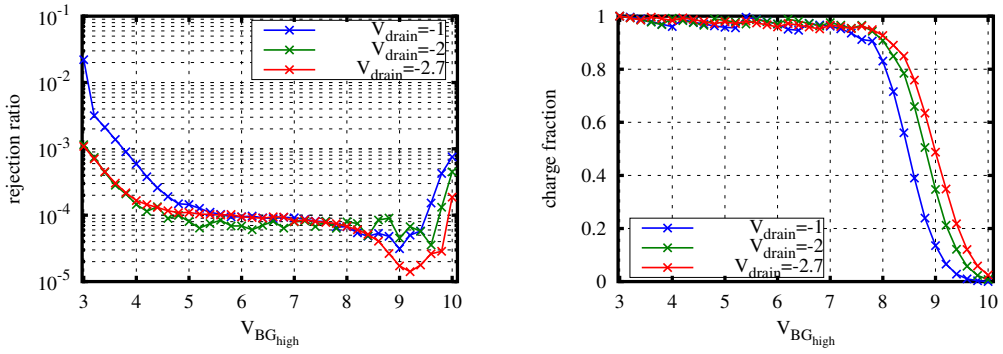

(a) **(b)**

Figure 4.27.: As discussed in section 4.2.2.1.2, the blind-gate high voltage is crucial for the functionality of the shutter. The influence of the blind-gate high voltage on the rejection is illustrated in a). For a voltage higher 4 V a rejection better $1 \cdot 10^{-3}$ was measured. Furthermore the rejection is affected by the applied drain voltage. While the rejection improves for higher blind-gate high voltages the retention of the device decreases for a voltage larger than 7 Vas shown in b). The loss mechanism is described in more detail in section 4.2.2.1.2.

rejection of a Blindgate Pixel. To evaluate the rejection ratio, charge was injected once while the device was sensitive and while the device was insensitive. To improve the statistics, 10 laser pulses were triggered in the insensitive phase. The measurement was done for blind-gate high voltages from 3 V up to 10 V. The ratio of the two observed signal levels in the sensitive and insensitive state, yields the rejection ratios shown in figure 4.27a. The measurement simultaneously provides the rejection ratio and the charge retention, i.e. the amount of collected charge lost from the internal gate over the source into the blind-contact. As shown in figure 4.27b the signal is nearly constant up to a blind-gate high voltage of 7 V and drops rapidly down to 0 with more positive voltages. The behaviour of rejection ratio and charge losses is in good agreement with the simulation result (see section 4.2.2). The existing deviations are attributed to the imperfect modeling of the doping profiles used for the simulations. The process simulator used only a basic set of diffusion equations that is insufficient for the exact modelling of boron p+-implantations. Especially the vertical extension of the p+-source implantation is usually underestimated in the process simulations. The deeper extension of the real source implantation partially compensates the deep-n implantation underneath and improves the barrier between internal-gate and blind-gate respectively. That in turn improves the charge retention of the device.

As simulations suggested, the drain-voltage has a crucial impact on the rejection ratio. However, for a blind-gate high voltage above 4V, even with a drain voltage of -1V, rejection ratios better than $1 \cdot 10^{-3}$ have been measured. Furthermore, no significant charge losses are observable for voltages lower than 7V. Thus, the operation window for the blind-gate voltage is in the range of [4V;7V].

The variation of the charge seen in figure 4.27 is attributed to instabilities of the laser

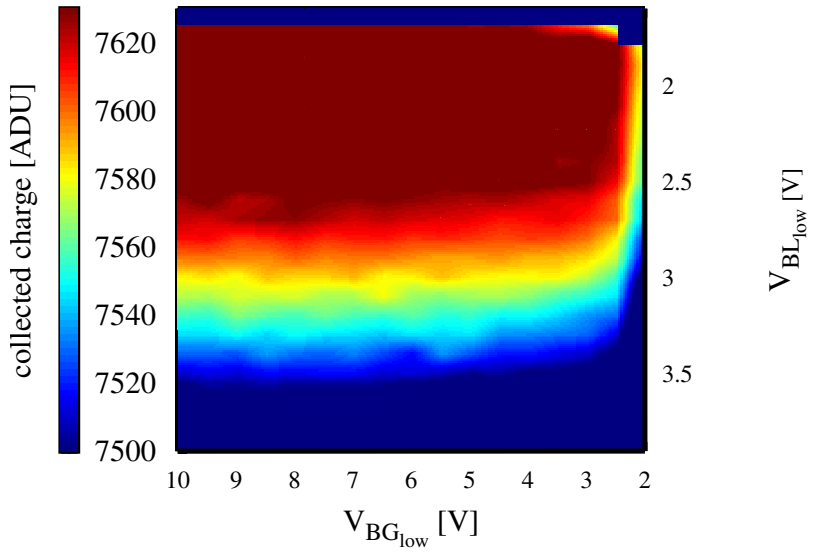

Figure 4.28.: The blind contact is a n+-implantation embedded in the blind-gate and surrounded by a deep-p implantation. A too negative blind may inject charge into the device, while a too positive voltage induces charge losses. This can be seen in the measurement data. For blind-voltages smaller 1.7 V electrons are pushed into the internal gate. That causes the step-like change from complete charge collection to no charge collection observed. Too positive blind-voltages on the other hand decrease the signal amplitude. The maximum signal is 7660 ADU. The red area marks a signal larger than 7620 ADU or respectively, if the maximum amplitude corresponds to complete charge collection, a collection ratio of 99.5 percent. The limit for this area is a blind-low voltage of 2.5 V. For more negative voltages, the blind-gate voltage has only minor effects.

diode intensity due to self-heating. Furthermore the pulse time for this laser is limited to not less than one µs. Since stability and pulse length are insufficient for the following measurements a different laser was implemented into the SPIX-II setup. It provides better stability and a pulse width of less than 100ps.
Despite the shortcomings caused by the laser used, the following conclusion can be drawn. The results from measurements and simulations are in agreement. Deviations are related to the layout of the real device and differences between real and simulated implantation profiles. The Blindgate Pixel design provides an operation window of approximately 3V for the blind-gate high voltage. The best measured rejection ratio is in the range of $1 \cdot 10^{-4}$.

4.3.3.1.3. Blind and Blind-gate Low Voltage The voltages applied to blind-gate and blind determine their attractiveness for electrons. As discussed in section 4.1.1.2, the device is set into the insensitive state by applying a sufficiently positive bias to both contacts. In contrast, the sensitive state requires a biasing that both avoids charge losses from the internal gate into the blind and at the same time prevents charge injection from the blind into the internal gate.

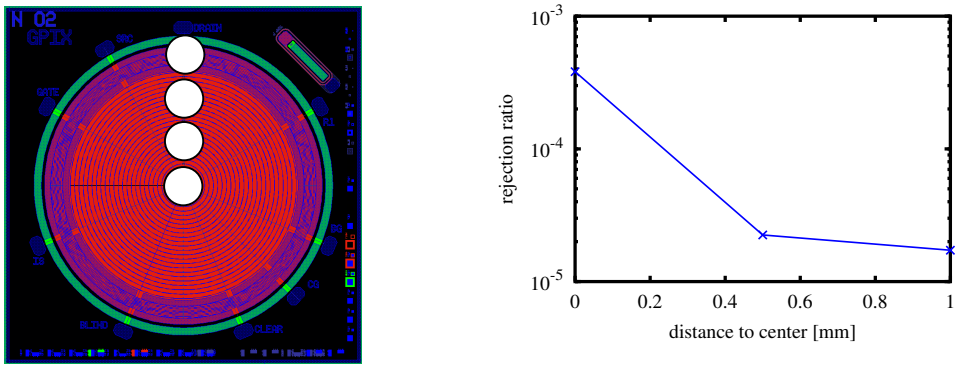

(a) (b)

Figure 4.29.: To evaluate the position dependency of the charge rejection and charge collection time, the laser spot on the sensor was focussed to about 500 µm. The spot size as well as the injection position were defined using a manual positioning stage. Three injection positions and the approximated spot diameter are illustrated in a). The charge rejection with respect to the injection position is shown in b). With optimized operational parameters, a rejection of $4 \cdot 10^{-4}$ for an injection directly above the Blindgate Pixel was measured. An injection further outside improves the charge rejection up to $2 \cdot 10^{-5}$. The improvement is related to the drift path of the incident charge through the device. For an injection off-center, the charge has to cross the complete width of the blind-gate leading to a smaller probability to be collected in the internal gate or respectively an improved rejection ratio.

A two dimensional parameter scan for both low voltages has been done to evaluate their influence. The measured charge signal is shown as color coded map in figure 4.28.
The maximum signal is 7660 ADU. The dark red area marks the region, at which the signal exceeds a value of 7620 ADU, which corresponds to a charge loss of less than a fraction of 5‰ (provided the maximum signal is equal to no charge losses). This criterion is met for -10 V $\leq V_{BG_{low}} \leq -3$ V and 1.7 V $\leq V_{BL_{low}} \leq 2.5$ V. The lower limit for the blind-gate low voltage is related to measurement constrains imposed by the Switcher-S, while the upper limit marks the point at which the blind-gate is no more capable to shield the blind and avoid charge losses.
Furthermore, to avoid charge losses, a maximum for the blind-low voltage of 2.5 V may not be exceeded. The lower limit is given by the injection of charge into the internal gate. That happens for a blind-low voltage below 1.7 V.
The measurement shows that the blind-gate low voltage has only small influence on charge losses or back-injection as long it is below -3 V, thus providing a comparably large operation window. However, the blind low voltage has a narrow operation window of approximately 0.8 V.

4.3.3.1.4. Position Dependence The SPIX-II setup is equipped with a manual x-y-stage that can be used for position dependent measurements. The sensor chip was equipped with an on-chip collimator. The central position on the chip as well as the

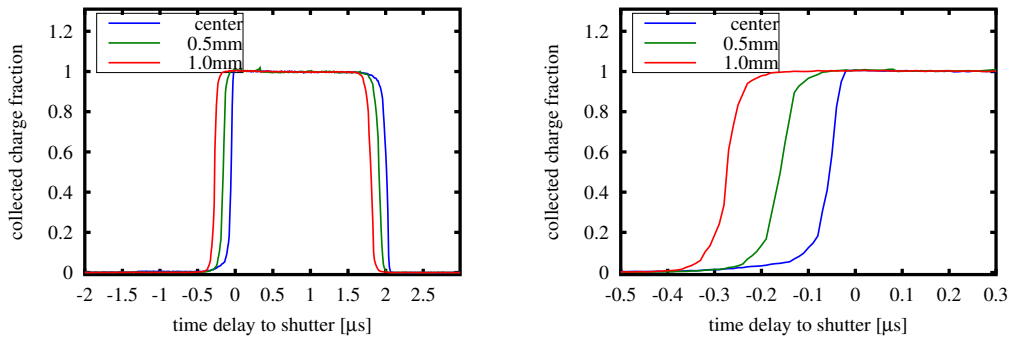

Figure 4.30.: Figure a) shows the measured signal for different injection times of the pulsed laser. The injection time was swept and is shown with respect to the shutter opening time. Incident charge requires several ns to drift through bulk and is successively either collected in the internal gate or discarded into the blind-contact. If the switching from the insensitive to sensitive happens while the charge still drifting is collected, only a fraction of the signal is collected in the internal gate. The measured signal dependency on the injection time is thus given by the collection time for incident charge carriers. For laser spot of 500 µm and injection in the center of the device, a collection time of 70.5 ns for a signal change from 10 % to 90 % amplitude was measured. For two injection positions further outside, rise times of 89.4 ns and 89.3 ns have been measured. A zoom in of the data is shown in b).

spot diameter were evaluated by moving the spot over the sensor and observing the signal amplitude on an oscilloscope. For the measurements shown here this spot diameter is in the range of 500 µm. With these constraints, charge was injected into the center of the device and at three equidistant positions with a distance of 500 µm as illustrated in figure 4.29a.
The most important properties of the built-in shutter are for once the rejection ratio shown in figure 4.29b. As can be seen the rejection ratio is worst for an injection directly above the Blindgate Pixel and improves to values as good as $2 \cdot 10^{-5}$. But even the worst rejection ratio of $5 \cdot 10^{-4}$ should be sufficient for most applications.
The second property that shows a position dependency is the measured shutter switching time. For each position, a sweep of the laser injection time was done. The measured signal amplitudes with respect to the shutter opening time are shown in figure 4.29.
The laser pulse has an extension of about 100 ps in time. As described its spacial extension is in the order of 500 µm for about 90% intensity. From the measurements it is possible to extract the switching time in terms of the signal rise time from 10% up to 90%. For the injection in the center the rise time is 70.5 ns. For the two measurement points further outside the rise time is 89.4 ns and 89.3 ns[4]. The observed rise time is primarily caused by the charge cloud extension and the time required to fully collect

[4]For the fourth measurement point the rise time is strongly distorted by the large drift times in the edge region of the device.

its electrons in the device. For the injection above the center, the charge drifts towards the DEPFET from all directions leading to a shorter charge collection time and thus a faster rise time. Similarly, the larger rise time for the off-center charge injection is related to the size of the charge cloud. As the measurement data also shows, a shift of the sensitivity in time with respect to the injection position can be observed that is related to the drift time of the charge cloud from its point of origin into the readout node.

4.3.3.2. Spectral Measurements

In this section, a series of spectroscopic measurements using a Blindgate Pixel in macropixel configuration will be presented. In the following, the spectral performance will be characterized by the energy resolution of the K_α peak of ^{55}Fe and the peak-to-background ratio for a background evaluated over different energy ranges as it was done in section 4.3.2.1.
The measurements can be divided into two categories. The first will henceforth be referred to as "normal operation" of a Blindgate Pixel. For these measurements, the device was operated similar to a standard DEPFET, i.e. with inactive blind and blind-gate, to study the effects of misfits and confirm the model derived in section 3.4. The second set of measurements, named "gated operation", were done to study the influence of the built-in shutter on the spectroscopic performance and to have a direct comparison between normal and gated operation.
The section starts with a direct comparison of normal and gated operation before investigating the timing properties of the single modes in more detail.

4.3.3.2.1. Direct Comparison One interesting result of this section is shown in figure 4.31. Here, two spectra recorded with the Blindgate Pixel once in normal and once in gated operation are compared directly. For both modes, an illumination time of 14 µs was chosen alongside a sampling time of 1.5 µs and a flat top of 1.7 µs, including a 700 ns clear.

While the built in shutter has neither a positive nor a negative effect on the energy resolution, a decrease of the flat shelf by a factor of 10 as can be seen. The reduction is related to the use of the built-in shutter, that efficiently suppresses any kind of misfits as indicated e.g. by the total absence of negative misfits.
However, the built in shutter still has a lowered peak to background ratio when compared to the time continuous measurements presented in section 4.3.2, as the effective shutter switching time is limited by the charge collection of the DEPFET.

4.3.3.2.2. Spectral Performance in Normal Operation The spectral performance can be quantified in terms of energy resolution and peak to background ratio. For a normal DEPFET, the two main drivers for these are the sampling and illumination time. The first determines the ENC of the device, while the latter is crucial for the ratio of correctly reconstructed events to misfits events. In the following, sweeps of both times are presented.

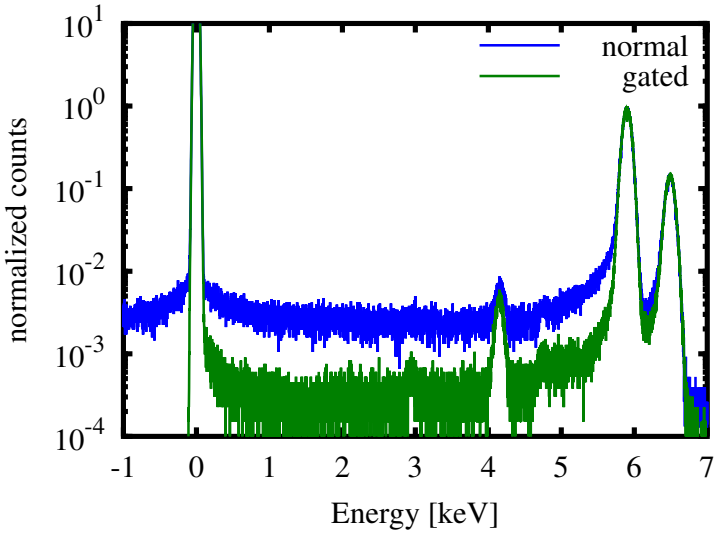

Figure 4.31.: Shown are two spectra recorded with the same Blindgate Pixel DEPFET device, once operated like a normal DEPFET without the use of the built-in shutter and once with the rejection of charge collection during the device readout. As the measurements indicate, the rejection of misfits in gated operation provides a reduction of the flat shelf by a factor of 10 for an illumination time of 14 µs.

4.3.3.2.3. Dependency of the Spectral Performance on Sampling Time The sampling time of the trapezoidal weighting function directly affects the noise of the spectroscopic system. In addition, the sampling time also determines the time the device is sensitive to misfit events. Thus, by varying the sampling time, both parameters are changed simultaneously. An example for such a variation from 375 ns up to 7 µs is shown in figure 4.32.

For these measurements the illumination time was set to 14 µs. The flat top was kept constant at a value of 1.7 µs. As can be seen for a sampling time as short as 375 ns, which is equal to a total processing time of less than 2.4 µs, an energy resolution of 147 eV and a peak to background ratio of 520 : 1 was measured.

By increasing the sampling time, the noise reduces. This in turn improves the energy resolution of the spectroscopic system. On the other hand, the longer sampling time increases the probability for misfits, which is the reason for the observed degradation of the peak to background ratio.

4.3.3.2.4. Dependency of the Spectral Performance on the Illumination Time While the previous measurements already demonstrate the dependency of the peak to background value on the ratio of sampling t_s and illumination time t_i, further analysis of the time dependency were done by varying the illumination time and keeping the signal processing at a constant value. The sampling time was set to 1 µs for the measurement data shown in figure 4.33. As seen in figure 4.33a the energy resolution shows a rather

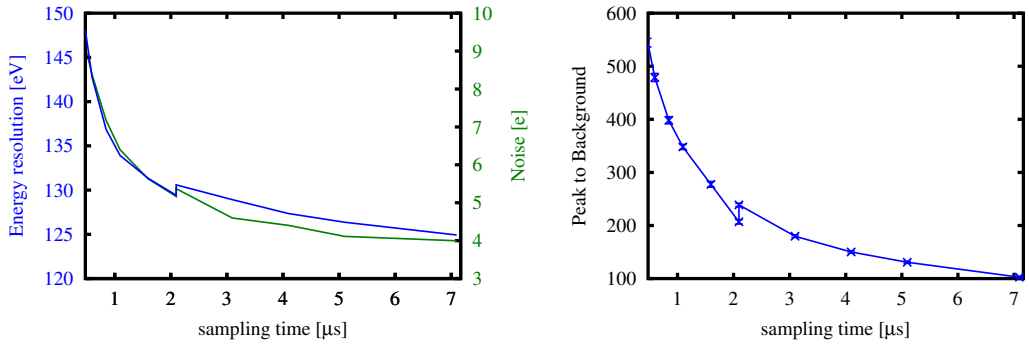

(a) (b)

Figure 4.32.: a) shows the dependency of electronic noise, expressed as ENC, and energy resolution, in terms of FWHM, on the sampling time. The trapezoidal weighting determines the electronic noise of a DEPFET and thus the energy resolution of the spectroscopic system. At the same time a longer sampling increases the probability for misfit events and reduces the peak to background ratio as shown in b). The steps present in the measurement data for a sampling time of 2 µs is caused by a change of the ASTEROID's pre-amplifier gain required to adjust the output voltage range of the ASIC

complex behaviour on the illumination time. The steep increase for very short integration times is directly related to the low peak to background ratio shown in figure 4.33b, leading to a broadening of the performed gaussian fit. At an illumination times of 7 µs the background induced by misfits is as small as 100:1. If the integration time is further reduced, this ratio decreases down to 45 at the shortest illumination time.

According to the relations derived in section 3.4, the peak to background ratio of a DEPFET sensor read out on demand depends on illumination time, sampling time, effective clear time, the leakage current and the electronic noise of the detector system and the detected count rate.

The leakage current of the device can be extracted either from the energy resolution, by neglecting the short illumination times, or from the ENC values. Since the FWHM values are affected by the high misfit background the complementary values derived from the ENC are used. The ENC is then 5.26 e^- and the leakage current is 0.199 $e^-\mu s^{-1}$. To estimate the count rate, it is necessary to estimate the probability for an event in the respective collection time. With a given spectrum, the probability for an event can be found by dividing the number of events by the counts of the zero peak. The former quantity is estimated by neglecting negative events and summing over the range $5\sigma_{ROD} < E < \infty$ where the σ_{ROD} defines the width of the zero peak due to electronic noise and leakage current. The number of counts in the zero peak is found by summing all counts in the range $-5\sigma_{ROD} \leq E \leq 5\sigma_{ROD}$. To avoid any unknown timing effects, the estimation for the count rate only includes the last four measurements with an illumination time of 100 µs and above. The estimated count rates for these measurements are summarized in table **??** giving a mean value of 1025 s^{-1}.

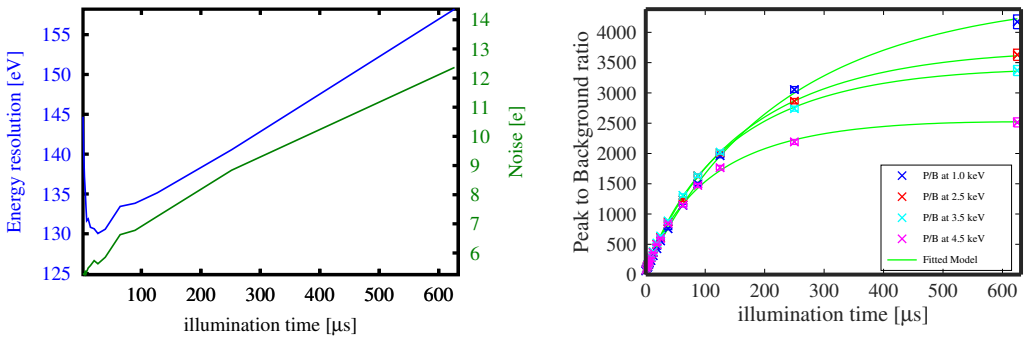

(a) **(b)**

Figure 4.33.: a) and b) show the energy resolution and peak to background ratio measured for a Blindgate Pixel operated like a normal DEPFET and illumination times from 0 up to 625 µs. The energy resolution reduces with longer illumination because of the larger amount of leakage current electrons collected in this time while the peak to background ratio improves due to the decreasing probability for misfits with increasing illumination time.

The height of the K_α peak is given by

$$P = \frac{\eta cr \cdot t_c}{\sqrt{2\pi \left(\sigma_{fano}^2 + ENC^2 + I_{lc} \cdot t_c\right)}}, \tag{4.10}$$

and the background can be expressed by

$$B = \eta cr \cdot \left(\left(t_s + t_{cl_{eff}} + \eta_{cr} t_c \left(t_s + t_{cl_{eff}}\right)\right) \left(\frac{1}{E_{K\alpha}} + \frac{p_{K\beta}/p_{K\alpha}}{E_{K\beta}}\right) + t_c \cdot \frac{P/B_{max}^{-1}}{\sqrt{2\pi}\sigma_{fano}} \right). \tag{4.11}$$

Dividing these two quantities provides the model for the peak to background ratio in dependency of the illumination time. The unknown parameters are the reachable peak-to-background ratio $\frac{P}{B}max$, and the effective clear time t_{clear}. The device timing included an overhead time outside the signal shaping, so that even with an illumination time of zero, the collection time is larger than zero. Furthermore, it has to be taken into account, that negative misfit events can fully contribute to the signal peak. Denoting the sum of overhead time and time for these negative misfits as t_n, the collection time t_c is the sum of illumination time t_i and t_n, $t_c = t_i + t_n$. The value of t_n is left as additional fit parameter. The measured peak-to-background ratios and the fitted curves are shown in figure 4.33b. The value of t_n has to be equal for all four curves. In contrast, $\frac{P}{B}max$ depends on the energy and is left free for each curve. The same was done for the effective clear time $t_{clear_{eff}}$ to account for the non-linear nature of the clear process. The fit-parameters are summarized in table 4.5 and table 4.6.

The measurement data show, that a DEPFET sensor read out on demand is in principle capable to reach a good spectral performance. However, misfit events deteriorate the spectral response. Especially at fast timings a large fraction of events contributes to

Fit Values for Normal Operation	
Parameter	Value
noise [e^-]	5.3
leakage current [$e^-/\mu s$]	0.199
t_n [μs]	-2.895 $\pm$ 0.007

Table 4.5.: The table lists the used electronic noise, leakage current and the fitted value of t_n.

Fit Values for Normal Operation				
	at 1 keV	at 2.5 keV	at 3.5 keV	at 4.5 keV
$t_{clear_{eff}}$[μs]	0.831 $\pm$ 0.001	0.535 $\pm$ 0.001	0.450 $\pm$ 0.001	0.458 $\pm$ 0.002
$\frac{P}{B} max$	16543 $\pm$ 492	9175 $\pm$ 163	7676 $\pm$ 120	4929 $\pm$ 73

Table 4.6.: Shown are the fitted timing and peak-to-background values for normal operation

misfits leading to peak-to-background ratios of 50:1 and worse.
From these values, a linear approximation of the effective clear time $t_{clear_{eff}}$ for the peak-to-background in the 1 keV regime of 830 ns can be drawn. For spectral simulation a value of 450 ns for the linear approximation of the clear time appears a reasonable choice.

4.3.3.3. Spectral Performance in Gated Operation

As seen in the previous section, misfits have a large impact on the spectroscopic performance of a DEPFET based sensor. In this section the improvement offered by a Blindgate Pixel due to the rejection of misfit events will be evaluated. Furthermore limitations of the achievable performance will be pointed out.
To assess the effect of the shutter, the measurements of section 4.3.3.2.2 are repeated with active shutter.

4.3.3.3.1. Dependency of the Spectral Performance on the Sampling Time By varying the shaping time from 375ns up to 7μs, it is possible to improve the energy resolution from 145eV to 123eVas seen in figure 4.34a.

In contrast to the measurements in normal operation shown beforehand, the peak to background ratio shows only a minor dependence on the sampling time and is, for the chosen illumination time, in the order of 3200:1-3600:1. The observable dependency is related to the increased height of the K_α peak with improving energy resolution.
The measurements show that the peak to background ratio for a Blindgate Pixel is independent from the chosen sampling time and thus demonstrates the rejection of misfits events.

4.3.3.3.2. Dependency of the Spectral Performance on the Illumination Time As shown in figure 4.35, the active shutter improves the peak-to-background ratios of the tested device. In addition, even the high background observed at short illumination times

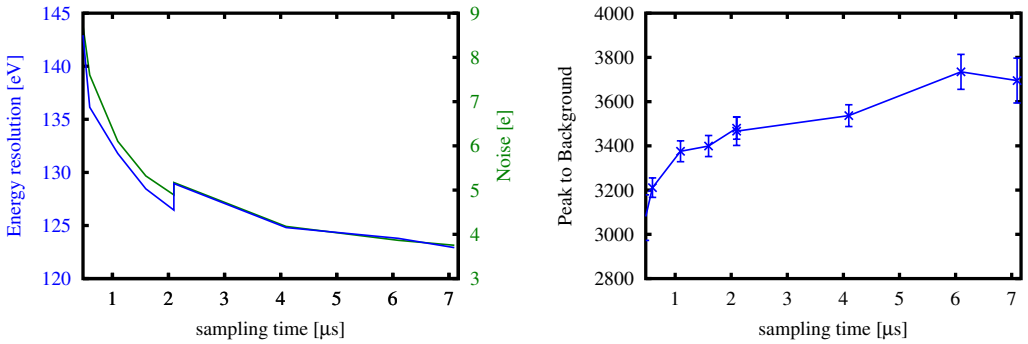

(a) **(b)**

Figure 4.34.: a) The use of the built-in shutter to suppress misfits has no effect on the electronic noise. The rejection of misfits, however, causes the peak to background ratio to be nearly independent from the sampling time b). The remaining dependency is primarily caused by the improved energy resolution and thus increasing peak height of the $^{55}Fe\ K_\alpha$ peak.

does not affect the energy resolution of the sensor. These measurements demonstrate that the rejection of misfits improves the spectral performance. The improvement in terms of peak to background ratio drops from roughly 10 at short signal integration times down to a factor of 3 for longer signal integration times.

It is again possible to approximate the dependency of peak to background ratio on the illumination time by an analytical function. The absolute limit is given by the charge generation and collection process. In contrast to the normal operation the only time for a partial collection of charge is the effective switching time of the shutter that is a convolution of the shutter response time and the charge drift time. If the signal dependence on the charge arrival time is approximated by a linear function, the peak-to-background ratio can be modelled by

$$\frac{P}{B} = \frac{t_c}{\sqrt{2\pi\left(\sigma_{fano}^2 + ENC^2 + I_{lc}\cdot t_c\right)}} \frac{1}{t_{shutter}\left(\frac{1}{E_{K_\alpha}} + \frac{p_{K\beta}/p_{K\alpha}}{E_{K_\beta}}\right) + t_c \cdot \frac{P/B_{max}^{-1}}{\sqrt{2\pi}\sigma_{fano}}}. \tag{4.12}$$

The fit-values have similar degrees of freedom as for the data evaluation in normal operation. Again, the device was operated with a certain overhead time that in not included in the illumination time. Furthermore, it is expected that events that arrive shortly after the switching of the built-in shutter will still contribute to the signal peak. The sum of these two times is denoted as t_u and the collection time is then $t_c = t_i + t_u$. Furthermore, each peak-to-background value and the approximated time for misfits are left for optimization. The characteristic time constant is actually twice the shutter rise-times t_{sr} as events are possible when switching from the collection into the insensitive state and vice versa. The fitted values are summarized in table 4.8.

If the optimum peak-to-background ratio $\frac{P}{B}max$ is only caused by intrinsic processes on the entrance window side of the sensor, it would be expected, that the values of the same device are independent from the operation mode. Although the values match

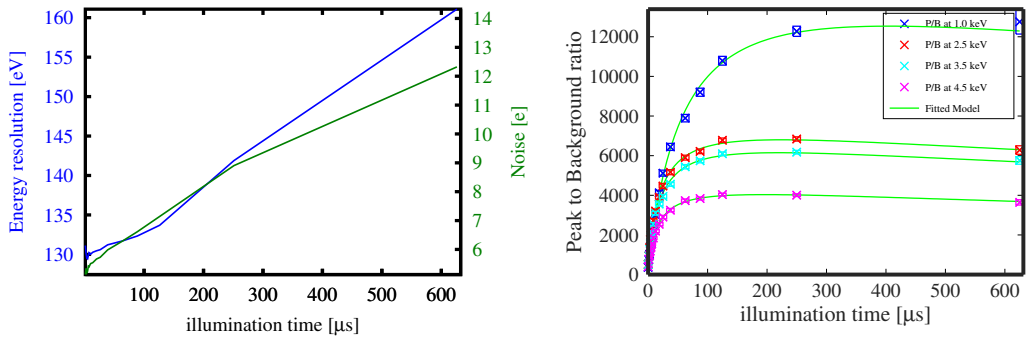

(a) **(b)**

Figure 4.35.: a) and b) show the energy resolution and peak to background ratio measured for a Blindgate Pixel. This time the built-in shutter is active while the signal is processed. The illumination time is again varied from 0 up to 625 µs. The dependency of electronic noise and energy resolution is still subject to the larger amount of leakage current electrons collected. While the peak to background ratio is, depending on the illumination time by up to one order of magnitude larger, a dependency on the illumination time is still observed. This dependency is a result of the limited switching time of the built-in shutter.

Fit Values for Gated Operation	
Parameter	Value
noise [e^-]	5.3
leakage current [e^-µs]	0.199
t_u [µs]	-1.644 ± 0.008

Table 4.7.: The table lists the used electronic noise, leakage current and the fitted value of t_u.

Fit Values for Gated Operation				
	at 1 keV	at 2.5 keV	at 3.5 keV	at 4.5 keV
$2t_{sr}$[µs]	0.1449 ± 0.0003	0.1001 ± 0.0003	0.1068 ± 0.003	0.1330 ± 0.004
$\frac{P}{B}\,max$	18184 ± 232	8750 ± 92	7885 ± 84	5083 ± 67

Table 4.8.: Shown are the fitted timing and peak-to-background values

within 3 standard deviations, especially the deviation of the peak-to-background ratio in the low energy appears large. Although the operating conditions were similar, they were not identical. Since already smallest changes of the charge collection behaviour are capable to introduce large changes onto the peak to background ratio the deviation may be caused by those.
What is even more interesting is, that the peak-to-background ratio around 1000 eV is noticeably larger than what is expected from section 3.3.4 and also larger than the values found for the two macropixel devices. There is a viable explanation. The first assumption is that the charge losses present for both macropixel measurements actually

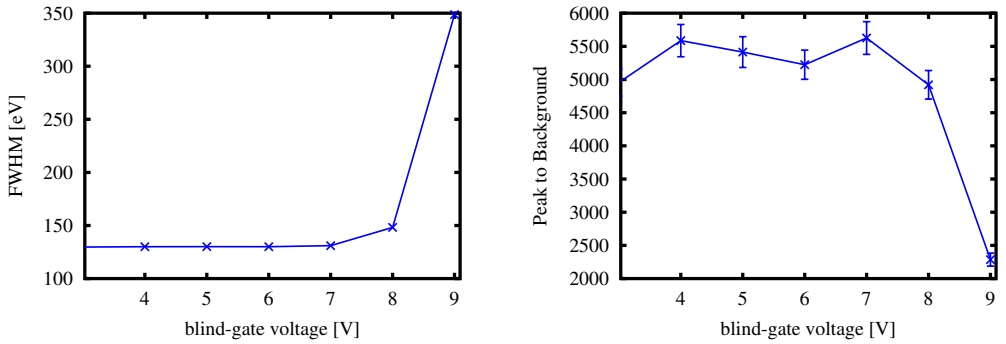

(a) (b)

Figure 4.36.: It was already demonstrated, that the blind-gate high voltage has a major effect on the device performance as it influences the charge rejection and the charge retention. For spectroscopic applications, even a rejection of a few percent would cause the average collection of a few undesired electrons per incident photon. The corresponding noise contribution is given by Poisson statistics and proportional to the square root of the electron number. As the measurement data show, the rejection ratio is sufficiently large to neither affect the energy resolution (left) nor the peak-to-background ratio. However, the loss of already collected charge, induced by a too positive blind-gate-high voltage drastically decreases both, energy resolution and peak-to-background ratio.

extend down to even lower energies and reduce their peak to background ratio. In the derivation of the flat shelf, the simplification was made that the energy deposition for events generated in the silicon-dioxide and silicon-nitride can be approximated by a simple flat shelf. As discussed there, especially for photoelectrons generated in these top layers (see figure 3.13c), this simplification appears to be too coarse. If the photoelectron distribution is approximated by the analytical function, a peak to background value in the order of 22000:1 would be expected. Overall, this discrepancy is a hint into the direction that a re-evaluation of the spectral response model may be required, which is, however, beyond the scope of this thesis.

4.3.3.3.3. Blindgate High Volage and Charge Losses From simulations ((see section 4.2.2)) as well as laser measurements ((see section 4.3.3.1)) it is already known that a too small blind-gate high voltage causes an insufficient charge rejection. Furthermore, it was discussed in section 4.2.2 that a too large value of the blind-gate high voltage induces the loss of charge from the internal gate toward the blind-structure.

Both these effects should be observable in spectroscopic measurements. Unfortunately, the lower limit for the applicable blind gate high voltage as provided by the SPIX-II setup is 3 V. The corresponding variation from 3 V up to 9 V is shown in figure 4.36 and shows the dependency of energy resolution as well as peak to background ratio. With a drain voltage of -5 V, the rejection ratio even for the smallest blind-gate high voltage is in the order of $1 \cdot 10^{-3}$. Thus the effect of an insufficient charge rejection can

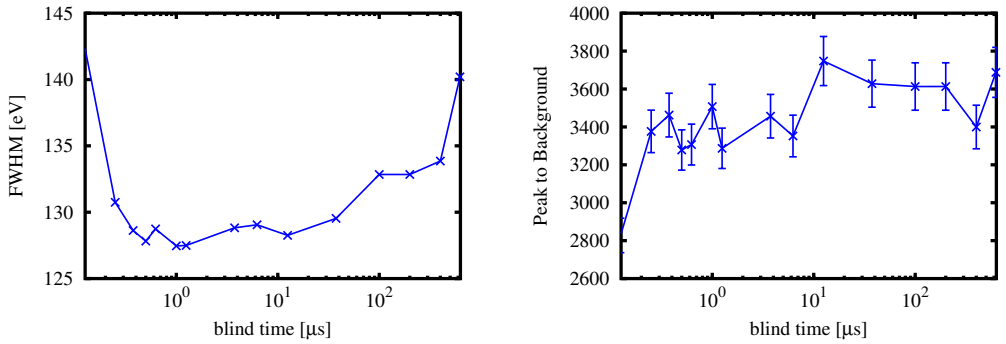

(a) **(b)**

Figure 4.37.: The switching from sensitive into the insensitive state showed a parasitic incoupling on the source node. To evaluate the minimum time required for that disturbance to settle the time between switching into the insensitive state and the start of the readout cycle was varied. a) illustrates the energy resolution in term of FWHM and b) the corresponding peak to background ratio. As the measurement shows, a too short settling drastically affects the spectral performance. Since the source node shows an rc-like settling behaviour, a sampling of the signal level with a too short settling time results in a decreased signal amplitude thus reducing the spectral performance. Accordingly, a too long settling times causes the collection of leakage current and incomplete photon events which also reduces the spectral performance.

not be determined. Nevertheless, the effects of charge losses caused by a too large blind-gate high voltage are evident. For a blind-gate high voltage above 7 V a steep increase of the energy resolution and a decrease of the peak to background ratio for voltages can be observed. For the given geometry a blind-gate high voltage in the range from 3V up to 7V can be applied without a significant change of the spectroscopic performance.

4.3.3.3.4. Blind Time Sweep After switching from the sensitive state into the insensitive state, a minimum time is required for the source node to settle, before the device can be read out. In addition, it is valuable to study the effects of a long insensitive state on both energy resolution and peak-to-background ratio. To investigate both effects, it is sufficient to vary the time between switching from the sensitive into the insensitive state and the device readout. The result of such a measurement is shown in figure 4.37.

As the measurement shows, starting the readout very shortly after the switching process worsens the energy resolution. The cause is a parasitic modulation of the DEPFET channel-conductivity influenced by the switching of blind and blind-gate. In source follower readout the modulation results in a sudden change of the source node voltage followed by an current-dependent exponential settling. Before the readout starts, the voltage must be sufficiently stable. Otherwise, as the measurements show, the ENC and thus the energy resolution worsens. While the energy resolution is mostly constant and below 130 eV for a blind time from 1 µs up to 50µs, it increases for longer settling times. Two effects may be causing that behaviour. The first is leakage current. While bulk

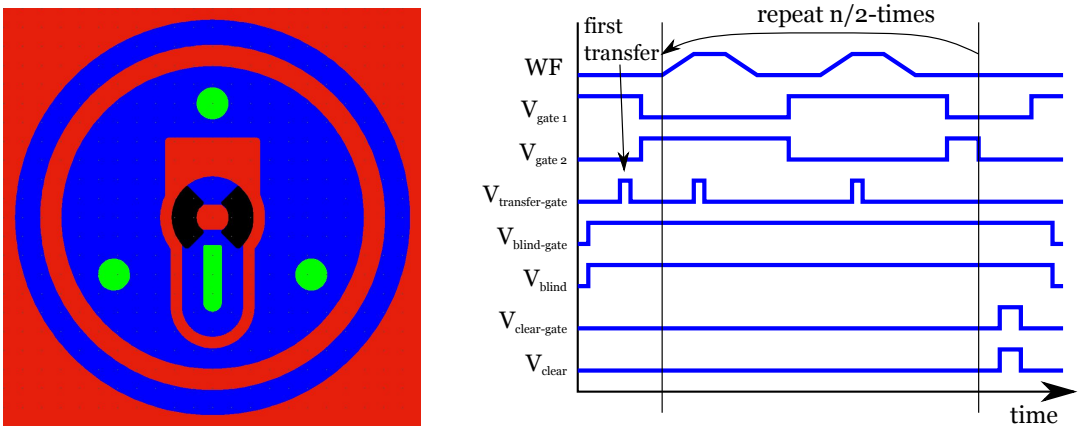

Figure 4.38.: The Blindgate Pixel layout provides the option to exchange the cut-gate DEPFET with a compact-RNDR device (Bähr 2010). A RNDR-DEPFET is capable to read collected charge carriers multiple times by moving the charge between its two internal gates. By averaging the signals, it is possible to reduce the noise according to the central limit theorem. The readout sequence is shown in b). In contrast to a standard RNDR device the combination with a Blindgate Pixel avoids distortion by charge incident during the device readout.

generated leakage current cannot reach the internal gate when the device is insensitive, electron hole pairs generated at the interface close to the internal gate are still attracted and collected in the internal gate. Also this should be a small contribution it is obviously not negligible.
The second effect is the increasing probability that a photon arrives in the insensitive state the longer that state lasts. While most of the photons charge will be discarded, a small fraction of it is able to reach the internal gate. As long as the rejection is sufficiently large, these events generate a small contribution to the noise equivalent to an additional leakage current.

4.3.4. Blindgate Pixel Repetitive Non Destructive Readout

The DEPFET principle can be modified to implement additional features as e.g. the built-in shutter studied in the course of this thesis. Another property that was subject to extensive investigations is the Repetitive Non Destructive Readout (RNDR) principle (S. Wölfel 2007; Bähr 2010). A RNDR device is capable to read the charge collected in the internal gate multiple time. By averaging the single statistically independent measurements it is possible to improve the noise performance down to sub-electron levels. The noise ENC_{RNDR} scales thereby with

$$ENC_{RNDR} = \frac{ENC_{ROD}}{n_{RNDR}} + N_{lc} \cdot \left(\frac{1}{2} - \frac{5}{6n_{RNDR}} + \frac{n}{3} \right). \tag{4.13}$$

Here ENC_{ROD} is the noise of a single readout on demand, N_{lc} the number of leakage current electrons collected between two consecutive readout cycles and n_{RNDR} the number

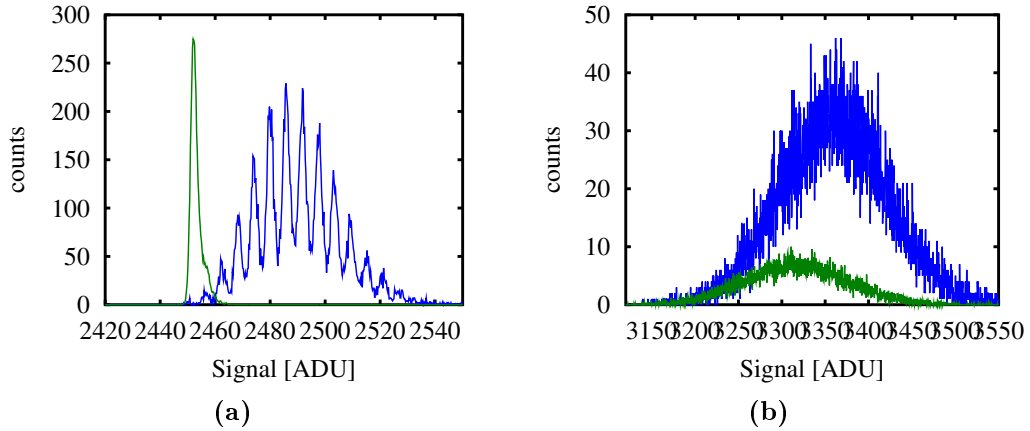

Figure 4.39.: a) A Blindgate PixelRNDR device was operated as indicated in figure 4.38b without using the shutter. The multiple readout of injected charge provided a noise of 0.25. In b) charge was injected between two readout cycles. As shown, the artificial leakage current corrupts the single-electron resolution.

of performed readouts. Since the topology of the cut-gate DEPFET forming the read node of the Blindgate Pixel is near identical to the so-called Compact-RNDR structure it was an obvious step to combine the two, forming the first Gated-RNDR device. The layout is shown in figure 4.38a.
As the layout picture shows, especially the asymmetry of the source node is drastically larger than for a standard Blindgate Pixel. Likely for this reason it was e.g. not possible to find an operation point in the standard drain center configuration.
Nevertheless, the device was successfully operated by exchanging source and drain. The timing of a Blindgate Pixel RNDR device is composed of an illumination time and a readout sequence schematically shown in figure 4.38b. The device readout is comprised of the known weighting function repeated n_{RNDR} times. During the flat top, charge is transferred from one DEPFET to the other by applying a sufficient positive voltage to the transfer gate. By applying a positive voltage to blind and blind-gate the device is set insensitive. Accordingly, it is again possible to operate the device like a RNDR DEPFET without built-in shutter by not switching these voltages.
For the measurements shown in the following, a sampling time of 2 µs was applied. The flat top was 1.25 µs including a charge transfer of 100 ns and the source node settling of about 1 µs. To minimize leakage current, the device was cooled down to -60 °C.

4.3.4.0.1. Rejection of Bulk Charge Similar to the Blindgate Pixel tested in the previous section the device was operated both with and without rejection of charge collection during the device readout. In both cases charge was injected in the dedicated illumination time before the readout started. The corresponding response for normal operation is shown in figure 4.39a while figure 4.40a illustrates the result for the gated operation. The baseline signal is shown in green while the laser signal is shown in blue. The distinct

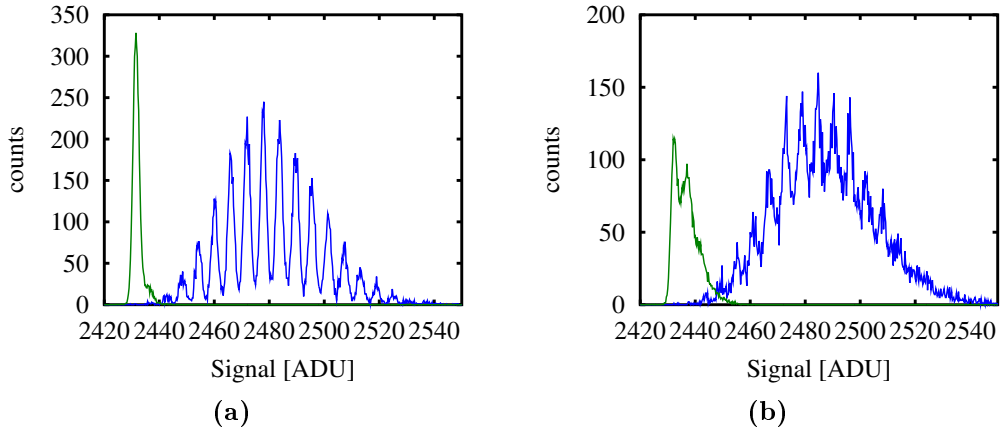

Figure 4.40.: a) The same Blindgate PixelRNDR device as in figure 4.39 was operated using the shutter and a noise of 0.2 e^- was reached (a)). The artificial leakage current degrades the noise performance to 0.35 e^- (b)) but the single electron resolution is maintained.

peaks are related to the quantization of electrons in the sensor and the sub-electron noise resolution.
As the measurements show, the laser signal follows a Poisson distribution while the baseline is composed of a peak at zero e^- and a smaller peak at one e^- with a relative ratio of 10 % to the main peak. The composition of the baseline is subject to the dark current of the device. As single electrons can be discriminated, it is possible to directly calibrate the device using the position information of the single peaks. The read noise for a single readout is then in the order of 2.5 e^- and the RNDR noise for 200 readouts is 0.25 e^- without the built-in shutter and 0.2 e^- with the shutter active during readout. In addition, a second measurement with charge injection between the single readout cycles was done. The mean number of electrons injected between the single readout cycles is 7 e^-. The results for normal operation is shown in figure 4.39b. As the measurement shows, the extremely good noise performance is corrupted by the artificial leakage current generated by the laser and the noise performance degrades to about 20 e^-ENC. If however, the built-in shutter is active during the Repetitive Non Destructive Readout, it is still possible to identify the single electron peaks, since that artificial leakage current is suppressed. However, the noise performance degrades to 0.35 e^-.

4.3.4.0.2. Large Signal Response For the measurement shown in figure 4.41 multiple measurements were taken and put together. In each measurement the number of incident photons was varied by sending multiple trigger signals to the laser. In this way it was possible to vary the number of generated charge carriers from 0 e^- up to 1400 e^-. In figure 4.42a to figure 4.42d enlargements of the signal response over 20 e^- centered around 10, 110, 1010 and 1310 e^- are illustrated. Although the peak width increases with electron number, a single electron resolution was achieved over the whole range of 1400 e^-. The degradation of the noise performance with increasing electron number

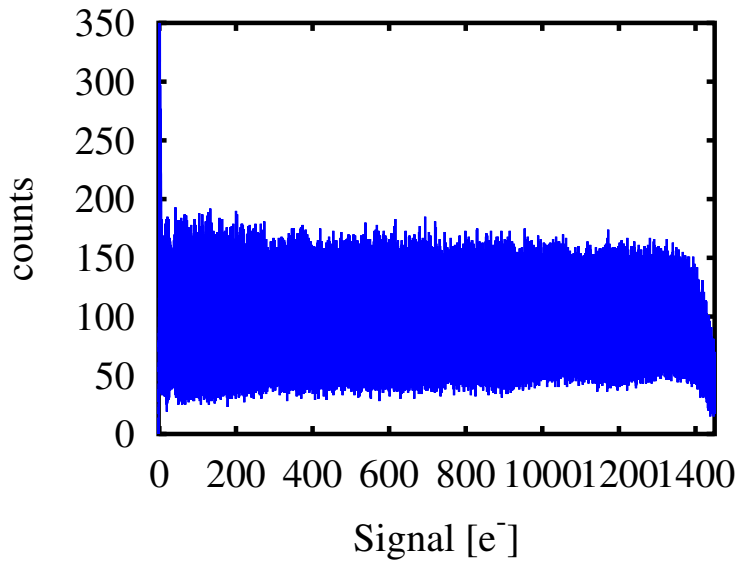

Figure 4.41.: The figure shows a measurement where the number of charge pulses during the device illumination was increased successively thus slowly increasing the number of electrons injected. Here, the complete measured range of electrons is shown. Cutouts are shown in figure 4.42.

may have one of two explanations. Depending on the bias conditions, electrons have a certain probability to cross the barrier formed by the drain surrounding the RNDR DEPFET. The more electrons collected in the internal gate, the large the probability to lose an electron. The effect of that charge loss would be similar to an additional leakage current. The second explanation would be a limited efficiency of the charge transfer. Depending on the electron number, a small fraction of charge may stay in the read DEPFET. While the mean number of electrons transferred per readout cycle, a statistical fluctuation dependent on the electron number would be introduced leading to a reduction of the achievable resolution. Which effect dominates is at the moment not known. An optimization of the device implementing a more symmetrical source node should prevent charge losses. The transfer efficiency may be improved by adapting the implantation profiles. However, that requires a more thorough analysis of the effect, e.g. using three dimensional device simulations and is left for future work.

4.3.4.0.3. Further Steps For long term measurements, a drift of the signal baseline and gain was observed. While the first could be compensated by a common mode correction, the latter would require a constant re-calibration of the device that is at the moment not feasible. The drifts were attributed to temperature changes in the order of 3 Kcaused by the climatic chamber used to cool the device to -60 °C. Furthermore the chamber inflicts mechanical vibrations on the measurement setup. Since the SPIX-II provides its flexibility by multiple mechanical connections it is also prone to variations of the contact

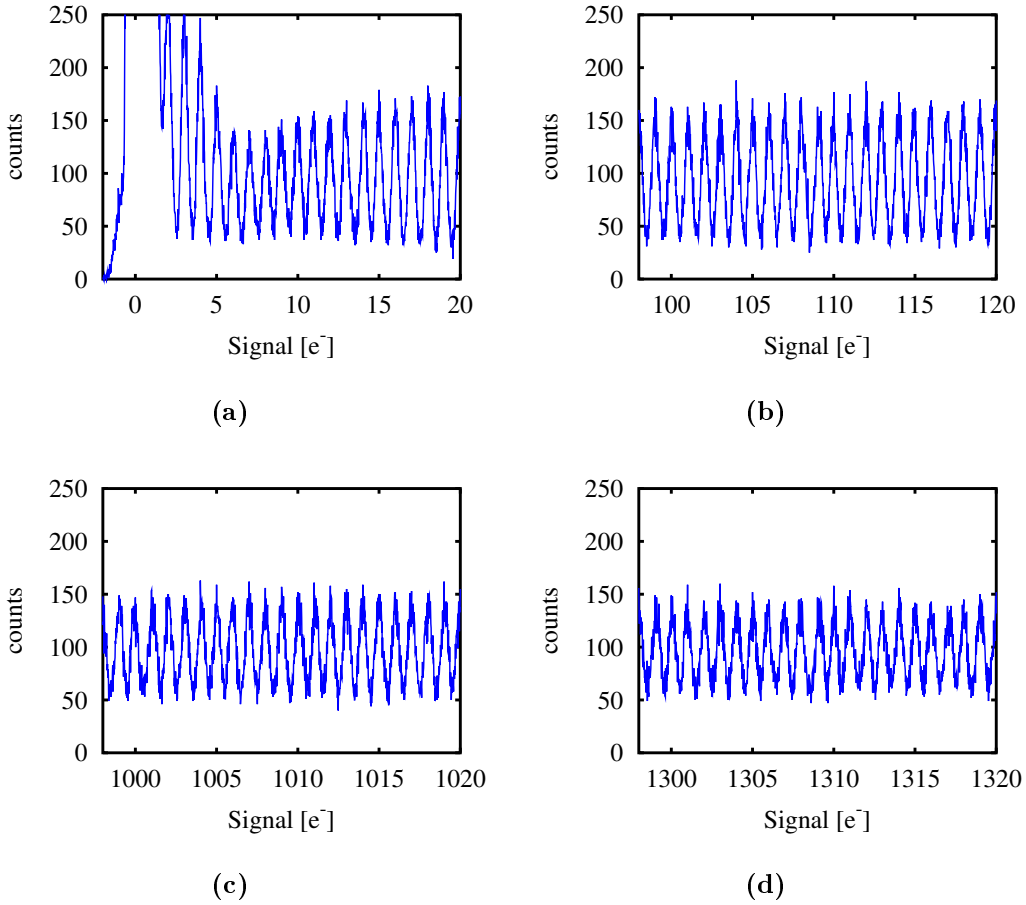

Figure 4.42.: The cutouts show that the tested Blindgate Pixel RNDR device is capable to provide single electron resolution for small numbers of electrons (a) as well as larger electron numbers (b,c and d). The measured range is up to about 1400 e^-.

resistance caused by those vibrations. While that seemed to have no effect on previous measurements, even slightest changes of gain or baseline level will hamper the single electron resolution especially for larger electron numbers [5]. To overcome these issues, an optimized setup is required.

4.3.5. Infinipix

The concept of the Infinipix is discussed in section 4.1.2.2 and section 4.2.3. The layout of the investigated wide gate Infinipix structure is shown in figure 4.43a.
The device geometry, especially the size of source and drain differ from the simulated optimum values due to layout constraints. In addition, the vertical extension of the device is limited by the clear structures, which were also not included in the simulations.

[5] A gain change of 1 ‰ would change the position of e.g. the 1000 e^- peak by 1 e^-, leading to an overlap with either the peak at 999 e^- or 1001 e^-.

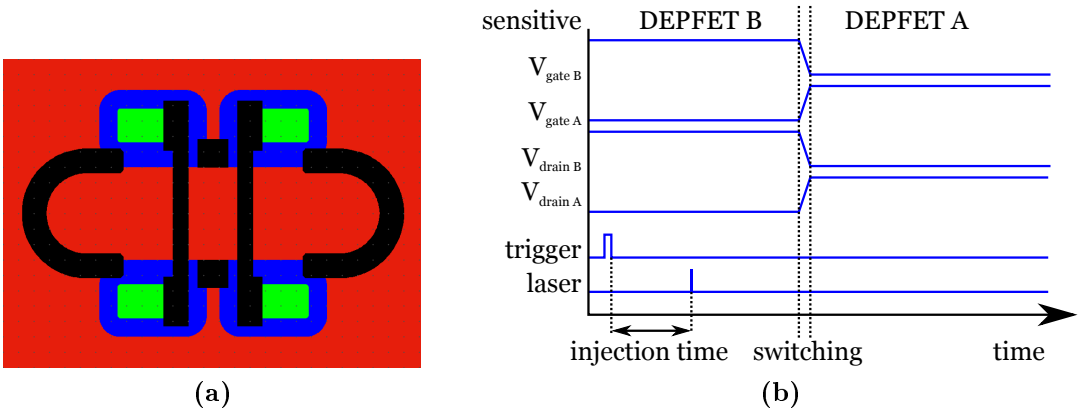

Figure 4.43.: Based on the simulations discussed in section 4.2.3 the layout shown in a) was developed. To operate the device, the timing scheme shown in b) was used.

To test the concept of the Infinipix, first measurements were carried out on a single pixel device. The tested single-pixel has a diameter of 100 µm and is surrounded by a single p-guard ring to suppress surface leakage currents. The device was operated applying the timing scheme shown in figure 4.43b. Hence always one DEPFET is insensitive and can be read out, while the other collects incident charge carriers. Setting both DEPFETs into the off state simultaneously is problematic as the ASTEROID current-source always draws the set current. Disabling the current-flow through the device leads to an undefined state of the current-source and a undesired swing of the source node. To avoid this state it is necessary to always keep one DEPFET in the "On"-state.
The following prove-of-concept consists of a calibration using the known ^{55}Fe-source (see section 3.3.1) to provide a reference for the following measurements. The primary driver for the performance are the timing properties or, more exactly, the switching time between the two DEPFETs of one pixel and the rejection ratio of the device. Again, these properties were investigated using a pulsed laser.

4.3.5.0.1. Calibration To provide a reference for the deposited number of electrons the single-pixel was illuminated with the already known ^{55}Fe source. Since the chip size is only 150 µm^2 the spectrum shows a large number of unrecognized split events at the device border. These cause the comparably high shelf in the spectra shown in figure 4.44a. In addition, the measurements were recorded at room temperature with a non-optimized switching electronic.
However, a number of conclusions can be drawn from the calibration. First of all the principle of redirecting charge while reading the insensitive DEPFET is functional. Furthermore, the absence of any pronounced features on the negative side of the zero peak indicate negligible negative misfits and event. As a low rejection would cause a second peak beneath the zero peak, this in turn indicates a rejection better $1 \cdot 10^{-2}$.

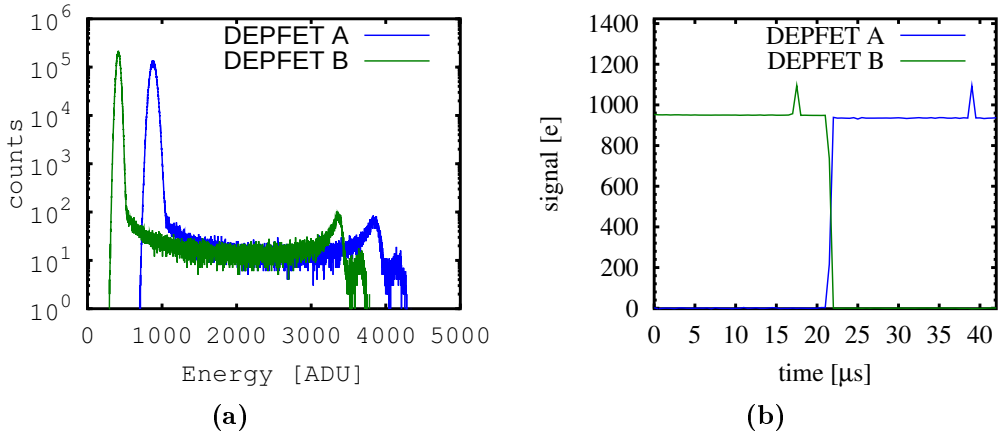

(a) (b)

Figure 4.44.: a) shows the spectra of the two DEPFETs of the tested Infinipix. Also noise and offset are different, the signal amplitude is equal within less than one percent. The timing sequence was evaluated using a fast ps laser. As b) shows, the switching of the sensitivity is functional as intended.

4.3.5.0.2. Switching Time and Charge Rejection To evaluate the switching time, charge was injected using a fast laser pulse. The injection time was swept with respect to a trigger signal at the begin of the sequence. The result of this sweep is shown in figure 4.44b. Easily visible ist the switching of the sensitivity from DEPFET B to DEPFET A. In addition, an artifact at 16 µs and 39 µs can be observed. For these measurements, the laser was not focussed, resulting in a near flat field illumination of the whole chip. The artifact shows up parallel to the clear of the insensitive pixel. Due to the large positive voltage applied in this time interval, the potential distribution inside the sensor is modulated, resulting in a larger amount of charge collected in the sensitive DEPFET. Measurements carried out with a focussed laser, using matrices or macropixel devices should not show such effects.
To measure the switching time in more detail, the respective time interval was evaluated with a timing step of 10 ns. The result is shown in figure 4.45a. A switching from 1% sensitivity to 99% sensitivity happens in less than 200 ns.
Furthermore, the measurements can be used for a first estimation of the signal rejection. In figure 4.45b, the measurement data are normalized to the sum of the signals in both DEPFETs and plotted using a logarithmic scale for the y-axis. As shown, the average relative signal collected in the insensitive pixel is in the order of $5 \cdot 10^{-4}$.

4.3.5.0.3. Overflow To investigate the charge retention between the two DEPFETs, the timing scheme was kept, but the amount of injected charge was increased by triggering the laser multiple times. This was done once while DEPFET B was sensitive (see figure 4.46a and figure 4.46b) and once while DEPFET A was sensitive (see figure 4.46c and figure 4.46d).
The average amount of injected charge with a single laser pulse is 470 e^-. The figure

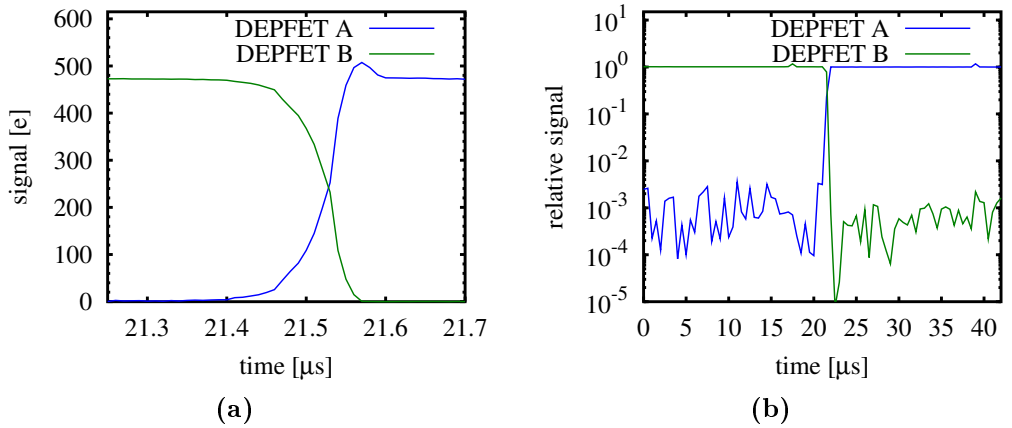

Figure 4.45.: a) A closer look at the switching time shows that the switching happens in less than 200 ns while the charge collected in the insensitive pixel is as low as $3 \cdot 10^{-4}$ as shown in b).

4.46 a) and c) illustrate the signals in the respective DEPFET as well as the sum of both signals. On the other hand figure 4.46 b) and d) show the amount of charge collected in the insensitive pixel with respect to the overall amount of injected charge with a logarithmic scale for the y axis. For low amounts of charge the rejection is again in the range of $5 \cdot 10^{-4}$. With increasing charge the rejection worsens and more signal is collected in the insensitive pixel. The sum of both signals, however, still increases linearly. This gives rise to the assumption that the for increasing number of charge carriers charge moves from the sensitive pixel over the source into the insensitive pixel. That path is especially likely since the technology was optimized for the DSSC for X-FEL, providing signal compression by an overflow region below the DEPFET source node. As the first Infinipix prototypes are processed in the same technology, the barrier between the two DEPFETs is hampered and limits the charge handling capacity.
Even with the imitated charge handling capacity caused by the technology, a separation of the two DEPFETs better $5 \cdot 10^{-4}$ for up to 40 laser pulses was measured. With the calibrated signal of 470 e^- for a single pulse that is equal to $N_{overflow} = 40 \cdot 470$ $e^- = 18800$ e^- or 68.8keV. Taking into account the typical energy range of X-ray telescopes from 0.1 keV to 15-20 keV, the available range appears sufficient for applications in astrophysical X-ray spectroscopy.

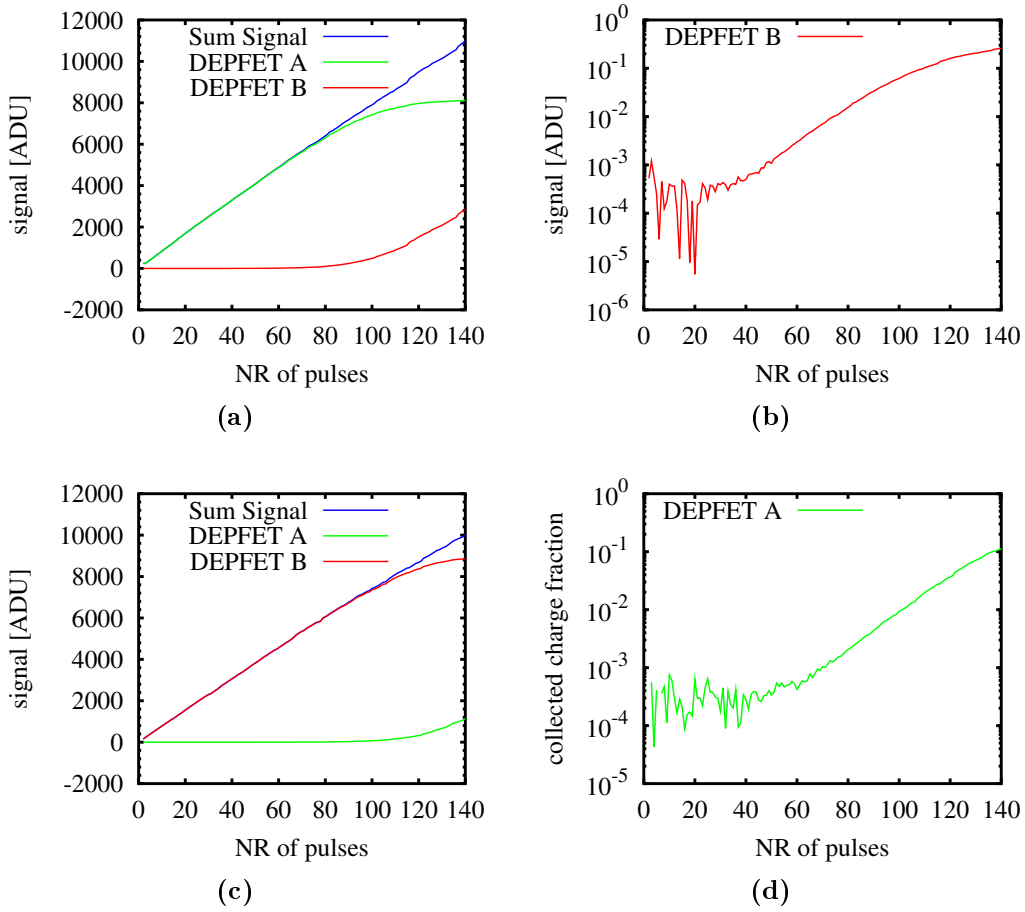

Figure 4.46.: To evaluate the charge rejection with respect to the amount of incident charge, the laser was pulsed multiple times. To provide a sufficient dynamic range, the gain of the ASTEROID was set to the possible minimum. The results for a charge injection while DEPFET A was sensitive are shown in a) and b) while the data for an injection while DEPFET B was sensitive are illustrated in c) and d). A the shown, the signal of the respectively sensitive DEPFET increases linearly with the number of laser pulses until a certain threshold. From this point on, an increasing fraction of charge is collected in the actually insensitive pixel, while The sum of the two signals still increases linearly. The comparably early overflow is cause by the production technology.

4.4. Spectral Simulations

In recent years, a rather large variety of different DEPFET types was developed (see e.g. section 3.2 and section 4.1.1). Although all these are based on the same working principle (given by the silicon base material and the DEPMOS-transistor) there is a variety of features, which is provided by distinct DEPFET variants. Some of these features can be used to improve the spectral response for a DEPFET read out on demand as a function of readout time. In the following sections, the effect of different timings on the spectral response of three DEPFET types will be considered. This will be done for the standard DEPFET as discussed in section 3.2. Furthermore the spectral properties of a so-called Gateable DEPFET and a Storage DEPFET will be discussed. A Gateable DEPFET implements an electronic shutter into a DEPFET pixel, while Storage DEPFET devices provide an additional storage area (see section 4.1.1). These devices are selected as they are suggested to improve the spectral performance at fast timings, that is required to achieve highest count-rates with optimized spectral performance. Details about layout, implementation and properties of these devices are provided in section 4.1, section 4.2 and section 4.3.
For the spectral simulations the following simplifications are introduced. The effects of a X-ray mirror optics, which would be present in a real experimental environment, as well as the sensors quantum efficiency are neglected and suggested to be unity over the considered energy range. Furthermore, the spectral response of the material is always represented by a normalized Gaussian. The width is given by the Fano- and electronic noise. The simulations include a simplified model of the time response of the respective DEPFET type. In particular, any entrance window related effects as discussed in section 3.3 are neglected. The entrance window especially affects the spectral response for low energetic photons. For the discussed science case (see section 2.1.3), the identification of a relativistically broadened iron line at around 6 keV is necessary. In the discussed timing regime, the effects of the entrance window are small and will thus be neglected.
In the next sections, the output signal and the spectral response of the different DEPFET concepts with respect to their timing is introduced. At that point it will become obvious that the Gateable DEPFET concept provides only minor benefits for high count-rate, high throughput applications. For that reason the spectral response to typical X-ray spectra is discussed only for two types of DEPFET.

4.4.1. Time Dependent Spectral Response DEPFET Devices

In section 3.2.5 and section 3.4 the signal weighting of DEPFET devices and their timing dependent spectral response was discussed. The typical readout-on-demand method applied to a DEPFET leads to a distortion of the signal by misfit events and the possibility that one photon may contribute twice to the energy spectrum. This was illustrated in terms of the energy signal $E_1(t)$ and $E_2(t)$ and results in the formulation of the timing dependent spectral redistribution TF.
All simplifications discussed therein are applied here as well. The radiation source is considered to have a non-varying emission probability and the dependence of the output

signal on the arrival time for the first signal sampling, the effective clear time $t_{clear_{eff}}$ as well as the second sampling is considered to be linear. For the Gateable DEPFET and Storage DEPFET the shutter switching times will be described in a similar manner.

4.4.1.1. Standard DEPFET

The signal of a DEPFET can be described in terms of the signal $E_1(t)$ in this frame and the signal $E_2(t)$ in the following frame. In that way, the time dependent signal response of a single pixel inside a matrix was derived in section 3.2.5. While the time dependence considered in section 3.2.5 can be implemented e.g. for the simulation of matrices, the following sections are explicitly only suggested for the simulation of single-pixel devices. For that reason and to provide a better context for the following sections, the discussion made in section 3.2.5 will be repeated partially. For the start, the distinction of t_{mux} and t_i made in figure 3.15 shown on page 81 is meaningless for a single pixel device. Therefore, these distinct intervals are replaced by a common time interval. The output signal of a DEPFET single pixel can then be represented by

$$E_1(t) = E_{ph} \cdot \begin{cases} 1 & 0 < t < t_1 \\ (1 - (t - t_1)/t_{sample} & t_1 < t < t_2 \\ (t3 - t)/t_{clear} & t_2 < t < t_3 \\ 1 & t_3 < t < t_4 \\ (t_5 - t)/t_{sample} & t_4 < t < t_5 \end{cases}, \tag{4.14}$$

in the first readout cycle followed by

$$E_2(t) = E_{ph} \cdot \begin{cases} 0 & 0 < t < t_2 \\ 1 - (t3 - t)/t_{clear} & t_2 < t < t_3 \\ 1 & t_3 < t < t_5 \end{cases}, \tag{4.15}$$

in the next readout cycle as illustrated in figure 4.47a. The timing is divided in an illumination time t_i, the two sampling times t_{sample}, the clear time t_{clear} and the settling time t_{set}. The ends of the different time intervals are marked by $t_1 - t_5$. In addition, the time t_5 marks the end of the first and the beginning of the successive readout cycle. For the simulations, the clear time is suggested to be as short as possible, thus an additional dead time due to the clear is neglected. The spectral response of a DEPFET can be derived from these two equations (see section 3.4 for more details). If the clear process is approximated linearly, the spectral response $\frac{\mathrm{d}p_D}{\mathrm{d}E}$ can be represented by

$$\frac{\mathrm{d}p_D}{\mathrm{d}E} = \begin{cases} \eta_{cr} t_c & E = E_{ph} \\ \frac{\eta_{cr} t_{shelf}}{E_{ph}} & -E_{ph} < E < E_{ph} \\ \eta_{cr}(t_{set} + t_{sample}) & E = -E_{ph} \end{cases}, \tag{4.16}$$

where η_{cr} is the count rate, $t_c = t_i + t_{set} + t_{sample}$ the collection time and $t_{shelf} = t_{clear} + 2t_{sample}$ the time events contribute to the shelf. The equation indicates, that even

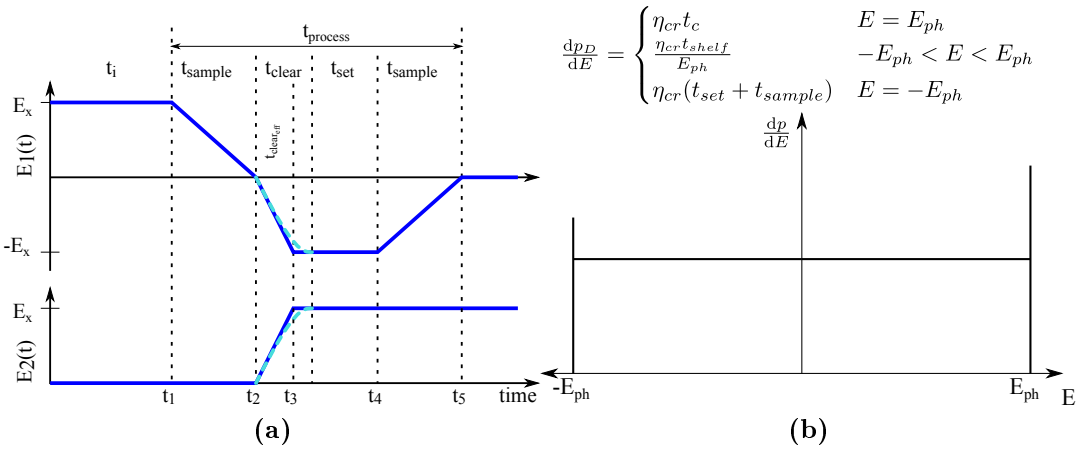

Figure 4.47.: Figures a) shows the signal in tow consecutive readout cycles, caused by the signal charge corresponding to an incident photon collected at the time t while Figures b) illustrates the resulting timing related spectral redistributions for a standard DEPFET.

for an illumination time of zero, the collection time is larger than one and thus a signal peak is always present. However, with such an operation mode, the flat shelf due to misfits, will be a significant contribution to the spectral response shown schematically in figure 4.47b.

4.4.1.2. Gateable DEPFET

As discussed in section 4.1.1 a Gateable DEPFET provides a built-in shutter capable to suppress the charge collection in the internal gate by deviating charge into the blind-contact. Besides their use for precise illumination timing, the obvious use of this shutter for a spectroscopic device is the rejection of charge collection during the readout and thus the negation of misfit events. Provided the rejection ratio is sufficiently large, misfits are fully suppressed. However, charge arriving while the shutter is active will be lost and can thus not be detected. The switching from sensitive to insensitive and reverse requires the time t_{switch}. Charge arriving during this time will only be partially removed from the device. Suggesting a linear dependence of arrival time and detected energy during the switching process, the signal can be modelled by

$$E_1(t) = E_p h \cdot \begin{cases} 1 & 0 < t < t_1 \\ (1 - (t - t_1)/t_{switch} & t_1 < t < t_2 \\ 0 & t_2 < t < t_3 \end{cases} \tag{4.17}$$

in the first frame and

$$E_2(t) = E_p h \cdot \begin{cases} 0 & 0 < t < t_3 \\ (t - t3)/t_{switch} & t_3 < t < t_4 \end{cases} \tag{4.18}$$

for the signal in the following frame. A schematic of that is shown in figure 4.48a. The figure shows the 4 time intervals, that are the charge collection time, the two switching

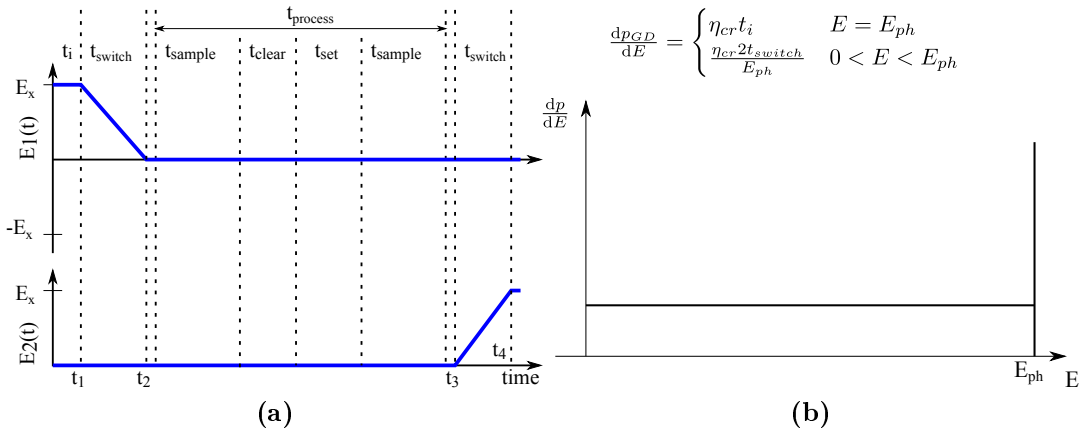

Figure 4.48.: Figures a) shows the signal in tow consecutive readout cycles, caused by the signal charge corresponding to an incident photon collected at the time t while Figures b) illustrates the resulting timing related spectral redistributions for a Gateable DEPFET.

times and the readout time. The end of each interval is marked by the the times t_1 to t_4. These are different to those of a standard DEPFET. The resulting spectral response of a Gateable DEPFETis illustrated in figure 4.48b. The corresponding equation is

$$\frac{\mathrm{d}p_{GD}}{\mathrm{d}E} = \begin{cases} \eta_{cr} t_i & E = E_{ph} \\ \frac{\eta_{cr} 2 t_{switch}}{E_{ph}} & 0 < E < E_{ph} \end{cases} . \tag{4.19}$$

In contrast to a standard DEPFET, the spectral response of a Gateable DEPFET is completely governed by the flat shelf if the illumination time is zero.

4.4.1.3. Storage DEPFET

In addition to a built-in shutter, a Storage DEPFET provides an additional storage region per pixel. Two examples for Storage DEPFET concepts are presented in section 4.1.2. Although the implementation of the storage area is different, both devices can be modelled using the same assumptions. The main difference of the two devices is that for the GPIX device charge is preserved in the adjacent storage area and must be transfered from this region into the DEPFET. For the Infinipix design, the charge is already collected in the DEPFET. However, here the region of charge collection has to be transferred from DEPFET one to DEPFET two. In both cases a transfer is required that takes the time $t_{transfer}$. Events collected during this time interval will be distributed over two successive readout cycles. It is again assumed that the relation of deposited Energy and time is linear. Furthermore, while charge collected in the storage region should not be affected by a clear of the internal gate, charge carriers arriving during the clear time may be removed from the device. Taking all that together, the time-signal relation can be expressed by

$$E_1(t) = E_{ph} \cdot \begin{cases} 1 & 0 < t < t_1 \\ (1 - (t - t_1)/t_{transfer} & t_1 < t < t_2 \end{cases} \tag{4.20}$$

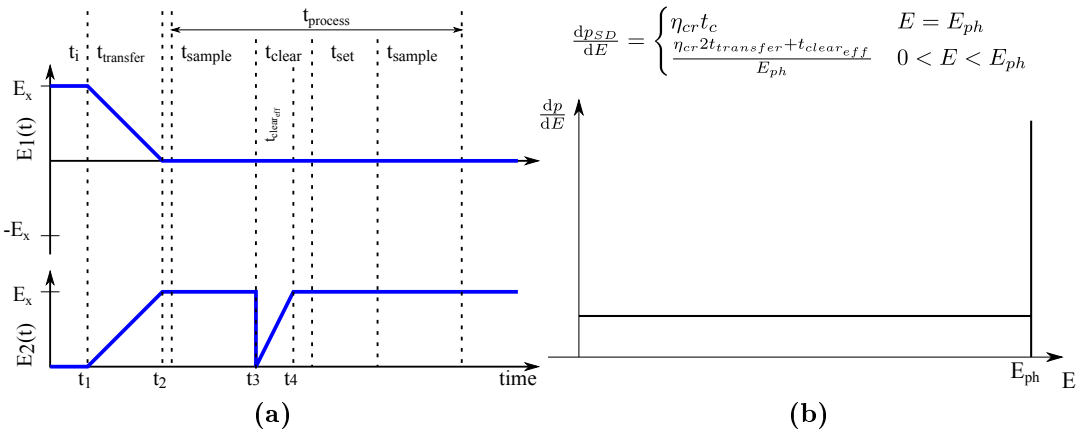

Figure 4.49.: Figures a) shows the signal in two consecutive readout cycles, caused by the signal charge corresponding to an incident photon collected at the time t while Figures b) illustrates the resulting timing related spectral redistributions for a Storage DEPFET.

in the first readout cycle and

$$E_2(t) = E_{ph} \cdot \begin{cases} 0 & 0 < t < t_1 \\ (t - t1)/t_{transfer} & t_1 < t < t_2 \\ (t - t3)/t_{clear_{eff}} & t_3 < t < t_4 \\ 1 & t_2 < t < t_3 \text{ and } t_4 < t \end{cases} \tag{4.21}$$

in the following one. The output signal of a Storage DEPFET is illustrated in figure 4.49a. The spectral response is shown in figure 4.49b and given by

$$\frac{\mathrm{d}p_{SD}}{\mathrm{d}E} = \begin{cases} \eta_{cr} t_c & E = E_{ph} \\ \frac{\eta_{cr} 2t_{transfer} + t_{clear_{eff}}}{E_{ph}} & 0 < E < E_{ph} \end{cases} . \tag{4.22}$$

The collection time t_c of a Storage DEPFET device is the sum of illumination time t_i and the processing time $t_{process}$ minus the effective clear time $t_{clear_{eff}}$, $t_c = t_i + t_{process} - t_{clear_{eff}}$. In this respect, a comparison of the the spectral response of the Storage DEPFET to that of Gateable DEPFET and standard DEPFET devices shows that with identical timing parameters, the flat shelf is lower and furthermore, the fraction of events contributing to the signal peak is always larger than for the other two concepts.

4.4.2. Analytical Model

The simulations neglect effects related to the entrance window. In other words, the material redistribution function is one for all incident photon energies. An analytical model for the redistribution matrix of a given device is then found by convolving the respective timing depended redistribution TF with a gaussian of width $\sigma = \sqrt{\sigma_{Fano}^2 + ENC_R^2}$ representing Fano and electronic noise.

4.4.3. Device Selection

Before going into details of the performed spectroscopic simulations the number of DEPFET types will be reduced, as the deadtime of a Gateable DEPFET has a rather large shortcoming for high timing, high throughput applications.
As one of the core drivers of the device timing is the required noise and since the ENC is directly related to the sampling time (see section 3.2.4.2), a certain noise performance is coupled to a respective sampling time. Provided that all devices have the same noise properties and require the same time to remove all charge carriers from the internal gate, the fastest possible timing of a device is given by the processing time. This is equal with setting the illumination time of the device to zero. While a DEPFET as well as a Storage DEPFET provide about 50 respectively 90 percent throughput at this timing scheme, practically all incident photons are lost using a Gateable DEPFET. As this is a serious limitation, these devices are not regarded in the following.

4.4.4. Device Timings

For the chosen devices, the timing sets shown in table 4.9 were simulated. For comparability, clear-, settling- and sampling-times were chosen equal for both devices. The timings were chosen based on results from recent matrix measurements and are chosen such that the readout-cycle is minimized.
The clear time of about 0.1 µs was reached with the first Infinipix prototypes and is a

DEPFET type	$t_{i_{fast}}$	$t_{i_{slow}}$	t_{sample}	t_{clear}	$t_{transfer}$	t_{set}
standard DEPFET	0	100	1	0.1	-	0.1
Storage DEPFET	0	100	1	0.1	0.1	0.1

Table 4.9.: Time constants for the spectral simulations.

result of their small gate width. Similar clear times are expected for standard-DEPFET devices with a linear geometry. The settling time of 0.1 µs was lately reached with the VERITAS 2.1 ASIC in a drain-current readout. To achieve a noise of 3-4 e^- ENC a sampling time of the order of 1 µs is required . For the linear approximation of the Storage DEPFETś transfer-time, a value of 0.1 µs was chosen, based on the measurement results shown in figure 4.45a.

4.4.5. Results

To study the effect of the different signal responses on incident spectra a three step simulation was done. First, an incident spectrum is defined. Then the energy of incident photons as well as their arrival time during a frame is simulated using the Monte Carlo method. The incident spectrum is hereby processed using the energy response for a normal DEPFET and a Storage DEPFET discussed in the previous section 4.4.1. Finally, the spectra are post-processed using the known models for the incident spectra and the corresponding Redistribution Matrix Function (RMF) for each type of DEPFET. Time

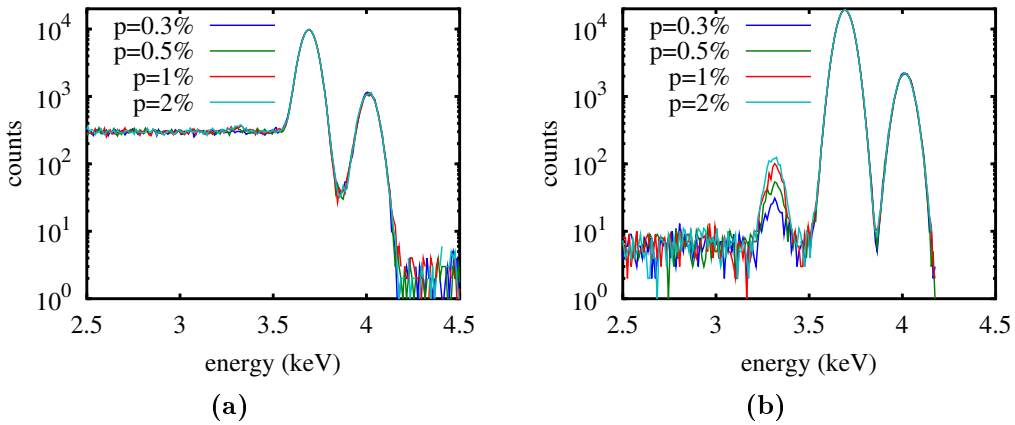

Figure 4.50.: The figures show the simulated spectra for a normal DEPFET for short (a)) and long (b)) illumination times. Each figure shows four different intensities for the potassium line. With respect to the calcium line the relative intensities are 0.1%, 0.2%, 0.4% and 0.6%.

dependent effects, as misfits, are then included in the RMF.

4.4.5.1. Line Spectrum

X-Ray Fluorescence (XRF) is a standard procedure to probe the composition of a sample material. By bombarding the surface of a specimen with X-rays, its atomic shells are excited. In the process of de-excitation these atoms emit characteristic radiation as discussed in section 3.1.1.2. That emission can in turn be used to determine the elemental composition of the probed material. XRF is limited to the first few micrometers of the material that the exciting and emitted photons are able to traverse. Nevertheless XRF is a powerful tool for material analysis.

An example for the application of a DEPFET based sensor for XRF experiments is the MIXS instrument on board of BepiColombo. Here, the exciting X-ray spectrum is emitted by the sun while the probed surface is the regolith covering the surface of the planet mercury. This satellite mission will determine the elemental composition of Mercury's crust and provide insight on its formation history.
Of special interest is the determination of the elemental composition of the regolith. Therefore, the relative concentration of oxygen, iron, silicon, sulfur, phosphorus, potassium, calcium, manganese, chromium, nickel, aluminum, sodium and titanium have to be determined (see Fraser et al. 2010).
E.g. the identification of potassium and the determination of its chemical abundance is a strong indicator for mercuries formation history.
"**K**: Effectively absent in lunar anorthositic crust,but exceeds 1% in some KREEP basalts sourced from areas representing residual melt at the end of primary crust formation. Less abundant in mare basalts. If detected on Mercury's surface, would be a strong indicator of incompatible element-enriched primary crust,either in situ or in a magmasource

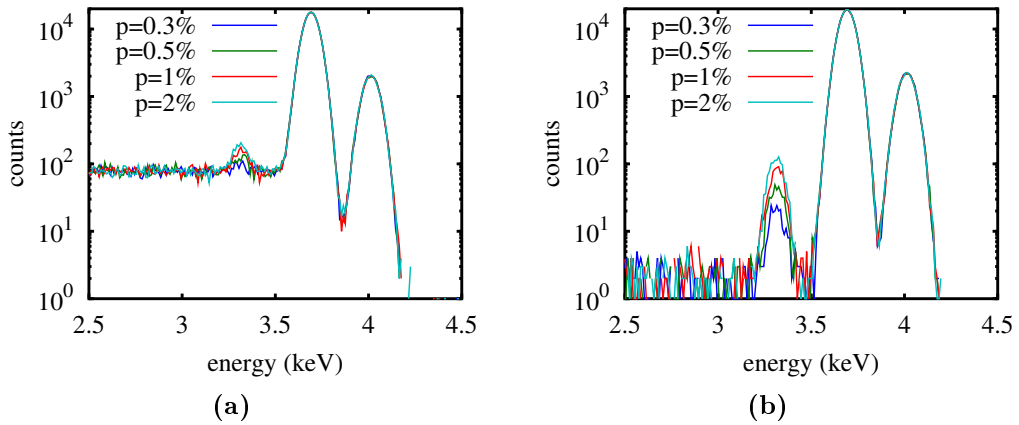

Figure 4.51.: The figures show the simulated spectra for a Storage DEPFET for short (a)) and long (b)) illumination times. The intensity ratios for the potassium line are equal to those shown in figure 4.50.

region. **K** is also a major component of the exosphere." (Fraser et al. 2010)
While the DEPFET sensor on MIXS should be well suited to fulfil the science requirements, the following will discuss the possible benefit of a storage DEPFET for XRF applications.
Although the discussion below is limited to the identification of the potassium K_α line (3.3 keV) in the presence of the calcium K_α and K_β lines (3.7 keVand 4.0 keV), the results of this chapter are significant for the identification of traces of elements in any kind of material compounds as long as the line energy emitted by the trace element is lower than that of the other compounds. The intensity of the potassium line is varied with respect to that of calcium to study the minimum relative intensity required to detect it. That will be done for two different illumination times, representing a fast and a slow operation of the DEPFET sensor. Furthermore, the overall number of detected calcium counts and the number of frames is kept constant.
The two DEPFET types are modeled using the considerations made in section 4.4.1. The simulated relative intensity of the potassium K_α line , due to the alleged low potassium content, with respect to the calcium line are $1 \cdot 10^{-3}$, $2 \cdot 10^{-3}$, $4 \cdot 10^{-3}$ and $6 \cdot 10^{-3}$. The simulated spectra are shown in figure 4.50 and figure 4.51.
As figure 4.50b and figure 4.51b show, in slow operation, both types of DEPFET are capable to identify the potassium K_α line.[6] Even the lowest intensity ratio can be identified.
In contrast, the fast operation deteriorates the capabilities of both DEPFET types, as figure 4.50a and figure 4.51a illustrate. To further quantify the capabilities of the two DEPFET types, the analytical model for the two calcium lines can be fitted to the simulated data. Next these values are subtracted from the simulated values and each bin

[6]The energy of the potassium K_β line is 3.55 keV and its intensity is one order of magnitude below that of the K_α line. Thus it is completely covered by the spectral features of the calcium K_α line.

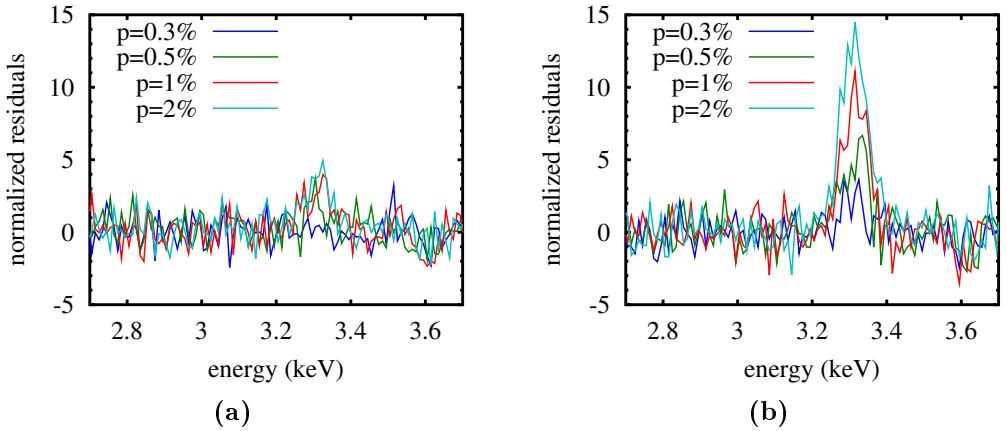

Figure 4.52.: To compare the capability of the two DEPFET concepts, the response without potassium contribution was subtracted from the simulation data and these residuals were divided by the square root of the analytical response. a) shows the standard DEPFET while the b) illustrates the behaviour of the Storage DEPFET, both for a fast timing. It is obvious that the Storage DEPFET provides a systematically better significance.

is divided by the square root of the number of counts expected from the model for this specific bin. In this way, the residuals from the expected response to the calcium line are represented in multiples of the expected standard deviation for each bin. These values for fast timings are shown in figure 4.52a for a standard DEPFET and figure 4.52b for a storage DEPFET. The observed deviation is obviously caused by the simulated potassium line. As the figures show, the Storage DEPFET is able to detect the presence of potassium for all simulated intensity ratios. Furthermore, the Storage DEPFET provides about a factor of three higher statistical significance than the simulated standard DEPFET. Overall, the Storage DEPFET provides a better capability to identify the potassium K_α line in the presence of the calcium K_α and K_β lines. As stated beforehand, this is always true for trace elements that are to be detected in the presence of other elements, that emit intense, higher energetic lines.
However, the improvement is practically a higher statistical significance for the same number of observed frames, that is provided by a Storage DEPFET. The same improvement in statistics could be reached using a longer observation time respectively a larger number of frames and photons.

4.4.5.2. Power Law Spectrum

The spectral properties of black hole binary systems are briefly discussed in section 2.1.3. In the following, a black hole spectrum is approximated as a power law continuum superimposed by a broad gaussian distribution. Of interest is how well a given type of DEPFET is capable to reconstruct the parameters of the incident spectrum.
The basic simulation scheme is as described in the introduction of this section (see section 4.4). The incident spectrum consists of a distribution proportional to E^{-n} in

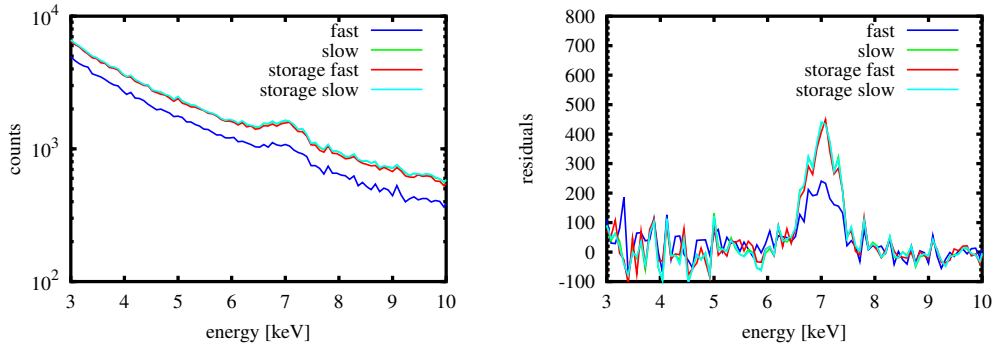

(a) **(b)**

Figure 4.53.: a) shows the simulated black hole spectra (consisting of a power law continuum superimposed by a broad Gaussian) for two DEPFET types at a fast and a slower timing. In b) the power law continuum was subtracted from the data.

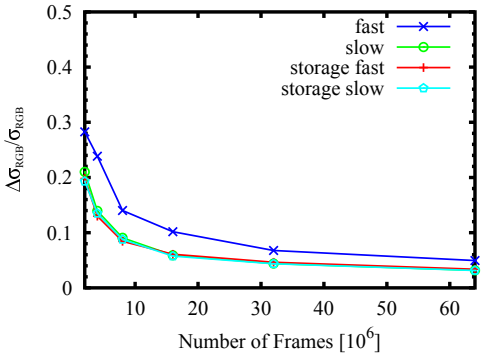

Figure 4.54.: The simulated spectra were fitted using the analytical model discussed in section 4.4.1 and section 4.4.2. The quality of the fit is evaluated using the relative error of the Gaussians width, which is plotted against the number of frames. As expected, the fit quality improves with frame number. In addition, a Storage DEPFET always provides a smaller error.

the range from E_{low} to E_{high} and a Gaussian with a mean energy of E_μ and a width of σ_{RBG}. The relative probability to observe a photon corresponding to the gaussian distribution with respect to the power law continuum is r. The probability to observe a photon in one readout cycle is set to a value of 0.5%, sufficiently low to neglect pile up. The spectral response was simulated for two illumination times. These are $t_{i_1} = 0$ µs and $t_{i_2} = 100$ µs. Overall, 64 million readout cycles were simulated. For 1, 2, 4, 8, 16, 32 and 64 million readout cycles, the simulated data were collected in histograms. An example of such a histogram for the fast and slow operation is shown in figure 4.53a. For the shown data, the number of simulated readout cycles is 64 million. The cutoff at $E_{low} = 2$keV and $E_{high} = 15$keV as well as the broad gaussian feature are clearly visible in all four spectra. Furthermore, the effect of misfits, especially the extension to negative energy values for the DEPFET can be seen. Besides these apparent features of the spectra, a dependence of the spectra on device (standard DEPFET or Storage

DEPFET) and illumination time is obvious. For the two simulated illumination times the Storage DEPFET always provides a better statistic. However, while the benefit is in the order of a factor of two for the fast operation, that advantage diminishes to a few percent for the slow timing regime. This is made clear further by subtracting the analytical model for the power law continuum from the simulated data shown in figure 4.53b. To further evaluate the performance difference of the two devices, spectra with different frame-numbers were fitted using an analytical model based on section 4.4.1. In addition to the fit parameter itself, a least-square fit also provides an estimation of the parameter error. The error of the fitted Gaussian width $\Delta\sigma_{RGB}$ is depicted in figure 4.54. As expected, the error reduces with increasing number of frames, since this also increases the number of observed photons and improves the statistics. Furthermore, it can be seen, that at the Storage DEPFET provide a systematically better estimation for the corresponding fit parameters. This benefit is of the order of 2 for fast timings. However, this edge decreases for more relaxed timing parameters.
The behaviour at fast timings could also be interpreted such that especially the Storage DEPFET devices are capable to provide a certain statistical significance already for shorter observation times.

4.5. Summary and Discussion

In the course of chapter three different DEPFET devices were investigated using device simulations, measurements and spectral simulations. In the following conclusions for each type of device are given. The summary is thereby divided into conclusions referring to the actual device layout or technology based on section 4.2 and section 4.3 and conclusions concerning the benefit of a given device for a X-ray spectroscopy based on section 4.4.

4.5.1. DEPFET Macropixel

In section 4.3.2 a series of measurements on a DEPFET macropixel devices were presented. The measurements were intended to qualify the SPIX-II measurement setup designed in the scope of this work and investigate the spectral performance of DEPFET macropixel devices. For these measurements, the devices were read out using a semi-gaussian shaper.
The energy resolution is subject to the operation conditions of the DEPFET as presented in section 4.3.2.3. The Energy resolution was studied with respect to the DEPFET channel current and the drain voltage. A higher current flow trough the DEPFET leads to a higher charge gain and respectively improves the energy resolution as the corresponding measurements confirmed. In addition, the shape of the internal gate is subject to the voltage difference between drain and source V_{DS}. For V_{DS} from -3 V to -6 V the energy resolution gradually improves. For even more negative drain voltages, beyond -6.5 V the energy resolution worsens rapidly. The phenomenon is explained by a high field region in the vicinity of the drain, causing a multiplication of present charge carriers, which

adds additional leakage current and thus noise to the pixel.
The temperature dependence is governed by leakage current and reduces with falling temperatures. The estimated leakage current of 1.19 pA at room temperature is comparably good but still within the range known e.g. from diode leakage current measurements done in the HLL.
Although the contribution of electronic noise is already in the range of a few electrons ENC, it should be possible to improve the noise of the readout circuit. From the circuit analysis provided in appendix B it can be concluded, that a lowering of the parasitic capacity at the read node will reduce the noise at high frequencies and should improve the circuits rise time. Both will successively improve the energy resolution especially at very short shaping times.

4.5.2. Blindgate Pixel

The Blindgate Pixel DEPFET devices are the first version of Gateable DEPFET (GD) that can be read out while insensitive. In the course of section 4.3.3, this feature was demonstrated and used extensively. The effective shutter switching speed is a function of the time necessary to recharge the respective contacts, the time required for the field retardation and the charge drift time through the device. The last quantity is thereby the largest and thus most dominant contribution.
Although the Blindgate Pixel are functional, the current layout limits the reachable rejection due to its asymmetry. While it is not possible to get rid of the present clear structure it would be possible to avoid the asymmetries of the source node. As simulations have shown, an increase of the source size should improve the range of the operational window for the blind-gate voltage.
In addition, a Blindgate Pixel was used to confirm the spectral model of a DEPFET read out on demand that was derived in section 3.4. The approximated limitation caused by the entrance window was thereby in the same range as for a DEPFET macropixel. At the same illumination time, the device was capable to provide a spectral response with up to a magnitude improved peak-to-background ratio by using the built-in shutter during the device readout. The large improvement is related to the short switching time of the built in shutter. However, since the built-in shutter is not infinitely fast, the peak to background ration is still dependent on the illumination time. For further improvements, it would be necessary to perform an in-depth study of the drift path through the device and the corresponding drift time.

4.5.3. Blindgate Pixel Repetitive Non Destructive Readout

In addition to the operation of a Blindgate Pixel and the readout of the device in the insensitive state, it was possible to demonstrate for the first time that it is also feasible to combine different features of DEPFET based concepts. The functionality of devices combining a built-in shutter with the RNDR feature, for instance, was success-

fully demonstrated in the pace of this thesis. Although the device could benefit from the same layout changes as a Blindgate Pixel it was shown that the rejection of charge during the RNDR is possible. In addition, single electron resolution for few electrons as well as several hundred up to 1300 e^- was demonstrated.

4.5.4. Infinipix

The work presented in section 4.2.3 was a valuable contribution to the first Infinipix prototype devices. Probably the biggest issue for any DEPFET device with a built-in shutter that is supposed to be used in a large scale matrix is the variation of the bulk doping concentration. For the standard float zone base material, these are in the range of 20-30 %. The simulations shown herein indicate that an optimized Infinipix detector should be able to cope with these fluctuations.
For a first test a single-pixel Infinipix prototype was operated successfully. Although measurements on single-pixel devices inherently lack the spectral performance for sophisticated characterizations, a combination of spectral and laser measurements showed that the basic principle of the Infinipix is functional. Furthermore, it was demonstrated that a fraction of less than $5 \cdot 10^{-4}$ of the injected charge is collected in the respectively insensitive pixel.
In addition, a limitation for the fabricated devices was found. In contrast to expectations, the device showed a limited charge handling capability in the order of 20000 e^-. The reason for the limited charge handling capacity is the fabrication technology, that was optimized for a nonlinear signal response, achieved by providing an overflow-region below the source. A technology optimized for the Infinipix should enhance the charge handling capacity significantly.

4.5.5. Spectral Simulations

In section 4.4 models based on device simulations as well as measurements for three types of DEPFET devices read out on demand were developed and used to simulate the response to different incident spectra. One first conclusion for high count rate, high throughput applications is, that the benefit of a Gateable DEPFET in this respect is dubitable because of its limited throughput. Furthermore, within the restrictions of these simulations, it is possible to conclude that the main benefit of a Storage DEPFET is an improved statistical significance for the different spectral features.
As had to be expected, the benefit of a Storage DEPFET is especially large at fast timings. If all DEPFETs are read in parallel and no dedicated illumination time is introduced, it provides a factor of two higher statistical significance. However, for longer illumination times this benefit decreases down to a few percent. For a real device, the benefit at this timing would be less, since the simulations neglect the contributions of the entrance window and only include the timing-related redistribution, Fano- and electronic noise.
For future work it is emphasized to extend the simulations done herein to matrices and include the entrance window effects discussed in section 3.3. The simulations could also

benefit from an improved model for the charge removal as well as the shutter switching of Storage DEPFET devices.
Furthermore, the simulations only predict the performance for radiation sources that show a homogeneous spectral composition over time. Spectral variation in time and their effect may be an interesting topic for future studies.

5. Conclusion

Options for a High Count-Rate Spectrometer As the spectral simulations have demonstrated, the disadvantages caused by misfits significantly reduce the spectral performance of a DEPFET based sensor especially at fast timings. As mentioned in the introduction, high count-rates can be accommodated either by spreading the incident flux over several pixels and using a moderate readout speed or by reading a smaller number of pixels respectively faster.
It is possible to sketch two examples that require similar resources. The first is based on a 64x64 Pixel Matrix read out into two directions with a readout time of 2.5 µs per line respectively a full frame time of 80 µs. The incident count-rate is spread over the complete sensor by placing the sensor out of focus, sacrificing any spatial resolution. A similar count-rate performance should be achieved by spreading the incident count-rate over 128 pixels which are read out fully parallel. This sensor would require the same amount of readout ASICs but could provide a time resolution of about 2.5 µs.
Considering the results of the spectral simulations, a standard DEPFET should be sufficient for the first concept. However, the large fraction of misfits would limit the spectral performance of the second concept. Here the device of choice is a Storage DEPFET.
In terms of feasibility, the first concept is very similar to the sensor used on the MIXS instrument, while the second concept requires further development. Taking into account the requirements listed in table 2.1, the first concept appears suitable for ATHENA.

Spectral Response Model The spectral response of a silicon based sensor is limited by its intrinsic properties related to the interaction of radiation and matter as discussed in section 3.3. Additionally, readout artifacts distort the ideal response. This is why a model for the response of a DEPFET sensor, based on analytical considerations and measurements was developed (see section 3.4 and section 4.3.3.2.2). Especially at fast timings, as required to provide highest count-rate capability, readout artifacts hamper the spectroscopic properties of a DEPFET based sensor (see section 4.4).
It was demonstrated that the built-in shutter of Gateable DEPFET devices can be utilized to suppress charge collection in the readout phase and thus reduce the degradation of the spectral performance by up to one order of magnitude (see section 4.3.3.3). Although these devices improve the spectral performance of a DEPFET read out on demand, they also inflict a dead time that limits the device throughput.
As discussed in this work, a DEPFET can be extended not just for a built-in shutter (see section 4.1.1) but also for an adjacent storage area (see section 4.1.2). The resulting Storage DEPFET devices are capable to minimize the dead time while providing the same optimized spectral response as Gateable DEPFET devices. In the scope of this thesis, device simulations were made to optimize the design of one of these concepts (see

section 4.2.3). Follow-up measurements on the a prototype device confirmed the basic functionality.
Based on the response model for a standard DEPFET response models for a Gateable DEPFET as well as a Storage DEPFET were developed (see section 4.4.1). These were successively utilized to perform spectral simulations of a standard DEPFET and a Storage DEPFET with respect to different incident spectra. As those simulations show, especially at fast timings a Storage DEPFET provides by up to a factor of two better statistics (see section 4.4.5.1 and section 4.4.5.2).
The storage feature should ultimately be capable to provide a better reconstruction of spectral features. For a DEPFET based sensor which is read on demand either fully parallel or in a fast window mode a Storage DEPFET is the device of choice.

Device Improvements The properties of Gateable DEPFET devices were investigated using device simulations (see section 4.2.2) and measurements (see section 4.3.3). Although the tested implementation was functional device simulations revealed, that a modification of the layout, especially a larger and homogeneous source size, should improve their performance. From these simulations it was taken that the most crucial operational parameter is obviously the voltages applied to the shutter contacts. Furthermore, the devices combining DEPFET with built-in shutter functionality studied herein are highly susceptible to the applied backside bias. Since the DEPFET is based on the principle of sidewards depletion and the potential profile inside the bulk is determined by the applied backside voltage, this seems to be a general limitation that requires thorough investigation especially for the designs of new devices. Dimensional variations to the most relevant contacts, however, can contribute to create a larger parameter plateau, for which the device operates with the desired specifications.
It was demonstrated, that the first Infinipix prototypes are functional. While device simulations provided valuable input for the geometry of the Infinipix devices (see section 4.1.2.2), the non-optimum fabrication technology compromised the performance of the first prototypes (see figure 4.3.5). Apart from a possible optimization of the fabrication technology, a latest design study showed that it is possible to improve the device geometry to closely meet the geometric optimum obtained from 2-dimensional device simulations.

Future Developments and other Applications The considerations for the spectral performance of DEPFET based sensors provided herein neglect effects as split events in space and time. Therefore, they are only valid for macroscopic single pixel devices. Although the analytical expression derived herein can be used as a starting point, further in-depth analysis of matrix spectra and measurements on those devices are required to provide a sophisticated model for the spectral response of DEPFET matrices. Furthermore, spectral simulations especially including sources with time dependent spectral features are emphasized. It is likely that a Storage DEPFET provides even more benefits than the improved spectral response discussed in this thesis.

The simulation results of section 4.2.2 can be used to design a possible second generation of Blindgate Pixel devices. Especially the combination with a compact RNDR DEPFET is interesting in this context. The single-electron resolution of these devices could for example be utilized to investigate the Fano-factor of silicon with unprecedented accuracy.
The Infinipix concept requires further investigation. First of all, measurements on accessible prototype matrices should yield further information about spectral performance and possible limitations. Since the performance of the currently available prototypes is limited by the utilized technology, further device simulations are required. These should include technology variations as well as full three dimensional simulations of the Infinpix.
Based on the Infinipix, a new class of device is currently being developed. These QuadPix devices implement four DEPFETs ("subpixels") into one single imaging pixel ("superpixel"). The subpixels switch between sensitive and insensitive state in such a way, that always one subpixel ist sensitive at a time, while the other three can be read out. In this way, four images can be recorded simultaneously. An application of that feature would be the use for high frequency optical polarimetry. Here it would be possible to synchronize the signal integration in the four subpixel with a fast polarimeter.

A. Material Redistribution Function

The material redistribution MF describes the distribution of the average energy deposited by photons of energy E_{ph} in the silicon bulk. The single contributions are summarized in the following. A detailed description is given in section 3.3. To describe the response of an ideal silicon-sensor, the redistribution due to Fano-noise and electronic noise have to be taken into account. For a DEPFET sensor read out on demand, an additional redistribution accounting for time dependent readout artifacts must be taken into account.

- Main Peak

$$\frac{\mathrm{d}p_{main}}{\mathrm{d}E_x} = \begin{cases} p_{main} & E_x = E_{ph} \\ 0 & E_x \neq E_{ph} \end{cases}$$

  with $p_{Main} = p_{Event} - p_{Tail} - p_{Loss} - p_{Escape} - p_{Shelf}$. as the probability that an event contributes to the main peak.

- Escape Peak

$$\frac{\mathrm{d}p_{EscapePeak}}{\mathrm{d}E_x} = \begin{cases} p_k \cdot \omega_k (1 - \frac{\mu_k}{\mu_{Si}} ln(1 + \frac{\mu_{Si}}{\mu_k}) & E_x = E_{ph} \\ 0 & E_x \neq E_{ph} \end{cases}$$

  A recombination close to the surface may lead to the escape of a fluorescence photon. The probability for such an event is given by the above equation.

- Low Energetic Tail

$$\frac{\mathrm{d}p_{tail}}{\mathrm{d}E_x} = \begin{cases} 2\mu_{Si} z_0 \frac{E_x - E_{ph} \cdot C_0}{E_{ph}^2 (1-C_0)^2} & E_{ph} \cdot C_0 \leq E_x \leq E_{ph} \\ 0 & E_{ph} \leq Ex \leq E_{ph} \cdot C_0 \end{cases}$$

  A recombination close to the surface may lead to a loss of generated charge due to recombination centers at the silicon interface.

- Charge Losses

$$\frac{\mathrm{d}p_{Loss}}{\mathrm{d}E_x} = \begin{cases} 2p_{Loss} \frac{E_x - E_{ph} \cdot C_C}{E_{ph}^2 (1-C_C)^2} & E_{ph} \cdot C_C \leq E_x \leq E_{ph} \\ 0 & E_{ph} \leq Ex \leq E_{ph} \cdot C_0 \end{cases}$$

  Apart from interface traps close to the device surface, the sensor structure may cause additional charge losses.

- Shelf generated in the silicon bulk

$$\frac{\Delta p_{Shelf_{Si}}}{\Delta E_x} = \begin{cases} \frac{\mu_{Si} y}{4} \left(1 - \frac{1}{8}\beta - \frac{2}{15}\gamma - \frac{2}{3}\delta\right) \frac{R}{E_{kin}} & E_{ph} - E_{kin} < E_x < E_{ph} \\ 0 & E_{ph} < E_x < E_{ph} - E_{kin} \end{cases} .$$

The energetic electrons primarily generated in the silicon bulk may leave the sensitive volume and deposit only part of their energy inside the sensitive volume. This causes a characteristic contribution to the shelf of the sensors response.

- Shelf generated in layer a

$$\frac{\Delta p_{shelf_a}}{\Delta E_x} = \begin{cases} \frac{\mu_{Si} y}{4} \frac{R}{E_{kin}} \left[\left(2 + \frac{1}{4}\gamma + \delta\right) \frac{A}{R} - \left(1 + \frac{\beta}{4}\right) \frac{A^2}{R^2} \right. \\ \quad \left. - \left(\frac{\gamma}{6} + \frac{\delta}{3}\right) \frac{A^3}{R^3} + \frac{\beta}{8} \frac{A^4}{R^4} + \frac{\gamma}{20} \frac{A^5}{R^5}\right] & 0 < E_x < E_{kin} \\ 0 & E_{kin} \leq E_x \leq 0 \end{cases} .$$

An event may recombine inside the passivation layer a and move towards the silicon bulk, depositing part of its energy inside the sensitive volume. This causes a characteristic contribution to the shelf of the sensors response.

- Shelf generated in layer b

$$\frac{\Delta p_{shelf_b}}{\Delta E_x} = \begin{cases} \frac{\mu_{Si} y}{4} \frac{R}{E_{kin} - E_A} \left[\left(2 + \frac{\gamma}{4} + \delta\right) \frac{B - A}{R} - \left(1 + \frac{\beta}{4}\right) \frac{B^2 - A^2}{R^2} \right. \\ \quad \left. - \left(\gamma + 2\delta\right) \frac{B^3 - A^3}{6R^3} + \beta \frac{B^4 - A^4}{8R^4} + \gamma \frac{B^5 - A^5}{20R^5}\right] & 0 \leq E_x \leq E_{kin} \\ 0 & E_{kin} \leq E_x \leq 0 \end{cases} ,$$

An event may recombine inside the passivation layer b and move towards the silicon bulk, depositing part of its energy inside the sensitive volume. This causes a characteristic contribution to the shelf of the sensors response.

- Shelf generated in layer c

$$\frac{\Delta p_{shelf_c}}{\Delta E_x} = \begin{cases} \frac{\mu_{Si} y}{4} \frac{R}{E_{kin} - E_B} \left[1 - \frac{\beta}{8} + \frac{2\gamma}{15} + \frac{2\delta}{3} + \left(-2 - \frac{\gamma}{60} - \frac{\delta}{3}\right) \frac{B}{R} \right. \\ \quad \left. + \left(1 + \frac{\beta}{4}\right) \frac{B^2}{R^2} + \left(-\frac{\gamma}{6} - \frac{\delta}{3}\right) \frac{B^3}{R^3} - \frac{\beta}{8} \frac{B^4}{R^4} + \frac{\gamma}{20} \frac{B^5}{R^5}\right] & 0 \leq E_x \leq E_{kin} - E_B \\ 0 & E_{kin} - E_B \leq E_x \leq 0 \end{cases} .$$

An event may recombine in the layer c and move towards the silicon bulk, depositing part of its energy inside the sensitive volume. This causes a characteristic contribution to the shelf of the sensors response.

B. Drain Current Readout Noise and Stability

This appendix provides considerations for the noise and stability of the discrete drain-current readout circuit implemented in the Drain-Readout-Board of the SPIX-II measurement setup.

Circuit Noise Although the DEPFET provides an intrinsic amplification, its signal is as low as a few hundred pA per electron. The noise properties of DEPFET devices have been studied e.g. in (Porro et al. 2006). Especially the spectral noise density of DEPFETs were investigated in this context. At a transconductance $g_m = 68$ µS, the measured value for the $1/f$-noise is $v_{1/f}^2 = 4.5 \cdot 10^{-12}$ V^2 and the white noise density is $v_w^2 = 1.53 \cdot 10^{-16} \frac{\mathrm{V}^2}{\mathrm{Hz}}$. Multiplying the square root of these values with the transconductance g_m results in the current noise density of the DEPFET. The values are $i_{1/f} = 1.44 \cdot 10^{-10}$A for the 1/f noise and $i_w = 0.84 \cdot 10^{-12} \frac{\mathrm{A}}{\sqrt{\mathrm{Hz}}}$ for the white current noise density. To provide low noise measurements, the DEPFET signal has to be amplified. The noise contribution of the amplifier and its passive parts must be small with respect to the DEPFET noise.
The equivalent circuit used for noise analysis is shown in figure B.1. To include parasitic capacities in the feedback circuit and the substraction path, the resistive values are exchanged by the complex impedances Z_{sub} and Z_F. The main noise sources are the current noise i_{DEPFET} of the DEPFET itself, the current noise i_n and i_p as well as the voltage noise v_p of the operational amplifier, and the current noise of the substraction and feedback resistors i_{sub} and i_F. To compare the noise of each part with the noise density of the DEPFET it is necessary to reference all noise sources to the negative input of the operational amplifier.
The feedback and substraction resistors are already connected to the negative input. Thus their current noise density can directly be compared to the noise of the DEPFET. The current noise density of a resistor is given by

$$i_n^2(f) = \frac{4 k_B T}{R}, \tag{B.1}$$

with the boltzman-constant $k_B = 1.38064 \cdot 10^{-23} \frac{\mathrm{J}}{\mathrm{K}}$ and T as the absolute temperature. At room temperature the white noise density of a resistor is $i_{Rw} = \frac{128}{\sqrt{R}} \frac{\mathrm{pA}}{\sqrt{\mathrm{Hz}}}$. An ideal ideal resistor of 24kΩ produces the same thermal noise density as the one stated before for the DEPFET. To introduce only half the noise of the DEPFET the resistance value has to be quadrupled.

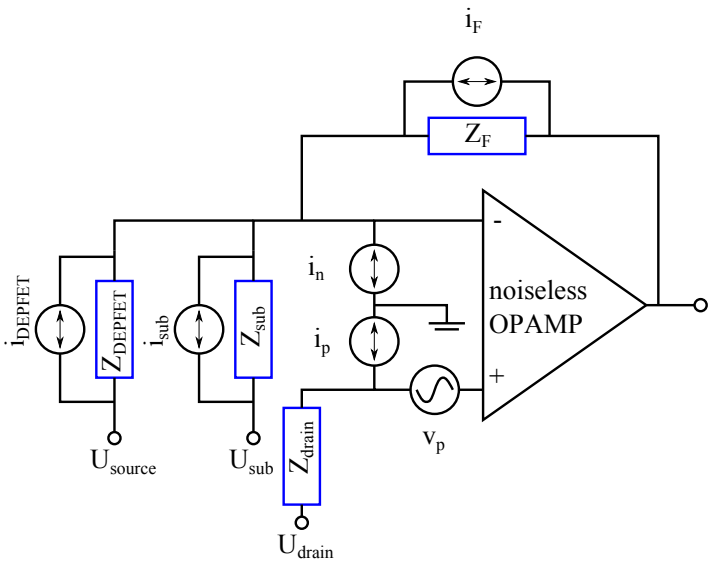

Figure B.1.: The noise of the I-to-V converter can be calculated using the shown equivalent circuit.

For an ideal operational amplifier in feedback operation, a signal at its positive input is directly reproduced at its negative input. Unfortunately, this statement is also true for noise. The voltage noise $v_p$of the operational amplifier can thus be moved from the positive to the negative input. Here the voltage induces a current-flow through the input impedance Z_{in}. The current caused by v_p is then $i_p = \frac{v_p}{Z_{in}}$, with Z_{in} including the output resistance of the DEPFET, the resistivity of the subtraction resistor as well as the overall capacity at the negative input. So the contribution of the operational amplifiers voltage noise is $i_p = v_p \frac{1+R_{in}C_{in}j\omega}{R_{in}}$. For low frequencies, the noise is determined by the values of v_p and the summed resistance R_{in} at the input. For higher frequencies the current noise density is determined by the parasitic capacity and increases with a factor of 20 dB per decade. A cutoff for the noise at the output of the I to V converter is provided by the feedback impedance Z_F and the limited bandwidth of the operational amplifier. The current noise source at the positive input induces a voltage drop $v_{ip} = i_p \cdot R_{drain}$ over the drain resistor R_{drain}. This voltage noise can otherwise be treated equally to v_p. The last contribution of the operational amplifier is the current noise density of the negative input i_p. It can be compared directly to the DEPFET noise.
The noise contribution of the operational amplifier is on the one hand defined by its noise properties, hence its current and voltage noise density provide a direct measure for its performance in the I to V converter. Furthermore its input capacitance affects the high frequency of its voltage noise. Especially for DEPFET devices with a low output resistance, the voltage noise of the operational amplifier may become significant. However, there exists a large variety of operational amplifiers providing low current and voltage noise, granting high bandwidth and low input capacity. Two examples are the THS4631 and the ADA4817.
Provided the noise density of the chosen operational amplifier is sufficiently low, the

noise performance of the current-to-voltage converter is determined by the values of feedback and substraction resistor. To keep the additional noise contribution below 10 percent, with respect to the white noise of the DEPFET, the additional contribution must be smaller than half the DEPFETs white noise density. For a single resistor this would lead to a value of 94 kΩ. For two resistors, the noise density increases by the square root of two. To meet the 10 percent criteria a minimum value of 132 kΩ for feedback and subtraction resistor is required.

Stability For the discussed I to V converter an instability will occur if the feedback voltage V_{FB} has a phase shift of 180 ° with respect to the voltage V_{in} at the negative input and the ratio of V_{FB} to V_{in} is equal to, or larger than one. The ratio of input and feedback voltage, also called loop gain G_L, depends on the gain $G(j\omega)$ of the operational amplifier, its output resistance R_O as well as load, feedback and input impedances Z_{load}, Z_F and Z_{in}. It can be expressed as

$$G_L = G(j\omega)\frac{Z_L}{R_O + ZL}\frac{Z_{in}}{Z_{sub} + Z_F}. \tag{B.2}$$

The feedback and input impedance are composed of a resistor in parallel with a capacitance leading to

$$Z = \frac{R}{RCj\omega + 1}, \tag{B.3}$$

while the load impedance is chosen to be a resistor in series with a capacitance towards the ground potential

$$Z_{load} = \frac{R_{load}C_{load}j\omega}{C_{load}j\omega}. \tag{B.4}$$

In the simplest case, the frequency dependence of the amplifier gain is described by the DC-gain G_0 and the corner frequency f_g as

$$G(j\omega) = \frac{G_0}{s/f_g + 1}. \tag{B.5}$$

With these equations the loop gain becomes

$$G_L = \frac{G_0}{j\omega/f_g + 1}\frac{R_{load}C_{load}j\omega + 1}{(R_O + R_{load})C_{load}j\omega + 1}\frac{R_{in}}{R_{in} + R_F}\frac{R_F C_F j\omega + 1}{\frac{R_{in}R_F}{R_{in}+R_F}(C_{in}C_F)j\omega + 1}. \tag{B.6}$$

To determine the stability of the I to V converter, numerator and denominator of the loop gain can be analysed separately. Every zero in the numerator increases the loop gain by 20 dB per decade and adds a phase shift of $\pi/2$. Respectively every zero in the denominator (also referred to as pole) decreases the loop gain by 20 dB per decade and adds a phase shift of $-\pi/2$. As its transfer function indicates, the operational amplifier itself already causes a phase shift of $-\pi/2$. In addition, the feedback and input network add another factor of $-\pi/2$, so that the phase shift is directly compensated by the feedback network. However, if the feedback resistor is large compared to the

input resistor, a phase shift of $-\pi/4$ appears at $f_in = \frac{1}{R_{in}(C_{in}+C_F)}$ and further decreases to $-\pi/2$ until the compensation by the feedback network starts. To avoid this, it is meaningful to keep the input resistance and the feedback resistance at least in the same order of magnitude. The most crucial part for the stability is the load impedance. Without the resistor R_L, the feedback capacitor always introduces a phase shift, whereby the corresponding corner frequency is determined by the load capacitance C_L and the output resistance R_O. For large load capacities, the corner frequency is low, causing a phase shift of $-\pi$ while the loop gain is larger than one. To avoid the resulting instability of the readout circuit a large capacitive load should be avoided.

C. Material Constants

This chapter lists the physical parameters used to calculate the spectral redistribution functions shown in figure 3.14 in section 3.3.4.
In figure C.1, the absorbtion coefficient over the energy range from 0.01 keV up to 10 keVis shown. The graphs were taken from `http://www.nist.gov/pml/data/xraycoef/`. From the absorbtion coefficient and the material density the absorbtion lengths can be calculated. The absorbtion length of silicon, silicon-nitride and silicon-dioxide for $Mn - K_\alpha$, $Mn - K_\beta$ and silicon K-fluorescence photons is shown in table C.1. In addition the values for the photoelectron asymmetry parameters β, γ, and δ for the photoelectron emission distribution are provided in table C.2. These were taken from Trzhaskovskaya, Nefedov, and Yarzhemsky 2001; Trzhaskovskaya et al. 2006. Where necessary, the data were extrapolated using the there shown values.
Furthermore the transition probabilities for radiative and non-radiative relaxations for silicon as well as their energies are listed in table C.3a and table C.3b. The shown values were taken from (Perkins, Chen, and Hubbel 1991).

layer	1.74keV	5.9keV	6.4keV
Si_3N_4	x	29.3	37.0
SiO_2	x	52.4	66.3
Si	12.22	28.1	35.4

Table C.1.: This table lists the absorbtion length α in µm of Si_3N_4, SiO_2 and Si for the Si fluorescence line (1.74keV) and $Mn - K_{alpha}$ and $Mn - K_\beta photons$ (5.895keVand 6.492keV). The values were calculated using cross sections and densities from NIST X-com database *Tables of X-Ray Mass Attenuation Coefficients and Mass Energy-Absorption Coefficients from 1 keV to 20 MeV for Elements Z = 1 to 92 and 48 Additional Substances of Dosimetric Interest.*

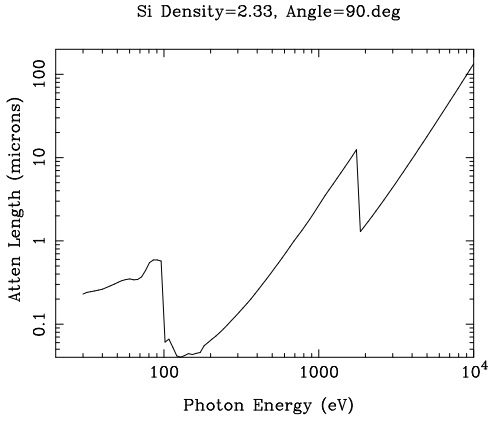

(a) Silicon

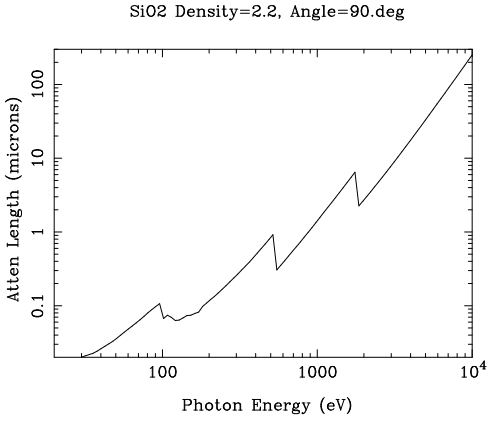

(b) Siliocn oxide

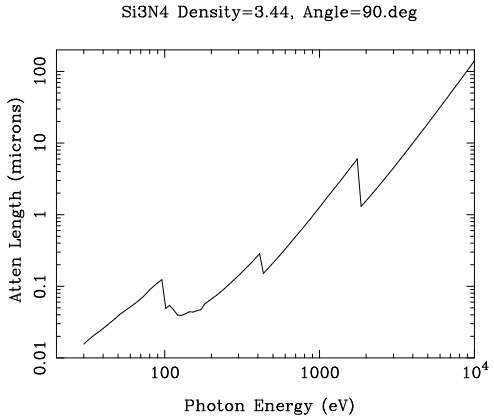

(c) Siliocn Nitride

Figure C.1.: Shown are the absorbtion lengths for a) silicon, b) silicon-oxide and c) silicon-nitride. Graphs from *X-Ray Interaction With Matter*

$Energy$[keV]	β	γ	δ
1.5	1.985	0.711	$-7.520 \cdot 10^{-6}$
2	1.980	0.863	$-6.76 \cdot 10^{-6}$
3	1.970	1.110	$-4.97 \cdot 10^{-6}$
4	1.960	1.320	$-2.94 \cdot 10^{-6}$
4.05	1.959	1.329	$-2.82 \cdot 10^{-6}$
4.65	1.954	1.436	$-1.46 \cdot 10^{-6}$
5	1.950	1.500	$-6.59 \cdot 10^{-7}$
10	1.960	2.196	$1.10 \cdot 10^{-4}$

Table C.2.: Shown is a list of asymmetry parameters for photoelectron emission (see Trzhaskovskaya, Nefedov, and Yarzhemsky 2001 and Trzhaskovskaya et al. 2006). In the range from 2-5keVthe values of β, γ and δ are fairly linear. Thus, a linear approximation was used for the asymmetry parameters at 4.05keV and 4.55keV.

transition	p_x	E_{Auger}[keV]
KL_IL_I	0.075	1.54
$KL_IL_{II,III}$	0.236	1.59
$KL_{II,III}L_{II,III}$	0.573	1.64
$KL_{II,III}M$	0.0656	1.85
KMM	0.00134	1.74
$L_IL_{II,III}M$	0.97	0.05
$L_{II,III}MM$	1.00	0.10

(a) nonradiative transitions

transition	ω_x	$E_{fluo}[eV]$
$KL_{II,III}$	0.0485	1738
$L_IL_{II,III}$	$4 \cdot 10^{-4}$	49
$L_{II.III}M$	$5 \cdot 10^{-5}$	100

(b) radiative transitions

Table C.3.: Table a) lists non-radiative transition probabilities for an excited silicon atom. As seen a K-shell vacancy will emit an auger electron with a probability of about 95%. The mean energy of the auger electron is 1.600keV. Table b) lists the fluorescence probabilities and energies for different vacancies. Data from Perkins, Chen, and Hubbel 1991

D. Measurement Data

Model	ideal	1	2	3
Variable	Value			
p_L	0	$1.5 \cdot 10^{-2}$	$2.5 \cdot 10^{-3}$	$5 \cdot 10^{-2}$
C_C	0	0.28	0.3	0
	Energy Resolution			
FWHM	126.9	127.1	126.9	127.8
Energy Range	P/B ratio of Model			
900-1100	15851	15527	15522	1977

Table D.1.: Fitted values of the Model data presented in section 3.3

Measurement Values for Normal operation					
clocks	ENC	FWHM	P/B	P/B error	cts/s
0	5.26	144.76	45	1	1043
100	5.28	140.13	62	2	1035
200	5.26	137.15	82	3	1035
300	5.39	135.36	100	3	1033
400	5.29	133.37	119	3	1031
500	5.37	131.64	143	4	1028
700	5.49	131.87	174	3	1026
1000	5.57	130.81	226	4	1025
1500	5.74	130.63	315	5	1022
2000	5.63	130.04	392	7	1020
3000	5.85	130.57	568	10	1019
5000	6.63	133.44	812	13	1016
7000	6.78	133.83	1099	17	1016
10000	7.26	135.14	1442	21	1016
20000	8.84	140.55	2168	29	1014
50000	12.36	158.20	2867	65	1017

Table D.2.: Noise, energy resolution, peak-to-background ratio and the number of observed counts per second in dependence of the set integration time in clocks (1 clock equals 12.5 ns) for normal operation

Measurement Values for Gated operation					
clocks	ENC	FWHM	P/B	P/B error	cts/s
0	5.13	131.13	364	17	1024
100	5.34	130.11	750	31	1015
200	5.20	129.52	1024	39	1014
300	5.25	129.43	1418	53	1016
400	5.42	129.84	1615	57	1012
500	5.40	130.21	1970	69	1012
700	5.51	130.02	2487	84	1014
1000	5.54	130.27	3013	95	1011
1500	5.67	130.45	4127	125	1013
2000	5.73	130.59	5117	150	1012
3000	5.98	131.21	6441	175	1011
5000	6.29	131.71	7893	187	1011
7000	6.61	132.33	9201	202	1011
10000	7.14	133.67	10790	220	1012
20000	8.90	141.88	12276	255	1012
50000	12.32	161.08	12754	617	1203

Table D.3.: Noise, energy resolution, peak-to-background ratio and the number of observed counts per second in dependence of the set integration time in clocks (1 clock equals 12.5 ns) for gated operation

List of Acronyms

ADC Analog to Digital Converter
ADU Arbitrary Digital Units
AGB Asymptotic Giant Branch
AGN Active Galactic Nucleus
ASIC Application Specified Integrated Circuit
ATHENA Advanced Telescope for High ENergy Astrophysics
ASTEROID Active current Switching Technique ReadOut In x-ray spectroscopy with Depfet
APS Active Pixel Sensor
CRXO The Center for X-ray Optics
DEPFET DEPleted Field Effect Transistor
ESA European Space Agency
FDM Frequency Domain Multiplexing
FOV Field of View
FPA Focal Plane Array
FPGA Field Programmable Gate Array
FWHM Full Width at Half Maximum
GD Gateable DEPFET
GRB Gamma Ray Burst
ICM Intra Cluster Medium
ICPU Instrument Control and Power conditioning Unit
NIST National Institute of Standards and Technology
MOS Metal Oxide Semiconductor
MOSFET Metal Oxide Semiconductor Field Effect Transistor
NASA National Aeronautics and Space Agency
ENC Equivalent Noise Charge
ISCO Innermost Stable Circular Orbit
P/B Peak to Background
CCD Charge Coupled Device
RMF Redistribution Matrix Function
pnCCD pn-Charge Coupled Device
DSSC DEPFET-Sensor with built in Signal Compression
MIXS Mercury Imaging X-ray Spectrometer
PMCA Pulse Sensitive Multi Channel Analyzer
RNDR Repetitive Non Destructive Readout
SDD Silicon Drift Detector
SMBH Super Massive Black Hole

SPO Silicon Pore Optics
SQUID Superconducting Quantum Interference Device
TES Transition Edge Sensor
UFO Ultra Fast Outflow
WFI Wide Field Imager
WHIM Warm Hot Intergalactic Medium
XIFU X-Ray Integrated Field Unit
XRF X-Ray Fluorescence
X-FEL X-ray Free Electron Laser

List of Symbols

A_1 filter coefficient for white noise.

A_2 filter coefficient for 1/f noise.

A_3 filter coefficient for leakage current noise.

B_{CL} background caused by events incident during the clear protest.

B_{EW} background caused by the sensor entrance window.

B_{MF} background caused misfit events.

B_{MMF} sum of the misfit contibution to the peak to background for caused by readout and clear events, provided that negative misfits can be neglected.

B_{nCL} background at negative energies caused by events incident during the clear protest.

B_{nMF} background caused by negative misfit events.

B_{split} contribution to the peak to background ratio by split events inside a matrix that are distributed over two consecutive frames.

B_{split} background caused by split events between two or more pixels that are distributed over several frames.

$CCE(z)$ describes the fraction of charge collected finally detected by the sensor.

C_0 the fraction of charge collect for a charge cloud originating at the sensor interface.

C_C minimal fraction of charge collected when charge losses other than at the entrance window are present.

C_G external gate capacity.

C_{ox} sheet capacity of the MOS insulator.

E electrostatic Field.

EN redistribution due to electronic noise.

$ENCR$ ENC of a DEPFET read out on demand.

ENC_{RNDR} ENC noise of a repetetive none destructive readout.

ENC_{sh} ENC of the readout system with a given weighting function.

$E_1(t)$ energy signal caused in this readout cycle by an event incident at the time t.

$E_2(t)$ energy signal caused in the succeeding readout cycle by an event incident at the time t.

E_i mid band energy.

E_r remaining energy of an electron that travelled the distance d inside the senitive volume.

E_t band energy level of an intermediate state introduced by a chrystal defect.

E_x energy deposited inside the sensitive volume without accounting for statistical fluctuations.

E_y the weighted energy signal without statistical fluctuations.

E_{Ae} energy of a generated Auger-electron.

E_{Pe} energy of a generated photoelectron.

E_{bind} Binding energy of an electron.

E_{kin} kinetic energy of an electron.

E_{ph} energy of the incident photon.

F fraction of fluorescence photons following a photoelectric absorbtion that are capable to leave the sensitive volume of the sensor.

FN redistribution due to fano noise.

$FWHM$ full width at half maximum height.

G gain for source follower readout.

$I_{drain,sat}$ saturation current through a transistor.

I_{drain} drain current.

I_{lc} leakage current.

L transistor length.

MF the material redistribution function.

N_A acceptor doping concentration.

N_D donor doping concentration.

N_e number of generated electrons.

N_{lc} number of leakage current electrons collected between two repetetive readouts.

P peak height.

Q_{acc} charge in an accumulation layer.

Q_{sig} signal charge.

RF the sensor redistribution function.

R_{A1} feedback resistor of the positive amplification stage.

R_{A2} resistor towards the offset voltage of the positive amplification stage.

R_{B1} input resistor of the differential output buffer.

R_{B2} feedback resistor of the differential output buffer.

R_F feedback resistor.

R_{max} maximum range an electron is able to traverse inside a solid (Herein calculated according to Fitting).

R_{sub} subtraction resistor.

T temperature.

TF time dependent redistribution function.

T_0 room temperature.

V_B bias applied to the backside contact.

V_F bias applied to the frontside contact.

V_G gate voltage applied to a MOS structure.

V_T transistor threshold voltage.

V_{BG_H} blind gate high voltage.

V_{BG_L} blind gate low voltage.

V_{B_H} blind high voltage.

V_{B_L} blind low voltage.

V_D drain voltage.

V_{FB} flat band voltage.

$V_{G_{off}}$ gate off voltage.

$V_{G_{on}}$ gate on voltage.

V_{I-V} voltage at the I-V output.

V_S source voltage.

$V_{backside}$ backside voltage.

V_{bi} built-in potential of a diode in thermal equilibrium.

V_{ext} external applied reverse bias to a diode.

V_{off} offset voltage.

V_{out} output voltage of the discrete drain-current readout.

V_{sub} subtraction voltage.

W transistor width.

W_D depletion width of a pn-junction.

$\Delta V_{backside}$ simulated operation window for the Infinipix concept.

Ω solid angle.

$\Phi(x)$ potential inside a sideward depleted device.

α exponent characterizing charge losses.

β asymmetry parameter of the differential electron emission, related to electric dipole transitions.

δ asymmetry parameter of the differential electron emission, related to magnetic dipole transitions.

η_{cr} count rate of incident photons.

$\frac{P}{B_{CL}}$ contribution to the peak to background ratio due to events incident in the clear phase.

$\frac{P}{B_{EW}}$ limitation of the peak to background ratio caused by the sensor entrance window.

$\frac{P}{B_{MF}}$ contribution to the peak to background ratio due to positive misfits.

$\frac{P}{B_{nCL}}$ contribution to the peak to background ratio due to events incident in the clear phase and pile-up.

$\frac{P}{B_{nMF}}$ contribution to the peak to background ratio due to negative misfits.

$\frac{P}{B}max$ maximum peak to background ratio achievable with a sensor thats spectral response is only limited by its entrance window.

γ asymmetry parameter of the differential electron emission, related to electric quadrupole transitions.

μ charge carrier mobility.

μ_K absorbtion coefficient for K-shell fluorescence photons inside silicon.

μ_{Si} absorbtion coefficient for incident photons in silicon.

μ_p hole mobility.

ϕ emission angle of a fluorescene photon or an electron with respect to the sensor entrance window normal vector.

$\phi(r)$ electrostatic potential at the position r.

ρ material density.

$\rho(r')$ charge distribution.

σ_{ENC} RMS noise at the sensor output expressed by the equivalent amount of elctrons at the input.

σ_{Fano} fano noise.

σ_{shell} Interaction cross section for photoelectric absorbtion by the respective atomic shell.

τ_n electron lifetime.

τ_p hole lifetime.

τ_{sg} shaping time constant of the shaper.

θ angle between incident photon and emitted photoelectron.

ε relative material permittivity.

ε_0 vacuum permittivity.

ε_{Si} relative permittivity of silicon.

ε_{ox} relative permittivity of silicon-dioxide.

φ azimuthal emission angle.

a_1 white noise density in $[\frac{\mathrm{V}^2}{\mathrm{Hz}}]$.

a_2 1/f noise.

a_3 leakage current noise.

d distance a fluorescence photon or secondary electrons travels inside the sensors sensitive volume.

d_s depletion width below a MOS-structure.

$d_s d$ thickness of the sidewards depleted device.

d_{ox} oxide thickness of the MOS-structure.

d_{sens} thickness of the sensitive Volume.

f the Fano-factor.

$f(z)$ describes the behaviour of charge losses with increasing distance to the entrance window interface.

f_m proportionality factor for the modification of the drain current by signal charge.

g_m transconductance of the transistor.

g_q charge gain of a DEPFET transistor.

k boltzman constant.

$k1$ fit parameter for the contribution of fano, white, and 1/f noise.

$k1$ fit parameter for the contribution of leakage current.

n electron carrier density.

n_i intrinsic charge carrier density.

n_r white noise density of a MOS transistor.

n_{RNDR} number of repetetive readouts.

n_R number of rows in the matrix.

p hole carrier density.

p_1 probability that a split event contributes to the background.

p_K probability that a photon is absorbed through the interaction with a K-shell electron.

p_d probability that an electron travels the distance d inside the sensitive volume.

p_{Escape} probability that an event contributes to the escape peak.

p_{Event} probability of an event inside the sensors sensitive volume.

p_{Loss} probability that an event is subject to charge losses.

p_{Main} probability that an event contributes to the main peak.

p_{Shelf} probability that an event contributes to the flat shelf.

p_{Tail} probability that an event contributes to the low energetic tail.

$p_{shelf_{Si}}$ probability that an electron with origin inside the sensitive volume contributes to the flat shelf.

p_{shelf_a} probability that an electron with origin inside the layer a contributes to the flat shelf.

p_{shelf_b} probability that an electron with origin inside the layer b contributes to the flat shelf.

p_{shelf_c} probability that an electron with origin inside the layer c contributes to the flat shelf.

q elemental charge.

r position inside the semiconductor.

r' position of a charge distribution.

t time.

t_c time the sensor collects incident charge.

t_i illumination time of the sensors.

t_u correction factor for inter-frame split events.

t_x sum of sampling time t_{sample} and effective clear time $t_{clear_{eff}}$.

t_{-c} time interval in that incident photons cause a negative signal.

t_{1-6} Point of time marking the end of a certain time interval that comprises the readout of a DEPFET device.

$t_{clear_{eff}}$ linear approximation to the time required to fully remove charge from the device.

t_{clear} time applied to clear charge from the internal gate.

t_{frame} time required to read out a complete DEPFET matrix.

t_{mux} time required to multiplex multiple signals to the ADC.

t_{rise} rise time of the DEPFET signal in source follower readout.

t_{row} time duration a row of a matrix is active.

$t_{sample1}$ first integration time of the readout ASIC, has to be equal to $t_{sample2}$.

$t_{sample2}$ second integration time of the readout ASIC, has to be equal to $t_{sample1}$.

t_{sample} integration time of the readout ASIC.

t_{set} settling time for the read-node.

$t_{shutter}$ linear approximation for the shutter rise time.

t_{switch} switching time for the built-in shutter.

t_s sum of all times that can be related to misfit events.

v charge carrier velocity.

v_{sat} charge carrier saturation velocity.

v_{sg} form of the output signal of a semi-Gaussian shaper.

w mean energy required to generate a single electron hole pair inside a semiconductor.

x_d width of the inversion layer of a MOS-structure in inversion.

z_0 distance from the sensor entrance window, at which charge losses are suggested to be zero.

Acknowledgements

This work would not have been started and even less likely finished without the encouragement and aid of of several people. First I want thank Prof. Dott. Andrea Santangelo and Dr. Jan-Christoph Tenzer for the opportunity to graduate at the Univerity of Tübingen.
My gratitude is also towards the different superiors at MPE who ensured the financial support of this work. Over the course of the last years these are Dr. Lothar Strüder, Prof. Kirpal Nandra and Dr. Norbert Meidinger.
Then there are Dr. Johannes Treis and Dr. Petra Majewski who convinced me to start a PhD and supported me throughout the past years. A special thanks for all the discussions, proofreading and valuable remarks. In addition to these two, a number of colleagues provided help, worthwhile discussions and also the motivation to get this work finished. Without any specific order these were Dr. Peter Lechner, Dr. Alexander Stefanescu, Dr. Thomas Lauf, Dr. Jelena Ninkovic, Rainer Richter and Dr Christian Sandow.
A special thanks I want to express towards Bettina Bergbauer for countless discussions, her friendship and the nice office atmosphere.
Also I would like to mention Danilo Miesner who always had an open ear and made even complex bondplans and chip assemblies possible.
Last but not least I want to thank my family and friends who supported me over the course of this work.

Bibliography

Abe, T. et al. (2010). "Belle II, Technical Design Report". In: *to be published*.

Akylas, A. et al. (2012). "Constraining the fraction of Compton-thick AGN in the Universe by modelling the diffuse X-ray background spectrum". In: *AaA* 546, A98, A98. DOI: 10.1051/0004-6361/201219387. arXiv: 1209.5398 [astro-ph.HE].

Alexander, D. M. and R. C. Hickox (2012). "What drives the growth of black holes?" In: *NewAR* 56, pp. 93–121. DOI: 10.1016/j.newar.2011.11.003. arXiv: 1112.1949.

Arid, J. et al. (2013). "The Hot and Energetic Universe: The formation and growth of the earliest supermassive black holes". In: *astro-ph*.

Aschauer, S. et al. (2014). "Prospects and limitations of DEPFET active pixels sensors as high speed spectroscopic x-ray imager for the ATHENA wide field imager". In: *Proc. SPIE 9144, Space Telescopes and Instrumentation 2014: Ultraviolet to Gamma Ray* 9144K. doi:10.1117/12.2056398 http://dx.doi.org/10.1117/12.2056398.

Bähr, A. (2010). "Experimenteller Betrieb neuartiger DEPFET-RNDR-Detektoren und mathematische Beschreibung der Mehrfachauslese". Diploma Thesis. Hochschule für Angewandte Wissenschaften-FH München.

Bähr, A. et al. (2014). "Spectral performance of DEPFET and gateable DEPFET macropixel devices". In: *JINST* 9. doi:10.1088/1748-0221/9/03/P03018 http://dx.doi.org/10.1088/1748-0221/9/03/P03018.

Barret, D. et al. (2013). "The X-ray Integral Field Unit (X-IFU) for Athena+". In: *[astro-ph.IM]*. arXiv:1308.6784 http://arxiv.org/abs/1308.6784.

Bautz, M. et al. (2009). "Active Pixel X-ray Sensor Technology for the Generation-X Wide-Field-Imager". In: *White paper, Astro2010: The Astronomyand Astrophysics Decadal Survey, EOS Discipline Program Panel*.

Beijersbergen, M. et al. (2004). "Silicon pore optics: novel lightweight high-resolution X-ray optics developed for XEUS". In: *UV and Gamma-Ray Space Telescope Systems*. Ed. by G. Hasinger and M. J. L. Turner. Vol. 5488. Proc. SPIE, pp. 868–874. DOI: 10.1117/12.585122.

Benkhoff, J. et al. (2010). "BepiColombo - Comprehensive exploration of Mercury: Mission overview and science goals". In: *Planetary and Space Science* 58, pp. 2–10.

Beole, S. et al. (2001). "Study of the uniformity of high resistivity neutron doped silicon wafers for silicon drift detectors". In: *Nuclear Instruments and Methods in Physics Research A* 473, pp. 319–325.

Bergbauer, B. (2015). "Study of macroscopic and microscopic homogeneity of DEPFET X-ray detectors". Dissertation. Chemnitz University of Technology.

Blandford, R. D. and D. G. Payne (1982). "Hydromagnetic flows from accretion discs and the production of radio jets". In: *MNRAS* 199, pp. 883–903. DOI: 10.1093/mnras/199.4.883.

Blustin, A. J. et al. (2005). "The nature and origin of Seyfert warm absorbers". In: *AaA* 431, pp. 111–125. DOI: 10.1051/0004-6361:20041775. eprint: astro-ph/0411297.

Bondi, H. (1952). "On spherically symmetrical accretion". In: *MNRAS* 112, p. 195. DOI: 10.1093/mnras/112.2.195.

Bouwens, R. J. et al. (2009). "UV Continuum Slope and Dust Obscuration from z 6 to z 2: The Star Formation Rate Density at High Redshift". In: *The Astrophysical Journal* 705.1, p. 936. URL: http://stacks.iop.org/0004-637X/705/i=1/a=936.

Canali, C. and G. Ottaviani (1970). "Saturation Values of the Electron Drift Velocity in Silicon Between 300°K and 4.2°K". In: *Physics Letters* 32A.3, pp. 147–148.

Cappi, M. et al. (2013). "The Hot and Energetic Universe: Astrophysics of feedback in local AGN". In: *astro-ph*.

Cen, R. and J. P. Ostriker (1999). "Where Are the Baryons?" In: *The Astrophysical Journal* 514.1, p. 1. URL: http://stacks.iop.org/0004-637X/514/i=1/a=1.

Chandra X-ray Center Chandra Project Science, MSFC, Chandra IPI Teams (2016). *The Chandra Proposers' Observatory Guide*. 19th ed. cited 04.09.2016.

Chruściel, P. T., J. L. Costa, and M. Heusler (2015). "Stationary Black Holes: Uniqueness and Beyond". In: *Living Rev. Relativity* 15.7. Online Article cited 9.3.2015 http://www.livingreviews.org/lrr-2012-7.

Civano, F. et al. (2011). "The Population of High-redshift Active Galactic Nuclei in the Chandra-COSMOS Survey". In: *ApJ* 741, 91, p. 91. DOI: 10.1088/0004-637X/741/2/91. arXiv: 1103.2570.

Cooper, J. W. (1992). "Photoelectron-angular-distribution for rare-gas subshells". In: *Physical Review A* 47.3, pp. 1841–1851.

Croston, J. H. et al. (2013). "The Hot and Energetic Universe: AGN feedback in galaxy clusters and groups". In: *astro-ph*.

Done, C. et al. (2012). "Intrinsic disc emission and the soft X-ray excess in active galactic nuclei". In: *MNRAS* 420, pp. 1848–1860. DOI: 10.1111/j.1365-2966.2011.19779.x. arXiv: 1107.5429 [astro-ph.HE].

Dovciak, M. et al. (2013). "The Hot and Energetic Universe: The close environments of supermassive black holes". In: *astro-ph*.

Ecker, D. et al. (2013). "The X-ray/SZ view of the virial region". In: *AaA* 551.A22. DOI: http://dx.doi.org/10.1051/0004-6361/201220402.

Ettori, S. et al. (2013). "The Hot and Energetic Universe: The astrophysics of galaxy groups and clusters". In: *astro-ph*.

Fabian, A. C. (2012). "Observational Evidence of Active Galactic Nuclei Feedback". In: *ARaA* 50, pp. 455–489. DOI: 10.1146/annurev-astro-081811-125521. arXiv: 1204.4114.

Fabian, A. C. et al. (2000). "Broad Iron Lines in Active Galactic Nuclei". In: *PASP* 112, pp. 1145–1161. DOI: 10.1086/316610. eprint: astro-ph/0004366.

Fabian, A. C. et al. (2009). "Broad line emission from iron K- and L-shell transitions in the active galaxy 1H0707-495". In: *Nature* 459, pp. 540–542. DOI: 10.1038/nature08007.

Fang, T. et al. (2010). "CONFIRMATION OF X-RAY ABSORPTION BY WARM-HOT INTERGALACTIC MEDIUM IN THE SCULPTOR WALL". In: *ApJ* 714.2.

Fano, U. (1947). "Ionization Yield of Radiations. II. The Fluctuation of the Number of Ions". In: *Physical Review* 72.1, pp. 26–28.

Fitting, H. J. (1974). "Transmission, Energy Distribution, and SE Excitation of Fast Electrons in Thin Solid Films". In: *Phys. Stat. Sol.* a.26.

Fraser, G. W (1989). *X-ray detectors in astronomy*. Ed. by J. E. Pringle. Cambridge university press. ISBN: 0-521-32663-X.

Fraser, G. W. et al. (2010). "The Mercury imaging X-ray spectrometer (MIXS) on Bepi-Colombo". In: *Planetary and Space Science* 58, pp. 79–95.

Gaspari, M., M. Ruszkowski, and P. Sharma (2012). "Cause and Effect of Feedback: Multiphase Gas in Cluster Cores Heated by AGN Jets". In: *The Astrophysical Journal* 746.1, p. 94. URL: http://stacks.iop.org/0004-637X/746/i=1/a=94.

Gatti, E. and P. Rehak (1984). "Semiconductor Drift Chamber - An Application of a Novel Charge Transport Scheme". In: *Nuclear Instruments and Methods in Physics Research* 225.3. doi:10.1016/0167-5087(84)90113-3, pp. 608–614.

Gatti, E. et al. (1990). "Subobtimal filtering of 1/f-noise in detector charge measurements". In: *Nuclear Instruments and Methods in Physics Research* A.297, pp. 467–478.

Genzel, R. et al. (2003). "Near-infrared flares from accreting gas around the supermassive black hole at the Galactic Centre". In: *Nature* 425, pp. 934–937. DOI: 10.1038/nature02065. eprint: astro-ph/0310821.

Georgakakis, A. et al. (2009). "Host galaxy morphologies of X-ray selected AGN: assessing the significance of different black hole fuelling mechanisms to the accretion density of the Universe at z ˜ 1." In: *MNRAS* 397, pp. 623–633. DOI: 10.1111/j.1365-2966.2009.14951.x. arXiv: 0904.3747.

Georgakakis, A. et al. (2013). "The Hot and Energetic Universe: Understanding the build-up of supermassive black holes and galaxies at the heyday of the Universe". In: *astro-ph*.

Giacconi, R. et al. (1962). "Evidence for X Rays From Sources Outside the Solar System". In: *Phys. Rev. Lett.* 9. http://dx.doi.org/10.1103/PhysRevLett.9.439.

Granato, S. (2012). "The respone of silicon PNCCD sensors with aluminum on-chip filter to visible light, UV- and X-ray radiation". Dissertation. Universität Siegen.

Gullikson, E. M. *X-Ray Interaction With Matter*. website. cited on 28.8.2014 http://henke.lbl.gov/optical_constants/atten2.html.

Hawking, S. (1973). "The Event Horizon". In: ed. by C. De Witt and B. S. De Witt. New Yourk: Gordon and Breack, pp. 5–34.

Henke, B. L., E. M. Gullikson, and J. C. Davis (1993). "X-Ray Interactions: Photoabsorbtion, Scattering, Transmission, and Reflection at E=50-30,000eV, Z=1-92". In: *Atomic Data and Nuclear Data Tables* 54.2. doi:10.1006/adnd.1993.1013, pp. 181–342.

Holl, P. et al. (2003). "Active pixel sensors for imaging X-ray spectrometers". In: *Proceedings SPIE: X-Ray and Gamma-Ray Telescopes and Instruments for Astronomy*, pp. 770–778.

Hopkins, A. M. and J. F. Beacom (2006). "On the Normalization of the Cosmic Star Formation History". In: *ApJ* 651.1, pp. 142–154.

Hubbell, J. H. and S. M. Seltzer. *Tables of X-Ray Mass Attenuation Coefficients and Mass Energy-Absorption Coefficients from 1 keV to 20 MeV for Elements Z = 1 to 92 and 48 Additional Substances of Dosimetric Interest*. website. http://www.nist.gov/pml/data/xraycoef/ cited: June 2015.

Illustration: NASA/CXC/ M. Weiss; Spectra: NASA/CXC/SAO/ J. Miller (2003). *Spinning Black Hole Chandra*. http://www.nasa.gov/centers/marshall/images/content/99164main_bhspin_comp.jpg.

Irwin, K. D. and G. C. Hilton (2005). "Transition-Edge Sensors". In: *Topics Apl. Phys.* 99, pp. 63–149.

Iskeff, H., J. W. Cunningham, and D. E. Watt (1983). "Projected ranges and effective stopping powers of electrons with energy between 20 eV and 10 keV". In: *Phys. Med. Biol.* 28.5, pp. 535–545.

J.Kemmer and G. Lutz (1987). "NEW DETECTOR CONCEPTS". In: *Nucl. Instr. and Meth. A* 253, pp. 365–377.

Kaastra, J. et al. (2013). "The Hot and Energetic Universe: The missing baryons and the warm-hot intergalactic medium". In: *astro-ph*.

Kazanas, D. et al. (2012). "X-ray Absorbers, MHD Winds, and AGN Unification". In: *AGN Winds in Charleston*. Ed. by G. Chartas, F. Hamann, and K. M. Leighly. Vol. 460. Astronomical Society of the Pacific Conference Series, p. 181.

Kerr, R. P. (1963). "Gravitational Field of a Spinning Mass as an Example of Algebraically Special Metrics". In: *Phys. Rev. Lett* 11.

Kirkpatrick, C. C., B. R. McNamara, and K. W. Cavagnolo (2011). "Anisotropic Metal-enriched Outflows Driven by Active Galactic Nuclei in Clusters of Galaxies". In: *The Astrophysical Journal Letters* 731.2, p. L23. URL: http://stacks.iop.org/2041-8205/731/i=2/a=L23.

Knoll, G. F. (1999). *Radiation Detection and Measurement*. 3rd ed. John Wiley and Son. ISBN: 978-0-471-07338-3.

Kocevski, D. D. et al. (2012). "CANDELS: Constraining the AGN-Merger Connection with Host Morphologies at z 2". In: *The Astrophysical Journal* 744.2, p. 148. URL: http://stacks.iop.org/0004-637X/744/i=2/a=148.

Lauf, T. (2011). "Analysis and Operation of DePFET X-ray Imaging Detectors". Dissertation. Technische Universität München.

Li, Y. et al. (2007). "Formation of z˜6 Quasars from Hierarchical Galaxy Mergers". In: *ApJ* 665, pp. 187–208. DOI: 10.1086/519297. eprint: astro-ph/0608190.

Lowe, B.G. and R.A. Sareen (2007). "A measurement of the electron-hole pair creation energy and the Fano factor in silicon for 5.9 keV X-rays and their temperature dependence in the range 80-270 K". In: *Nuclear Instruments an Methods in Physics Research A* 576, pp. 367–370.

Lumb, D.H. et al. (2012). "Athena Assessment Study Report". In: *ESA SRE* 17. http://sci.esa.int/jump.cfm?oid=49835, pp. 1–126.

Lutz, G. (1999). *Semiconductor Radiation Detectors*. 1st ed. Springer. ISBN: 978-3-540-71678-5.

Lutz, G. et al. (2007). "DEPFET Detector-Amplifier Structure: Properties, Achievements and New Developments, Concepts and Applications". In: *NSS* N18-5.

Macculi, C. et al. (2014). "The Cryogenic AntiCoincidence Detector Project for ATHENA+: An Overview Up to the Present Status". In: *Journal of Low Temperature Physics* 176.5, pp. 1022–1032. ISSN: 1573-7357. DOI: 10.1007/s10909-014-1150-4. URL: http://dx.doi.org/10.1007/s10909-014-1150-4.

Matt, G. and G. C. Perola (1992). "The iron K-alpha response in an X-ray illuminated relativistic disc and a black hole mass estimate". In: *MNRAS* 259, pp. 433–436. DOI: 10.1093/mnras/259.3.433.

Mazur, P. O. (2000). "Black Hole Uniqueness Theorems". In: *hep-th*. arXiv:hep-th/0101012 http://arxiv.org/abs/hep-th/0101012v1.

McGaugh, S. S. et al. (2010). "The Baryon Content of Cosmic Structures". In: *ApJ* 708, pp. L14–L17. DOI: 10.1088/2041-8205/708/1/L14. arXiv: 0911.2700 [astro-ph.CO].

McKernan, B., T. Yaqoob, and C. S. Reynolds (2007). "A soft X-ray study of type I active galactic nuclei observed with Chandra high-energy transmission grating spectrometer". In: *MNRAS* 379.4, pp. 1359–1372. DOI: doi:10.1111/j.1365-2966.2007.11993.x.

McNamara, B. R. and P. E. J. Nulsen (2007). "Heating Hot Atmospheres with Active Galactic Nuclei". In: *ARaA* 45, pp. 117–175. DOI: 10.1146/annurev.astro.45.051806.110625. arXiv: 0709.2152.

Merloni, A., G. Rudnick, and T. Di Matteo (2004). "Tracing the cosmological assembly of stars and suppermassive black holes in galaxies". In: *astro-ph*.

Mortlock, D. J. et al. (2011). "A luminous quasar at a redshift of z = 7.085". In: *Nature* 474, pp. 616–619. DOI: 10.1038/nature10159. arXiv: 1106.6088 [astro-ph.CO].

Motch, C. et al. (2013). "The Hot and Energetic Universe: Endpoints of stellar evolution". In: *astro-ph*.

Nandra, K. (2006). "On the origin of the iron Kα line cores in active galactic nuclei". In: *MNRAS* 368, pp. L62–L66. DOI: 10.1111/j.1745-3933.2006.00158.x. eprint: astro-ph/0602081.

Nandra, K. et al. (2013). "The Hot and Energetic Universe: A White Paper presenting the science theme motivating the Athena+ mission". In: *[astro-ph.HE]*. arXiv:1306.2307 http://arxiv.org/abs/1306.2307.

Nandra, K. et al. (2014). "The Athena Mission Proposal". In: http://www.the-athena-x-ray-observatory.eu/, cited on the 13.11.2015.

Nicastro, F. et al. (2013). "Chandra View of the Warm-hot Intergalactic Medium toward 1ES 1553+113: Absorption-line Detections and Identifications. I." In: *ApJ* 769, 90, p. 90. DOI: 10.1088/0004-637X/769/2/90. arXiv: 1210.7177.

Perkins, S. T., M. H. Chen, and J. H. Hubbel (1991). "Tables and graphs of atomic subshell and relaxation data derived from the LLNL Evaluated Atomic Data Library (EADL), Z=1-100". In: *Lawrence Livermore National Laboratory*.

Peterson, J. R. et al. (2003). "High-Resolution X-Ray Spectroscopic Constraints on Cooling-Flow Models for Clusters of Galaxies". In: *ApJ* 590, pp. 207–224. DOI: 10.1086/374830. eprint: astro-ph/0210662.

Pointecouteau, E. et al. (2013). "The Hot and Energetic Universe: The evolution of galaxy groups and clusters". In: *astro-ph*.

Porquet, D. et al. (2008). "X-ray hiccups from Sagittarius A* observed by XMM-Newton. The second brightest flare and three moderate flares caught in half a day". In: *AaA* 488, pp. 549–557. DOI: 10.1051/0004-6361:200809986. arXiv: 0806.4088.

Porro, M. et al. (2006). "Spectroscopic performances of DePMOS detector/amplifier device with respect to different filtering techniques and operating conditions". In: *IEEE TNS* 53.1. http://ieeexplore.ieee.org/stamp/stamp.jsp?tp=&arnumber=4437181&isnumber=4437154, pp. 401–408.

Porro, M. et al. (2010). "ASTEROID: A 64 channel ASIC for source follower readout of DEPFET arrays for X-ray astronomy". In: *Nucl. Instr. and Meth. A* 617, pp. 351–357.

Porro, M. et al. (2012). "Development of the DEPFET Sensor With Signal Compression: A Large Format X-Ray Imager With Mega-Frame Readout Capability for the European XFEL". In: *Trans. on Nucl. Sci.* 59.6, pp. 3339–3351.

Pratt, R. H., Akiva Ron, and H. K. Tseng (1973). "Atomic Photoelectric Effect above 10 keV". In: *Reviews of Modern Physics* 45.2, pp. 273–325.

Psaltis, D. (2004). "Accreting Neutron Stars and Black Holse: A Decade of Discoveries". In: *astro-ph*. arXiv:astro-ph/0410536 http://arxiv.org/abs/astro-ph/0410536, p. 42.

Rando, N. et al. (2010). "ESA assessment study activities on the International X-ray Observatory". In: vol. 7732, pp. 77321C–77321C–11. DOI: 10.1117/12.856825. URL: http://dx.doi.org/10.1117/12.856825.

Rauch, M. (1998). "The Lyman Alpha Forest in the Spectra of QSOs". In: *ARaA* 36, pp. 267–316. DOI: 10.1146/annurev.astro.36.1.267. eprint: astro-ph/9806286.

Reed, S. J. B. and N. G. Ware (1972). "Escape peaks and internal fluorescence in x-ray spectra recorded with lithium drifted silicon detectors". In: *Journal of Physics E: Scientific Instruments* 5, pp. 582–584.

Remillard, R. A. and J. E. McClintock (2006). "X-ray Properties of Black Hole Binaries". In: *Ann.Rev.Astron.Astrophys* 44. arXiv:astro-ph/0606352 http://arxiv.org/abs/astro-ph/0606352, pp. 49–92.

Roosbroeck, W. van (1950). "Theoy of the Flow of Electrons and Holes in Germanium and Other Semiconductors". In: *Bell System Technical Journal* 29, pp. 560–607.

Rosario, D. J. et al. (2012). "The mean star formation rate of X-ray selected active galaxies and its evolution from z ~ 2.5: results from PEP-Herschel". In: *AaA* 545, A45, A45. DOI: 10.1051/0004-6361/201219258. arXiv: 1203.6069 [astro-ph.CO].

Ross, R. R. and A. C. Fabian (2005). "A comprehensive range of X-ray ionized-reflection models". In: *MNRAS* 358, pp. 211–216. DOI: 10.1111/j.1365-2966.2005.08797.x. eprint: astro-ph/0501116.

S. Wölfel (2007). "Neuartige DEPFET-RNDR-Detektoren im experimentellen Betrieb". Dissertation. Universität Siegen.

Sanders, J. S. and A. C. Fabian (2013). "Velocity width measurements of the coolest X-ray emitting material in the cores of clusters, groups and elliptical galaxies". In: *MNRAS* 429.3. DOI: doi:10.1093/mnras/sts543.

Sanders, J. S. et al. (2008). "Cool X-ray emitting gas in the core of the Centaurus cluster of galaxies". In: *MNRAS* 385, pp. 1186–1200. DOI: 10.1111/j.1365-2966.2008.12952.x. arXiv: 0711.2456.

Sauter, F. (1931a). "Über den atomaren Photoeffect bei großer Härte der anregenden Strahlung". In: *Annalen der Physik* 5.9, p. 217.
– (1931b). "Über den atomaren Photoeffect in der K-Schale nach der relativistischen Wellenmechanik Diracs". In: *Annalen der Physik* 5.9, p. 454.
Scholze, F. and M. Procop (2009). "Modelling the response function of energy dispersive X-ray spectrometers with silicon detecotrs". In: *X-RAY Spectrometry* 38. doi:10.1002/xrs.1165 http://onlinelibrary.wiley.com/doi/10.1002/xrs.1165/abstract, pp. 312–321.
Scholze, F., H. Rabus, and G. Ulm (1998). "Mean energy required to produce an electron-hole pair in silicon for photons of energies between 50 and 1500 eV". In: *Journal of Applied Physics* 84.5. http://dx.doi.org/10.1063/1.368398.
Schottky, W. (1918). "Über spontanen Stromschwankungen in verschiedenen Elektrizitätsleitern". In: *Annalen der Physik* 362, pp. 541–567.
Schötzig, U. (2000). "Half Life and emission probabilities of ^{55}Fe". In: *Applied Radiation and Isotopes* 53, pp. 469–472.
Schwarzschild, K. (1916). "Über das Gravitationsfeld eines Massenpunktes nach der Einsteinschen Theorie". In: *Sitzungsbericht der KöniglichPreussischen Akademie der Wissenschaften*, pp. 189–196.
Seltzer, S. M. (1993). "Calculation of Photon Mass Energy-Transfer and Mass Energy-Absorbtion Coefficients". In: *Radiation Research* 136.2, pp. 147–170.
Shull, J. M., B. D. Smith, and C. W. Danforth (2012). "The Baryon Census in a Multiphase Intergalactic Medium: 30% of the Baryons May Still be Missing". In: *ApJ* 759, 23, p. 23. DOI: 10.1088/0004-637X/759/1/23. arXiv: 1112.2706.
Springel, V. et al. (2005). "Simulations of the formation, evolution and clustering of galaxies and quasars". In: *Nature* 435.2. DOI: doi:10.1038/nature03597.
Sze, S. M. and Kwok K. Ng (2007). *Physics of Semiconductor Detectors*. 3rd ed. John Wiley and Son. ISBN: 978-0-471-14323-9.
Tietze, U. and Ch. Schenk (2002). *Halbleiter-Schaltungstechnik*. 12th ed. Springer. ISBN: 3-540-42849-6.
Tombesi, F. et al. (2010). "Evidence for ultra-fast outflows in radio-quiet AGNs. I. Detection and statistical incidence of Fe K-shell absorption lines". In: *AaA* 521, A57, A57. DOI: 10.1051/0004-6361/200913440. arXiv: 1006.2858 [astro-ph.HE].
Tombesi, F. et al. (2013). "Unification of X-ray winds in Seyfert galaxies: from ultra-fast outflows to warm absorbers". In: *MNRAS* 430, pp. 1102–1117. DOI: 10.1093/mnras/sts692. arXiv: 1212.4851 [astro-ph.HE].
Treis, J. et al. (2010). "MIXS on BepiColombo and its DEPFET based focal plane instrumentation". In: *Nucl. Instr. and Meth. A* 624, pp. 540–547.
Trichas, M. et al. (2012). "The Chandra Multi-wavelength Project: Optical Spectroscopy and the Broadband Spectral Energy Distributions of X-Ray-selected AGNs". In: *The Astrophysical Journal Supplement Series* 200.2, p. 17. URL: http://stacks.iop.org/0067-0049/200/i=2/a=17.
Trzhaskovskaya, M. B., V. I. Nefedov, and V. G. Yarzhemsky (2001). "Photoelectron angular distribution parameters for elements Z=1 to Z=54 in the photoelectron energy

range 100-5000 eV". In: *Atomic Data and Nuclear Data Tables* 77. doi:10.1006/adnd.2000.0849, pp. 97–159.

Trzhaskovskaya, M. B. et al. (2006). "Non-dipole second order parameters of the photoelectron angular distribution for elements Z=1 to Z=100 in the photoelectron pnergy pange 1-10000 keV". In: *Atomic Data and Nuclear Data Tables* 92. doi:10.1016/j.adt.2005.12.002, pp. 245–304.

Tsividis, Y. (1999). *Operation and Modeling of The MOS Transistor*. Vol. Second Edition. Oxford University Press. ISBN: ISBN: 0195170148.

Tumlinson, J. et al. (2011). "The Large, Oxygen-Rich Halos of Star-Forming Galaxies Are a Major Reservoir of Galactic Metals". In: *Science* 334, p. 948. DOI: 10.1126/science.1209840. arXiv: 1111.3980.

Veilleux, S., G. Cecil, and J. Bland-Hawthorn (2005). "Galactic Winds". In: *ARAA* 43, pp. 769–826. DOI: 10.1146/annurev.astro.43.072103.150610. eprint: astro-ph/0504435.

Voit, M. G. (2005). "Tracing cosmic evolution with clusters of galaxies". In: *Rev. Mod. Phys.* 77.1.

Voort, F. van de et al. (2011). "The rates and modes of gas accretion on to galaxies and their gaseous haloes". In: *MNRAS* 414.3, pp. 2458–2478. DOI: doi:10.1111/j.1365-2966.2011.18565.x.

Wagner, A. Y., M. Umemura, and G. V. Bicknell (2013). "Ultrafast Outflows: Galaxy-scale Active Galactic Nucleus Feedback". In: *The Astrophysical Journal Letters* 763.1, p. L18. URL: http://stacks.iop.org/2041-8205/763/i=1/a=L18.

Walton, D. J. et al. (2013). "Suzaku observations of 'bare' active galactic nuclei". In: *MNRAS* 428.4, pp. 2901–2920. DOI: doi:10.1093/mnras/sts227.

Weinberg, D. H. et al. (1997). "A Lower Bound on the Cosmic Baryon Density". In: *The Astrophysical Journal* 490.2, p. 564. URL: http://stacks.iop.org/0004-637X/490/i=2/a=564.

Werner, N. et al. (2008). "Observations of Metals in the Intra-Cluster Medium". In: *Space Science Reviews* 134.1, pp. 337–362. ISSN: 1572-9672. DOI: 10.1007/s11214-008-9320-9. URL: http://dx.doi.org/10.1007/s11214-008-9320-9.

Willingale, R. et al. (2013). "The Optical Design of the Athena+ Mirror". In: http://athena2.irap.omp.eu/IMG/pdf/athenapp_optics_design.pdf.

Wolter, H. (1952). "Spiegelsysteme streifenden Einfalls als abbildende Optiken für Röntgenstrahlen". In: *annalen der physik* 445.1-2, pp. 94–114. DOI: 10.1002/andp.19524450108.

XMM-Newton SOC (2016). *XMM-Newton Users Handbook*. 2nd ed. cited 04.09.2016. ESA.

List of Figures

List of Tables